Technische Universität München

TECHNISCHE UNIVERSITÄT MÜNCHEN

Lehrstuhl für Lebensmittel- und Bio-Prozesstechnik

On the displacement of non-Newtonian fluids from spiral-wound membranes

Ingrun Edith Kieferle

Vollständiger Abdruck der von der Fakultät Wissenschaftszentrum Weihenstephan für Ernährung, Landnutzung und Umwelt der Technischen Universität München zur Erlangung des akademischen Grades eines

Doktor-Ingenieurs

genehmigten Dissertation.

Vorsitzende: Prof. Dr. Mirjana Minceva

Prüfer der Dissertation:
1. Prof. Dr.-Ing. Ulrich Kulozik
2. Prof. Dr.-Ing. Harald Klein
3. Prof. Dr.-Ing. Stefan Panglisch

Die Dissertation wurde am 22.10.2019 bei der Technischen Universität München eingereicht und durch die Fakultät Wissenschaftszentrum Weihenstephan für Ernährung, Landnutzung und Umwelt am 18.05.2020 angenommen.

’Essentially, all models are wrong, but some are useful.’

(George Box)

Preface

This thesis was prepared between November 2015 and October 2019 under the supervision of Prof. Dr.-Ing. Ulrich Kulozik to whom I want to express my sincere thanks. The comprehensive freedom of decisions he provided with regard to the project management is considered a great sign of confidence and gave me the possibility to design the project according to my own ideas.

In terms of the time-consuming examination of this thesis, I thank Prof. Dr.-Ing. Ulrich Kulozik, Prof. Dr.-Ing. Stefan Panglisch and Prof. Dr.-Ing. Harald Klein. Besides, I am grateful that Prof. Dr. Mirjana Minceva accepted the role of the chairman.

Beyond that, I would like to thank Prof. Dr. David Meintrup, Dr. Hannes Petermeier, and Dr. Volker Kraft who contributed to my personal development in diverse respects. Also the cooperation with Prof. Dr. Natalie Germann and her staff is gratefully acknowledged.

Concerning the support in the implementation of experiments, I am deeply indebted to the helping hands of the technical staff members. Furthermore, the long-term employees in the secretary's office and the IT support were always ready to help. With regard to modifications of the experimental setup, the workshop team provided advice and practical assistance whenever I needed it. Last but not least, I want to emphasize the contribution of my colleagues and my former students to this thesis. I am very grateful for your individual commitment.

Finally, it remains for me to express my gratitude to my immediate and extended family who supported me along the whole path. Particularly Mario Nast was always at my side – no matter how high the mountains were.

Abstract

In the industrial practice, cleaning cycles are usually initiated by the displacement of the product from the plant by water. While the displacement process is well-understood for simple geometries such as pipes, the displacement of viscous fluids from spiral-wound membranes is barely investigated. Hence, this thesis aims at contributing to the understanding of the hydrodynamic processes determining the residence time behavior of non-Newtonian fluids in spiral-wound membranes during the displacement process.

In order to reach this aim, two approaches are presented. Firstly, the residence time, which is the time required to complete the displacement, is described as a function of the process conditions based on response surface models. Here, the flow rate, the geometric dimensions of the feed spacers, the viscosity of the product, and the displacing fluid's viscosity and temperature are considered as possible influencing factors. Secondly, the advection-dispersion model, the compartment model, and a combination of both models are applied. These mechanistic models can give an idea of the hydrodynamic processes prevailing in the spiral-wound membranes during the displacement process.

The response surface models confirm the initial assumption that the key influencing factors are the flow rate, the viscosity of the product, and the geometric dimensions of the feed spacers. In contrast, the displacing fluid's temperature and viscosity do not affect the residence time significantly in the considered factor space. Consequently, the flow rate and the dimensions of the spacers should be adapted to the product viscosity when aiming at the manipulation of the residence time. The mechanistic models allow the characterization of the hydrodynamic behavior of the different plant sections and suggest that the spiral-wound membrane behaves like a plug flow reactor with axial dispersion. Furthermore, a bypass around the membrane module needs to be considered as it affects the observed residence time behavior to an appreciable extent. Finally, the estimation of the residence time behavior of viscous products in a filtration plant on an industrial scale equipped with spiral-wound membranes is possible based on an adapted model. The results underline once again the importance of the flow rate as a factor influencing the residence time behavior during the displacement.

Kurzfassung

In der industriellen Praxis werden Reinigungszyklen in der Regel durch das Ausschieben des Produktes aus der Anlage mit Wasser eingeleitet. Während der Ausschiebeprozess für einfache Geometrien wie Rohre gut verstanden ist, ist das Ausschieben viskoser Flüssigkeiten aus Spiralwickelmembranen kaum untersucht. Demnach, ist es das Ziel dieser Arbeit, zum Verständnis der hydrodynamischen Prozesse beizutragen, welche die Verweilzeit nicht-Newton’scher Fluide in Spiralwickelmembranen während des Ausschiebeprozesses bestimmen.

Zur Erreichung dieses Ziels, werden zwei Ansätze vorgestellt. Im ersten Ansatz wird die Verweilzeit, welche die Zeit ist, die zur Beendigung des Ausschiebens benötigt wird, mit Hilfe statistischer Modelle als Funktion der Prozessbedingungen beschrieben. Hierbei werden der Volumenstrom, die geometrischen Dimensionen der Feed-Spacer, die Viskosität des Produktes sowie die Temperatur und Viskosität des Ausschiebe-Fluids als mögliche Einflussfaktoren berücksichtigt. Im zweiten Ansatz werden das Advektions-Dispersions-Modell, das Kompartimente-Modell und eine Kombination beider Modelle angewandt. Diese mechanistischen Modelle können einen Eindruck der hydrodynamischen Prozesse vermitteln, die während des Ausschiebens in der Spiralwickelmembran vorherrschen.

Die statistischen Modelle bestätigt die anfängliche Annahme, dass der Volumenstrom, die Viskosität des Produktes und die geometrischen Dimensionen der Feed-Spacer die Haupteinflussfaktoren darstellen. Im Gegensatz hierzu wird die Verweilzeit von der Temperatur und der Viskosität des Ausschiebe-Fluids im untersuchen Faktorraum nicht signifikant beeinflusst. Folglich sollten der Volumenstrom und die geometrischen Dimensionen der Feed-Spacer an die Viskosität des Produktes angepasst werden, wenn eine Minimierung der Verweilzeit angestrebt wird. Die mechanistischen Modelle erlauben eine Charakterisierung des hydrodynamischen Verhaltens der unterschiedlichen Anlagensegmente und deuten darauf hin, dass sich die Spiralwickelmembran wie ein Rohrreaktor mit axialer Dispersion verhält. Außerdem muss eine Bypass-Strömung um das Membranmodul berücksichtigt werden, da diese die beobachteten Verweilzeiten maßgeblich beeinflusst. Schließlich ist es möglich, das Verweilzeitverhalten viskoser Produkte in einer mit Spiralwickelmembranen ausgestatteten Filtrationsanlage im Industriemaßstab mit Hilfe eines angepassten Modells abzuschätzen. Die Ergebnisse unterstreichen die Wichtigkeit des Volumenstroms als ein die Verweilzeit während des Ausschiebens beeinflussender Faktor erneut.

Contents

Symbols

Latin	Unit	Description
A	AU	Absorption
A_c	m^2	Cross-sectional area
A_0	AU	Initial absorption
A_{cal}	AU	Calculated initial absorption
A_{max}	AU	Maximal absorption
A_s	m^2	Area of the spacer
A_M	$\frac{s}{m}$	Membrane constant
$AICc$	$-$	Corrected Akaike information criterion
c	$-$	Relative concentration
C	$-$	Compartment
C_C	$\frac{kg}{kg}$	Concentration in the core flow
C_J	$\frac{kg}{kg}$	Concentration in the permeate
C_M	$\frac{kg}{kg}$	Concentration in the direct vicinity of the membrane
C_P	$\frac{kg}{kg}$	Protein concentration
C_X	$\frac{kg}{kg}$	Xanthan concentration
d	m	Pipe diameter
d_f	m	Filament diameter
d_h	m	Hydraulic diameter
D_a	$\frac{m^2}{s}$	Axial dispersion coefficient
D_m	$\frac{m^2}{s}$	Molecular dispersion coefficient
erf	$-$	Gaussian error function
$E(t)$	$-$	Distribution function
f	$-$	Frequency/mathematical function
F	$-$	Test statistics of the F-test

Latin	**Unit**	**Description**
$\mathcal{F}\{\}$	$-$	Fourier transform operator
$F(t)$	$-$	Cumulative distribution function
$F^*(t)$	$-$	Residue function
$F_w(t)$	$-$	Cumulative distribution function (Weibull distribution)
G'	Pa	Loss modulus
G''	Pa	Storage modulus
G^*	Pa	Complex shear modulus
h_c	m	Channel height/spacer thickness
$h(t)$	$-$	Transfer function
H	$Pa \cdot s$	Characteristic viscosity constant
$H(\omega)$	$-$	Fourier transform of the transfer function
j	$-$	Imaginary unit
J	$\frac{kg}{m^2 \cdot s}$	Flux
k	$Pa \cdot s^n$	Consistency index
k_B	$\frac{m^2 \cdot kg}{s^2 \cdot K}$	Boltzmann constant (= 1,38065 × 10^{-23})
k_{DF}	$Pa \cdot s^n$	Consistency index of the displacing fluid
k_{MP}	$Pa \cdot s^n$	Consistency index of the model product
k_{PC}	$Pa \cdot s^n$	Consistency index of the protein concentrate
k_{XS}	$Pa \cdot s^n$	Consistency index of the xanthan solution
l_m	m	Mesh length
l_s	$\frac{m}{m^2}$	Specific length of the spacer
L	m	Reactor length
L_i	m	Length of the compartment i
$\hat{L}$	$-$	Maximum value of the likelihood function
L_c	m	Characteristic length
L_m	m	Length of the module

Latin	**Unit**	**Description**
$\dot{m}$	$\frac{kg}{s}$	Mass flow
n	$-$	Fluid index
n_{PC}	$-$	Fluid index of the protein concentrate
n_{XS}	$-$	Fluid index of the xanthan solution
N	$-$	Number of observations
Δp	$\frac{N}{m^2}$	Pressure drop
Δp_{TM}	$\frac{N}{m^2}$	Transmembrane pressure
Pe	$-$	Péclet number
R^2	$-$	Coefficient of determination
r_0	m	Particle radius
r_e	m	Equivalent radius
Re	$-$	Reynolds number
Re_{DF}	$-$	Reynolds number of the displacing fluid
Re_{MP}	$-$	Reynolds number of the model product
$RMSE$	$variable$	Root mean square error
s^2	$variable$	Estimate for the variance
S_s	$\frac{m^2}{m^2}$	Specific surface of the spacer
S_c	$\frac{m^2}{m^2}$	Specific surface of the channel
Sc	$-$	Schmidt number
Sh	$-$	Sherwood number
SSE	$variable$	Sum of squared errors
t	s	Time
$\bar{t}$	s	Mean residence time (1st raw moment)
t_d	s	Delay time
u	$\frac{m}{s}$	Flow velocity
u_a	$\frac{m}{s}$	Average flow velocity

Latin	**Unit**	**Description**
V	m^3	Volume
V_s	$\frac{m^3}{m^2}$	Specific volume of the spacer
V_P	m^3	Volume of the plug-flow compartment
V_T	m^3	Volume of the stirred-tank compartment
$\dot{V}$	$\frac{m^3}{s}$	Flow rate
$\dot{V}_a$	$\frac{m^3}{s}$	Flow rate in the main stream
$\dot{V}_b$	$\frac{m^3}{s}$	Flow rate in the side stream
$\dot{V}_F$	$\frac{m^3}{s}$	Flow rate
W	$-$	Test statistics of the Shapiro-Wilk test
x	m	Position
$x(t)$	$-$	Input function
x_i	$variable$	Independent factor
$X(\omega)$	$-$	Fourier transform of the input function
y	$variable$	Response variable
$y(t)$	$-$	Output function
$\bar{y}$	$variable$	Mean of the response variables
$\hat{y}$	$variable$	Estimate of the response variable
y_i	$variable$	Observations of the response variable
$Y(\omega)$	$-$	Fourier transform of the output function

Greek	**Unit**	**Description**
α	°	Flow attack angle
α_i	–	Share of the total volume flow in the compartment i
α_R	–	Aspect ratio
β	°	Internal strand angle
β_i	–	Regression coefficients
β_m	$\frac{m}{s}$	mass transfer coefficient
$\dot{\gamma}$	$\frac{1}{s}$	Shear rate
ε_s	–	Porosity of the spacer
ε_{SWM}	–	Porosity of the spiral-wound membrane
ϵ	–	Pipe roughness
ζ	–	Relative position
η	$Pa \cdot s$	Dynamic viscosity
η_a	$Pa \cdot s$	Average dynamic viscosity
θ	–	Dimensionless time
Θ	s	Characteristic time constant
κ	$\frac{S}{m}$	Conductivity
λ	–	Scale parameter (Weibull distribution)
ξ	$variable$	Residual
π	–	Constant (= 3.14159)
π_i	–	Dimensionless numbers
$\Delta\pi$	$\frac{N}{m^2}$	Osmotic pressure difference
ρ	$\frac{kg}{m^3}$	Density
σ	$variable$	Standard deviation
σ^2	$variable$	Variance
σ_e^2	$\frac{1}{s^2}$	Experimental variance (2nd central moment)
σ_m^2	$\frac{1}{s^2}$	Model variance

Greek	Unit	Description
τ	Pa	Shear stress
τ_r	s	Relaxation time
τ_t	s	Hydraulic residence time
ϕ	–	Mathematical function
φ	–	Shape parameter (Weibull distribution)
ψ	–	Number of parameter estimates
ω	–	Angular frequency
ω_c	$\frac{1}{s}$	Critical frequency

Abbreviations

	Description
ADM	Advection-dispersion model
AICc	Corrected Akaike information criterion
DoE	Design of experiments
DF	Displacing fluid
MP	Model product
PC	Protein concentrate
RMSE	Root mean square error
SSE	Sum of squared errors
SW	Soft water
SWM	Spiral-wound membrane
XS	Xanthan solution

1 Introduction

Initially used in all aspects of water treatment, spiral-wound membranes have become indispensable in further fields of application such as concentration or fractionation in the manufacture of food (Beckman and Barbano, 2013; Roblet et al., 2012; Ghosh et al., 2000). Reasons for their large popularity are the high membrane area at low space requirements and the flexibility of the design allowing the rapid introduction of technical innovations into the industrial practice (Antrim et al., 2005, p. 313). Besides, spiral-wound membranes are available for the whole range of filtration tasks, from microfiltration to reverse osmosis, while other membrane types are limited to particular types of filtration. As shown in Fig. 1, spiral-wound membranes have a multi-layered design, where the product flow passes through a feed spacer along the entire module length. Here, the retained product gets successively concentrated as the permeate is withdrawn and discharged via the permeate collection tube.

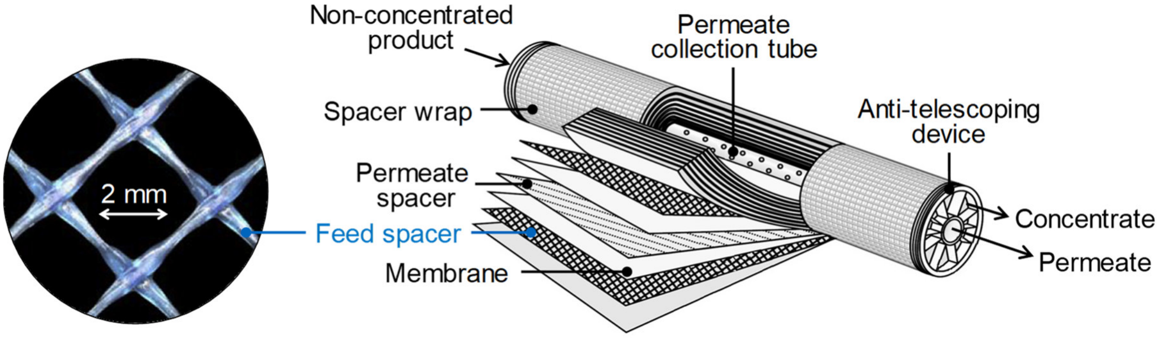

Fig. 1: Photograph of a feed spacer, adapted from Siddiqui et al. (2017, p. 307) and schematic representation of a spiral-wound membrane module, adapted from Wagner (2001, p. 16).

Once the end of the service time is reached, the membrane plants are cleaned in a multi-step process. In general, the first cleaning step is the displacement of the product from the core area of the spacer-filled channels by water. Subsequently, the detachment of the deposit layer requires further rinsing until the desired water flux is achieved. Fig. 2 serves for clarifying the difference between the displacement and the detachment process. While displacing leads to the removal of the product from the core area of the flow channel, the deposit layer is detached to a certain extent by rinsing. As soon as the physical cleaning step is complete, the chemical cleaning by means of caustic agents and acids follows (Li and Chen, 2010, p. 224).

Besides the shut-down and start-up related to the cleaning, the change from one product to another or the end of business hours are further occurrences of displacement processes (Wiklund et al., 2010, p. 330; Henningsson et al., 2007, p. 166). Thus, given the fact that the displacement of fluids is a particularly frequent process linked to big amounts of mixed phase, its efficiency is of great interest to plant operators.

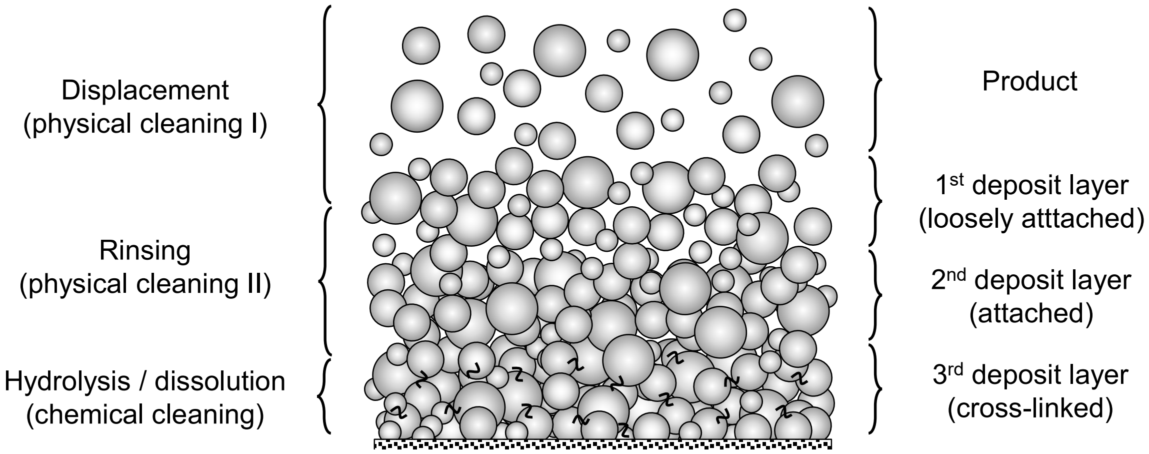

Fig. 2: Distinction between the displacement of the product from the core area of the flow channel and the detachment of the deposit layer by rinsing. The structure of the deposit layer forming on the membrane throughout the filtration of milk is depicted according to Steinhauer et al. (2015, p. 458).

The efficiency of the displacement process depends on the flow rate and the geometric dimensions of the flow channels (Haaksman et al., 2017, p. 135; Picioreanu et al., 2009, p. 349). Besides, the properties of the involved fluids are reported to affect the displacement process (Kieferle et al., 2019a, p. 162; Mishra et al., 2008, p. 4). However, the interactions of these factors are not known in detail, which is why the displacement of products from filtration plants equipped with spiral-wound membranes is commonly based on experiential values gained throughout industrial practice.

The aim of this study is to close this knowledge gap by clarifying how the mentioned process conditions interact and how they affect the time required for the displacement of non-Newtonian products from industrial-scale spiral-wound membranes, which is denoted as residence time. Besides, it is aspired to characterize the hydrodynamic flow patterns prevailing in a membrane plant during the displacement. The working assumption is that the observed residence time (distribution) is the consequence of the hydrodynamic flow patterns arising out of the interaction of the flow rate, the geometric dimensions of the flow channels, and the properties of the involved fluids.

Compared to existing studies, this thesis differentiates in two respects. Firstly, non-Newtonian complex media are considered, while an overwhelming majority of the publications only focuses on water or diluted aqueous solutions (Bucs et al., 2015; Picioreanu et al., 2009; Hasson et al., 2006; Gauwbergen and Baeyens, 1997). Secondly, researchers frequently refer to experiments carried out with spacer-filled flat channels instead of full-scale spiral-wound membranes (Bucs et al., 2015; Khayet et al., 2010; Koutsou et al., 2009; Vrouwenvelder et al., 2007). While the flat-channel experiments are convenient to study particular flow phenomena, the results lack transferability to industrial-scale spiral-wound membranes due to distinct differences in geometry.

In order to reach the above-formulated aims, displacement experiments were carried out with a pilot-scale test rig equipped with a housing for one spiral-wound membrane on an industrial scale. By using milk protein concentrates and xanthan solutions as non-Newtonian model fluids, a certain range of fluid viscosities and flow properties was covered. Moreover, the spacer dimensions were varied by employing spiral-wound membranes with different feed spacers. The first part of the thesis deals with the description of the residence time as a function of the flow rate, the dimensions of the spacers, and the properties of the involved fluids. Here, statistical design of experiments and response surface methodology were used. The second part of the thesis focuses on the mathematical description of the residence time distribution curves in order to characterize the hydrodynamic processes inducing the observed residence times. Therefore, mechanistic models such as the compartment model and the advection-dispersion model were applied. Finally, it was aspired to expand the relevance of the results by estimating the residence time behavior of a viscous product in a filtration plant on an industrial scale.

2 Theoretical framework

The superordinate aim of this study is to improve the understanding of the displacement of non-Newtonian fluids from industrial-scale spiral-wound membranes. Therefore, it is expedient to have a general idea of the factors affecting the flow patterns in spacer-filled channels and to know the essential characteristics of displacement processes. A common practical approach for gaining insights into the prevailing hydrodynamic processes is to monitor the residence time (distribution). While the residence time indicates the required time until completing the displacement step, the residence time distribution equals the progression of the displacement process. Besides the experimental approach, developing mechanistic models for the description of the residence time distributions is an appropriate concept.

For the functional description of the residence times, the rheological properties of the involved fluids are important influencing factors. However, the flow properties of non-Newtonian fluids such as milk protein concentrates and xanthan solutions change in dependence of the process conditions.

2.1 Rheological characterization of fluids

Particularly liquid food products deviate in various respects from the flow characteristics of Newtonian fluids such as water. These fluids may exhibit inter alia shear-dependent or viscoelastic properties. Concerning the shear-dependency, the power law in Eq. 1 is frequently applicable to describe the apparent viscosity η as a function of the consistency index k, the fluid index n, and the local shear rate $\dot{\gamma}$.

$$\eta = k \cdot \dot{\gamma}^{n-1} \qquad (1)$$

For Newtonian liquids, the fluid index equals 1, while it deviates from 1 for non-Newtonian fluids. This is the case for yoghurt, mayonnaise, xanthan solutions or milk protein concentrates, which show shear-thinning and thus non-Newtonian flow behavior (Choppe et al., 2010; Vélez-Ruiz and Barbosa-Cánovas, 1998; Ké and Turcotte, 1980). The extent to which the viscosity decreases with increasing shear rates is expressed by values of n below 1. In contrary, there are some food liquids showing shear-thickening behavior with n being greater than 1. The viscosity of pastes from maize or potato starch, for instance, increases with increasing shear rates (Ptaszek, 2010). Finally, viscoelastic properties are reflected by the complex shear modulus G^* (Eq. 2). Again, milk protein concentrates can serve as examples (Kieferle et al., 2019b, p. 462; Dahbi et al., 2010, p. 5; Bouchoux et al., 2009, p. 6).

$$|G^*| = \sqrt{(G')^2 + (G'')^2} \qquad (2)$$

$$\tau_r = \frac{1}{\omega_c} \quad (3)$$

The storage modulus G' is a measure for the deformation energy stored in a sample and the loss modulus G'' represents the amount of dissipated energy. The relaxation time τ_r is related to the viscoelastic properties and is defined in Eq. 3 as the reciprocal value of the critical frequency ω_c. This frequency is observed at the intersection point of the loss and storage modulus throughout frequency sweep measurements. The practical significance of the relaxation time is that it indicates the time it takes until the viscosity of the liquid has adapted to a deformation.

Considering the flow of a non-Newtonian fluid through a spiral-wound membrane, the spacer determines the local shear rate $\dot{\gamma}$ and consequently the viscosity of the fluid (Eq. 1). Hence, the geometric dimensions of the spacer play a decisive role with regard to the hydrodynamics because they affect the viscosity of the fluids and the flow pattern.

2.2 Hydrodynamics in spacer-filled flow channels

The motion of fluids in spiral-wound membranes is determined by the spacers. However, these play an ambiguous role. On the one hand, they fulfill the important task of keeping the membrane leaves apart and thus allowing the longitudinal flow through the main flow channel. Furthermore, the spacers promote eddies behind the spacer filaments improving the distribution of the solutes or dispersed particles in the direct vicinity of the membrane and in the core flow. On the other hand, the feed spacers are an obstacle in the flow channel fostering the deposition of particles due to flow shadows. Fig. 3 shows a nuclear magnetic resonance microscopy image visualizing the flow through a spacer-filled flat channel, where regions of high and low flow velocities are marked by light and dark colors, respectively. The flow shadows behind the crossing points of the spacer filaments are immediately visible (white circle). Besides, zones of very high flow velocities are present in the opposite of the filaments (black circle). These characteristic flow patterns depend inter alia on the geometry of the spacers, the flow rate, and the rheological properties of the fluid (Kieferle et al., 2019a, p. 162; Haaksman et al., 2017, p. 135; Picioreanu et al., 2009, p. 349). The amount of influencing factors and their interactions make it difficult to predict these complex flow patterns and the resulting mass transfer, which in turn is important with regard to the filtration efficiency and the displacement process. In general, the term mass transfer describes the (re)distribution of fluid elements or

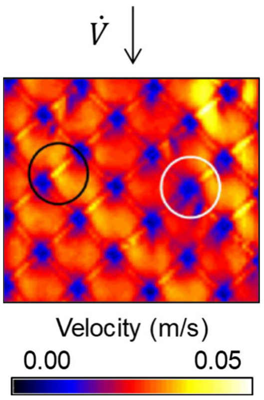

Fig. 3: Velocity distribution in a spacer-filled flat channel, adapted from Schulenburg et al. (2008, p. 42).

particles in the flow channel, which is a consequence of the fluid motion. The filtration efficiency is primarily determined by the mass transfer in the direct vicinity of the membrane. In the absence of mass transfer, the accumulation of solutes or particles held back by the membrane has adverse effects with regard to the permeate flow rate. Consequently, the mass transfer in the direct vicinity of the membrane is in the focus of many studies. In contrast, little attention is paid to the displacement of fluids from spacer-filled channels. However, the mass transfer doubtlessly affects the mixing of the fluid elements along the longitudinal axis of the flow channel, which in turn influences the displacement process. Hence, studying the mass transfer in the direct vicinity of the membranes provides first insights into the mechanisms underlying the displacement process.

One of the most important key figures affecting the mass transfer is the Reynolds number because it relates decisive influencing factors.

2.2.1 Flow conditions in spacer-filled channels

The Reynolds number Re in Eq. 4 is generally used to characterize the flow conditions. It is a dimensionless number comprising the average flow velocity u_a, the characteristic length L_c, the density ρ and the average viscosity η_a of the fluid.

$$Re = \frac{u_a \cdot L_c \cdot \rho}{\eta_a} \tag{4}$$

As long as there is no interchange of fluid elements between adjacent fluid layers (= streamlines), the flow is considered laminar, which is also denoted as streamline flow. As shown in Fig. 4, this holds also true for the partial existence of curved streamlines in recirculation zones or eddies behind the spacer filaments.

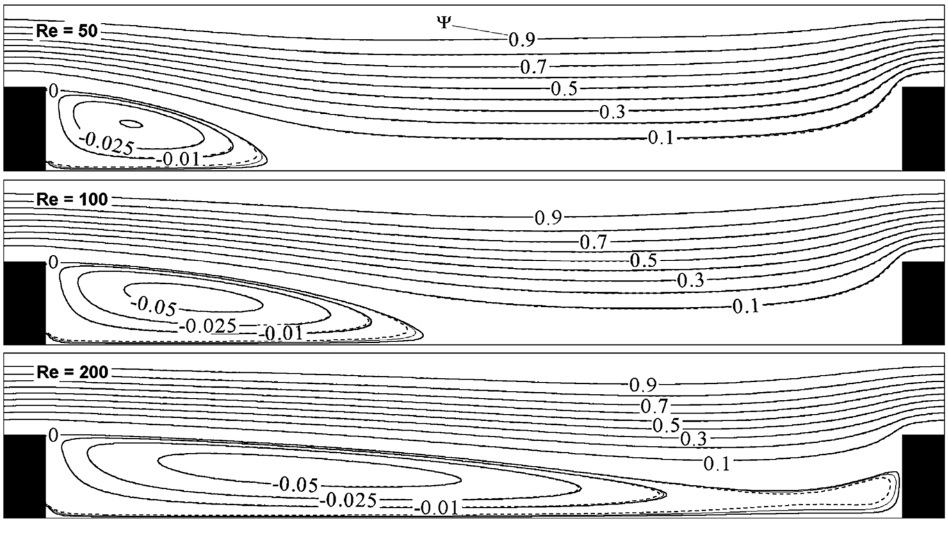

Fig. 4: Streamlines in a flow channel with eddy-promoters for increasing Reynolds numbers (top to bottom: 50, 100, 200) (Geraldes et al., 2002, p. 97). Ψ is the dimensionless stream function.

These results of numerical simulations performed by Geraldes et al. (2002, p. 97) visualize that the size of the recirculation zones grow with increasing Reynolds numbers. As of a particular Reynolds number, denoted as critical Reynolds number, the distinction of the single streamlines is not possible anymore. Here, the flow becomes unsteady and subsequently turbulent with a further increase of the Reynolds number. For pipes with open flow channels, the most frequently quoted critical Reynolds number is 2300 (Rott, 1990, p. 7). However, this value cannot be applied for the flow in spacer-filled channels because the geometry is distinctly different. Hence, the characterization of the flow state in spacer-filled channels takes its place in many scientific studies. Before focusing on these studies, however, the definition of the Reynolds numbers with regard to the interpretation of the characteristic length is addressed as it differs in literature.

Definition of the Reynolds number

With regard to the general definition of the Reynolds number in Eq. 4, there is general agreement in literature. However, concerning the characteristic length, discrepancies can be observed among the studies because this variable lacks its unambiguousness for spacer-filled channels in contrast to the diameter of a circular pipe. Frequently, the hydraulic diameter or the height of the flow channel are considered as characteristic length L_c, although the results differ. In this respect, Ransohoff and Radke (1987, p. 392) state that using the hydraulic diameter in order to quantify the dimensionless flow resistance throughout laminar flow through pores of a triangular cross section leads to deviations on the order of at least 50%. Concerning the question, which measure to choose, Santos et al. (2007, p. 109) conclude that the Reynolds numbers calculated based on the hydraulic diameter are more suitable for the characterization of the flow state in spacer-filled channels. This suggestion is based on computational fluid dynamics simulations, which show that the statistical dispersion (variability) is lower when using the hydraulic diameter. Hence, many researchers apply the hydraulic diameter for calculating the Reynolds number (Sreedhar et al., 2018, eq. 10; Haaksman et al., 2017, eq. 3; Kavianipour et al., 2017, eq. 2; Bucs et al., 2015, eq. 1; Schwinge et al., 2004a, eq. 1).

The hydraulic diameter d_h equals four times the ratio of the flow channel volume and the wetted surface. Schock and Miquel (1987, eq. 14) define it for spacer-filled channels in Eq. 5 by assuming that the spacer filaments are ideal cylinders. Herein, the volumes V and the surface areas S of the empty flow channel (index C) and the spacers (index S) are used.

$$d_h = \frac{4 \cdot (V_c - V_s)}{S_c + S_s} \tag{5}$$

Despite the fact that the channel height may lead to unsuitable results, some authors consider it as characteristic length anyway (Sousa et al., 2014, eq. 7; Gimmelshtein and Semiat, 2005, eq. 4).

Besides the definition of the characteristic length, the determination of the required dimensions is problematic since the available methods do not provide equal results. Siddiqui et al. (2017, p. 308) compare different methods for the determination of the porosity, which also concerns the hydraulic diameter since the porosity is a function of the spacer volume. The authors conclude that using microscopic fibre volume measurements is not recommendable – independently of the assumed filament shape (cuboidal, cylindrical, or ellipsoid). They rather propose computer tomography scanning combined with numerical modelling, measuring the weight and the density of the spacers or quantifying the volume displaced by the spacers as these methods deliver comparable results. Also the velocity value inserted into the Reynolds number equation is afflicted with uncertainty because it differs from position to position in the spacer-filled channels. However, in literature on hydrodynamics in spacer-filled channels, it is not clear how the velocity values for the assumed Reynolds number are determined. The same holds true for the viscosity because it is a function of the velocity gradient. The question when turbulent flow can be expected for the flow in spacer-filled channels is subject of the following paragraph.

Determination of the critical Reynolds number

In general, the critical Reynolds number Re_c marks the onset of local flow instabilities, which is unsteady flow. Tab. 1 gives a small overview of the critical Reynolds numbers for different Reynolds number definitions and flow channel geometries.

Tab. 1: Comparison of critical Reynolds numbers determined for different geometries based on different Reynolds number definitions. The variables flow velocity u, hydraulic diameter d_h, density ρ of the fluid, viscosity of the fluid η, channel height h_c, channel volume V_c, and wall shear stress τ_w are mentioned.

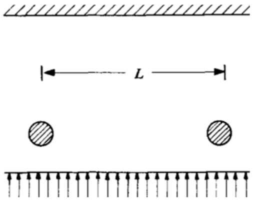	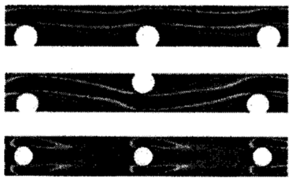	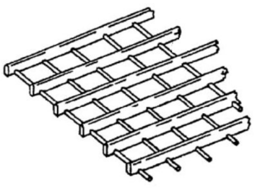	
$Re = \frac{\tau_w \cdot V_c \cdot \rho}{\eta \cdot h_c}$	$Re = \frac{u \cdot d_h \cdot \rho}{\eta}$	$Re = \frac{u \cdot h_c \cdot \rho}{\eta}$	$Re = \frac{u \cdot d_h \cdot \rho}{\eta}$
$Re_c \approx 300$	$Re_c \approx 300 - 400$	$Re_c \approx 250 - 300$	$Re_c \approx 250 - 350$
(Karniadakis et al., 1988, p. 385)	(Schwinge et al., 2002a, pp. 199)	(Geraldes et al., 2002, p. 93)	(Mojab et al., 2014, p. 575)

Karniadakis et al. (1988, p. 385) investigate heat transfer in channels equipped with cylinders as turbulence promoters. They report that the development of unsteady flow starts at Reynolds number of about 300. Schwinge et al. (2002a, p. 199) provide the results of two-dimensional computational fluid dynamics simulations for the characterization of the hydrodynamics in flow channels equipped with different filament configurations. These configurations are chosen to cover the whole range of filament positions existing in a three-dimensional spacer with circular filaments. Depending on the configuration, the transition from laminar to unsteady flow is observed in the Reynolds number range from 300 to 400. Geraldes et al. (2002, p. 93) focus on the hydrodynamics in flow channels filled with ladder-type spacers. Based on two-dimensional numerical simulations and dye-release experiments as shown in Fig. 5, the authors show that the transition from laminar to turbulent flow occurs at Reynolds numbers of about 250.

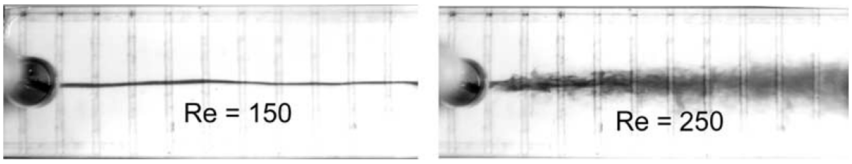

Fig. 5: Transition from laminar to unsteady flow in a channel filled with a ladder-type spacer (Geraldes et al., 2002, p. 94)

However, the exact critical Reynolds number depends on the length of the recirculation zones behind the filaments, which in turn are affected by the flow velocity and the spacer geometry (Fig. 4). Santos et al. (2007, p. 109) support these findings since they show that smaller mesh lengths stabilize the flow when using spacers having a square cross-section. They explain that the transition from laminar to turbulent flow is shifted to higher critical Reynolds numbers, which range from 130 to 330. Wang et al. (2014, p. 278) provide the results of dye-release experiments as well and indicate that instabilities begin at Reynolds numbers of 440 for diamond-shaped spacers. Finally, Mojab et al. (2014) use particle image velocimetry as experimental approach in order to characterize the flow state in spacer-filled channels. They state that supercritical flow sets on at Reynolds numbers ranging from 250 to 350.

Concerning the onset of fully turbulent flow, Mojab et al. (2014, p. 574) and Wang et al. (2014, p. 278) indicate Reynolds numbers of about 1000. This is supported by Gimmelshtein and Semiat (2005, p. 145), who observe turbulent flow patterns at Reynolds numbers of 1000 by means of particle image velocimetry measurements. Comparing these results, the deviations of the critical Reynolds numbers for the onset of flow instabilities are surprisingly small given the fact that the researchers assume differently shaped turbulence promoters, different definitions of the Reynolds number, and different measurement techniques. Thus, it is reasonable to remember a critical Reynolds number of approximately 300 as a rough orientation for the onset of flow instabilities in spacer-filled channels.

Having reviewed the Reynolds number concept for the flow in spacer-filled channels, the mass transfer over the channel cross-section is addressed. The following section serves for clarifying the impact of the most important factors on the mass transfer, which in turn affects the longitudinal dispersion being related to the displacement process.

2.2.2 Mass transfer over the cross-section of spacer-filled flow channels

In general, the term mass transfer denotes the exchange of solutes or dispersed particles between adjacent fluid elements due to fluid motion and consequently describes the distribution characteristics of the solutes or dispersed particles within the flow channel. Prior to moving on to the itemization of the influencing factors, the most common measure for the quantification of the mass transfer is presented.

Measures for the quantification of the mass transfer

The most common measure for the quantification of the mass transfer is the Sherwood number Sh in Eq. 6, which gives the ratio of advective to diffusive mass transfer. In analogy to the Nusselt number for heat transfer problems, the Sherwood number depends on the mass transfer coefficient β_m, the characteristic length L_c, and the molecular diffusion coefficient D_m.

$$Sh = \frac{\beta_m \cdot L_c}{D_m} = a \cdot Re^b \cdot Sc^c \cdot \left(\frac{L_c}{L}\right)^d \qquad (6)$$

$$Sc = \frac{\eta}{D_m \cdot \rho} \qquad (7)$$

Furthermore, the Sherwood number is a function of the Reynolds number Re (Eq. 4) and the Schmidt number Sc in Eq. 7. Da Costa et al. (1991, p. 282) propose an expression for the relation of the dimensionless numbers based on four proportionality constants a, b, c, and d as fitting parameters. In Eq. 6, the characteristic length L_c equals the hydraulic diameter and L is the length of the flow channel. The Schmidt number considers the fluid viscosity η and density ρ as well.

The calculation of these numbers for practical applications requires further efforts because estimates for the mass transfer coefficient and the molecular diffusion coefficient are required. For low-molecular-weight substances such as sodium chloride, the molecular diffusion coefficient D_m can be found tabulated or calculated using the Stokes-Einstein equation (Eq. 8). Therefore, the Boltzmann constant k_B, the particle radius r_0, the fluid viscosity η, and the absolute temperature T are used.

$$D_m = \frac{k_B \cdot T}{6 \cdot \pi \cdot \eta \cdot r_0} \qquad (8)$$

In order to determine the mass transfer coefficient β_m, the osmotic pressure model in Eq. 9 and the solution-diffusion model in Eq. 10 are frequently applied in combination (Sreedhar et al., 2018,. p. 92; Thiess et al., 2017, p. 441; Shi et al., 2015, p. 13; Da Costa et al., 1991, p. 279; Schock and Miquel, 1987, p. 346). The permeate flux J during the filtration of aqueous solutions depends on the membrane constant A_M, the transmembrane pressure Δp_{TM}, and the osmotic pressure difference $\Delta\pi$. This latter one is the difference of the osmotic pressures of the retentate in direct vicinity of the membrane of the concentration C_M and the permeate having the concentration C_P. The solution-diffusion model furthermore contains the concentration of the retentate in the core flow C_C as well as the mass transfer coefficient β_m, which can be derived when equating the expressions for the permeate flux. This derivation indicates that the mass transfer coefficient decreases with increasing concentration polarization. Thus, a high concentration of the solutes or dispersed particles in the core flow also leads to a reduction of the mass transfer.

$$J = A_M \cdot (\Delta p_{TM} - \Delta\pi) \qquad (9)$$

$$J = \beta_m \cdot ln\left(\frac{C_M - C_P}{C_C - C_P}\right) \qquad (10)$$

The presented approach for the quantification of the mass transfer based on the Sherwood number concept appears to be very convenient. However, considering complex media with a high viscosity such as milk protein concentrates, the presented concept it to be regarded critically. Firstly, the applicability of the Stokes-Einstein equation is limited to diluted aqueous solutions. Thus, an estimate for the dispersion coefficient is not readily accessible for concentrates. Secondly, concentration of proteins by means of membrane filtration is always accompanied by deposit layer formation, which affects the effective transmembrane pressure (Kulozik and Kessler, 1988, p. 1381). Besides, the osmotic pressure is a function of the number of dissolved particles as it is a colligative property (Hofmann, 2018, p. 134). This means that proteins in milk protein concentrates induce a low osmotic pressure compared to the serum phase containing the salts and lactose. These facts complicate the exact determination of the osmotic pressure exerted by the proteins. Altogether, the estimation of the mass transfer coefficient for milk protein concentrates is related to severe difficulties or uncertainties as well.

For these reasons, the presented Sherwood number concept is not always applicable. Nevertheless, it allows studying the impact of the spacer geometry on the mass transfer in the direct vicinity of the channel wall when using salt solutions.

Impact of the geometric characteristics of the spacer

Presumably, the first quantitative correlation between the Sherwood number and the Reynolds number for the flow in spacer-filled channels is published by Schock and Miquel (1987, p. 238). They observe that the Sherwood numbers increase from 20 to 80 with increasing Reynolds numbers (100 – 500) for a Schmidt number of 660. Several studies confirm this trend, in which the Sherwood numbers take values ranging from 30 to 600 for Schmidt numbers of up to 5700 (Sreedhar et al., 2018, p. 94; Koutsou et al., 2009, p. 245; Da Costa et al., 1991, p. 283).

In order to understand how these variations come about, attention is to be dedicated to the geometric characteristics of the spacers. Among many others, frequently used spacer configurations are the woven or non-woven/ladder-type spacers, where the spacer filaments have an approximately circular, ellipsoid or square cross-section. Besides the spacer configuration and the shape of the filaments, the filament thickness, the mesh length l_m, and the filament orientation are geometric characteristics of a spacer. The filament orientation is characterized by a flow attack angle α and an internal strand angle β as depicted in Fig. 6. These characteristics affect the hydrodynamics and thus the spacer efficiency, which is generally considered high if the mass transfer rate is high in relation to the induced energy losses due to viscous dissipation or friction manifesting themselves in the pressure drop. The false-color representation in Fig. 7 adapted from Haaksman et al. (2017, p. 134) conveys an idea of the velocity distribution in a three-dimensional flow channel filled with a conventional feed spacer.

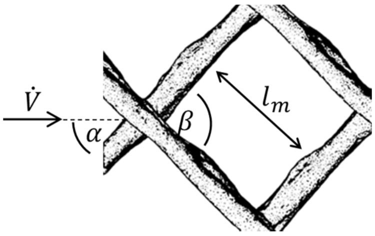

Fig. 6: Non-woven spacer in diamond configuration, adapted from Haaksman et al. (2017, p. 127).

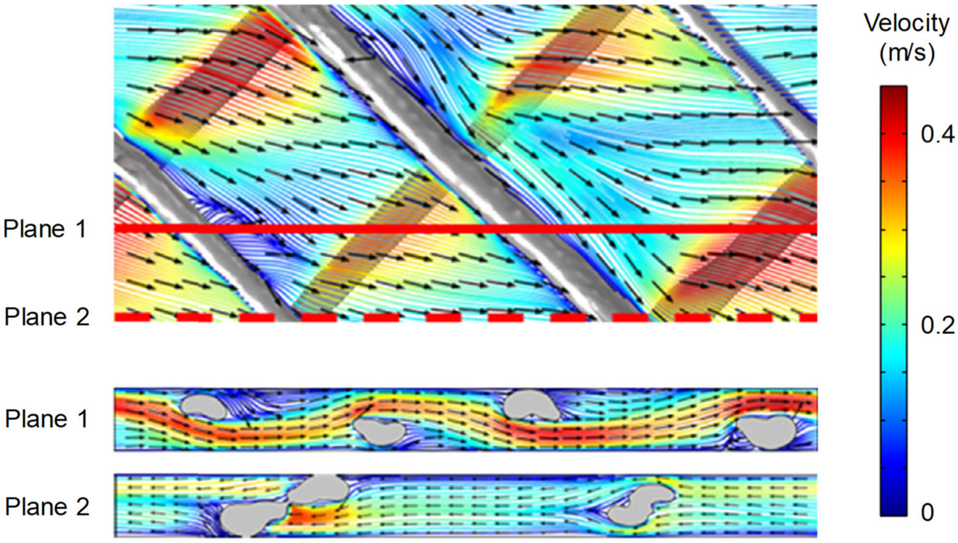

Fig. 7: Flow fields in a spacer-filled channel, adapted from Haaksman et al. (2017, p. 134).

Directly above or below a spacer filament, the flow velocity is highest, while it drops significantly behind the filaments. Haaksman et al. (2017, p. 127) report that the friction factors are twice as high when considering irregularly shaped spacer filaments instead of cylindrical filaments at Reynolds numbers above 100. Hence, the shape of the spacer filaments, which is frequently simplified for computational fluid dynamics simulations, affects the mass transfer significantly. Based on two-dimensional computational fluid dynamics simulations, Schwinge et al. (2002b, pp. 4885) visualize the correlation between the local shear stress exerted by the fluid motion and the local mass transfer coefficients (Fig. 8). It is clearly visible that high shear stress induces high mass transfer coefficients.

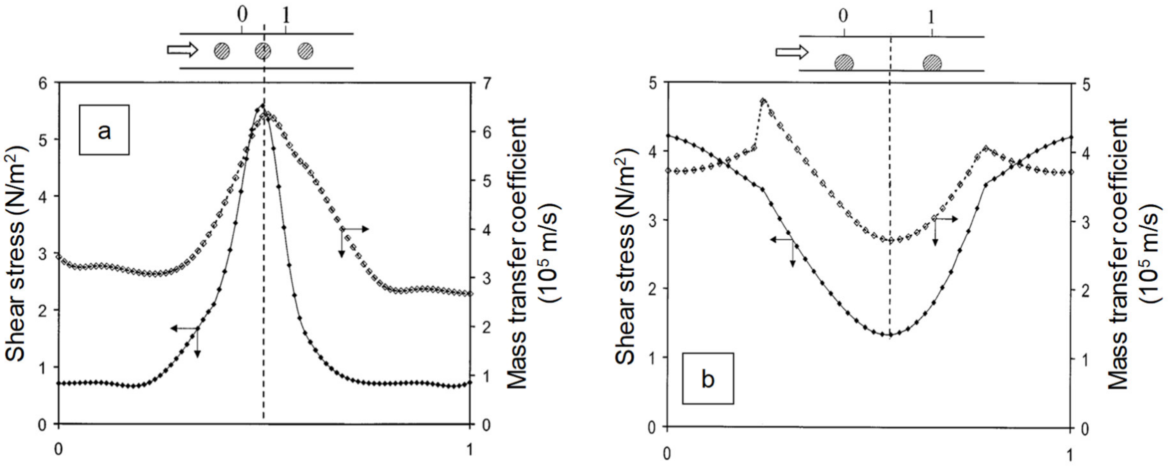

Fig. 8: Relation of local shear stress and local mass transfer between the a) submerged and b) cavity spacer configuration, adapted from Schwinge et al. (2002b, pp. 4885).

These results are supported by Koutsou et al. (2009, p. 243), who explore the relation between the mass transfer coefficient and the shear stress based on three-dimensional computational fluid dynamics simulations (Fig. 9a and b). Besides, they provide a fouling pattern resulting from a filtration experiment (Fig. 9c) for comparison purposes. It is obvious that the membrane areas exposed to high shear stress (Fig. 9b, dark blue) show only weak fouling (Fig. 9c, light areas) and high mass transfer coefficients (Fig. 9a, turquoise areas).

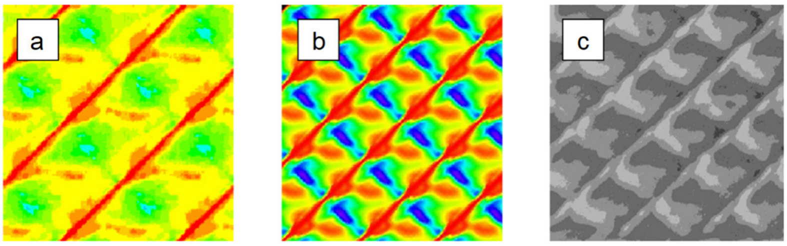

Mass transfer (Sc = 25, Re = 90)

Shear stress (Re = 90)

Fouling pattern (Reverse osmosis)

Fig. 9: Local distribution of mass transfer coefficient, shear stress, and fouling intensity (Koutsou et al., 2009, p. 243). Red/light and blue/dark colors indicate the minimum and maximum values.

Hence it is concluded that the differences in the velocity fields and thus the shear stress and mass transfer are induced by the geometric characteristics of the spacers. This is also observed by other researchers (Tang et al., 2011, p. 135; Shakaib et al., 2009, p. 274; Song and Ma, 2005, p. 7645; Cao et al., 2001, p. 168). The following paragraph focuses on the impact of the different geometric characteristics on the spacer efficiency or the mass transfer.

A commonly indicated spacer dimension is the spacer thickness or channel height. However, it turns out that this geometric dimension alone is not compulsorily decisive for the actual mass transfer in the spacer-filled flow channel – it is rather the aspect ratio α_R (Eq. 11). Decreasing the thickness of the spacer filaments d_f at a constant channel height h_c, which is a reduction of the aspect ratio, induces an increase of the mass transfer coefficient (Shakaib et al., 2009, p. 281).

$$\alpha_R = \frac{d_f}{h_c} \tag{11}$$

Considering the velocity profiles published by Schwinge et al. (2002c, p. 2983), it can be concluded that increasing the aspect ratio from 0.16 to 0.7 induces a severe increase of the velocity differences over the channel cross-section. While the flow velocity is approximately equally high above the cross-section of the channel for a small aspect ratio, high aspect ratios induce insufficient mixing behind the spacer filaments. Bucs et al. (2014, p. 35) observe a pressure drop increase by a factor of 5 when decreasing the spacer thickness from 1.17 mm to 0.71 mm.

With regard to the mesh length, the general trend is noticed that the mass transfer increases for a decreasing ratio of the mesh length and the filament diameter (Koutsou et al., 2009, p. 346; Shakaib et al., 2009, p. 281; Schwinge et al., 2002b, p. 4881). Thus, in order to obtain high mass transfer rates, the mesh length should be small as well, if the filament diameter is small. While there is some evidence that low aspect ratios and small mesh lengths improve the mass transfer, the results diverge with regard to the optimal internal strand angle.

Zimmerer and Kottke (1996, p. 133) present results of experiments with non-woven spacers having internal strand angles in the range from 60 to 150°. The authors report higher Sherwood numbers at smaller internal strand angles at super-critical flow (Re = 1000). Da Costa et al. (1991, p. 289) investigate spacers with internal strand angles ranging from 0 to 135°. They conclude that the optimal spacer exhibits an internal strand angle of 80° under consideration of the maximum achievable flux at acceptable pressure drops. In contrast, Koutsou et al. (2009, p. 245) observe that the Sherwood number increases if the internal strand angle increases from 90 to 120°. Also Lau et al. (2009, p. 32) conclude, based on three-dimensional computational fluid dynamics simulations for non-woven spacers with cylindrical filaments, that spacers with a flow attack angle of 120° (and an internal strand angle of 30°) are most effective.

Finally, the impact of the curvature of the flow channel is disputed. In general, it is assumed that the centrifugal forces decrease from the center of a spiral-wound membrane to the outer wall (Ranade and Kumar, 2006, p. 12). By means of computational fluid dynamics simulations, Li and Tung (2008, p. 294) indicate that the curvature of the spiral-wound membrane induces slightly lower wall shear stresses at the outer membrane wall of a spacer-filled flow channel compared to the inner one (Fig. 10).

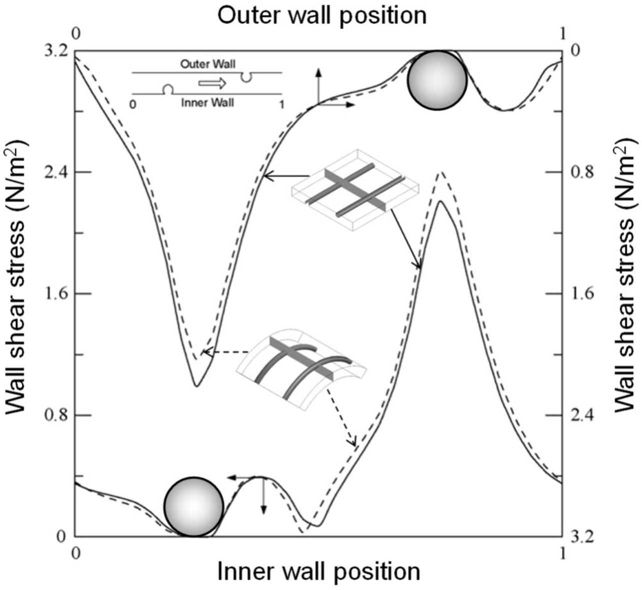

Fig. 10: Wall shear stress at the outer and inner membrane of a flat (straight line) and a curved (dashed line) spacer-filled flow channel at Re = 165, adapted from Li and Tung (2008, p. 289, 294).

Using computational fluid dynamics simulations as well, Ranade and Kumar (2006, p. 12, 14) assess the pressure drop in a curved and a flat spacer-filled channel. However, they consider the differences ‘not very significant’ and indicate that similar results are obtained for the wall shear stress and vorticity. The authors assume that the effect of the curvature of the channels is superimposed by the secondary flow induced by the spacers and thus does not affect the flow behavior significantly.

In conclusion, the geometric characteristics of the spacers determine the mass transfer over the cross section of the flow channel and the direct vicinity of the membrane. In particular high velocity gradients are effective with regard to the increase of the mass transfer. Instable or turbulent flow is an effective mixer affecting the fluids at length scales on the order of the flow channel width or less. Thus, the extent of longitudinal dispersion is doubtlessly related to the mass transfer over the cross section of the flow channel but is also affected by larger-scale motions.

2.2.3 Dispersion along the longitudinal axis of spacer-filled flow channels

Dispersion describes the spreading of solutes or dispersed particles due to velocity gradients or diffusion (Fischer, 1973, p. 59). Thus, dispersion is also a consequence of hydrodynamics. On a microscopic level, the extent of dispersion is determined by diffusion, which is random molecular motion obeying Fick's first law. On a macroscopic level, however, diffusion is superimposed completely by advective or convective mass transport and can therefore be neglected (Delgado, 2006, p. 291). The term advection indicates that the fluid movement is induced by external forces exerted by pumps or stirrers, for instance (Stevens and Fuller, 2015, p. 121; Phillips and Castro, 2003, p. 457). Convection, strictly speaking, describes fluid motion due to a temperature gradient in adjacent fluid layers (Stevens and Fuller, 2015, p. 120). The velocity gradients can either affect the fluid elements in the direction of the flow, which induces axial/longitudinal dispersion, or dispersion perpendicularly to the flow direction, which results in radial/transverse dispersion. In order to quantify the extent of dispersion in either direction, the dispersion coefficient is used, which is considered in the Péclet number.

Definition of the Péclet number

The Péclet number, also denoted as Bodenstein number predominantly in German references, is a dimensionless number serving for the quantification of the dispersion. In the dimensionless expression of the general transport equation (Eq. 12), the reciprocal Péclet number is the proportionality factor (Weinekötter and Gericke, 1995, p. 88). Herein, c, θ, and ζ are dimensionless expressions for tracer concentration, time, and position, respectively. The Péclet number can be estimated based on Eq. 13 and depends on the average flow velocity u_a, the characteristic length L_c, and the axial dispersion coefficient D_a. It can also be expressed as a function of the Reynolds number Re and the Schmidt number Sc.

$$\frac{\partial c}{\partial \theta} = \frac{1}{Pe} \cdot \frac{\partial^2 c}{\partial \zeta^2} - u \frac{\partial c}{\partial \zeta} \qquad (12)$$

$$Pe = \frac{u_a \cdot L_c}{D_a} = Sc \cdot Re \qquad (13)$$

As already discussed for the Reynolds number, the characteristic length lacks unambiguousness. The relation in Eq. 13 characterizes the dispersion over the cross-section of the flow channel when considering the hydraulic diameter or the channel height of a spacer-filled channel as the characteristic length. For the description of the displacement of fluids from spiral-wound membranes, however, the Péclet number is used as a measure for the dispersion in the axial direction. Thus, it must be a function of the length of the considered flow channel. At this point it is important to mention that the Reynolds number in Eq. 13 loses its initial meaning as a measure for the flow state in the flow channel.

Besides the characteristic length, an estimate for the axial dispersion coefficient is required for the calculation of the Péclet number. According to Danckwerts (1953, p. 3861), the axial dispersion coefficient represents the interaction of the material parameters (fluid viscosity and density), the flow velocity, and the geometry of the flow channel. To find out which relations of these physical quantities need to be considered, the Buckingham π-theorem is a valuable tool.

Factors influencing the axial dispersion coefficient

The Buckingham π-theorem serves for the assessment of the relations among physical quantities by means of dimensionless numbers (Curtis et al., 1982, p. 118). For determining the extent of axial dispersion in circular pipes, characterized by the axial dispersion coefficient D_a, Levenspiel (1958, p. 344) provides three dimensionless π-numbers (Eq. 14).

$$D_a = \phi\left(\pi_1 = \frac{u \cdot d \cdot \rho}{\eta}\ ,\ \pi_2 = \frac{\eta}{\rho \cdot D_m}\ ,\ \pi_3 = \frac{\epsilon}{d}\right) \qquad (14)$$

Herein, the parameters pipe diameter d, flow velocity u, fluid density ρ, pipe roughness ϵ, dynamic viscosity η, and molecular diffusion coefficient D_m are considered. π_1 corresponds to the Reynolds number and π_2 to the Schmidt number. According to the authors, the relative roughness number π_3 can be neglected for laminar flow.

Another approach is provided by Walenta and Kessler (1990b). They focus on the question to which extent the rheological properties of a non-Newtonian product or a non-Newtonian displacing fluid affect the displacement progress, which depends on the axial dispersion coefficient D_a. For their analysis they consider the pipe diameter d, the flow velocity u, the density ρ, the pipe length L, the pressure drop Δp, and the dynamic viscosity η. As indicated before, the viscosity of non-Newtonian fluids depends on the velocity gradient in the flow channel. Hence, the dimensionless analysis must be based on the power-law parameters instead of the viscosity as these are independent of the velocity gradient. However, a requirement for the applicability of the Buckingham π-theorem is that the units' exponents are 1, which is not the case for the consistency index having the unit Pa·s^n. In order to meet this requirement, Walenta and Kessler (1990b) use Eq. 15, which is derived by Pawlowski (1971, p. 125). Herein, the consistency index k is expressed by a characteristic viscosity constant H in Pa·s and a characteristic time constant Θ in s.

$$k = H \cdot \Theta^{n-1} \qquad (15)$$

The result of their dimensional analysis are five dimensionless π-numbers listed in Eq. 16. π_1 and π_2 are friction factors, while π_3, π_4, and π_5 correspond to the Reynolds number, to a modified Reynolds number, and presumably a Strouhal number.

$$D_a = \phi\left(\pi_1 = \frac{L}{d}\ ,\ \pi_2 = \frac{\Delta p}{\rho \cdot u^2}\ ,\ \pi_3 = \frac{u \cdot d \cdot \rho}{\eta}\ ,\ \pi_4 = \frac{u \cdot d \cdot \rho}{H}\ ,\ \pi_5 = \frac{d}{u \cdot \Theta}\right) \qquad (16)$$

This last-mentioned dimensionless number is commonly used for describing flow oscillations (Katopodes, 2019, p. 384). In contrast to the numbers π_3, π_4 and π_5, the authors do not attribute a particular meaning to π_1 and π_2 with regard to the displacement process. A conclusion, which is particularly interesting with respect to the displacement of non-Newtonian fluids from spiral-wound membranes, is that the same mixing behavior can only be observed if the pipe diameter is constant because it determines the rheological properties of the fluids. Furthermore, Walenta and Kessler (1990b, p. 66) conclude that the displacement behavior only depends on the Reynolds number of the displacing fluid, while the flow state of the displaced fluid is negligible. However, the practical relevance of π_4 and π_5 is limited as it is questionable which physically accessible values are to be used for H and Θ.

In conclusion, the dimensionless numbers resulting from the dimensional analysis following the Buckingham π-theorem characterizes the maximal physical framework of the axial dispersion coefficient, which covers all factors mentioned by Danckwerts (1953, p. 3861). Finally, judging the actual relevance of each π-number for the axial dispersion coefficient is only possible based on experiments (Walenta and Kessler, 1990b, 65).

Quantification of the axial dispersion coefficient

Gauwbergen and Baeyens (1997, p. 290) focus on the residence time behavior observed for the flow through the spacer-filled channels of a spiral-wound membrane on a laboratory scale (diameter: 1.8 inch, length: 12.6 inch, spacer thickness: 0.8 mm). In Fig. 11, the Péclet numbers are plotted against the Reynolds numbers.

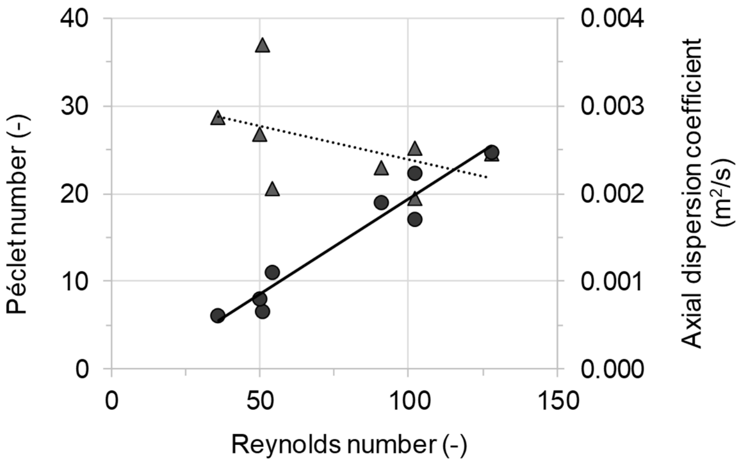

Fig. 11: Péclet numbers (triangles, dashed line) and axial dispersion coefficients (circles, straight line) plotted against the Reynolds number. Data originate from the study of Gauwbergen and Baeyens (1997, p. 297).

The observed Péclet numbers are in the range from 19 to 37, while the flow state can be considered laminar for all measurements since the Reynolds numbers are far below 300. However, there is no evident relation between the Reynolds number and the Péclet number. Based on the information given in this study, it is possible to estimate the axial dispersion coefficients also shown in Fig. 11. Using the module length as characteristic length for the calculation of the Péclet number, the axial dispersion coefficients take values in the range from 0.61 and 2.46 · 10^{-3} m^2/s (Gauwbergen and Baeyens, 1997, p. 297).In contrast to the Péclet numbers, the axial dispersion coefficients clearly show a linear relationship with the Reynolds number as the dispersion increases with increasing Reynolds numbers. A consecutive study carried out by the same authors provides further Péclet numbers (Gauwbergen and Baeyens, 2000, p. 90). However, the determination of the corresponding axial dispersion coefficients is not possible because the flow rates are not indicated. Although the Reynolds numbers account for up to 323, the Péclet number range is 21 to 33 and is thus essentially unaffected. Hasson et al. (2006, pp. 451) assess the dispersion coefficients for an unused spiral-wound membrane on a laboratory scale (diameter: 2.5 inch). Furthermore, they compare unused and used modules on an industrial scale with regard to the longitudinal dispersion (diameter: 8 inch). For the laboratory-scale membrane, the axial dispersion coefficients range from 0.7 to 3.5 · 10^{-3} m^2/s for Reynolds numbers between 40 and 220. These values are on the same order of magnitude as the axial dispersion coefficients and Reynolds numbers in Fig. 11 derived from the study of Gauwbergen and Baeyens (1997, p. 297). For the industrial-scale membranes, the axial dispersion coefficients are higher and take values in the range from 2 to 13 · 10^{-3} m^2/s for the new module and from 5 to 42 · 10^{-3} m^2/s for the old one, respectively. The corresponding Reynolds number range is between 50 and 350. In conclusion, the axial dispersion coefficient increases by a factor of 3 when increasing the module diameter. Concerning the effect of the module age on the extent of dispersion, the study does not indicate statistical figures, which would allow to assess whether the difference in the axial dispersion coefficients is significant or not. Thus, no clear conclusion can be drawn with regard to the impact of the overall service life on the dispersion along the modules.

Finally, the assumption that molecular diffusion is fully superimposed by advective motion is reviewed. The above-mentioned axial dispersion coefficients are determined using aqueous sodium chloride solutions (1%, 25°C) with molecular diffusion coefficients of approximately 1.5 · 10^{-5} m^2/s (Vitagliano and Lyons, 1956, p. 1550). Comparing this value to the presented axial dispersion coefficients, it can be concluded that the molecular diffusion is clearly subordinate in the flow through spacer-filled channels since the axial dispersion coefficients are 100 to 1000 times as large.

In summary, the factors affecting the Reynolds number are shown to influence the axial dispersion coefficient as predicted based on the Buckingham π-theorem. For the practical assessment of the relations between the extent of axial dispersion and the displacement efficiency, monitoring the displacement process is required in the first place.

2.3 Monitoring and interpreting displacement curves

The shape of a displacement curve contains information about the prevailing hydrodynamic processes and thus about the extent of axial dispersion (Jakubith, 1998, p. 300). In principle, monitoring the mixed phase progression can generally be realized by injecting a tracer substance upstream and measuring the tracer concentrations downstream a plant or component. To ensure that a recorded residence time curve represents the flow behavior of the fluid in the flow geometry under consideration, it is necessary that the tracer does not affect the physical properties of the fluid, that it is well miscible with the fluid, and that it is chemically inert. Furthermore, an easy analytical detection of the tracer concentration is required. Particularly colorants or electrolytes such as sodium chloride are good tracer materials because their detection by means of spectroscopy or conductivity measurement is practicable (Schwister, 2018, pp. 365). Depending on the objective of the investigation, a periodic, random, pulse or step input of the tracer is possible (Levenspiel, 1999, p. 261). While the periodic and random input require a rather sophisticated experimental setup and analysis method, the realization and interpretation of the pulse- and step-input experiments (Fig. 12) are straightforward.

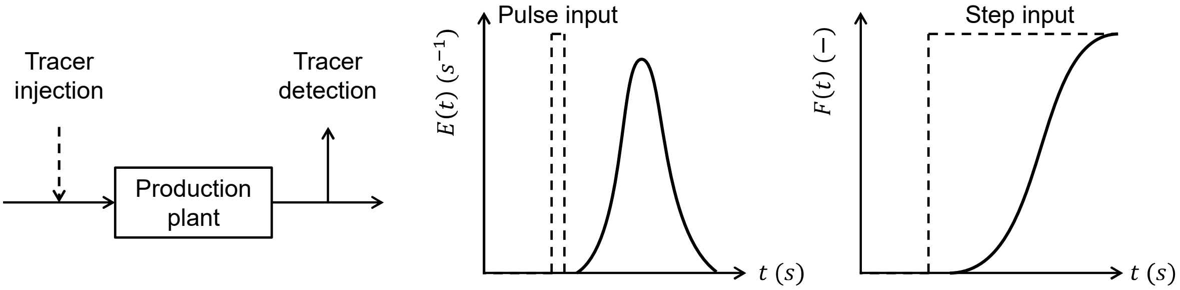

Fig. 12: Determination of the residence time behavior of a fluid in a production plant by means of the pulse and the step experiment.

The output of a pulse-input experiment is the (residence time) distribution curve or E-curve $E(t)$ represented by the expression in Eq. 17. The output of a step-input experiment is the cumulative (residence time) distribution curve or F-curve $F(t)$ in Eq. 18.

$$E(t) = \frac{C_{out}}{\int_0^{\infty} C_{out}\,dt} = \frac{dF(t)}{dt} \tag{17}$$

$$F(t) = \frac{C_{out}}{C_{out,0}} = \int_0^t E(t)\,dt \tag{18}$$

Because the conversion of the curves from one to the other is possible via derivation or integration, both experiments result in an equivalent outcome (if they are put into practice correctly). The mean residence time $\bar{t}$ in Eq. 19 is denoted as 1st raw moment of the time-dependent density function $E(t)$, while the variance σ^2 in Eq. 20 is known as the 2nd central moment. In general, the distribution and cumulative distribution curves are functions of the time t or the dimensionless time θ (Eq. 21). Besides, the hydraulic residence time τ_t in Eq. 22 is the ratio of the volume of the flow geometry V and the flow rate $\dot{V}$.

$$\bar{t} = \int_0^\infty t \cdot E(t)\, dt \tag{19}$$

$$\sigma^2 = \int_0^\infty (t - \bar{t})^2 \cdot E(t)\, dt \tag{20}$$

$$\theta = \frac{t}{\bar{t}} \tag{21}$$

$$\tau_t = \frac{V}{\dot{V}} \tag{22}$$

The interpretation of the residence time curves requires knowledge about the possible flow patterns. Danckwerts (1953, p. 3858) provides Fig. 13, which is a guide for diagnoses concerning the hydrodynamics based on F-curves. If the F-curve is rather a vertical (Fig. 13a) than an inclined curve, dispersion does not occur in the vessel. However, this so-called plug flow is an ideal result since the no-slip condition always induces a certain velocity distribution of the fluid elements (White, 2011, p. 26). Thus, actually observed F-curves frequently resemble the curves in Fig. 13b, c, or d, which suggest pseudo plug flow, complete mixing, and dead water zones, respectively. In general, wide E-curves with large variances indicate high extents of dispersion. Moving from Fig. 13a to d, the so-called hold-back increases. This measure expresses that the difference in residence times of single fluid elements or dispersed particles entering the system simultaneously increases. While some fluid elements or dispersed particles leave the system very quickly via a short-circuit route, others have long residence times as they stay undisturbed in flow shadows. Besides the hold-back, segregation is a further quality characterizing the flow through a system. Segregation denotes the deviation from ideal mixing and takes values between e^{-1} for plug flow (Fig. 13a) and −1 in case of systems, where an exchange of the fluid is virtually non-existent (dead water) (Danckwerts, 1953, pp. 3859). Consequently, positive values indicate that the displacement is more efficient than in an ideal tank reactor, while negative values indicate an inferior displacement efficiency.

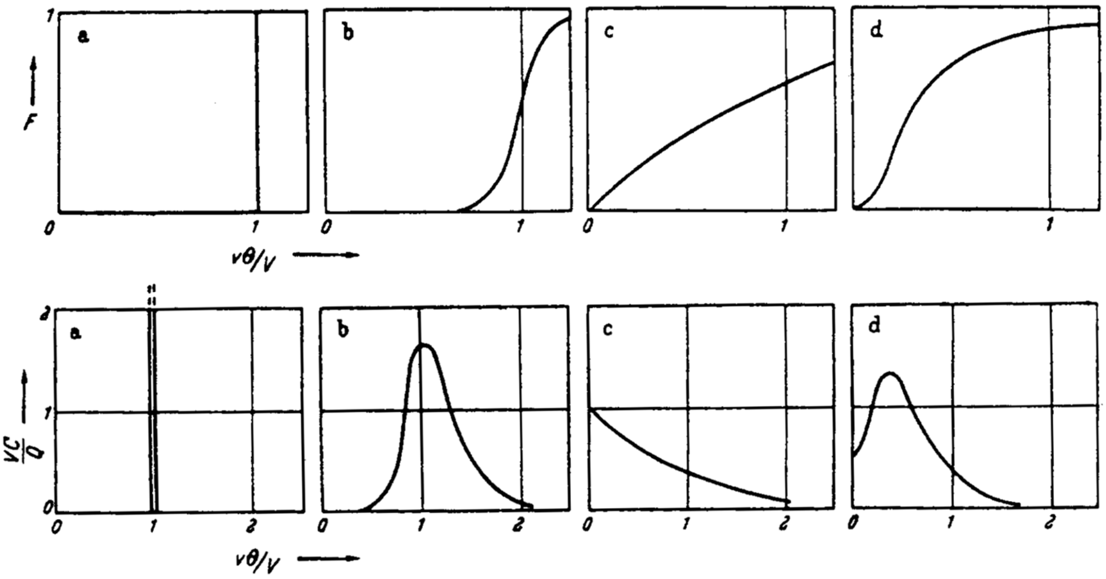

Fig. 13: Development of the relative tracer concentration (F-curve, top) and the corresponding tracer distribution (E-curve, bottom) as a function of the dimensionless time (here: v flow rate, θ absolute time, V volume, C tracer concentration, Q quantity of tracer) (Danckwerts, 1953, pp. 3858). a) Plug flow, b) plug flow with longitudinal mixing/pseudo plug flow, c) complete mixing, and d) dead water.

In general, displacement processes are always comparable to step-input experiments as the non-marked fluid is gradually displaced by the marked one or the other way around. The general characteristics of displacement processes are in the focus of the following section since these give an idea of what happens during the displacement of viscous fluids from the flow channels of spiral-wound membranes.

2.4 Characteristics of displacement processes

Depending on the nature of the fluids, miscible and immiscible displacement can be distinguished. Two fluids are miscible when they are soluble at any mixing ratio, which is the case for the displacement of hydrophilic products by water (Wade, 2006, p. 424). The realization of plug flow during the displacement process is aspired in order to maximize the displacement efficiency, which is the minimization of the mixed phase volume. However, as indicated before, this is a flow type barely observed in practice because the fluids interact with each other and the walls of the flow geometry. Besides diffusion (low impact) and turbulence (high impact), viscous fingering is a flow phenomenon contributing to the mixing of the involved fluids, which reduces the efficiency of the displacement process (Chen, 1987, p. 363). Viscous fingering in porous media is observed at very low flow velocities (Darcy flow), where the flow conditions are categorically laminar (Jha et al., 2011, p. 1). Moving on to unsteady or turbulent flow, the mixing of the fluids on the order of the channel width is intensified. However, the velocity gradients in the channel cross section vanish, which is the basic prerequisite for the aspired plug flow.

2.4.1 General flow patterns

The following section aims at giving a general idea of the flow in narrow channels under laminar and turbulent flow conditions characterized by the Reynolds number in Eq. 4. This structure is expedient as the flow patterns crucially depend on the flow conditions.

Laminar flow conditions

Taylor (1950, p. 193) provides a mathematical approach to describe the instability of a vertical interface between two fluids of different densities and shows that the rate of development of the observed corrugations is a function of the fluid densities (Taylor, 1950, p. 193). In order to verify the validity of this theoretical conclusion, Lewis (1950, p. 84) gives the results of corresponding experiments in a Hele-Shaw cell integrated into an experimental setup allowing to take shadow pictures such as in Fig. 14. A Hele-Shaw cell is an experimental device essentially consisting of two parallel plates enclosing a narrow flow channel.

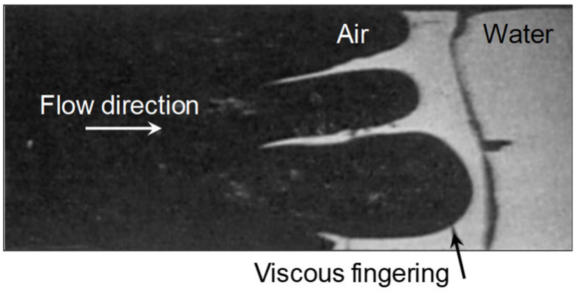

Fig. 14: Displacement of water by air in a Hele-Shaw cell, adapted from Lewis (1950, p. 88).

When displacing water by air (Fig. 14), Lewis (1950, pp. 86) observes that the air develops long fingers leading to a corrugation of the water boundary in a manner coinciding with the theory. In a consecutive study, Saffman and Taylor (1958, p. 324) presume that the traversed distance before the penetration of the displaced fluid by the displacing fluid is a function of the viscosity ratio η_2/η_1. They show that the development of corrugations starts earlier when displacing glycerin by air in comparison to the displacement of glycerin by oil. Consequently, both the density and the viscosity of the involved fluids determine the onset of instabilities during the displacement at laminar flow conditions.

In order to describe the penetration of the fluid interface by a less dense displacing fluid, the term viscous fingering is established. Epstein et al. (2001, pp. 42) investigate the stability during immiscible displacement in an U-tube with an internal diameter of 1 cm. Therefore, they displace silicone oil by a more dense but less viscous solution of zinc bromide salt at laminar flow conditions (Fig. 15). At low flow velocities, a liquid film of the salt solution adheres to the walls of the tube, while the silicone oil penetrates the salt solution (Fig. 15a). At higher velocities, however, the residues of the salt solution are disintegrated by entrainment and mixing (Fig. 15b).

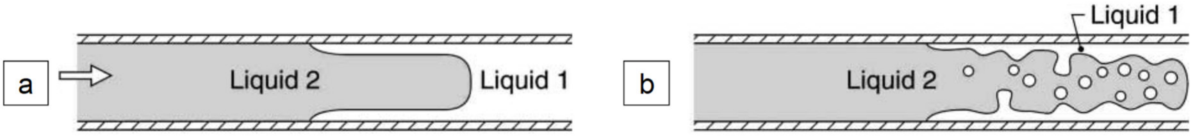

Fig. 15: Displacement of a viscous fluid (liquid 1) by another more dense but less viscous fluid (liquid 2) (Epstein et al., 2001, p. 38).

Fundamentally, the authors confirm the existence of a critical displacement velocity for instability which is a function of the tube radius, the acceleration, the fluid densities and viscosities (Epstein et al., 2001, eq. 12, p. 49). In other words, exceeding this critical velocity, the displacement becomes instable even at laminar flow conditions.

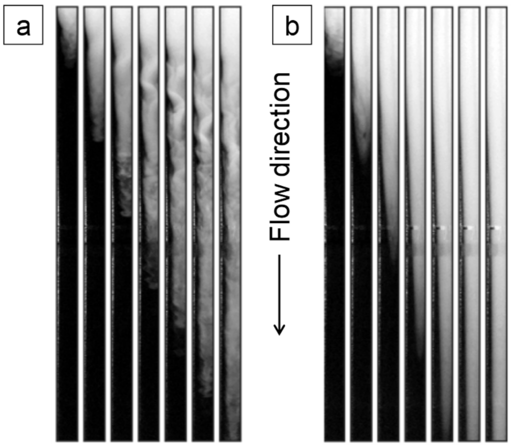

Fig. 16: Miscible displacement of a fluid (black) by a more dense fluid (light) for imposed flow velocities of a) 15 mm/s and b) 75 mm/s (Amiri et al., 2016, p. 7).

Amiri et al. (2016, p. 5) present the results of experiments in vertical tubes, where a more dense fluid displaces a less dense fluid dyed with ink as shown in Fig. 16. Both fluids are miscible and exhibit Newtonian, nearly identical flow properties. At low flow velocities (Fig. 16a), the displacement is instable. Increasing the imposed flow velocity stabilizes the flow (Fig. 16b) because the overall mixing is reduced (Amiri et al., 2016, pp. 7). The reason is that the imposed velocity must compensate the buoyancy of the less dense fluid (black). In order to investigate the stability of the interfaces of two miscible fluids in porous media numerically, Mishra et al. (2008, p. 2) couple Darcy's law with the general advection-diffusion equation. The comprised proportionality factor thus comprises the porosity and permeability characterizing the porous medium. The authors consider the situation that a plug of a liquid sample is injected into another fluid moving at a constant velocity. The results are visualized in Fig. 17 for two scenarios. If the viscosity η_2 of the sample is higher than the viscosity η_1 of the fluid, the rear interface is instable as viscous fingering can be observed (Fig. 17a). The frontal interface, however, is stable and the fluid in the upstream direction is displaced by a piston. In the inverse case, the viscous fingers penetrate the fluid in the upstream direction at the frontal interface, while the rear interface is stable (Fig. 17b). Fig. 17 allows the conclusion that the interface is stable during the displacement, if a viscous fluid displaces a less viscous fluid.

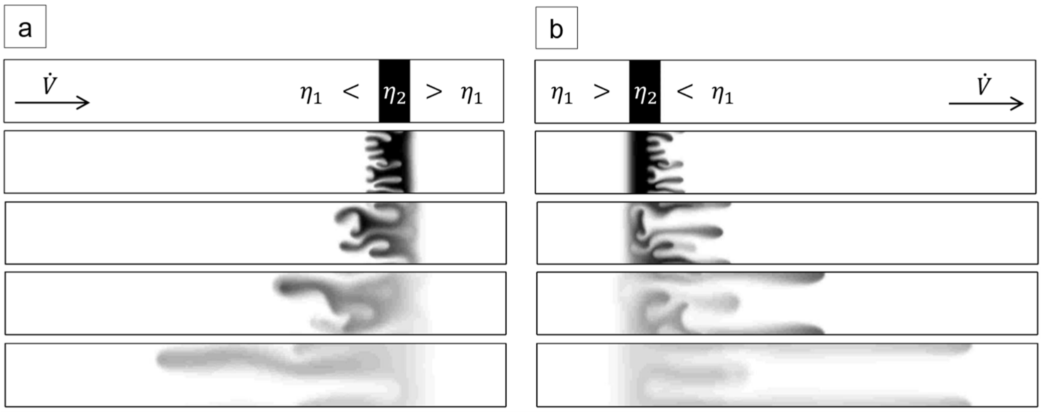

Fig. 17: Visualization of two-dimensional miscible displacement, adapted from Mishra et al. (2008, p. 4) for or two scenarios: a) $\eta_1 < \eta_2$ and b) $\eta_1 > \eta_2$. The color code indicates the concentration from 1 (black) to 0 (white). The time progresses from top to bottom.

The same holds true for the immiscible displacement, where the interface is found to be stable if the density of the displacing fluid is greater than the density of the displaced fluid (Epstein et al., 2001, p. 38). The visual appearance can be very complex since shielding, spreading or tip-splitting of the fingers is observed throughout displacement experiments (Scovazzi et al., 2017, p. 17). In this case, viscous fingering causes disorder in the velocity field, which in turn enhances the mixing of the fluids. On the other hand, long fingers can bypass the core flow, which results in an inefficient displacement process (Jha et al., 2011, p. 106).

Summarizing the studies cited above, differences in density and viscosity of fluids can induce flow instabilities during the displacement process. The displacement of a fluid from a horizontal system by a less viscous/dense fluid at low flow velocities is unfavorable as finger-like structures will penetrate the more viscous/dense fluid resulting in an inefficient displacement process. In the inverse case, a stable interface and thus an efficient displacement process can be expected.

Turbulent flow conditions

Above the critical Reynolds number, transient and subsequently turbulent flow is observed. Considering pipe flow, the flow profile passes from parabolic under laminar flow conditions to rather flat for fully turbulent flow. When displacing a fluid from a pipe, the resulting displacement curve can thus be described by a plug flow superimposed by axial dispersion (Taylor, 1954, p. 465). Besides the turbulence as defined based on the Reynolds number in Eq. 4, Brauer (1979, p. 935) distinguishes four further types of turbulence in multi-phase flow: interfacial turbulence, turbulence due to deformation of the interfaces, grid turbulence, and swarm turbulence.

The interfacial turbulence denotes various types of spontaneous interfacial agitation, which may manifest themselves in the spontaneous emulsification of liquids quietly placed one above the other (Sternling and Scriven, 1959, p. 514). The interfaces of the two liquids furthermore deform stochastically and are also the cause of turbulence. Based on the boundary layer theory, both the interfacial turbulence and turbulence due to deformation of the interface can be described (Brauer, 1979, p. 947). Grid turbulence as shown in Fig. 18 can be observed throughout the flow downstream of a grid of geometrically arranged obstacles such as rods or spheres. Kistler and Vrebalovich (1966, p. 46) provide experimental evidence for the proportionality between the turbulent energy and the pressure drop. Finally, swarm turbulence develops during the flow through freely moving particles. It is a combination of different turbulence types and closely related to the grid turbulence (Brauer, 1979, p. 947).

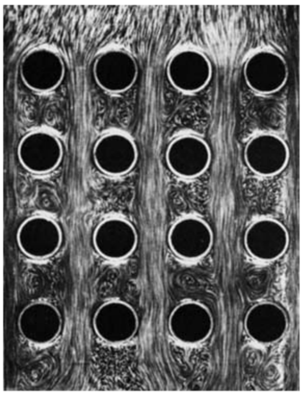

Fig. 18: Photograph of grid turbulence (Brauer, 1979, p. 944).

Altogether, the turbulence as defined by Reynolds is doubtlessly the most important turbulence type with regard to the displacement process in general. Besides, the grid turbulence may be important during the displacement of fluids from channels filled with spacers, which can be considered as a grid. However, references explicitly covering the grid turbulence in spacer-filled channels cannot be identified. Because the number of studies focusing on the displacement of fluids from spacer-filled channels is very limited, the factors influencing the displacement process are discussed including the displacement of fluids from tubes in the following.

2.4.2 Factors influencing the displacement

As shown in the previous section, the flow conditions crucially determine the flow patterns during the displacement. The Reynolds number in Eq. 4 indicates that the factors mainly determining the flow conditions are the characteristics of the involved fluids, the flow channel geometry, and the flow rate. Therefore, the effect of these factors on the displacement process are considered in the following.

Viscosity of the displaced fluid

Henningsson et al. (2007, p. 170) visualize the turbulent displacement of yoghurt from tubes using electrical resistance tomography as shown in Fig. 19. At a flow rate of 10.2 m^3/h, the displacement of the yoghurt from a tube with a diameter of 0.06 m and a length of 5 m takes about 12 s. The concentration profile suggests that gravity affects the displacement since the removal of the yoghurt from the bottom of the tube is delayed.

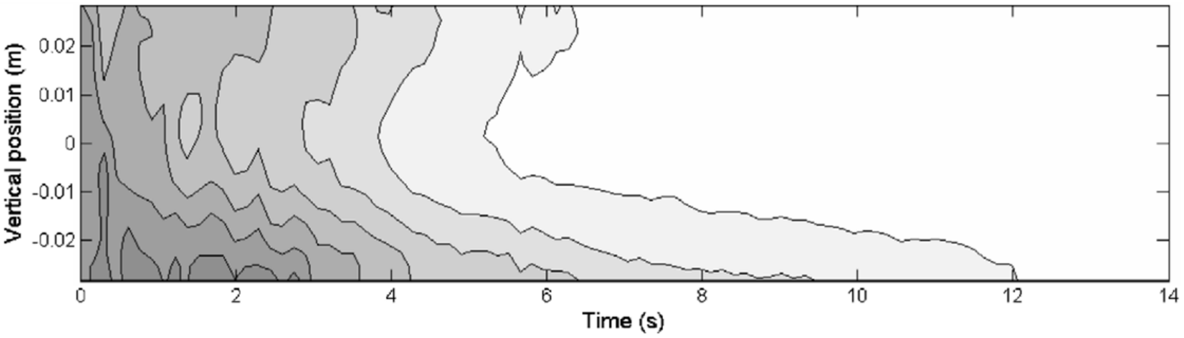

Fig. 19: Displacement of yoghurt (grey) from a tube by water (white) visualized by electrical resistance tomography (Henningsson et al., 2007, p. 170).

Furthermore, the authors show the results of computational fluid dynamics simulations for the displacement of the yoghurt from a 1.5 m long tube. The viscosity of the yoghurt follows the power law in Eq. 1 (k = 3.7 Pa·s$^{0.37}$, n = 0.37). These results suggest that it is possible to decrease the mixed phase volume by 95% by increasing the flow rate from 5.1 to 20.4 m^3/h (Henningsson et al., 2007, p. 171).

The displacement of yoghurt from tubes is shown by Wiklund et al. (2010, p. 336) in Fig. 20 as well. Using a so-called UVP-PD method, they monitor the real-time development of the power-law parameters k and n during the laminar displacement of standard yoghurt by mild yoghurt from a tube (diameter: 0.036 m).

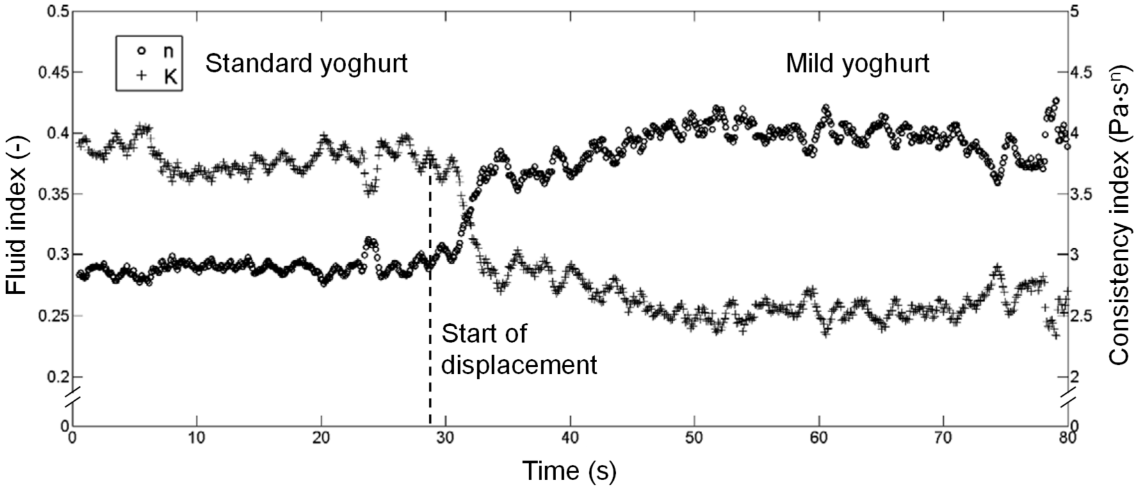

Fig. 20: Development of the fluid index n and the consistency index k during the displacement of standard yoghurt with mild yoghurt, adapted from Wiklund et al. (2010, p. 336).

The applied method is a combination of ultrasound Doppler velocity profiling (UVP) and pressure difference (PD) measurements. The results show that the power-law parameters of the yoghurt types approximately take the values determined throughout standard rheological measurements. Under laboratory conditions, the consistency indexes of the two yoghurt types are found to be 3.4 (standard yoghurt) and 2.6 Pa·s^n (mild yoghurt) and the flow indexes account for 0.3 (standard yoghurt) and 0.4 (mild yoghurt) (Wiklund et al., 2010, p. 334). The transition from one yoghurt type to the other starts with the attainment of the measurement position by the mild yoghurt (≈ 29 s). Regarding Fig. 20, the transition from one yoghurt type to the other is complete in about 20 s. This indicates that the mixing of high-viscous products during the displacement from tubular systems is not intense. With regard to industrial processes, the targeted manipulation of the residence time distribution is desirable in order to improve the process control. Based on the literature reviewed so far, this should be possible by increasing the viscosity of the displacing fluid. Walenta and Kessler (1990b, p. 65) compare the displacement processes in DN10 tubes. The results shown in Fig. 21 suggest that increasing the viscosity of the displacing fluid by increasing the xanthan concentration from 0.25 to 1% induces a reduction of the residence time (dashed lines) when displacing water. In the inverse case (straight lines), the increased viscosity of the displaced product leads to a slight prolongation of the displacement process.

While the preceding studies focus on the displacement of viscous products from tubes, Kieferle et al. (2019a, p. 162) quantify the volume of the mixed phase forming during the displacement of protein concentrates from spiral-wound membranes with a diameter of 6.3 inch and a length of 38 inch. They show that the volume of the mixed phase increases significantly when increasing the viscosity of the protein concentrate. The corresponding residence times can be determined based on the given flow rates and mixed phase volumes. The obtained results indicate that protein concentrates with a rather low viscosity can be displaced from the spiral-wound membrane within 10 s, while the displacement time increases to up to 20 s for more viscous concentrates at the same flow rate. Consequently, the viscosity of the displaced fluid affects the residence time remarkably. Apart from the viscosity of the displaced fluid, the flow pattern determines the displacement process. This depends on the combination of the flow channel geometry and the flow velocity.

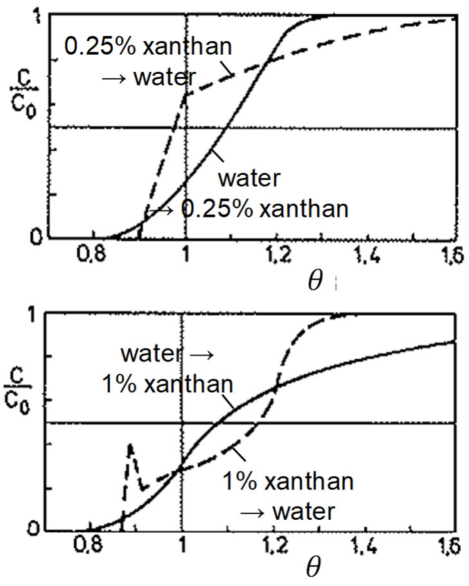

Fig. 21: Cumulative distribution curves for the displacement of water and xanthan solutions from DN10 pipes, adapted from Walenta and Kessler (1990b, p. 65).

Flow channel geometry and flow velocity

The study of Walenta and Kessler (1990b, p. 65) also focuses on the impact of the flow rate on the duration of the displacement process. For the displacement of a 0.25% xanthan solution from DN10 pipes by water (Fig. 22, straight lines), the increase of the flow velocity from 0.5 to 1.5 m/s reduces the residence time (Fig. 22, right to left). The same trend can be observed for the inverse displacement scenario (Fig. 22, dashed lines). Besides the fluid velocities and the sequence of the fluids, Walenta and Kessler (1990b, p. 63) compare two pipe diameters (DN10 and 50). They conclude that the narrowest residence time distributions are achieved by maximizing the pipe diameter in order to increase the Reynolds numbers.

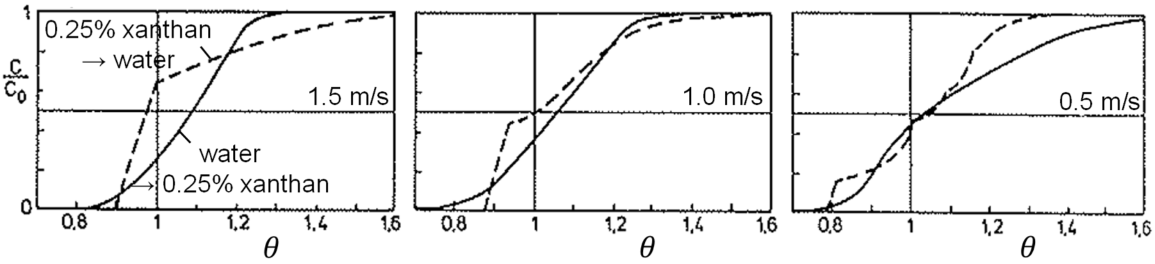

Fig. 22: Cumulative distribution curves for the displacement of water and xanthan solutions from DN10 pipes with different flow rates, adapted from Walenta and Kessler (1990b, p. 65).

While the determination of the flow velocity in pipes is easy as long as the flow rate and the pipe diameter are known, it is non-trivial for the flow in spacer-filled channels of spiral-wound membranes because the quantification of the effective face area is difficult. One reason for this difficulty is related to the design of spiral-wound membranes. Since the membrane leaves and the spacers are wound around the central permeate tube, the modules are not completely circular. This downgrades the fit of the modules in the housing as indicated in Fig. 23a.

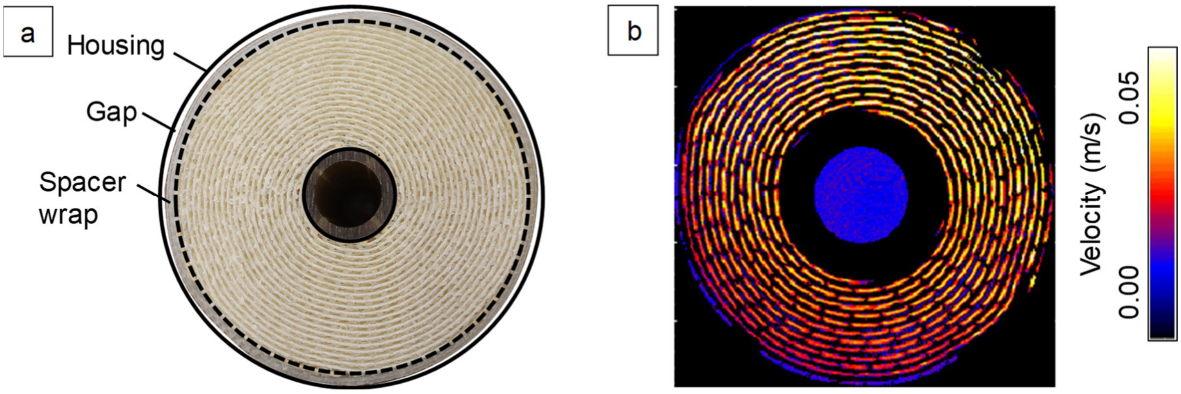

Fig. 23: a) Photograph of a spiral-wound membrane (diameter: 6.3 inch) and b) velocity distribution in a spiral-wound membrane (diameter: 2.5 inch), adapted from Schulenburg et al. (2008, p. 42)

Although, a so-called spacer wrap aims at improving the fit of the module, a small gap between the spiral-wound membrane and the housing is inevitable. In consequence, the fluid passes through the main part of the membrane module, the spacer wrap, and the gap at different flow velocities. Finally, the velocity distribution in a spiral-wound membrane is not always even as shown in Fig. 23b. The color code indicates that the flow velocity increases from the bottom to the top. In summary, the actual flow velocity in spiral-wound membranes depends on the position, which is why an average flow velocity is to be assumed for calculations. Besides, the geometric characteristics of the flow channels are important for the displacement of fluids from spiral-wound membranes. By means of a three-dimensional computational model for predicting the residence time behavior in a spacer-filled channel (length: 0.8 inch, spacer thickness: 0.78 mm), Picioreanu et al. (2009, p. 349) show that the width of the curves increases with increasing biofouling (Fig. 24). This is due to the fact that the biomass increases the aspect ratio defined as the ratio of the diameter of the spacer filament and the channel height (Eq. 11). According to the authors, the tailing aggravates with increasing biofilm formation because of the growth of existing flow shadows and the gradual washing out of tracer diffused in the fouling layer. Consequently, low aspect ratios are advantageous when aiming at a reduction of the residence time.

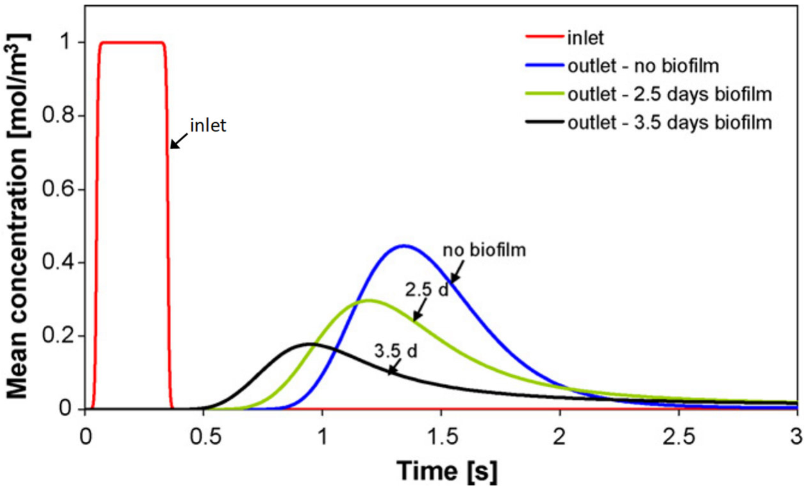

Fig. 24: Residence time distribution in spacer-filled channels with and without biofilm (Picioreanu et al., 2009, p. 349).

In addition to the impact of the viscosity of the displaced fluid, Kieferle et al. (2019a, p. 162) report on the influence of the spacer thickness on the mixed phase volume. Comparing the effect of the spacer thicknesses (0.7, 1.0, and 1.8 mm) it becomes evident that the module equipped with the thinnest feed spacer induces the highest mixed phase volume.

Also Gauwbergen and Baeyens (2000, p. 90; 1997, p. 297) provide experimental residence times for the displacement of water by marked water from spiral-wound membranes at different flow velocities. The Reynolds number as defined in Eq. 4 with the hydraulic diameter as characteristic length are also given. Plotting the residence times against the Reynolds numbers, Fig. 25 clearly shows that the residence time decreases sharply with increasing Reynolds numbers. In case this relationship is functional, the increase of the characteristic length, the increase of the fluid density or the decrease of the viscosity should induce the reduction of the residence time.

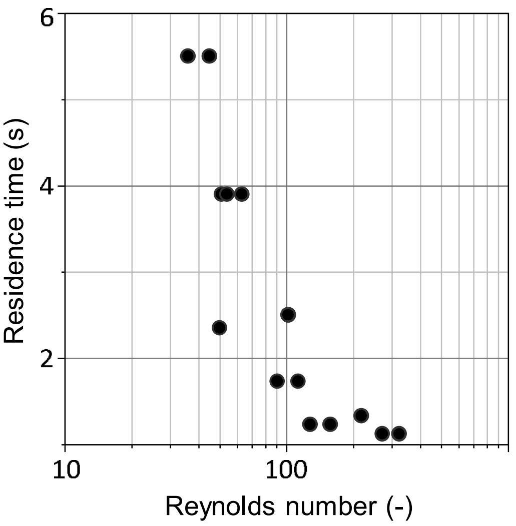

Fig. 25: Relationship between the residence time and the Reynolds number. Data originate from the study of Gauwbergen and Baeyens (2000, p. 90; 1997, p. 297).

In summary, all reviewed studies give evidence that high flow velocities and lower aspect ratios contribute to the improvement of the displacement process. Furthermore, in order to identify the hydrodynamic conditions prevailing in the experimental setup and particularly in the spiral-wound membrane, mechanistic models can be useful.

2.5 Mathematical description of residence time curves by mechanistic models

The mathematical description of displacement processes can be based on various types of models. Among the most frequently cited models are the advection-dispersion/plug flow with dispersion model, the random-walk model, the compartment model, and the tanks-in-series/ (perfect-mixing) cell model.

The denotation of the plug flow with dispersion model already conveys a basic idea of the underlying concept. The residence time distribution measured at the outlet of a plant evolves due to a plug flow superimposed by axial dispersion (Danckwerts, 1953, p. 3861). The proportionality constant quantifying the extent of dispersion is the axial dispersion coefficient. The main idea of the compartment model is that the hydrodynamic processes prevailing in the different sections of a system are each represented by an idealized reactor (Levenspiel, 1999, p. 283). Thus, the hydrodynamic behavior of the real system is described by the connection of ideal reactor models. Basically, these are the ideal continuous stirred tank reactor and the ideal plug flow reactor. The (continuous time) random walk model is a modification of the advection-dispersion model (Hennico et al., 1963, p. 4). However, it requires a set of parameters as input variables, which must be determined based on the data to be described. Hence, the random walk model serves as an empirical model for the formal description of measured curves but does not serve for prediction purposes (Hunt et al., 2011, pp. 428).

In order to learn more about the hydrodynamic conditions determining the displacement of viscous fluids from spiral-wound membranes, it is reasonable to choose models comprising physically meaningful parameters. Among the described models, the advection-dispersion model and the compartment model are the most promising approaches in this regard.

2.5.1 Compartment model

The compartment model has a wide-ranging application field as it can be used for the description of the flow behavior in fluidized bed reactors (Arora et al., 2017; Dehkordi and Memari, 2009), anaerobic sludge beds (Zeng et al., 2005), polymerization reactors (Alexopoulos et al., 2002) or solid oxide fuel cells (Hosseini et al., 2011). The ideal continuous stirred tank reactor and the ideal plug flow reactor are the two key elements of the compartment model. By connecting these reactor types in series or in parallel according to the prevailing hydrodynamic conditions, the residence time behavior of real systems can be approximated. The cumulative distribution curve measured at the outlet of an ideal stirred tank reactor as a response to a step-input function takes the shape of the curve in Fig. 13c and can be described by Eq. 23 (Danckwerts, 1953, eq. 1). The shape of the observed cumulative distribution curve depends on the time t, the flow rate $\dot{V}$, and the volume of the tank V_T.

$$F(t) = 1 - exp\left(-\frac{\dot{V}}{V_T} \cdot t\right) \tag{23}$$

$$F(t) = 1 - exp\left(-\frac{\dot{V}}{V_T} \cdot (t - t_d)\right) \tag{24}$$

In contrast to the ideal stirred tank reactor, the ideal plug flow reactor does not affect the shape of the input function. It merely introduces a time delay t_d equal to the ratio of the volume of the plug flow reactor and the flow rate. For a series connection (arbitrary sequence) of an ideal stirred tank reactor with the volume V_T and an ideal plug flow reactor, Levenspiel (1999, p. 286) suggests an expression equal to Eq. 24. Basically, however, arbitrary models can be applied in order to approximate the description of the hydrodynamic behavior of the respective compartment the best way possible. Like the compartment model, the advection-dispersion model is frequently well applicable.

2.5.2 Advection-dispersion model

Besides the description of the residence time in tubular systems (Walenta and Kessler, 1990a; Taylor, 1954), the advection-dispersion model can be applied for a wide variety of geometries such as horizontal fluidized beds (Bachmann and Tsotsas, 2015), natural rivers (Disley et al., 2015; Fischer, 1973), flotation columns (Yianatos et al., 2017) or spiral-wound membranes (Gauwbergen and Baeyens, 2000; 1997) to name just a few. The advection-dispersion model is derived from the general transport equation (Eq. 12) and allows the description of the concentration changes as a function of time and the position. In order to describe the axial dispersion during the displacement, it is necessary to insert an axial dispersion coefficient instead of a molecular diffusion coefficient. Because the axial dispersion coefficient represents the interaction of the material parameters, such as the fluid viscosities and densities, as well as the flow velocity, and the geometry of the flow channel, it must be determined experimentally (Danckwerts, 1953, p. 3861).

Eq. 25 is the governing equation for the description of the relative concentration c (related to the initial concentration of a tracer substance) as a function of the time t and the position x (Levenspiel and Smith, 1957, p. 228; Danckwerts, 1953, p. 3861). This diffusion-advection equation considers only one proportionality factor, the axial dispersion coefficient D_a.

$$\frac{\partial c}{\partial t} = D_a \cdot \frac{\partial^2 c}{\partial x^2} \tag{25}$$

Hence, one of the basic assumptions is concentration homogeneity in the radial direction, which means that no radial dispersion occurs. Besides, the axial dispersion is assumed to be constant in the whole system. Carslaw (1921, pp. 34) provides a solution for the linear flow of heat in semi-infinite solids using the error function approach, which is just one out of several possible solution approaches (Carslaw and Jaeger, 1959, pp. 50). The Gaussian error function erf has a sigmoid shape and is defined by Eq. 27. In analogy to this solution, Danckwerts (1953, eq. 18) provides the solution in Eq. 26 customized to describe the residence time distribution of fluids as a function of the reactor length L and the flow velocity u. A very detailed derivation of this solution is provided by Ogata and Banks (1961).

$$F(x,t) = \frac{1}{2}\left(1 - erf\left(\frac{L - u \cdot t}{2 \cdot \sqrt{D_a \cdot t}}\right)\right) \tag{26}$$

$$erf(z) = \frac{2}{\sqrt{\pi}} \cdot \int_0^z e^{-y^2} dy \quad with \quad y = z^2 = \frac{(L - u \cdot t)^2}{4 \cdot D_a \cdot t} \tag{27}$$

The closed-closed boundary conditions underlying Eq. 26 are visualized in Fig. 26. Upstream the dispersion zone, the relative concentration equals 1 and drops to 0 in the downstream direction. The interface between the two fluids is located in the middle of the dispersion zone at $x = 0$. Within the dispersion zone, the fluid motion is statistically distributed. Before the inlet and behind the outlet, no axial dispersion occurs.

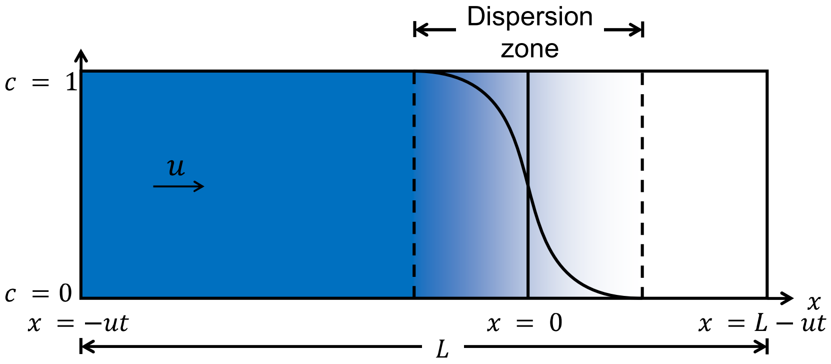

Fig. 26: Visualization of closed-closed boundary conditions assumed by Danckwerts (1953, eq. 16).

The ready-to-use solution in Eq. 28 for the residence time distribution of a fluid in motion under closed-closed boundary conditions is published by Levenspiel and Smith (1957, eq. 3). Herein, L is the length of the reactor, u_a is the average fluid velocity, D_a is the axial dispersion coefficient, x is the position, and t is the time.

This solution can be used to predict residence time distributions measured throughout pulse-input experiments. On rearranging Eq. 28, Eq. 29 gives the E-curve as a function of the Péclet number Pe (Eq. 13) and the dimensionless time θ (Eq. 21) (Levenspiel, 1999, p. 297).

$$E(x,t) = \frac{L}{2 \cdot \sqrt{\pi \cdot D_a \cdot t}} \cdot exp\left(-\frac{(x - u_a \cdot t)^2}{4 \cdot D_a \cdot t}\right) \tag{28}$$

$$E(Pe,\theta) = \frac{1}{\sqrt{4 \cdot \pi \cdot \left(\frac{1}{Pe}\right)}} \cdot exp\left(-\frac{(1-\theta)^2}{4 \cdot \left(\frac{1}{Pe}\right)}\right) \tag{29}$$

In order to apply this equation, an estimate for the Péclet number is required, which can be obtained based on experiments. Using non-linear least-squares regression for fitting Eq. 29 to the experimentally measured E-curve gives good results for small extents of dispersion. If the resulting Péclet numbers take values above 100, the assumption of small deviation from plug flow is doubtlessly justified (Levenspiel, 1999, p. 265). Péclet numbers below this threshold indicate increasingly skewed E-curves and thus increasing deviation from plug flow. An analytical expression for the E-curve for large extents of dispersion, however, does not exist (Levenspiel, 1999, p. 300). In these cases, the method of moments is to be used for the assessment of the Péclet numbers (Trinidad et al., 2006, p. 607). The variance σ_m^2 of the time-dependent density function depends on the Péclet number Pe (Eq. 13) and the dimensionless time θ (Eq. 21). Eq. 30 is provided by Laan (1958, p. 189, IV) for large deviations from plug flow and closed-closed boundary conditions. For small deviations from plug flow (Pe > 100), Eq. 30 approximates Eq. 31.

$$\sigma_m^2 = \theta^2 \cdot \left(\frac{2}{Pe} - \frac{2}{Pe^2} \cdot (1 - e^{-Pe}) \right) \tag{30}$$

$$\sigma_m^2 = \theta^2 \cdot \frac{2}{Pe} \tag{31}$$

Finally, Péclet numbers below 1 give evidence that the plant under consideration does not meet the model assumptions (Levenspiel, 1999, p. 301). Here, the advection-dispersion model is unsuitable.

3 Research focus

Every start-up and shut-down of an industrial plant is initiated by a displacement process. While the displacement of (non-)Newtonian liquids from rotationally symmetric geometries such as tubes is a well understood process, the displacement of fluids from membrane plants equipped with spiral-wound membranes has been studied very little so far. Concluding from literature, factors that undisputedly affect the displacement behavior are the flow rate, the geometry of the flow channel, and the viscosity of the involved fluids. It is expected that these factors essentially influence the displacement of fluids from spiral-wound membranes as well, however, the exact interrelations between the factors are unknown.

Therefore, the superordinate research focus of this thesis is on the characterization of the hydrodynamic processes during the displacement of (non-)Newtonian fluids from spiral-wound membranes. Besides, it is envisaged to identify the factors being relevant to industrial applications and to specify the contribution of the respective factors to the displacement efficiency.

In order to reach these aims, experiments are carried out. The variables are the flow rate, the flow channel height, the temperature of displacing fluid as well as the viscosity of the model product and the displacing fluid. The analysis of the experimental results is performed based on two different approaches. Firstly, statistical models are developed for the functional description of the residence time as a function of the above-mentioned process conditions. The target value is the residence time, which is a measure for the displacement efficiency and equals the time required to complete the displacement process. The underlying assumption is that all factors affecting the hydrodynamics do influence the residence time since they determine the mass transfer. However, the analysis of the residence times provides no insights into the local hydrodynamic processes. Consequently, different mechanistic models are used secondly. Due to their wide applicability, the advection-dispersion model and the compartment model are chosen. In case of good accordance of a model with the observed residence time distribution curves, the model represents the hydrodynamic conditions prevailing locally and contribute thus to the improvement of the understanding of the displacement process. The assumption underlying the mechanistic models is that the residence time behavior of the fluids in the spiral-wound membrane during the displacement can be described by plug flow superimposed by axial dispersion. In order to extend the practical relevance of the results, it is intended to estimate the residence time behavior of a viscous product in an industrial-scale plant equipped with spiral-wound membranes during the displacement based on the most suitable model.

While computational fluid dynamics simulations most frequently focus on spacer-filled channels of flat-sheet membranes, the experiments are carried out with a test rig on a pilot scale comprising an industrial-scale spiral-wound membrane. Thus, the results are very close to industrial reality and reveal the contribution of the plant design on the observed residence time behavior, which is nearly impossible based on computational fluid dynamics simulations due to the complexity of the system. Furthermore, most studies on hydrodynamics in spacer-filled channels focus on Newtonian fluids. In contrast, this thesis considers non-Newtonian as well because most food liquids that need to be displaced prior to the start-up and shut-down of the plants do not show Newtonian flow properties.

The benefit of the thesis is that it provides a data basis for the targeted enhancement of displacement processes as it discloses the relationships between the residence time behavior and the process conditions. Besides, the mechanistic models provide an idea of the hydrodynamic processes determining the displacement efficiency. This knowledge can be a starting point for the optimization of the displacement processes and the plant design with regard to reducing the required amount of displacing fluid and to minimizing the losses of valuable product as part of the discarded mixed phase.

4 Description of the applied materials and methods

In order to identify the impact of important process conditions on the displacement process, four data sets listed in Tab. 2 were used. To investigate the effect of different viscosities and flow properties on the displacement process, soft water, protein concentrates, and xanthan solutions were deployed as model products and displacing fluids. Besides the combination of the fluids, their sequence was varied to provide different displacement scenarios as described below.

Tab. 2: Overview of the experimental data basis.

Data set	**1** **SW → PC**	**2** **SW → PC**	**3** **XS → PC**	**4** **SW → XS**
Displacing fluid	**SW**: Soft water	**SW**: Soft water	**XS**: Xanthan solution (+ NaCl)	**SW**: Soft water
Model product	**PC**: Protein concentrate	**PC**: Protein concentrate	**PC**: Protein concentrate	**XS**: Xanthan solution (+ NaCl)
Signal	Absorption A	Absorption A	Conductivity κ	Conductivity κ
Monitored (discrete) signals	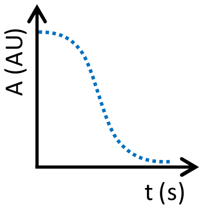	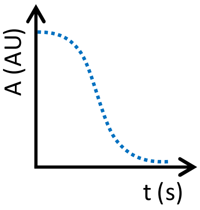	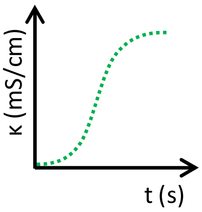	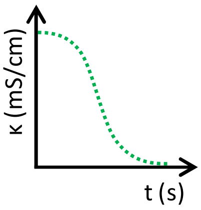

The displacement processes were monitored by means of a turbidity sensor and a conductivity sensor. The necessity of the two sensors is explained by the fact that protein concentrates show a very low conductivity, while the xanthan solutions' turbidity increases sharply with the xanthan concentration.

The materials and methods employed for the practical implementation of the experiments and the subsequent analyses are specified in the following.

4.1 Implementation of the residence time measurements

The displacement experiments were carried out with a single spiral-wound membrane on an industrial scale. A pilot-scale plant mimicking the design of an industrial plant was used. Besides the general experimental setup, the implementation of the residence time measurements required the choice and installation of appropriate sensors.

4.1.1 Experimental setup and procedure

The experiments were performed using the custom-made plant (SIMAtec GmbH, Schwalmtal, Germany) on a pilot-scale sketched in Fig. 27. The flow path of the displacing fluid is highlighted by blue, bold lines. The general arrangement of the plant components ought to be comparable the design of industrial production plants. However, it comprises a housing for only one instead of several spiral-wound membranes in series as one would find in industrial installations. Comparable to the setup of the housings in loop structures, the inlet and the outlet are perpendicular to the membrane module. The appendix N contains a sketch of the housing including the dimensions.

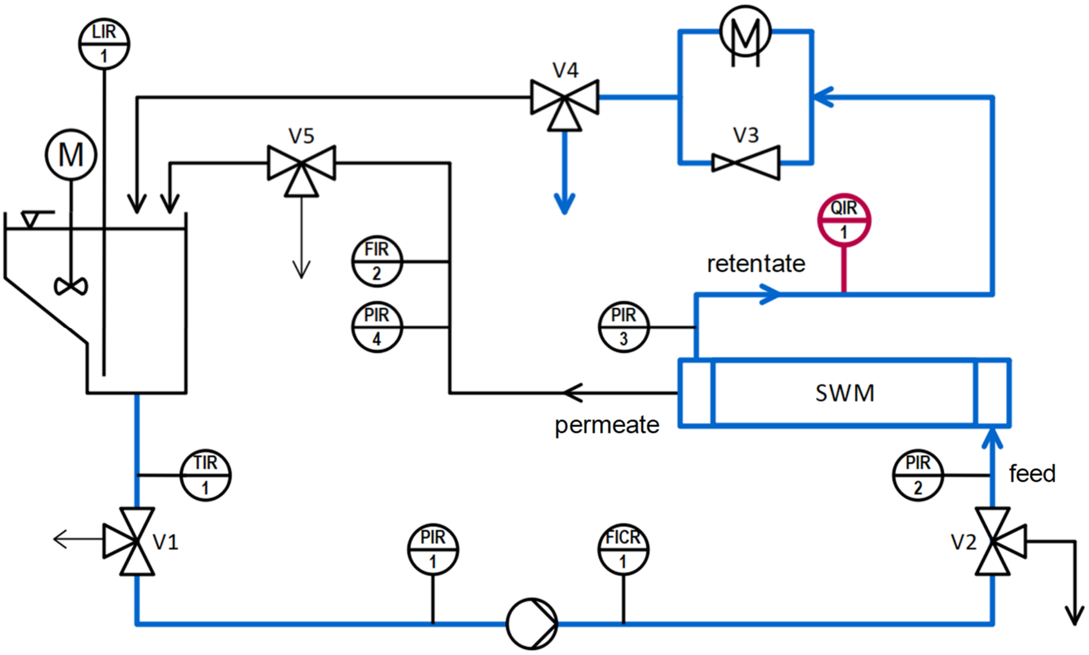

Fig. 27: Simplified piping and instrumentation diagram of the used test rig on a pilot scale. The flow path during the displacement the of model products from the spiral-wound membrane is highlighted by blue, bold lines. The position of the turbidity/conductivity sensor is indicated in red (QIR1).

To investigate the influence of the spacer dimensions on the residence time (behavior), three SpiraCel® spiral-wound membranes with differently thick spacers (0.7, 1.0, and 1.8 mm) were used. These industrial-scale modules were provided by MICRODYN-NADIR GmbH (Wiesbaden, Germany / diameter: 6.3 inch, length: 3.8 inch, material: PES, MWCO: 10 kDa, filament angles: α = 45°, β = 90°). The anti-telescoping device was of the cartwheel-type and from stainless steel. The turbidity sensor OUSAF11 (Endress+Hauser Messtechnik GmbH+Co. KG, Weil am Rhein, Germany) and the conductivity sensor GLMU 400MP-PG (GHM Messtechnik GmbH, Regenstauf, Germany) were used to monitor the displacement process. Their position in the experimental arrangement is also depicted in Fig. 27 (QIR1). The experimental procedure was the same for all displacement scenarios and is described in the following.

Firstly, the permeate valve V5 was closed in either direction to avoid permeation during the displacement process. Secondly, the module was filled with the model product before closing valve V2 towards the module housing. Thirdly, the storage tank and the pipeline were rinsed properly and filled with the displacing fluid. Finally, the displacement process was initiated by opening valve V2 and simultaneously turning on the centrifugal pump. Because the permeate valve V5 is closed during the displacement process, the retentate flow rate equals the feed flow rate and is denoted as flow rate in the following.

For all experiments, the residence time corresponded to the time, which passed from the turning-on of the pump until the attainment of a predefined turbidity or conductivity value. These sensor values depended on the displacement scenario. When protein concentrates were displaced by water, the detection limit of the turbidity sensor (0.015 AU) served as stop criterion for the displacement process. Concerning the experiments for which xanthan solutions were used as displacing fluid, a conductivity of 18.4 mS/cm was suitable since this value corresponded to 98% of the maximum attainable conductivity. When the xanthan solutions were displaced by soft water with a conductivity of 0.6 mS/cm at 10°C, the value of 0.8 mS/cm marked the end of the displacement process. The characteristics of the sensors determining these stop criteria are specified next.

4.1.2 Sensor characteristics

The utilization of the sensors depended on the displacement scenario because the turbidity of xanthan solutions made the application of the turbidity sensor unsuitable. Thus, the turbidity sensor was only used for experimental runs, where the protein concentrates were displaced by soft water.

Tracer quantification

Whenever protein concentrates were displaced by soft water, the turbidity sensor was deployed for monitoring the displacement process. In these cases, the protein served as tracer. Fig. 28 shows the dependence of the absorption on the protein concentration. The detection limit is 0 ± 0.03% protein, which corresponds to an absorption of 0.015 AU. To ensure the measurement accuracy of the turbidity sensor, the pipeline system was filled with soft water tempered to 10.0°C and the signal of the sensor was set to 0.000 AU prior to each experiment.

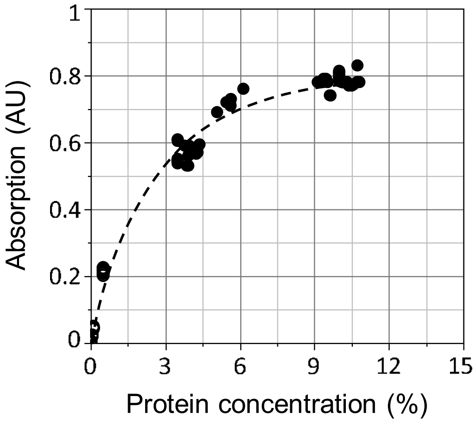

Fig. 28: Absorption as a function of the protein concentration.

Preliminary tests (not shown) revealed that the signal of the turbidity sensor does not depend on the flow velocity. Because the turbidity of xanthan solution increases with increasing xanthan concentration, it was necessary to use the conductivity sensor for experimental runs carried out with xanthan solutions. The correlation between the electrical conductivity and the content of sodium chloride is tabulated in literature and assumed to be linear independently of the flow velocity (Haynes, 2016, p. 5–71; Prausnitz and Wilhelm, 1956, p. 942). The measurement range of the conductivity sensor is variable and was set to 0.0 to 20.0 mS/cm. To examine proper calibration prior to each experiment, solutions of 0.5 and 1% sodium chloride were used.

Reproducibility of the measurements

The residence time during the displacement is the time required for attaining the predefined sensor values. In order to review the reproducibility of the residence time measurements, the results of experiments carried out under equivalent process conditions were analyzed. For this analysis, turbidity measurements were used as these are considered less accurate than the conductivity measurements and indicate thus the maximum error to be expected. Protein concentrates with high (10.30 ± 0.50%) and low (3.90 ± 0.04%) protein concentrations were displaced by soft water at a flow rate of 13.9 ± 0.1 m^3/h. The standard deviation of the residence times determined in triplicate accounted for 0.50 and 0.52 s for the protein concentrates with high and low protein concentrations, respectively. Besides the experimental procedure, the preparation of the model fluids always followed a fixed routine.

4.2 Preparation and flow properties of the model fluids

The model fluids soft water, reconstituted milk protein concentrates, and aqueous xanthan solutions were chosen to represent Newtonian and non-Newtonian behavior. Throughout the experiments, different displacement scenarios involving varying combinations of the model fluids were investigated with regard to their residence time behavior. While the preparation of the soft water as displacing fluid was limited to its temperature control, preparing reconstituted milk protein concentrates and xanthan solutions required the deployment of more resources.

4.2.1 Preparation procedures

Although both the milk protein concentrates and the xanthan solutions were prepared from powders, the preparation procedures were distinctly different. In order to ensure the comparability of the experimental results, the model fluids were always prepared following the standard operating procedures below.

Protein concentrates

To cover a large viscosity range occurring in a multistage plant for concentrate production, the concentrates were prepared by dispersing different amounts of milk protein concentrate powder in fresh pasteurized skim milk. The fresh skim milk was from a local dairy (Molkerei Weihenstephan GmbH & Co. KG, Freising, Germany / pasteurization conditions: 74°C, 28 s). The milk protein concentrate powders were supplied by Hochdorf Holding AG (Hochdorf, Switzerland/protein content: 77.2%) and Pienas Lt (Kaunas, Lithuania/protein content: 82.2 and 82.5%). Firstly, the milk protein concentrate powder was dispersed in the skim milk with a powder dispersion device (Fristam Powder Mixer, Fristam Pumpen GmbH, Hamburg, Germany/shear pump frequency: 15 Hz) for 10 min at 45 ± 2°C. Subsequently, batches of 130 L were cooled to less than 10°C and stirred in an isolated tank until usage on the following day. The temperature of the concentrates was adapted to 10 ± 1°C at least one hour before the start of the experiment. To quantify the actual protein concentration of the concentrate samples, the Dumas method was applied using the vario MAX cube (Elementar Analysensysteme GmbH, Langenselbold, Germany). As is the custom for milk products, a conversion factor of 6.38 was applied to estimate the protein concentration based on the detected amount of nitrogen (Ribadeau-Dumas and Grappin, 1989, p. 370). Furthermore, the density of the concentrates was determined at 10°C using a density measurement device for liquids (DMA 4100M, Anton Paar GmbH, Graz, Austria).

Xanthan solutions

The xanthan solutions were prepared by dispersing a mixture of xanthan gum powder (Xanthan 1000, Lanuco GmbH, Hamburg, Germany) and sodium chloride in soft water tempered to 15 ± 3°C using the powder dispersion device (see above). The amounts of xanthan gum powder were adapted to realize concentrations between 0 and 0.75% in the solutions with a batch size of 200 L. The salt concentration of the xanthan solutions always accounted for 1.1%. To allow full rehydration, the xanthan solutions were prepared one day in advance and stirred at 25 rpm in a vessel equipped with an anchor stirrer overnight in a cooling chamber at 4°C. The conductivity of the solutions accounted for 18.8 mS/cm since the addition of the xanthan gum does not affect the conductivity to an extent relevant for the performed measurements.

In order to provide a functional description of the displacement process, the flow properties of the deployed fluids must be known. Hence, the rheological key figures are determined for the reconstituted milk protein concentrates and the xanthan solutions on a laboratory scale.

4.2.2 Determination of the power-law parameters

The power-law model in Eq. 1 approximates the apparent viscosity of the reconstituted milk protein concentrates and the xanthan solutions very good. For the determination of the power-law parameters, the rheometer MCR 302 and the corresponding double gap geometry DG26.7 (Anton Paar GmbH, Graz, Austria) were used. The ramp-up and ramp-down measurements were performed in the shear rate range from 1 to 1500 s^{-1} at 10.00 ± 0.01°C under unsteady conditions. Fig. 29 provides the results of the measurements.

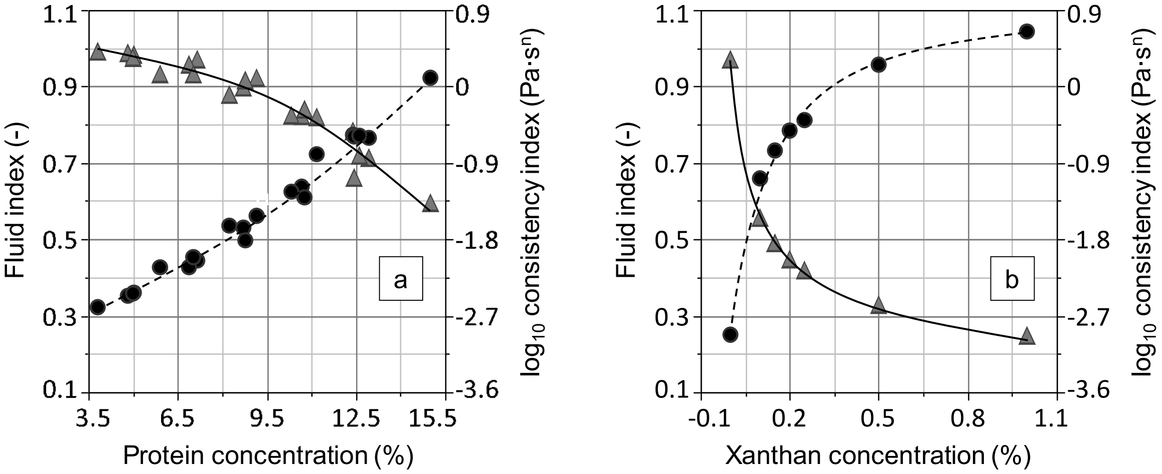

Fig. 29: Fluid index (triangles) and consistency index (circles) as a function of the a) protein content of the protein concentrates and the b) xanthan concentration of the xanthan solutions. Lines are guides for the eyes.

The consistency indexes k (circles) increase with increasing protein concentrations C_P or xanthan concentrations C_X, while the fluid indexes n (triangles) are always below 1 and decline with increasing concentrations. The formal dependences of the power-law parameters on the protein or xanthan concentration are given in Eqs. 32 to 35, which were applied in the following analyses. As already known from literature (Galván et al., 2018, p. 192; Carvalho, 1986, p. 61), both fluids exhibit shear-thinning flow behavior.

$$\log_{10}(k_{PC}) = -\,2.900 + 0.079 \cdot C_P + 0.009 \cdot C_P^2 \tag{32}$$

$$n_{PC} = 0.407 + \frac{1.00 - 0.407}{1 + e^{\,0.385 \cdot (C_P - 12.925)}} \tag{33}$$

$$\log_{10}(k_{XS}) = 0.770 - 1.318 \cdot e^{\,-27.296 \cdot C_X} - 2.375 \cdot e^{\,-2.992 \cdot C_X} \tag{34}$$

$$n_{XS} = 0.204 + 0.357 \cdot e^{\,-2.117 \cdot C_X} + 0.409 \cdot e^{\,-18.677 \cdot C_X} \tag{35}$$

However, both power-law parameters change more drastically for the xanthan solutions within the relevant concentration range. This is evident when having a look at Fig. 30. This figure suggests furthermore that the two power-law parameters always bear a certain proportion to each other. This means that one of the parameters suffices to estimate the apparent viscosity of the fluids. Besides, this plot clearly shows that the flow properties of the two model fluids are distinctly different.

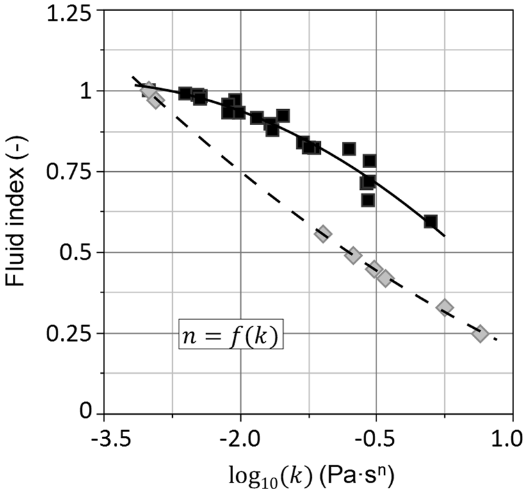

Fig. 30: Fluid index n as a function of the consistency index k for protein concentrates (squares) and xanthan solutions (diamonds).

Since the reconstituted milk protein concentrates and the xanthan solutions are non-Newtonian fluids, their viscosity is a function of the local shear rate, which is determined by the spacer dimensions. Consequently, the geometric characterization of the feed spacers is a prerequisite for the correct determination of the viscosity of the model products in the spacer-filled channels of the spiral-wound membranes during the displacement process.

4.3 Geometric characterization of the feed spacers

The spacers used for the manufacture of the spiral-wound membranes are shown in Fig. 31. While the feed spacers keep the membrane leaves apart, the spacer wrap envelopes the spiral-wound membrane in order to improve the fit of the module in the housing (Fig. 23).

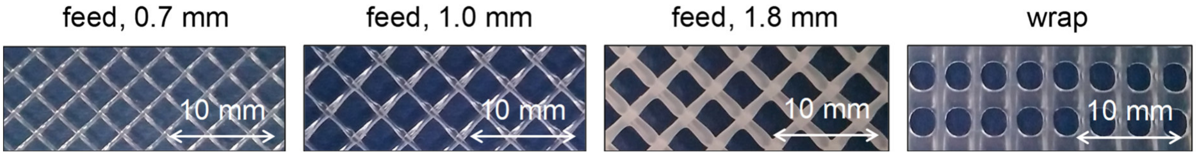

Fig. 31: Photographs of the feed spacers with different thicknesses (0.7, 1.0, 1.8 mm) in diamond configuration and the spacer wrap.

The precise geometric characterization of the feed spacers is particularly important with regard to the clarification of the hydrodynamics because the dimensions of the spacers affect the flow velocity and thus the apparent viscosity of the model fluids. Consequently, the required geometric dimensions were determined. Among these is the volume of the spacers, which was assessed based on the volume displacement method. The determination of the spacer surface was performed by linking the results of the volume displacement method with image analyses.

4.3.1 Volume displacement method

In order to quantify the specific volume of the spacer filaments depicted in Fig. 31, the volume displacement method was applied as described by Siddiqui et al. (2017, p. 307). Therefore, spacer pieces of defined areas were photographed, weighed and subsequently inserted into weighed measuring cylinders with a capacity of 10 mL. In the next step, the cylinders were filled up to a defined volume with lubricating oil (LFC 1046, Elkalub / Chemie-Technik GmbH, Vöhringen, Germany) and weighed again. The usage of oil instead of water was considered necessary to prevent a falsification of the measurement by air bubbles attached to the spacers as described by Siddiqui et al. (2017, p. 310). The density of the lubricating oil was measured by means of a density measurement device (DMA 4100M Anton Paar, Graz, Austria) and accounted for 0.875 ± 0.002 g/cm^3. Finally, the volume of the spacer pieces was determined as the difference of filling volume in the cylinders and the calculated oil volume. All measurements were carried out in triplicate.

Besides the specific spacer volume, it was necessary to assess the specific spacer surface in order to calculate the hydraulic diameter. This was done based on image analyses described in the following.

4.3.2 Image analysis

The specific spacer surface S_s was calculated assuming a cylindrical shape of the spacer filaments according to Eq. 36. Herein, r_e is the equivalent radius of the cylinders, A_s is the spacer area, l_s is the specific length of the spacer filaments, and l_m is the mesh length.

$$S_s = r_e^2 \cdot \left(2 \cdot \pi \cdot \frac{1}{A_s} - \frac{l_s}{l_m}\right) \tag{36}$$

$$r_e = \sqrt{\frac{V_s}{\pi \cdot l_s}} \tag{37}$$

The equivalent radius depends on the specific spacer volume V_s, which was determined using the volume displacement method. The mesh length and the total length of the filaments of a spacer piece with a defined area was determined by means of image analyses. These were performed with the photographs of the spacer pieces used for the volume determination and the computer program ImageJ (Version 1.51k, National Institute of Health, Washington DC, USA). This software allows the quantification of distances between marked points as long as the image allows the correlation between pixels and meters.

The results of the geometric characterization of the spacers are given in the appendix E. Having established the practical requirements for the experiments, the design and analysis of the experiments is in the focus of the next section.

4.4 Design and analysis of experiments

Prior to dealing with the details of design and analysis of experiments, the clarification of several technical terms is beneficial. In this context, a performed experiment itself is denoted as an observation which target value is the response. The physical variables amended in a targeted manner for each experiment are factors, while the different settings of these variables are called factor levels. Hence, the experiments are characterized by the factor level combinations and cover a certain factor space determined by the value range of the factor levels. Finally, the term factor interaction expresses that the effect of one factor depends on the value of a second factor. Thus, one factor may not affect the response unless the value of the other factor exceeds a certain threshold.

The general procedure for the clarification and/or optimization of a process comprises four steps. First of all, a statistical design of experiments covering the desired factor space is to be created. Having performed the experiments accordingly, the analysis of the results is based on the response surface methodology. It comprises different statistical and mathematical approaches for the clarification and optimization of processes. Among these is the statistical modelling, which allows the identification of factors and factor interactions being relevant for the process under consideration. The last but no less important step is the validation of the model by further experiments because this certifies the general validity of the model. For the realization of these steps, the software JMP® Pro (Version 13.1.0, SAS Institute Inc., Cary, USA) was used.

4.4.1 Statistical design of experiments

The aim of this thesis is to investigate the influence of the process variables listed in Tab. 3 on the residence time during the displacement of a product from spiral-wound membranes. Therefore statistical designs of experiments were created by means of the JMP® custom design platform. The resulting designs are orthogonal for the man effects and balanced since the estimated coefficients are independent and the number of implementations is equal for each factor level.

Tab. 3: Overview of experimental scenarios. The complete designs of experiments (DoE) as well as the target-actual comparison of the process parameters can be accessed in the appendices F, H, and 0.

Factors		**DoE 1**	**DoE 2**	**DoE 3**
Model product	Design role	continuous	continuous	continuous
	Values	Milk protein 3.6 … 11.9%	Milk protein 3.6 ... 16.2%	Xanthan 0 ... 0.75%
Displacing fluid	Design role	(constant)	continuous	constant
	Values	(Soft water)	Xanthan 0 ... 0.75%	Soft water
Flow rate	Design role	continuous	continuous	continuous
	Values	7.5 ... 17.5 m^3/h	5.0 ... 15.0 m^3/h	5.0 ... 15.0 m^3/h
Spacer thickness	Design role	categorical	categorical	categorical
	Values	0.7, 1.0, 1.8 mm	0.7, 1.0, 1.8 mm	0.7, 1.0, 1.8 mm
Displacement temperature	Design role	continuous	(constant)	(constant)
	Values	10 ... 30°C	(10°C)	(10°C)

The choice of the factors was taken based on the following considerations. First, the flow velocity and the geometry of the spacers are known to affect the flow conditions and thus the residence time (Kieferle et al., 2019a, p. 162; Picioreanu et al., 2009, p. 349). Consequently, the flow rate during the displacement and the thickness of the spacers in the spiral-wound membrane were considered as factors. Besides, the viscosity of the involved fluids affects the displacement behavior (Mishra et al., 2008, p. 4). In order to investigate this effect, milk protein concentrates and xanthan solutions are chosen as model fluids of different flow properties. Finally, the displacing fluid’s temperature is included into the design of experiments to answer a question arising in industrial practice: Does the temperature of the displacing fluid affect the displacement efficiency?

The designs of experiments are conceived in the way that they allow the identification of significant factors as well as relevant factor interactions, which is not possible based on an one-factor-at-a-time experimental design (Sachs, 1992, p. 684). For the design of experiments, it was assumed that the factors themselves, the interaction of two factors, and the squared values of the factors can affect the value of the response. These assumptions are made following the model presented by Khayet et al. (2010, p. 117).

Having performed the experiments specified in Tab. 3 (see details in the appendices F, H, and 0), the factors actually influencing the response and their relationships can be identified by using the response surface methodology.

4.4.2 Response surface methodology

In order to learn more about the relationships between the factors and the response, diagrams relating the measured values can be expedient. However, assessing whether a factor affects the response to a significant extent is not possible in this way whenever multiple factors are to be considered. In these cases, the response surface methodology is a suitable tool. The first step is developing a statistical model, which approximates the data points the best way possible. This model is the so-called response surface, which allows the determination of the response for any factor level combination within the factor space. Thus, it can be used for the interpretation and the improvement of the process. However, the benefit of the model depends on its quality, which is determined by the goodness of fit and its general validity. The goodness of fit depends on the distances between the data points and the model, which are called residuals. If these are small, the model represents the response accurately. The general validity can be checked using additional observations, which are not used for the modelling itself. In case the new observations correspond to the values calculated by means of the model, the general validity is good. Otherwise, the model is simply not suitable or overfitted, which means that the model has a low predictive power.

Because the statistical modelling is a decisive step towards interpreting the experimental results correctly, the details of developing the models presented later are addressed in the following. The first challenge is the definition of a model. This step is challenging as the detailed relationships between the factors are unknown a priori, which means that one has to rely on similar cases or on theoretical assumptions. As already mentioned in the previous section, the factors themselves, the interaction of two factors, and the squared values of the factors are assumed to affect the value of the response (Khayet et al., 2010, p. 117). In mathematical terms this assumption corresponds to the response surface in Eq. 38 (Myers et al., 2009, 131), which considers two instead of four factors for the sake of clarity (Tab. 3). Herein, the dependence of the response y on two independent factors x_i and x_j is described. β_0 is the intercept, β_i, β_{ii}, β_{ij} are partial regression coefficients for the factors and ξ is the residual.

$$y = \beta_0 + \sum \beta_i \, x_i + \sum \beta_{ii} \, x_i^2 + \sum \beta_{ij} \, x_i \, x_j + \xi \qquad (38)$$

Secondly, further models are derived from this comprehensive model by successively omitting model effects (≈ terms). The result of this step is a collection of models of decreasing level of detail. Subsequently, stepwise regression based on t-statistics is performed for all models with a maximum of ten terms. Finally, the best model is chosen based on the corrected Akaike information criterion (AICc) and under consideration of the heredity restriction (Akaike, 1974). The heredity restriction demands that a non-significant model effect remains in the model, if it is part of a significant factor interaction. The minimal corrected Akaike information criterion is considered because it indicates the best trade-off between the goodness of fit and the number of terms, which should be as low as possible to prevent overfitting. These steps were performed using the JMP® fit model platform.

In addition to the corrected Akaike information criterion, a number of other statistical key figures and concepts allow the analysis and interpretation of the experimental results.

4.4.3 General statistical methods

By applying statistical methods it is possible to draw clear and comprehensible conclusions from the experimental results. The required method depends on the task to be performed, which can be the comparison of means, the choice of a suitable model throughout statistical modelling or the comparison of different mechanistic models.

Comparison of means

In order to review whether two groups originate from the same population with regard to a certain physical measure, the mean values $\bar{y}$ (Eq. 39) of the groups comprising a number N of observations y_i can be compared on the basis of the analysis of variance (ANOVA). A common null hypothesis underlying the ANOVA is that the groups do not differ with regard to the considered measure.

$$\bar{y} = \frac{1}{N} \cdot \sum\nolimits_{1}^{N} y_i \tag{39}$$

$$s^2 = \frac{1}{N-1} \cdot \sum\nolimits_{1}^{N} (y_i - \bar{y})^2 \tag{40}$$

Therefore, the variances s^2 (Eq. 40) between and within the groups are calculated and related to each other, which gives the F-value. This resulting F-value is compared to the tabulated critical $F_{N-1,\alpha}$-value for the given degrees of freedom $N-1$ and the significance level α (0.05). In case the obtained F-value is greater than the critical F-value, the groups differ with regard to the physical measure under consideration. In order to decide whether the overall results are significant, the corresponding p-value is required as well. It yields the probability of getting comparable results by happenstance and is determined by the p-value. Thus, as long as the p-value is greater than the significance level, the groups are equal.

Choice of models

The choice of the models is based on the corrected Akaike information criterion (AICc) in Eq. 41. Herein, ψ is the number of estimated parameters such as the regression coefficients β_i. Besides, N is the number of observations and $\hat{L}$ is the maximum value of the likelihood function.

$$AICc = 2\,\psi - 2 \cdot ln(\hat{L}) + \frac{2\,\psi^2 + 2\,\psi}{N - \psi - 1} \tag{41}$$

The likelihood function is defined as the product of the probability density functions evaluated at the observed data values. Due to the application of the natural logarithm ln, the maximization problem is reformulated as a minimization problem. Thus, smaller values of the corrected Akaike information criterion indicate more suitable models. Due to the fact that the number of parameter estimates is in the numerator (up to the power of two), a large number of terms in a model is punished by high values of the corrected Akaike information criterion.

Prior to relying on a model chosen based on the minimal corrected Akaike information criterion for prediction purposes, it is recommended to check the residuals for normal distribution. This can be done based on the Shapiro-Wilk test, which is an analysis of variance test for normality. Thus, the procedure is the same as for the F-test while using the test statistics W, which relates an expected variance to the actual variance of the sample. In general, the null hypothesis is that the residuals follow normal distribution. It is maintained if the test statistics W is greater than the tabulated critical $W_{N,\alpha}$-value and if the p-value is higher than 0.05. In this case, the chosen model explains the variation of the data over the whole range of observations equally good and is accepted for prediction purposes.

Comparison of models

The sum of squared errors SSE in Eq. 42 equals the sum of the differences between actually measured responses y_i and the corresponding values $\hat{y}_i$ predicted on the basis of a model. By dividing this value by the number of observations N and calculating the square root, the root mean square error $RMSE$ in Eq. 43 is obtained.

$$SSE = \sum\nolimits_1^N (\hat{y}_i - y_i)^2 \tag{42}$$

$$RMSE = \sqrt{\frac{SSE}{N}} \tag{43}$$

These measures are valuable for different tasks. Compared to the root mean square error, the sum of squared errors is more suitable for the regression of curves since large deviations are not concealed by the averaging step. In contrast, the fact that the root mean square error indicates the average deviation between the model and the observed values makes this figure more convenient for the comparison of distinctly different models. Furthermore, the root mean square error has the unit of the response, which facilitates its interpretation and makes it easier to decide whether the existing deviation is acceptable or not.

Finally, the coefficient of determination R^2 in Eq. 44 is also a measure for the assessment of the suitability of a model. In case the coefficient of determination equals 1, the scatter of the data is explained completely by the applied model. With decreasing values, however, the representation of the data by the model decreases as well.

$$R^2 = \frac{SSE}{\sum_1^N (y - \bar{y})^2} \tag{44}$$

The statistical concepts presented in this section allow the analysis of the experimental results based on generally accepted key figures. Before moving on the presentation of the experimental results, however, mathematical procedures for the calculation of residence time distributions are in the focus of the following section.

4.5 Mathematical operations for calculating residence time distributions

Section 2.3 focuses on how residence time distribution curves are measured and interpreted. In contrast, this section addresses the problem of describing these curves mathematically. Considering the cases that different plant components are connected in parallel or in series, different mathematical approaches are required for the description of the residence time distribution curves $E(t)$.

Considering a parallel connection of N components, the resulting residence time distribution equals the sum (Eq. 45) of the single residence time distribution curves $E_i(t)$ in the different components i (Levenspiel, 1999, p. 285).

$$E(t) = E_1(t) + E_2(t) + \cdots + E_N(t) \tag{45}$$

In case of a series connection of plant components, the required mathematical operation to calculate the residence time distribution $y(t)$ is called convolution (Levenspiel, 1999, p. 271). The principle of convolution is visualized in Fig. 32. Each component affects the shape of the input function $x(t)$ in a particular way due to the prevailing hydrodynamic processes, which are represented by a system function $h(t)$.

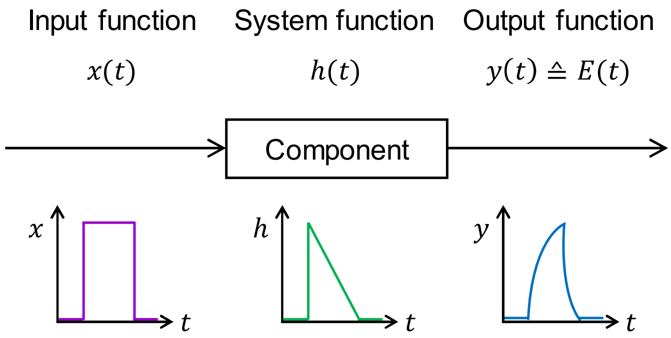

Fig. 32: Visualization of the convolution of curves.

Thus, the superimposition of the input function $x(t)$ and the system function $h(t)$ results in the output function $y(t)$ at the outlet of each component. The mathematical notation for the convolution of two functions is the asterisk $(*)$ in Eq. 46.

$$y(t) = x(t) * h(t) \tag{46}$$

This convolution can be solved using fast Fourier transforms of the time-dependent functions indicated by the operator $\mathcal{F}\{\}$ in Eq. 47 (Cooley et al., 1967, p. 83). The Fourier transforms are defined by the Fourier integral in Eq. 48 and are represented by capital letters (Eq. 49) in the following for the sake of simplicity. Herein, j denotes the imaginary unit ($j^2 = 1$) and ω is the angular frequency.

$$\mathcal{F}\{y(t)\} = \mathcal{F}\{x(t)\} \cdot \mathcal{F}\{h(t)\} \tag{47}$$

$$\mathcal{F}\{y(t)\} = Y(\omega) = \int_0^\infty y(t) \cdot e^{-j\omega t} dt \tag{48}$$

$$Y(\omega) = X(\omega) \cdot H(\omega) \tag{49}$$

$$\mathcal{F}^{-1}\{Y(\omega)\} = y(t) \tag{50}$$

To avoid confusion, it is worth mentioning that the term convolution denotes both the mathematical operation $(*)$ and the function $y(t)$ resulting from the inverse Fourier transform $\mathcal{F}^{-1}\{\}$ (Eq. 50). The convolution $y(t)$ and the observed residence time distribution $E(t)$ coincide if the system function $h(t)$ represents the hydrodynamic processes in the component under consideration sufficiently.

In practice, the measurement signals are usually discrete because the signal values are recorded at a certain frequency. Nevertheless, the principle of convolution is applicable (Hutter et al., 2011; Trachsel et al., 2005; Mao et al., 1998). Eq. 51 represents the discrete Fourier transform of the measurement signal $y(t)$. Compared to Eq. 48, the angular frequency ω is exchanged by $2\pi f$. Herein, y_i are the recorded values, N is the number of values, and f is the measurement frequency.

$$\mathcal{F}\{y(t)\} \approx \sum_{0}^{N-1} y_i \cdot e^{-j \cdot 2\pi f \cdot t} \tag{51}$$

While this section merely introduces of the general mathematical operations to calculate the residence time distribution curves, the application of the convolution principle to describe the series connection of different components mathematically is treated in the course of the following chapters dedicated to the results of the thesis (section 7.3.1).

5 Overview of the experimental data basis

This study aims at contributing to the understanding of the residence time behavior, which can be observed during the displacement of non-Newtonian fluids from spiral-wound membranes. Fig. 33 visualizes the idealized displacement of a model product (purple) from a housing equipped with a spiral-wound membrane (SWM) by a displacing fluid (blue).

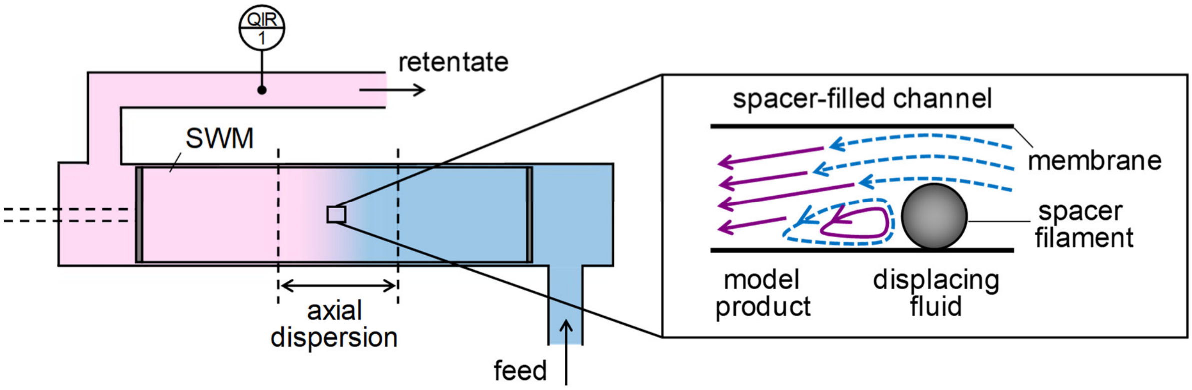

Fig. 33: Schematic representation of the displacement process.

The two fluids mix to a certain extent and create a dispersion zone. The transition of the model product to the displacing fluid can be monitored at the outlet of the system via turbidity or conductivity measurements (QIR1) when performing a displacement experiment. Such measurements are the experimental basis for the identification of factors influencing the residence time and for the mathematical description of the displacement curves based on mechanistic models. Essentially, this thesis comprises four data sets originating from four series of experiments, which are specified in Tab. 4. Apart from their differences concerning the displacement scenarios, which is the sequence and combination of the fluids, all displacement experiments are performed as described in section 4.1.1.

Data set 1 serves for the identification of relevant process parameters affecting the displacement process. By means of a statistical model, the functional description of the relationships between the process conditions and the residence time of products in the spiral-wound membranes during the displacement process is possible. The validation of this empirical model is performed by means of data set 2, which is the basis of the study of Kieferle et al. (2019a). Data set 3 allows to assess the influence of the displacing fluid's viscosity on the residence time in spiral-wound membranes. Data set 4 serves for validation purposes with regard to the way of data processing described in the following.

As indicated before, the displacement process is monitored by a turbidity or conductivity sensor. The sensor type used for the experiments depends on the displacement scenario as shown in Tab. 4 as well. While the turbidity sensor detects the decrease of the protein concentration, the conductivity sensor records changes in the sodium chloride concentration.

Tab. 4: Overview of the experimental data basis. Please find the complete designs of experiments combined with the target-actual comparison of the process parameters in the appendices F – 0.

Data set	**1** **SW → PC**	**2** **SW → PC**	**3** **XS → PC**	**4** **SW → XS**
Data source	DoE 1 (section 4.4.1)	(Kieferle et al., 2019a)	DoE 2 (section 4.4.1)	DoE 3 (section 4.4.1)
Displacing fluid	**SW**: Soft water	**SW**: Soft water	**XS**: Xanthan solution (+ NaCl)	**SW**: Soft water
Model product	**PC**: Protein concentrate	**PC**: Protein concentrate	**PC**: Protein concentrate	**XS**: Xanthan solution (+ NaCl)
Signal	Absorption A	Absorption A	Conductivity κ	Conductivity κ
Monitored (discrete) signals	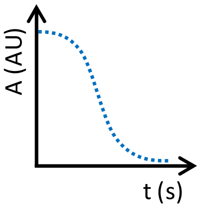	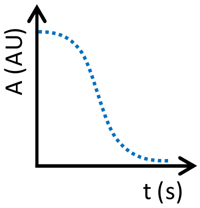	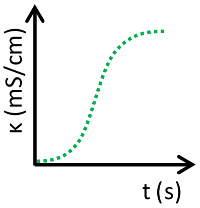	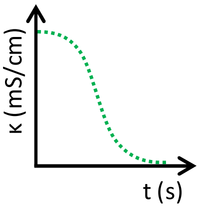
(Cumulative) distribution curves		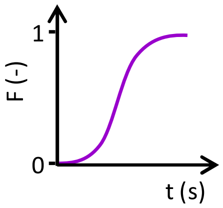	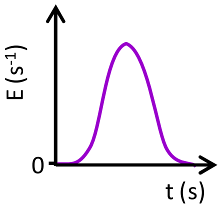	

Consequently, the information about the displacement process is coded in residue (data set 1, 2, 4) and cumulative distribution curves (data set 3). For the sake of a uniform data analysis, the raw data is processed as described in the following section to provide normalized and continuous cumulative distribution curves.

5.1 Processing of the raw data

The raw data are discrete measurement signals recorded by two different devices, a turbidity and a conductivity sensor. The first step after the transformation of the raw signals into the tracer concentration is the normalization. While this step is simple for the conductivity measurements, normalizing the turbidity signals requires the use of mathematical auxiliaries.

5.1.1 Normalization of displacement curves

Normalized and continuous displacement curves are appropriate for further analyses as these allow the comparison of the curve shapes and the calculation of density functions. To obtain the normalized and continuous displacement curves, the raw data is processed accordingly. The first step of data processing is the normalization of the data by dividing the actual tracer concentration by the initial (protein) or the final (sodium chloride) tracer concentration, depending on the displacement scenario. This is important because it allows the transformation of the residual curves $F^*(t)$ into the cumulative distribution curves $F(t)$ according to Eq. 52.

$$F(t) = 1 - F^*(t) \tag{52}$$

The normalization of the curves from data set 3 and 4 (XS → PC and SW → XS, Tab. 4) is straight-forward due to the linear relationship between the sodium chloride concentration and the conductivity. Normalizing the curves from data set 1 and 2 (SW → PC, Tab. 4), however, is more cumbersome because the relationship between the absorption and the protein concentration is only linear for lower protein concentrations (Fig. 28). Plotting the squared absorption against the protein concentration allows an enlargement of the linear range (Fig. 34b).

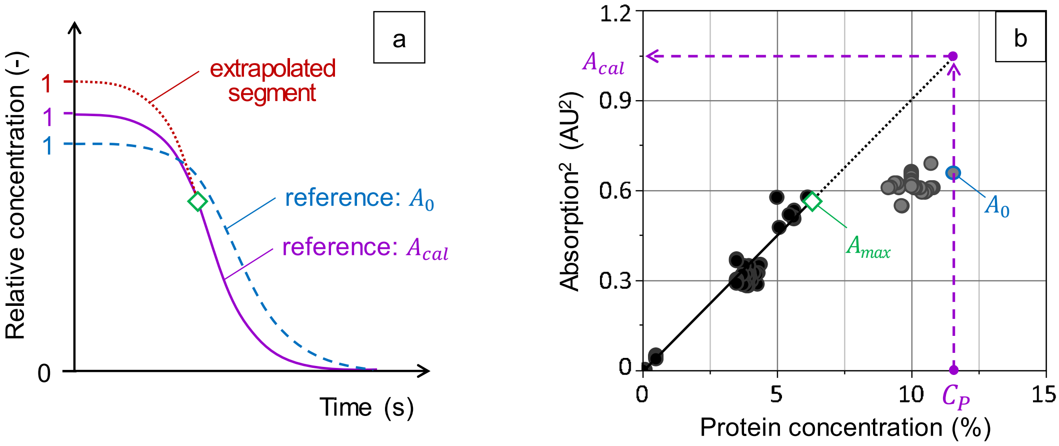

Fig. 34: a) Normalization of measured residue curves based on the b) linear relationship between the squared absorption and the protein concentration.

Nevertheless, the normalization of a measured curve based on the initially measured absorption A_0 falsifies the shape of the resulting curve. The reason is that the reference value A_0 may exceed the linear range (Fig. 34b, grey circles), which is bounded by the absorption A_{max}. The blue, dashed line in Fig. 34a indicates that the normalization of the curve based on the initially measured absorption A_0 leads to a compressed curve shape. To tackle this problem, the following steps are performed.

Using the relationship between the squared absorption and the protein concentration in Eq. 53 determined based on linear regression, a theoretical initial absorption A_{cal} can be calculated. For the linear regression, only data points of the linear range (Fig. 34b, black circles) are used, while the grey circles are neglected. The protein concentration C_p is known since it is quantified analytically by the Dumas method (section 4.2.1).

$$A_{cal} = \sqrt{0.0877 \cdot C_p} \tag{53}$$

In the following, the theoretical initial absorption A_{cal} is used as reference for the purple, straight curve in Fig. 34a. However, the shape of the curve calculated based on A_{cal} is only correct as long as the relative concentrations are derived from signals below A_{max} because the relative concentrations derived from signals above A_{max} exceed the linear range. Consequently, these values are omitted resulting in a trimmed curve.

Besides the curves from data set 1 and 2 (SW → PC, Tab. 4), the curves from data set 3 (XS → PC, Tab. 4) also contain unusable curve sections. These are located at the beginning as well because the protein concentrates have an electrical conductivity in the range from 3.5 to 4.5 mS/cm, which overlaps with the conductivity signal indicating the gradual mixing with the conductive xanthan solution. Hence, only conductivity values above 4.5 mS/cm are used for further analyses. Finally, the missing parts of the trimmed curves are extrapolated based on the cumulative Weibull distribution function.

5.1.2 Extrapolation of the curves by the cumulative Weibull distribution function

The cumulative Weibull distribution function $F_w(t)$ in Eq. 54 provides appropriate properties for the extrapolation as its definition range is between 0 and 1, just like the normalized cumulative distribution curves (Weibull, 1951, p. 293).

$$F_w(t) = 1 - e^{-(\lambda \cdot t)^{\varphi}} \tag{54}$$

The suitability of this fit is also due to the fact that the reciprocal scale parameter λ and the shape parameter φ can be interpreted in a physical way. As shown in Fig. 35, the scale parameter determines the position of the inflection point and corresponds to the reciprocal value of the half residence time for symmetric residence curves. Thus, increasing λ from 0.05 to 0.1 induces a shift of the curves to the left. The shape parameter serves for specifying the shape of the curve. Hence, plug flow can be assumed for $\varphi \rightarrow \infty$, while $\varphi \rightarrow 0$ indicates complete mixing.

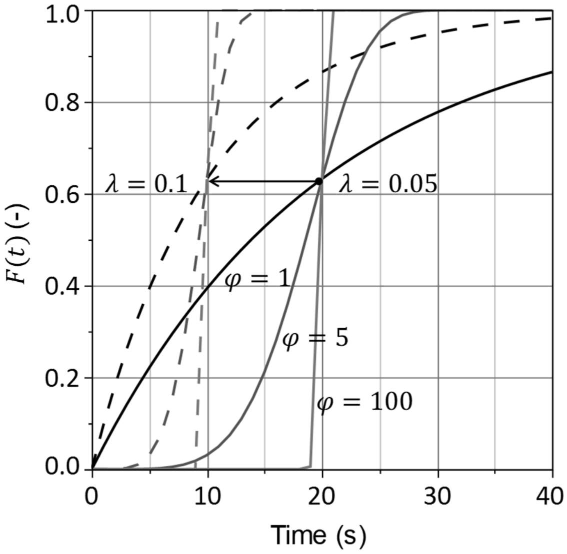

Fig. 35: Interpretation of the Weibull parameters λ (scale parameter) and φ (shape parameter).

For the purpose of the curve extrapolation, the Weibull parameters are adapted to the normalized curves using R (R Foundation for Statistical Computing, Vienna, Austria). Since the described data processing comprises normalization, data trimming, and curve fitting, reviewing the accuracy of the resulting curves is indispensable.

5.2 Validation of the data processing

The validation step ensures that the informative value of the experimental results is conserved despite the truncation of the signals. The truncation of the raw signals is necessary when protein concentrates are displaced by soft water (turbidity signal, data set 1 and 2, Tab. 4) or by xanthan solutions (conductivity signal, data set 3). In the first case (SW → PC), the turbidity signal is not reliable above a certain protein concentration and in the second case (XS → PC), the conductivity of the protein concentrates conceals the beginning mixing with the marked xanthan solutions. Since the signals from data set 4 (SW → XS) are reliable for the whole range, this data set is used for the validation of the data processing.

Fig. 36a shows an exemplary displacement curve (black circles), where water marked with sodium chloride displaces soft water without any tracer substance. As described in the previous section, the first step prior to further analyses is the truncation of the raw signals when particular signal sections are not reliable. This is the case when the linear relationship between the protein concentration and the signal of the turbidity sensor is exceeded or when the conductivity measurement is applied for monitoring the displacement of protein concentrates.

In order to validate the way of data processing, the signals from data set 4 (Fig. 36a) are truncated by 50% resulting in curves as represented in Fig. 36b. Omitting up to 50% of the signal is necessary for the curves from data set 1 and 2.

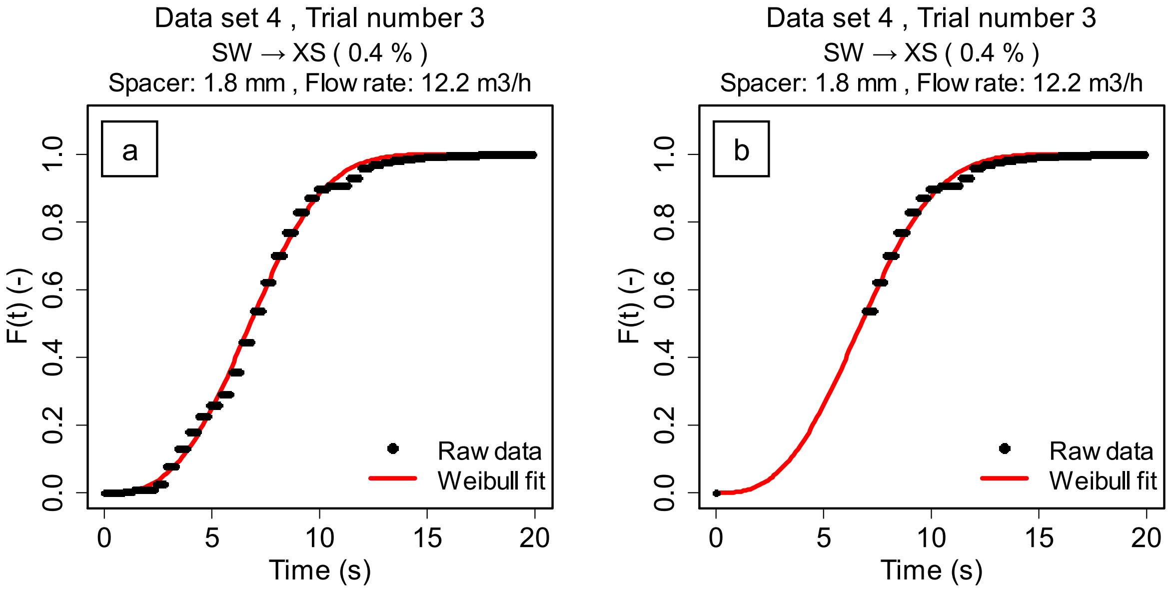

Fig. 36: Exemplary displacement signal (black circles) with cumulative Weibull distribution (red line) fitted based on a) the full signal (100% of data points) and b) the truncated signal (50% of data points).

Subsequently, the two parameters λ and φ of the cumulative Weibull distribution function are fitted to the complete and truncated signals based on least squares regression. Fig. 37 allows the comparison of the scale and shape parameters determined for the truncated and the complete signal.

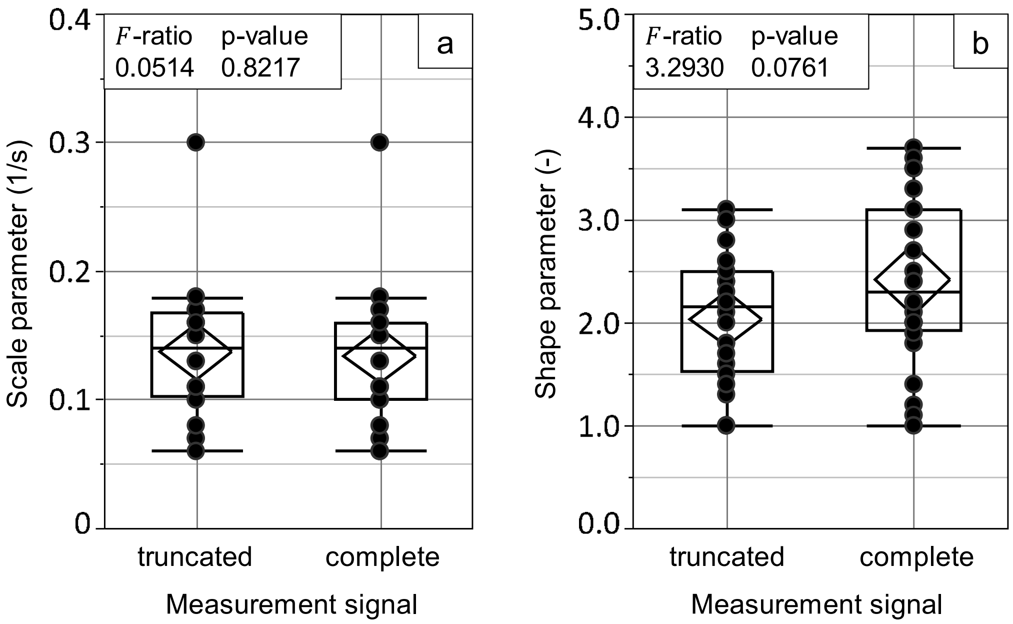

Fig. 37: Outlier box plots of the truncated and complete measurement signals and results of the analyses of variance. The confidence diamonds indicate the mean (horizontal edges) and the corresponding 95% confidence interval (vertical edges).

While the scale parameters are not affected by the truncation of the signals, the shape parameters determined based on the complete signal show a wider spread compared to the shape parameters derived from the truncated signal. However, to assess whether the observed differences between the parameters determined based on the truncated and the complete signal are significant, an ANOVA is performed. The p-values for the F-statistics are 0.82 for the scale parameter and 0.08 for the shape parameter (Fig. 37a and b). Since both p-values are greater than 0.05, it can be concluded that there are no significant differences between the parameter means determined based on the truncated or the complete signal. Consequently, the error introduced by the data processing is small enough to accept it.

With this kind of data processing, the analysis of the experimental results with regard to the residence time distribution is possible. Prior to moving on to the analysis of the curve shapes and the encoded information on the hydrodynamic processes, the focus is on the identification of factors influencing the residence time during the displacement.

6 Identification of factors influencing the residence time

In general, the residence time is a convenient measure for assessing the displacement efficiency since its determination and interpretation is simple. It equals the time required for the displacement of the product from the core area of the flow channel, which is completed when a predefined turbidity or conductivity value is attained (section 4.1.1). The residence time conveys some information with regard to the hydrodynamics in the way that long residence times indicate intense mixing of the model product with the displacing fluid, while short residence times suggest a rather stable interface between the fluids.

In the following, the functional relationships determining the residence time of model products in spiral-wound membranes are identified and discussed based on the response surface methodology.

6.1 Effects of displacement conditions

Practical experience and literature coincide in that the flow rate, the dimensions of the feed spacer, and the flow properties of the product determine the hydrodynamics and thus the displacement process. If a temperature difference between the product and the displacing fluid affects the residence time, however, is unknown. The relevance of this last-mentioned factor is that process streams such as reverse osmosis permeates are frequently used as displacing fluids in industrial practice. Since these permeates may have a temperature deviating from the temperature of the product to be displaced, the question arises whether the temperature of the displacing fluid affects the displacement process.

In the course of the test series comprised in data set 1 (Tab. 4), viscous model products with an average temperature of 10.3 ± 0.9°C are displaced from spiral-wound membranes by water. The experiments are carried out according to the design of experiments (DoE) 1 in Tab. 3. The actual factor space covers different flow rates (6.2 … 15.7 m^3/h) and product viscosities, which are amended by varying the protein concentration (3.7 … 15.3%). Besides, the height of the flow channels is modified by employing spiral-wound membranes equipped with spacers of three different thicknesses (0.7, 1.0, and 1.8 mm). The fourth investigated factor is the temperature of the displacing fluid (10.3 … 33.3°C), which impact on the residence time is unclear so far.

6.1.1 Presentation of the expectations

Referring to the data of Gauwbergen and Baeyens (2000, p. 90; 1997, p. 297) visualized in Fig. 25, it is expected that increasing the flow rate induces a reduction of the residence time as the Reynolds number increases. This is supported by Walenta and Kessler (1990b, p. 66) who conclude that the flow state of the displacing fluid determines the overall displacement efficiency. Furthermore, the effect of the product viscosity is also expected to be significant as Mishra et al. (2008, p. 4) indicate that the viscosity of the fluids affects the stability of the interface. Concerning the impact of the spacer dimensions on the residence time, the results published by Picioreanu et al. (2009, p. 349) give rise to the assumption that low aspect ratios are favorable. This means that the residence time is shorter if the filament diameter is small compared to the channel height. Finally, the effect of the temperature of the displacing fluid is rather unclear. Increasing the temperature leads to a viscosity decrease, which in turn ought to increase the Reynolds number. Consequently, using fluids with a higher temperature should improve the displacement process and shorten the residence time. However, the question is whether the extent of viscosity change induced by the temperature increase affects the displacement process. Another conceivable mechanism is that the displacing fluid warms up the model product, which decreases its viscosity. Whether the contact time between the fluids is long enough to affect the product viscosity is unclear. Altogether, it is expected that the increased temperature of the displacing fluid reduces the residence time. Whether these expectations prove true is reviewed in the following based on the experimental results.

6.1.2 Description and interpretation of the experimental results

Fig. 38 allows the direct comparison of three exemplary displacement curves. While the spacer thicknesses h_c and the protein concentrations C_P are comparable, the displacing fluid's temperatures ϑ_D and the flow rates $\dot{V}_D$ differ. These curves support the above expectation that higher flow rates induce shorter residence times and thus narrower residence time distributions.

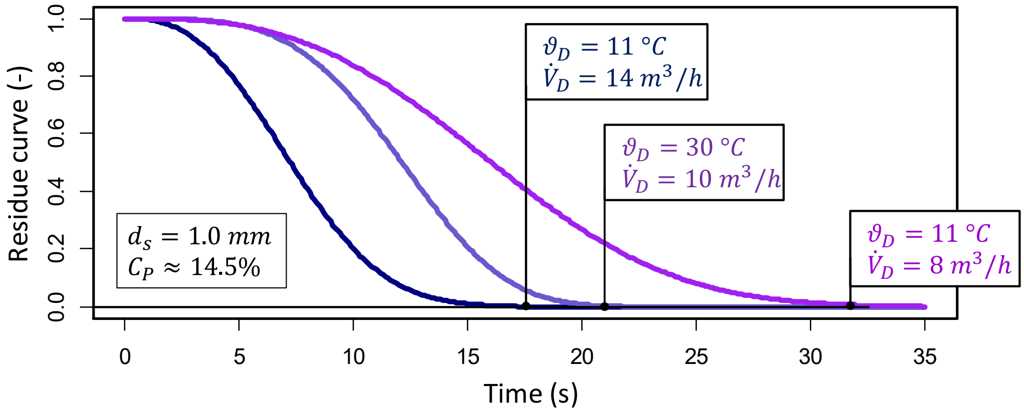

Fig. 38: Exemplary residence time distribution curves monitored by means of the turbidity sensor.

Concerning the displacing fluid's temperature, however, no trend can be observed. To judge whether and how the considered process parameters influence the residence time, the response surface methodology is a valuable tool. In a first approach, the four factors protein concentration, displacing fluid's temperature, flow rate, and spacer thickness are used as main effects for the statistical modelling (section 4.4.2). However, the models developed using these main effects do not represent the data sufficiently. Possible reasons for the inaccuracy of the models are that the signal-to-noise-ratio is too low, that the model is inappropriate to approximate the data, that at least one relevant factor is missing or that the chosen responses do not represent the underlying physical process.

Considering the last option, the protein concentration and the spacer thickness may be unsuitable as main effects for the statistical modelling. For modelling the mixed phase volume evolving during the displacement, Kieferle et al. (2019a, p. 157) use the logarithm of the consistency index instead of the protein concentration. The advantage of this main effect is that it is related to the actual viscosity of the fluids. Assuming an increase of the protein concentration by 2 percentage points, the viscosity changes barely between 4 and 6% protein. In contrast, the viscosity increases sharply when altering the protein concentration from 12 to 14%. Using the consistency index instead of the protein concentration has thus the advantage that a numerical change from –2.5 to –2 $\mathrm{Pa \cdot s^n}$ is proportional to the actual change in viscosity.

Concerning the spacer dimensions, the hydraulic diameter d_h (Eq. 5) and the aspect ratio α_R (Eq. 11) serve for the quantification of the spacer geometry throughout computational simulations (Kavianipour et al., 2017, p. 157; Schwinge et al., 2002c, p. 2979). The differences between these two measures are shown in Fig. 39, which contrasts the hydraulic diameters and the aspect ratios for the three spacer thicknesses. The spheres and the shaded area at the bottom of Fig. 39 visualize the aspect ratio as the ratio of the diameter d_f of the spacer filaments and the flow channel height/spacer thick-ness h_c.

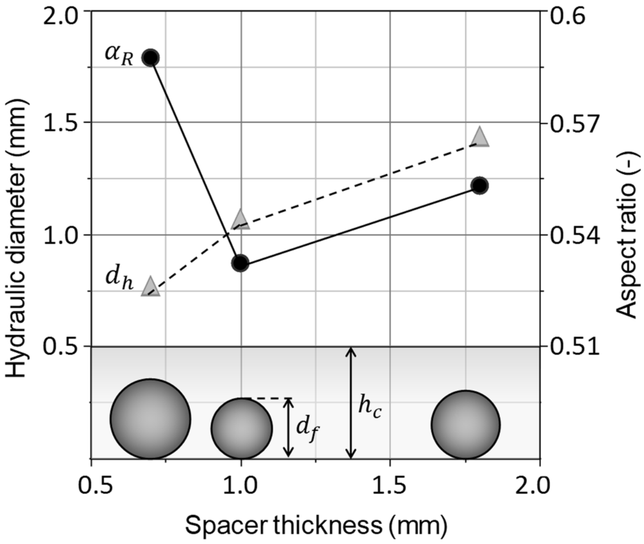

Fig. 39: Comparison of hydraulic diameters (triangles, dashed line) and aspect ratios (circles, straight line). Lines are guides for the eyes. The spheres visualize the sizes of the spacer filaments with the diameter d_f in relation to the flow channel height/spacer thickness h_c.

While the difference between the hydraulic diameters for the 0.7-mm and the 1.0-mm-spacer is comparably small, it is huge with regard to the aspect ratio. Because it is unclear whether the hydraulic diameter or the aspect ratio suits better as a measure representing the geometry or the dimension of the flow channel, the statistical modelling is repeated twice. In the first model, the hydraulic diameter is considered as spacer-characterizing factor and in the second model, it is the aspect ratio. Tab. 5 provides the parameter estimates and the corresponding p-values for both models. Herein, $\dot{V}_F$ is the flow rate, k_{MP} is the consistency index of the model product, d_h is the hydraulic diameter, and α_R is the aspect ratio.

Tab. 5: Parameter estimates and corresponding p-values of two models. Model 1 considers the hydraulic diameter and model 2 the aspect ratio as factor representing the spacer dimensions. The arrow (↓) marks model effects considered due to the heredity restriction (section 4.4.2).

Model 1			**Model 2**		
Effect	**Estimate**	**P-value**	**Effect**	**Estimate**	**P-value**
$Intercept$	$4.335\cdot10^{+1}$	$3.331\cdot10^{-6}$	$Intercept$	$-3.903\cdot10^{+1}$	$2.420\cdot10^{-1}$
$\dot{V}_F$	-3.908	$4.513\cdot10^{-1}$ ↓	$\dot{V}_F$	$2.552\cdot10^{+2}$	$9.227\cdot10^{-6}$
$\log_{10}(k_{MP})$	$1.350\cdot10^{+1}$	$3.381\cdot10^{-3}$	$\log_{10}(k_{MP})$	$-2.102\cdot10^{+1}$	$2.523\cdot10^{-1}$ ↓
d_h	$-2.289\cdot10^{+4}$	$2.260\cdot10^{-3}$	α_R	$1.068\cdot10^{+2}$	$7.872\cdot10^{-2}$ ↓
$\dot{V}_F * \dot{V}_F$	$2.029\cdot10^{+1}$	$2.169\cdot10^{-4}$	$\dot{V}_F * \dot{V}_F$	9.390	$4.391\cdot10^{-3}$
$\dot{V}_F * \log_{10}(k_{MP})$	-3.854	$2.371\cdot10^{-2}$	$\dot{V}_F * \log_{10}(k_{MP})$	$1.160\cdot10^{+2}$	$1.283\cdot10^{-4}$
$\log_{10}(k_{MP}) * d_h$	$-8.145\cdot10^{+3}$	$3.209\cdot10^{-2}$	$\dot{V}_F * \alpha_R$	$-4.886\cdot10^{+2}$	$4.846\cdot10^{-6}$
			$\log_{10}(k_{MP}) * \alpha_R$	$4.542\cdot10^{+1}$	$1.716\cdot10^{-1}$ ↓
			$\dot{V}_F * \log_{10}(k_{MP}) * \alpha_R$	$-2.197\cdot10^{+2}$	$7.082\cdot10^{-5}$

Firstly, it is worth mentioning that neither of the models in Tab. 5 contains the displacing fluid's temperature as model effect. This means that the consideration of the displacing fluid's temperature does not increase the approximation of the response surfaces to the experimental values. The parity plots in Fig. 40a and b contrast the residence times actually observed throughout the experiments with the values predicted by the models.

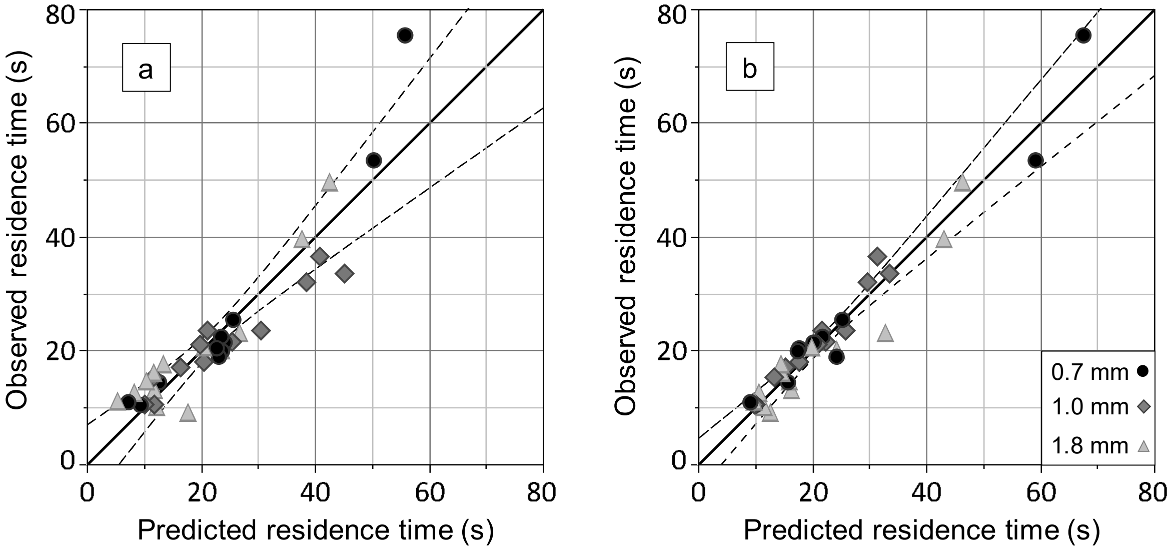

R^2 = 0.85, $RMSE$ = 5.9 s /
Shapiro-Wilk test: W = 0.918, p-value = 0.0109

R^2 = 0.94, $RMSE$ = 3.7 s /
Shapiro-Wilk test: W = 0.947, p-value = 0.086

Fig. 40: Comparison of the parity plots for model 1 (a) and model 2 (b). Dashed lines indicate the 95% confidence interval of the fit.

If the representation of the experimental data by the model is ideal, all points lie on the diagonal line. In other words, the smaller the residuals are, the better is the accordance between the model and the observations. Comparing the residuals in Fig. 40a and b, it is evident that model 1 describes the data less accurately than model 2. This impression is supported by the corresponding coefficients of determination R^2 and the root mean square errors $RMSE$ indicated below Fig. 40a and b. Furthermore, the distribution of the residuals for model 1 is not normal as suggests the Shapiro-Wilk test with a p-value lying clearly below 0.05. Consequently, model 1 is not appropriate to investigate the displacement process. In contrast, model 2 shows a satisfactory representation of the data and normally distributed residuals since the p-value obtained based on the Shapiro-Wilk test exceeds the significance level of 0.05. The distribution of the residuals with a fitted normal distribution is also shown in Fig. 41a. These key figures give evidence that model 2 can be used for further investigations. Prior to moving on to the interpretation of the results, however, the validation of the model is necessary to be sure that the model possesses a certain general validity. For the purpose of validation, the values originating from data set 2 are inserted into model 2 (Tab. 5). Fig. 41b shows a parity plot containing data set 1 (grey circles) and data set 2 (black circles), where the 95% prediction interval for data set 1 includes 97% of the observations of data set 2. This suggests strongly that model 2 has a certain extent of general validity. Otherwise, the approximation to the values from data set 2 would fail.

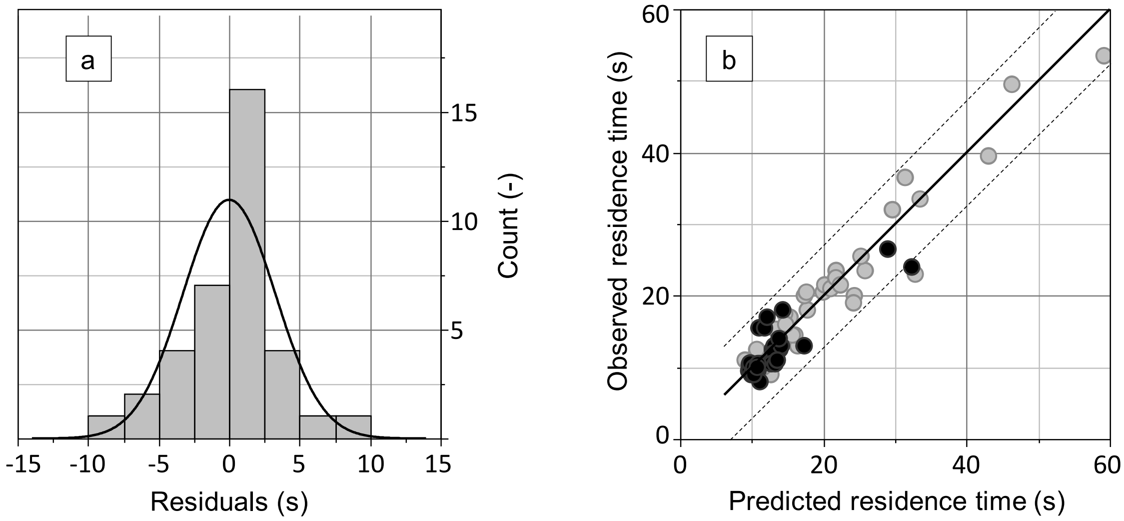

Fig. 41: Testing the general validity of model 2 (Tab. 5). a) Distribution of the residuals for model 2 with fitted normal distribution (straight line). b) Parity plot for reviewing the applicability of model 2 for a new data set (black circles, data set 2, Tab. 4). The dashed lines indicate the 95% prediction interval for data set 1 (grey circles).

In the following, the practical implications of the findings presented above are clarified. Furthermore, the issue concerning the suitability of the aspect ratio and the hydraulic diameter as geometric measures for the spacer dimensions is taken up.

6.1.3 Discussion of the results

For the assessment of the practical implications of the results, it is useful to consider particular process conditions. Fig. 42a and b show the residence time as a function of the flow rate and the aspect ratio for low ($log_{10}(k_{MP}) \approx -2.6 \pm 0.0$ Pa·s^n) and high ($log_{10}(k_{MP}) \approx -4.3 \pm 0.2$ Pa·s^n) consistency indexes. The corresponding viscosities are observed for model products with protein concentrations of 3.9 ± 0.2% (Fig. 42a) and 13.2 ± 0.8% (Fig. 42a), respectively. The low and high protein concentrations represent early and late stages in a concentration process, where the product viscosity increases successively. This plot allows the visual assessment of the representation of the data by the model as well as the derivation of the practical implications of the findings. In general, it can be stated that the greater the flow rate is, the shorter is the residence time.As can be derived from Fig. 42a, there are no measureable differences in the residence time between the different spacer thicknesses at low product viscosities. With regard to high product viscosities (Fig. 42b), the residence time range is distinctly wider. On the one hand, the flow rate has a greater impact on the residence time and on the other hand, the influence of the spacer thickness becomes apparent, particularly at flow rates below 12 m^3/h. Here, the shortest residence times can be attributed to spacers with aspect ratios of 0.53 and 0.55 (spacer thicknesses: 1.0 and 1.8 mm), while spacers with an aspect ratio of 0.59 (spacer thickness: 0.7 mm) induce the longest residence times.

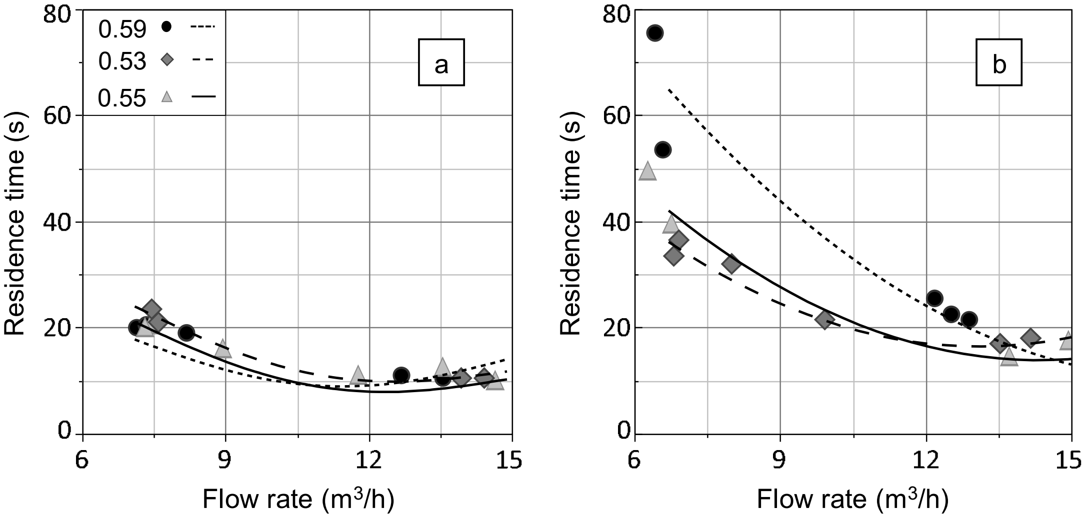

Fig. 42: Residence time as function of the flow rate and the aspect ratio (0.59, 0.55, and 0.53) for a) low ($log_{10}(k_{MP})$ ≈ – 2.6 ± 0.0 Pa·s^n) and b) high ($log_{10}(k_{MP})$ ≈ – 4.3 ± 0.2 Pa·s^n) consistency indexes of the model product. Points are observations and lines represent model 2 (Tab. 5).

Taking a look back at Fig. 39, it becomes evident why the aspect ratio and not the hydraulic diameter allows successful modelling: The lower the aspect ratio is, the lower is the residence time. In contrast, the hydraulic diameter cannot be correlated directly with the residence time.

This observation supports the declarative statement that the spacers are geometrically not similar. In other words, this means that it is not possible to obtain the same flow channel shape by uniform scaling, translation, rotation or reflection. In contrast, the aspect ratio is proportional to the ratio of the biggest and smallest cross-sectional areas $A_{c,1}$ and $A_{c,2}$ or the lowest and highest flow velocities u_1 and u_2 in the spacer-filled channel (Eq. 56). This physical relevance of the aspect ratio can be derived from Eq. 55, which formulates the conservation of mass. Herein, $\dot{m}$ is the mass flow, $\dot{V}$ is the flow rate, u is the flow velocity, d_f is the filament diameter, h_c is flow channel height or spacer thickness, l_m is the mesh length, and A_c is the cross-sectional area.

$$\frac{\dot{m}_1}{\dot{m}_2} = \frac{\dot{V}_1 \cdot \rho}{\dot{V}_2 \cdot \rho} = \frac{A_{c,1} \cdot u_1}{A_{c,2} \cdot u_2} = 1 \tag{55}$$

$$\frac{A_{c,2}}{A_{c,1}} = \frac{u_1}{u_2} = \frac{\left(h_c - d_f\right) \cdot l_m}{h_c \cdot l_m} = 1 - \frac{d_f}{h_c} = 1 - \alpha_R \tag{56}$$

The measures used for the reformulation of Eq. 55 are visualized in Fig. 43. The formulation of Eq. 56 in words is that the smaller the aspect ratio is, the lower is the velocity distribution over the cross-section of the spacer-filled channel. This is advantageous when aiming at short residence times because the mass transfer is distributed more evenly.

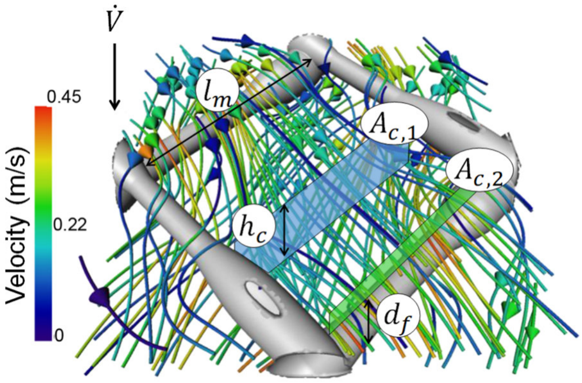

Fig. 43: Stream lines in a spacer-filled channel, adapted from Bucs et al. (2015, p. 308).

In summary, the statistical modelling reveals that three out of four investigated factors are relevant for the description of the residence time. The viscosity of the model product, the flow rate, and the spacer dimensions need to be considered, while the displacing fluid's temperature turned out to be negligible within the investigated factor space. Besides, the statistical modelling gives an important insight into the displacement process since the residence time is a function of the aspect ratio rather than the hydraulic diameter. This means that the hydraulic diameter is not a measure capable of representing the dimensions of the spacer-filled flow channels sufficiently.

The practical implication of these experimental results is that the flow rate and the dimensions of the spacers in the spiral-wound membranes should be adapted to the product viscosity in order to reduce the residence time. Another promising approach for the reduction of the residence time should be the increase of the density or viscosity of the displacing fluid. However, the manipulation of the fluid density is difficult compared to the increase of the fluid viscosity by adding hydrocolloids. In order to reach a further reduction of the residence time, the impact of the displacing fluid's viscosity on the residence time is investigated using xanthan solutions for the displacement of viscous products.

6.2 Impact of the displacing fluid's viscosity

Besides the decrease of the aspect ratio and the increase of the flow rate (Fig. 42), a further reduction of the residence time should be possible by using a displacing fluid of a higher viscosity such as xanthan solutions instead of water. The choice of xanthan solutions is based on the fact that xanthan gum is an inexpensive hydrocolloid being very effective with regard to the viscosity increase. In order to assess the impact of the viscosity of the displacing fluid on the residence time, appropriate experiments are carried out. Throughout these experiments (data set 3, Tab. 4), the model products are displaced from spiral-wound membranes by xanthan solutions of different viscosities.

Besides the xanthan concentration (0 … 0.75%), the protein concentration (3.6 … 14.4%), the flow rate (1.8 … 14.0 m^3/h), and the thickness of the feed spacer (0.7, 1.0, and 1.8 mm) in the spiral-wound membranes are varied following a statistical design of experiments (DoE2, Tab. 3). The average temperature of the protein concentrates and the xanthan solutions account for 10.0 ± 0.1°C and 8.8 ± 1.3°C, respectively. The particularity of these experiments is the fact that a non-Newtonian fluid displaces another non-Newtonian fluid showing distinctly different flow properties as shown in Fig. 29. However, this pairing of liquids introduces difficulties with regard to the anticipation of the results.

6.2.1 Presentation of the expectations

The results concerning the impact of the displacing fluid's viscosity on the residence time are not easy to predict as multiple effects have to be considered. On the one hand, the results of Walenta and Kessler (1990b, p. 65), also depicted in Fig. 21, suggest that decreasing the viscosity difference between the model product and the displacing fluid improves the displacement efficiency. On the other hand, they state that only the Reynolds number of the displacing fluid determines the displacement process. Consequently, the deployment of xanthan solutions as displacing fluid should be rather adverse since a higher viscosity reduces the Reynolds number compared to water. Furthermore, both the milk protein concentrates (model product) and the xanthan solutions (displacing fluid) show shear-thinning flow properties (Galván et al., 2018, p. 192; Carvalho, 1986, p. 61). However, as the shear-dependence of the viscosity of the xanthan solutions is much more pronounced compared to that of the milk protein concentrates, the viscosities change to a different extent. This is that the viscosity difference may decrease significantly depending on the prevailing shear rates in the three spacer-filled channels of the spiral-wound membranes. A low viscosity due to high shear gradients, though, induces high Reynolds numbers, which is likely to improve the displacement process. As an aside, this consideration questions the deployment of xanthan solutions as displacing fluid instead of water.

Taking these considerations into account, the expectation is that the residence times observed for the displacement of viscous products by xanthan solutions are either equal or lower compared to using water as displacing fluid.

6.2.2 Description and interpretation of the experimental results

The leading question is whether the residence time can be manipulated by the deployment of xanthan solutions instead of water for the displacement of the model product. According to the assumption underlying the experiments, increasing the viscosity of the displacing fluid should allow a reduction of the residence time. Fig. 44 shows the distribution of the residence times observed during the displacement by water and xanthan solutions, where the color code indicates the actual flow rate.

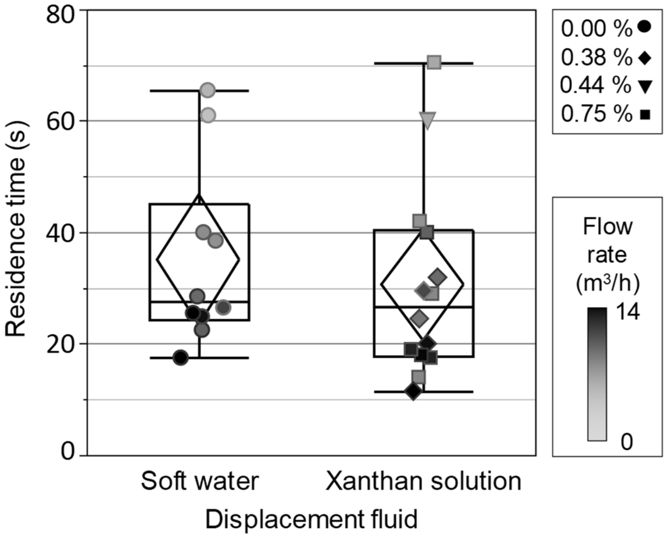

Fig. 44: Outlier box plots of the residence times observed for the displacement by soft water and xanthan solutions. The diamonds indicate the mean and the corresponding 95% confidence interval.

The maximum residence times are observed at flow rates of 2.7 m^3/h (soft water) and 3.5 m^3/h (xanthan solution) and the minimum residence times at flow rates of 14.0 m^3/h (soft water) and 14.1 m^3/h (xanthan solution). In general, the spread of the residence times observed when displacing by xanthan solutions is larger compared to the displacement by water. However, the diamonds, which indicate the mean values (horizontal edges) and the 95% confidence interval of the means (vertical edges), overlap. This is that the mean values do not differ significantly. Performing an ANOVA gives a p-value of 0.528 (F-ratio: 0.412), which is far from significance. Hence, there is no clear evidence for an impact of the viscosity ratio on the residence time.

In order to clarify the relationships between the process variables, the response surface methodology is applied. Under consideration of the conclusions drawn in the previous section, the main effects consistency index k_{MP} of the model product, consistency index k_{DF} of the displacing fluid, flow rate $\dot{V}_F$, and aspect ratio α_R are used for the statistical modelling. Tab. 6 specifies the resulting model and Fig. 45 shows the accordance of the model with the experimental data.

Tab. 6: Parameter estimates and corresponding p-values. The arrow (↓) indicates the heredity restriction.

Model

Effect	**Estimate**	**P-value**
$Intercept$	$1.976 \cdot 10^{+2}$	$2.968 \cdot 10^{-2}$
$\dot{V}_F$	-8.092	$8.114 \cdot 10^{-3}$
$\log_{10}(k_{MP})$	$1.424 \cdot 10^{+2}$	$1.057 \cdot 10^{-2}$
α_R	$-3.093 \cdot 10^{+2}$	$5.511 \cdot 10^{-2}$ ↓
$\dot{V}_F * \dot{V}_F$	$1.296 \cdot 10^{+1}$	$8.082 \cdot 10^{-4}$
$\log_{10}(k_{MP}) * \alpha_R$	$-2.486 \cdot 10^{+2}$	$1.188 \cdot 10^{-2}$

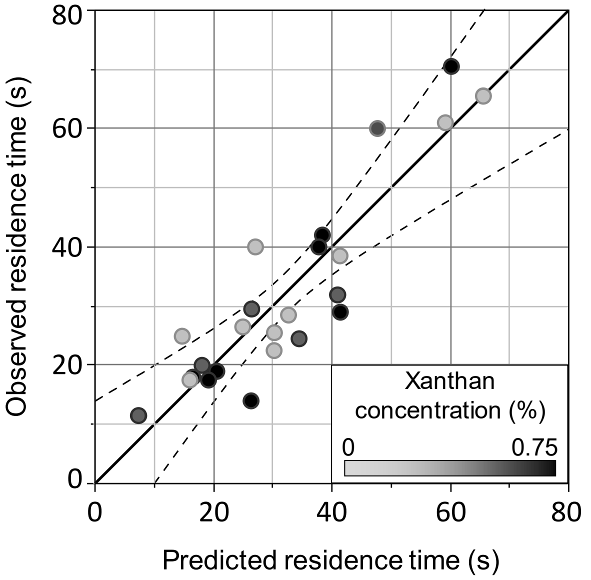

R^2 = 0.84, $RMSE$ = 7.6 s / Shapiro-Wilk test: W = 0.978, p-value = 0.892

Fig. 45: Parity plot for the model defined in Tab. 6. Dashed lines indicate the 95% confidence interval.

The check for normal distribution of the residuals based on the Shapiro-Wilk test suggests that the residuals are normally distributed since the p-value is 0.892 and thus above the significance level of 0.05 (Fig. 45). To sum up the results, the statistical modelling supports the conclusion already drawn based on the comparison of the means: The deployment of xanthan solutions instead of water does not affect the residence time during the displacement to a significant extent because the viscosity index of the displacing fluid is not comprised in the list of model effects in Tab. 6. Possible reasons for this result are discussed in the following.

6.2.3 Discussion of the results

The comparison of the mean residence times (Fig. 44) and the statistical modelling (Tab. 6) both suggest that the utilization of xanthan solutions does not lead to a significant reduction of the residence times. This result is rather unexpected with regard to the initial objective to reduce the residence time by deploying xanthan solutions instead of water for the displacement of viscous model products. However, it must be noted that the applied methods can only detect differences in the behavior of the system if the differences are greater than the noise. The fact that the residuals are very large compared to those observed for model 2 (Tab. 5) can be interpreted as evidence that the signal-to-noise-ratio is rather low and that the representation of the data by the model could be better. Hence, a more viscous displacing fluid with less shear-dependent flow properties (Fig. 29) is likely to induce clearer results.

For a milk protein concentrate with a protein concentration of 12.5%, the consistency index and the fluid index account for 0.13 Pa·s^n and 0.75, respectively. For a solution of 1.0% xanthan gum and 1.1% sodium chloride, the corresponding values are 4.47 Pa·s^n and 0.25.

Compared to the milk protein concentrate, the xanthan solution exhibits a much higher consistency index, while the fluid index is lower. The practical implication is that the viscosity of the xanthan solutions is 34 times the viscosity of the milk protein concentrates at a shear rate of 1 s^{-1}. At a shear rate of 300 s^{-1}, however, the viscosity ratio is 2. This is that the less dense xanthan solution (≈ 1010 kg/m^3) displaces the approximately equally viscous protein concentrate having a higher density (≈ 1070 kg/m^3). Considering the findings of Lewis (1950, p. 86) and Mishra et al. (2008, p. 4), it is questionable if the xanthan solutions and the milk protein concentrates have a stable interface in this case.

Besides, the two model fluids exhibit significant differences with regard to the relaxation times. For milk protein concentrates with protein concentrations between 3.5 and 13.5%, the relaxation times account for 0.01 to 1 s for at 10°C (Kieferle et al., 2019b, p. 462). Compared to the relaxation times of xanthan solutions, this is rather short as these have relaxation times in the range between 1 and 1000 s for xanthan concentrations ranging from 0.001 to 1% at 25°C (Wyatt and Liberatore, 2009, p. 4081). Considering the measurement temperatures (10 and 25°C), the difference of the relaxation times is likely to be even more pronounced as low temperatures reduce the reaction speed of a fluid. To which extent these differences in the relaxation time affect the residence time, however, is difficult to assess.

From a practical point of view, it is concluded that the expenses related to the preparation of the xanthan solutions are not justified by the outcome. Furthermore, the removal of the xanthan solutions or any other viscous displacing fluid from the plant and the devices after the displacement is also assessed as an undue expense reducing the overall process efficiency. Besides, it is questionable if a mixing of the product with the xanthan solutions or any other displacing fluid containing additives is desirable. In order to minimize the residence time, it is still more expedient to maximize the flow rate and to reduce the aspect ratio, which affects the Reynolds number.

6.3 Influence of the Reynolds number

According to Walenta and Kessler (1990b, p. 66), the displacement of viscous fluids from tubes is primarily determined by the Reynolds number of the displacing fluid, while the Reynolds number of the displaced fluid is negligible. The Reynolds number as defined in Eq. 4 is a function of the actual viscosity η_a (Eq. 57), which in turn depends on the power-law parameters k and n, the average flow velocity u_a during the displacement (Eq. 58), and the characteristic length L_c, which equals the hydraulic diameter (Kieferle et al., 2019a, p. 159). Assuming incompressible fluids, the average flow velocity is a function of the flow rate $\dot{V}$, the cross-sectional area A_c of the empty flow channel, and the porosity ε_s of the spacer.

$$\eta_a \approx k \cdot \left(\frac{u_a}{\frac{L_c}{2}} \right)^{n-1} \tag{57}$$

$$u_a = \frac{\dot{V}}{A_c \cdot \varepsilon_s} \tag{58}$$

The distribution of the flow velocities determined for the different feed spacers are compiled in Fig. 46. These results indicate that lower aspect ratios are accompanied by narrower velocity distributions. Considering the flow velocities indicated by Bucs et al. (2015, p. 304) and by Kavianipour et al. (2017, p. 169), the observed values are on the same order of magnitude.

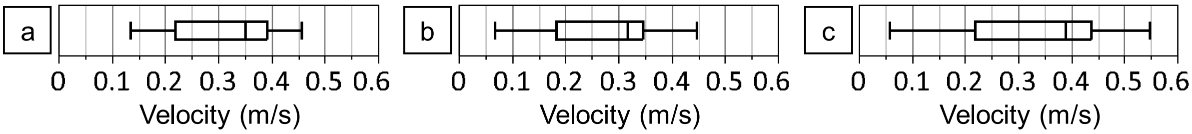

Fig. 46: Outlier box plots of the flow velocities observed for aspect ratios of a) 0.53, b) 0.55, and c) 0.59. This compilation comprises all observations listed in the appendices F – 0.

In order to review the statement of Walenta and Kessler (1990b, p. 66), all observations from the data sets (1 – 4, Tab. 4) are used. The values and formulas required for the calculation of the Reynolds numbers can be found in the appendixes F – 0.

6.3.1 Presentation of the expectations

The results presented in the preceding sections clearly show that the residence time decreases with increasing flow rates and that a high viscosity of the model product induces a prolongation of the residence time (Fig. 42). Concerning the geometry of the spacer, the findings indicate that low aspect ratios (Eq. 11) and rather higher hydraulic diameters (Eq. 5) contribute to shorter residence times. Taking these results into account, it can be concluded that high Reynolds numbers of the displacing fluid contribute to short residence times.

However, the fact that the residence times are nonetheless longer for high viscosity model products undermines the statement of Walenta and Kessler (1990b, p. 66) according to which the flow state of the displaced fluid can be unconsidered when describing the residence time behavior. This contradiction gives rise to discuss the explanatory power of the Reynolds number with regard to the residence times, which is related to the question whether the Reynolds number concept is applicable for the description of the flow states in spacer-filled channels.

6.3.2 Description and interpretation of the experimental results

Fig. 47a and b show the relationship between the residence times and the Reynolds numbers calculated for the model product (Re_{MP}) and the displacing fluid (Re_{DF}). In both diagrams, the residence times decrease with increasing Reynolds numbers. Regarding Fig. 47a, it becomes apparent that high viscosities of the model product (dark symbols) induce low Reynolds numbers and long residence times. However, there are also observations for high product viscosities showing residence times as low as 20 s, which can be related to high flow rates. In Fig. 47b, the residence time decreases in an approximately log-linear manner with increasing Reynolds numbers.

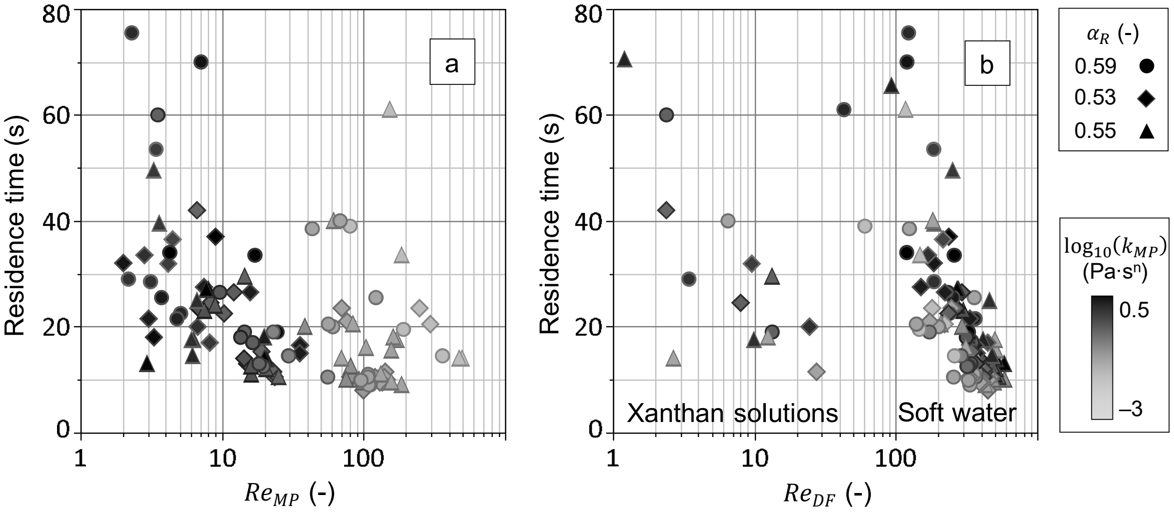

Fig. 47: Relationships between the residence time and the Reynolds number Re for the a) model product (Re_{MP}) and the b) displacing fluid (Re_{DF}), which is either water or xanthan solution.

Comparing the displacement by water and xanthan solutions, the residence times are on the same order of magnitude but the Reynolds numbers deviate by a factor of 10 and more. Furthermore, the color code indicates that the viscosity of the model product also affects the residence times since the residence times are higher for high viscosity products at comparable Reynolds numbers. Having a closer look at Fig. 47b, it is visible that the residence times decrease until the attainment of a Reynolds number of roughly 300 and fluctuate between 10 and 30 s for higher Reynolds numbers.

This observation suggests that the critical Reynolds number, which marks the transition from laminar to turbulent flow, accounts for approximately 300 for the considered spacers. This value coincides with the critical Reynolds numbers on the order of 300 reported in literature (Mojab et al., 2014, p. 575; Geraldes et al., 2002, p. 93; Schwinge et al., 2002a, p. 199). Also the results of Gauwbergen and Baeyens (2000, p. 90; 1997, p. 297) shown in Fig. 25, support the assumption that the critical Reynolds number is on the order of 300.

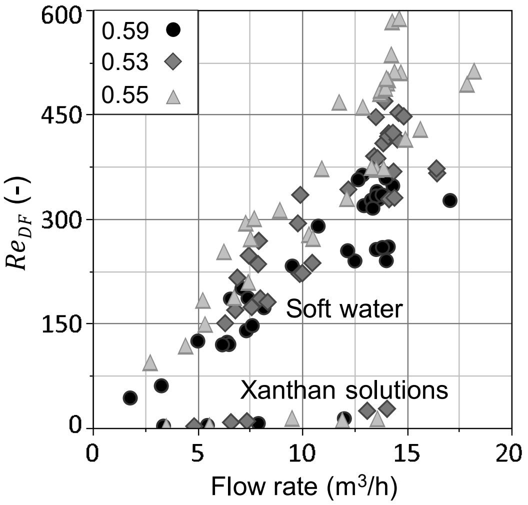

Fig. 48: Relationship between the Reynolds number Re_{DF} calculated for the displacing fluid and the flow rate.

Fig. 48 shows that Reynolds numbers on the order of 300 are observed for flow rates of about 9 to 14 m^3/h when displacing by water, while the Reynolds numbers never exceed a value of 30 for the displacement by xanthan solutions. This means that comparable residence times can be obtained at lower Reynolds numbers when using xanthan solutions.

Summarizing the presented observations, it is evident that the Reynolds numbers of the displacing fluid crucially influence the residence times but it is also undeniable that the viscosity of the model product plays an important role as well. Besides, the remarkably low Reynolds numbers observed for the xanthan solutions question the explanatory power of the critical Reynolds number with regard to residence time.

6.3.3 Discussion of the results

Fig. 47b shows that the residence times decrease with increasing Reynolds numbers of the displacing fluid. However, the residence times observed for the displacement by xanthan solutions are on the same order as those recorded for the displacement by soft water although the Reynolds numbers of the displacing fluid deviate strongly. Besides, the viscosity of the displaced fluid affects the residences times at equal Reynolds numbers. Hence, the Reynolds number of the displacing fluid is not capable of fully explaining the variance of the observed residence times. This is related to the fact that the Reynolds number only contains information on one of the fluids. Thus, the interactions of the displacing fluid and the displaced fluid are not considered when calculating the Reynolds number. However, the differences in the density and viscosity do affect the mixing of the fluids and thus the progression of the displacement.

Consequently, the Reynolds number concept is not suitable for representing the hydrodynamic processes during the displacement of one fluid by another since it only considers the properties of one fluid.

Besides, there are some aspects questioning the applicability of the Reynolds number concept for the flow in the spacer-filled channels of spiral-wound membranes in general. Firstly, the Reynolds number is designated for the comparison of flow states in geometrically similar flow channels. Considering the geometry of commercial feed spacers of different thicknesses, this is not the case. Furthermore, the Reynolds number is a function of the characteristic length, which is frequently the hydraulic diameter or the channel height. These measures have been shown to be not fully suitable for capturing the geometric characteristics of the spacer-filled channel relevant for the displacement process (section 6.1). A possible reason is that the utilization of the hydraulic diameter concept is subject to the requirement that the flow is turbulent (Wilde, 1978, p. 59). This is not the case in 50% of the observations when assuming a critical Reynolds number of 300 for the flow through spacer-filled channels (section 2.2.1). Judging on the applicability of the Reynolds number for spacer-filled channels, a further aspect is to be taken into account. Applying an incorrect or not representative value for the characteristic length (such as the hydraulic diameter) falsifies the Reynolds number (Eq. 4) severely. The reason is that this measure also affects the flow velocity (Eq. 58) and the viscosity (Eq. 57) of a non-Newtonian fluid. Thus, three out of four variables used for the calculation of the Reynolds number are afflicted with uncertainty.

Taking these considerations into account, the application of the resulting Reynolds number for the assessment of the flow state in spacer-filled channels should be revisited very carefully. Concerning the residence time, the Reynolds number of the displacement fluid possesses a limited explanatory power. Nevertheless, the Reynolds number is considered a helpful dimensionless number with regard to rough comparisons.

So far, the focus of the investigations was on the description of the residence time as a function of the process condition defined by the flow rate, the viscosity of the involved fluids, and the spacer dimensions. The presented statistical models give an idea of the relationships between the process conditions and the residence time but do not provide much information on the actual hydrodynamic processes. In order to gain insights concerning the hydrodynamics determining the residence time behavior during the displacement of one fluid by another, mechanistic models are developed and applied in the following.

7 Mathematical description of displacement curves by mechanistic models

Based on the statistical models presented in the preceding section, the residence times, which indicate the time required for the displacement of the model product from the spiral-wound membranes, can be predicted for given process conditions. However, these results do not convey an idea of the hydrodynamics determining the residence time. In order to gain insights into the processes entailing the observed displacement behavior, the residence time distribution curves are used as they contain information on the hydrodynamic processes (Jakubith, 1998, p. 300).

For decoding this information, all experimental residence time distribution curves are approximated by means of a compartment model, an advection-dispersion model and a combination of both models. Appendices A – D and J provide the results belonging to the following sections.

7.1 Compartment model

The idea of the compartment model is that the residence time behavior of a real plant, such as the test rig shown in Fig. 49, can be described by a series connection of reactor models.

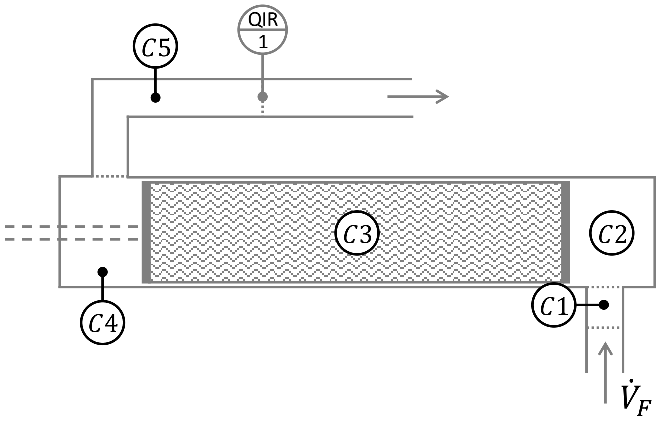

Fig. 49: Assignment of the compartments $C1$ to $C5$ to the sections of the used experimental setup.

The models are chosen in the way that they approximate the prevailing hydrodynamic behavior of the compartment ($C1 - C5$) they represent. Due to their simplicity, models of the ideal plug flow reactor and the continuous stirred tank reactor are frequently used to develop a compartment model.

7.1.1 Development of the compartment model

For the test rig under consideration (Fig. 49), the compartments $C1$, $C3$, and $C5$ are considered as ideal plug flow reactors, while the compartments $C2$ and $C4$, are treated as ideal continuous stirred tank reactors. The resulting model is visualized in Fig. 50.

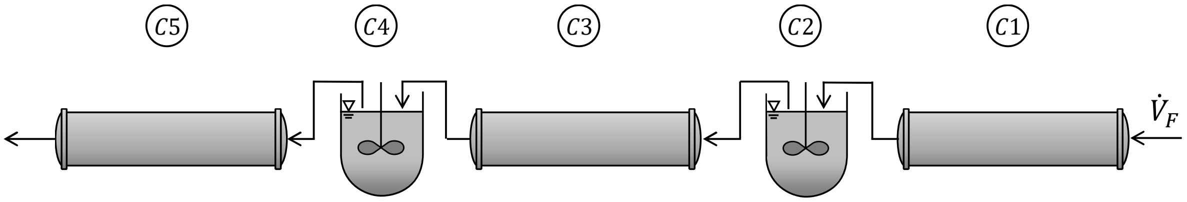

Fig. 50: Assignment of ideal reactor models to the sections of the experimental setup in Fig. 49.

As mentioned in section 2.5.1, an ideal continuous stirred tank reactor affects the shape of the residence time distribution curve, while an ideal plug flow reactor only induces a shift of the curve towards longer residence times. Hence, the model in Fig. 50 can be regarded as a series connection of two ideal stirred tank reactors, where the signal measured at the outlet is delayed due to the presence of the ideal plug flow reactors. The time delay of the signal equals the ratio of the total volume $\Sigma V_{P,i}$ of the plug flow reactors and the flow rate $\dot{V}$. In order to describe the cumulative residence time distribution $F(t)$ observed for the two stirred tanks connected in series mathematically, the tanks-in-series model in Eq. 59 can be used (Schwister and Leven, 2013, p. 173; Levenspiel, 1999, p. 323). According to this model, the shape of the cumulative distribution curve depends on the time t, the flow rate $\dot{V}$, and the volume V_T and number N of the (equal) stirred tanks. To describe the case under consideration by Eq. 60, Eq. 59 is adapted in two respects. Firstly the number of tanks N is set to 2 and secondly, the time delay is introduced according to the procedure described in section 2.5.1.

$$F(t) = 1 - e^{\left(-\frac{N \cdot \dot{V} \cdot t}{V_T}\right)} \cdot \left(1 + \frac{N \cdot \dot{V} \cdot t}{V_T} + \frac{1}{2!} \cdot \left(\frac{N \cdot \dot{V} \cdot t}{V_T}\right)^2 + \cdots + \frac{1}{(N-1)!} \cdot \left(\frac{N \cdot \dot{V} \cdot t}{V_T}\right)^{N-1}\right) \quad (59)$$

$$1 - F(t) = e^{-\frac{2 \cdot \dot{V} \cdot \left(t - \frac{\Sigma V_{P,i}}{\dot{V}}\right)}{V_T}} \cdot \left(1 + \frac{2 \cdot \dot{V} \cdot t}{V_T}\right) \quad (60)$$

On the one hand, the model in Eq. 60 is very convenient as it is simple. On the other hand it is likely that the price of simplicity is a low model performance. Particularly the fact that the model does not consider the viscosity of the fluids is regarded as an obvious limitation to its applicability. Thus, it is expected that the curves calculated for the displacement of a viscous model product by water deviate from the observations.

7.1.2 Application of the compartment model and interpretation of the results

The displacement curves are calculated using the R-script comprised in the appendix N. Fig. 51 shows the cumulative distribution curves (dashed line) determined for the position of the monitoring device (Fig. 49, QIR1), which should coincide with the experimental curves (straight line). It is apparent that the experimental curves show a more or less pronounced sigmoid shape, while the calculated curves are exclusively asymptotic, which is a characteristic of mixed flow.

Hence, the visual assessment of the curves suggests immediately that the applied compartment model is rather unsuitable to describe the observed residence time behavior. However, despite the striking differences in the curve shapes, the calculated curves attain the asymptote on the same order of time as the experimental curves. This is that the predicted residence times are at least comparable. Particularly in Fig. 51a, a good agreement between the experimental and the calculated residence times can be observed. Regarding Fig. 51b, this is not the case.

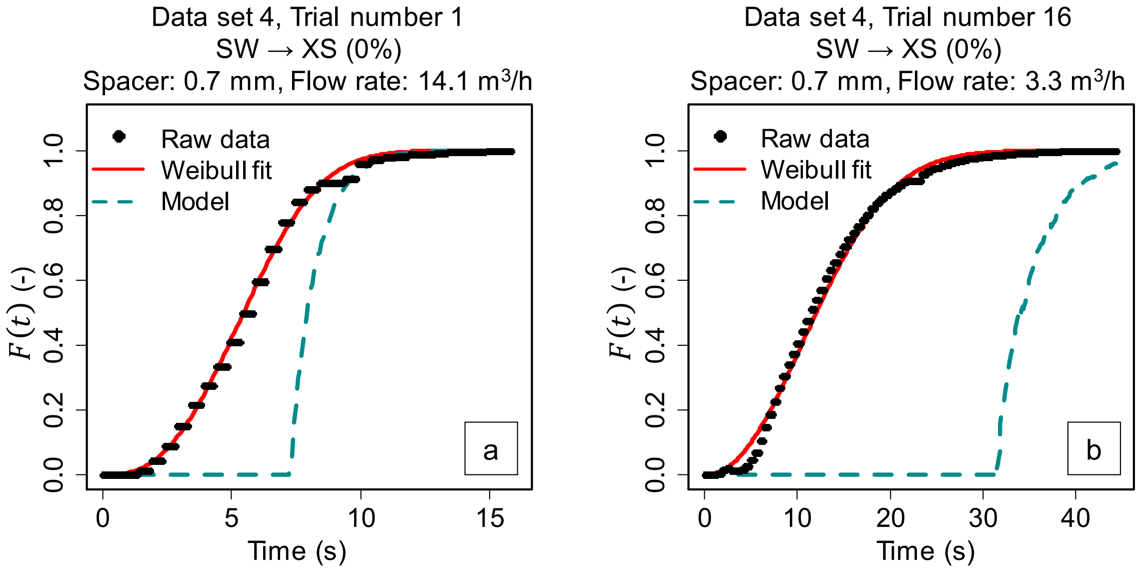

Fig. 51: Experimental residence time curves (straight line) and results of the compartment model (dashed line) for a a) high flow rate ($RMSE_{4,1}$: 28.2%) and a b) low flow rate ($RMSE_{4,16}$: 62.1%). Circles and straight lines represent the experimental observation and dashed lines result from the calculations.

While both diagrams show the displacement of soft water marked with sodium chloride by soft water from a spiral-wound membrane equipped with a 0.7-mm-spacer, they differ with regard to the applied flow rate. Hence, it seems as if the deviation of the calculated curve from the observed curve was much lower for high flow rates (Fig. 51a) than for low flow rates (Fig. 51b). The root mean square errors $RMSE$ indicated in the legend of Fig. 51 reflect the extent of deviation and differ by a factor of 2 for the considered flow rates.

In order to find out which factors affect the prediction accuracy, the root mean square errors for all observations are considered and discussed in the following. Furthermore, the reasons for the lack in the goodness of fit are explored.

7.1.3 Reviewing the general applicability of the compartment model

The central assumption of the applied compartment model is that the spiral-wound membrane can be considered as a plug flow reactor, which means that no axial dispersion or radial velocity distribution exists. The root mean square error $RMSE$ is a valuable statistical key figure to quantify and compare the deviations between the calculated and the observed curves because it expresses the mean deviation between the curves. In general, low root mean square errors are aspired since they indicate a good accordance between model and observation. Plotting the root mean square errors of all observations against the flow rate (Fig. 52), it becomes obvious that high flow rates and higher prediction accuracies go hand in hand.

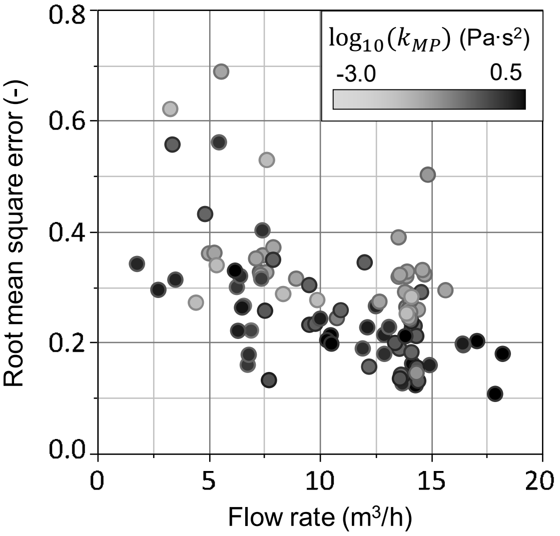

Fig. 52: Relationship between the root mean square error and the flow rate.

This proves evidence for the existence of axial dispersion or a radial velocity distribution, which decreases with increasing flow rates and approximates the presumed plug flow. Fig. 52 shows furthermore that increasing product viscosities, indicated by the color code, lead to larger deviations between the predicted and observed curves. The observation that the shapes of the curves in Fig. 51 differ can be explained by the fact that the applied model does not reflect the actual hydrodynamic processes sufficiently. Thus, the assumption that the residence time behavior in the spiral-wound membrane can simply be described by a plug flow reactor model proofs apparently not true. The sigmoid shape of the experimental displacement curves rather suggest that there is a certain extent of dispersion.

Concluding from the presented results, the above concern with regard to the neglect of the product viscosity turns out to be justified. Furthermore, the applied compartment model does not provide enough flexibility with regard to the hydrodynamic processes which leads to severe prediction inaccuracies. As ideal plug flow (without axial dispersion) does not alter the shape of the input curve, the asymptotic shape of the calculated curve is only determined by the mixing compartments. Thus, there is no possibility to develop the sigmoid shape required for the approximation of the experimental curves.

Despite its evident drawbacks, the presented compartment model is assessed very straight-forward since it is based on only a few and easily accessible variables. Furthermore, it allows a rough estimation of the residence time as long as the displaced fluid and the displacing fluid have comparable flow properties. However, in order to describe the displacement curves, the applied compartment model is not suitable. In contrast, the advection-dispersion model has already been shown to be applicable for describing the displacement of a Newtonian fluid from spiral-wound membranes (Gauwbergen and Baeyens, 1997).

Using this model, the presumed axial dispersion can be considered. However, to which extent the advection-dispersion model is also accurate in case of non-Newtonian fluids is reviewed in the following section.

7.2 Advection-dispersion model

The central assumption underlying the advection-dispersion model is that the spiral-wound membrane determines the residence time behavior in the first place and that surrounding plant components play only a secondary role. The basic prerequisite for the application of this model is to have estimates for the Péclet numbers because these indicate the extent of dispersion. High Péclet numbers imply low axial dispersion et vice versa. In practice, the most common way to determine the Péclet number is curve-fitting. By using the Péclet number in the advection-dispersion model as fitting parameter, the residence time distribution curve is fitted to the experimental curve. The method of moments is another approach, where the estimation of the Péclet number is based on the variance of the curves (Trinidad et al., 2006, p. 607).

7.2.1 Estimation of the Péclet number

The curve-fitting method is subject to the requirement that an analytical expression for the distribution curve exists. This holds true for small extents of dispersion but is not the case for large deviations from plug flow (Levenspiel, 1999, p. 300). Thus, it is necessary to review whether the deviation from plug flow is small enough to apply this method. Fig. 53 shows two experimental displacement curves (straight, red line) and the corresponding density curves (straight, green line), which are approximated by the advection-dispersion model (ADM, dashed, blue line) in Eq. 29.

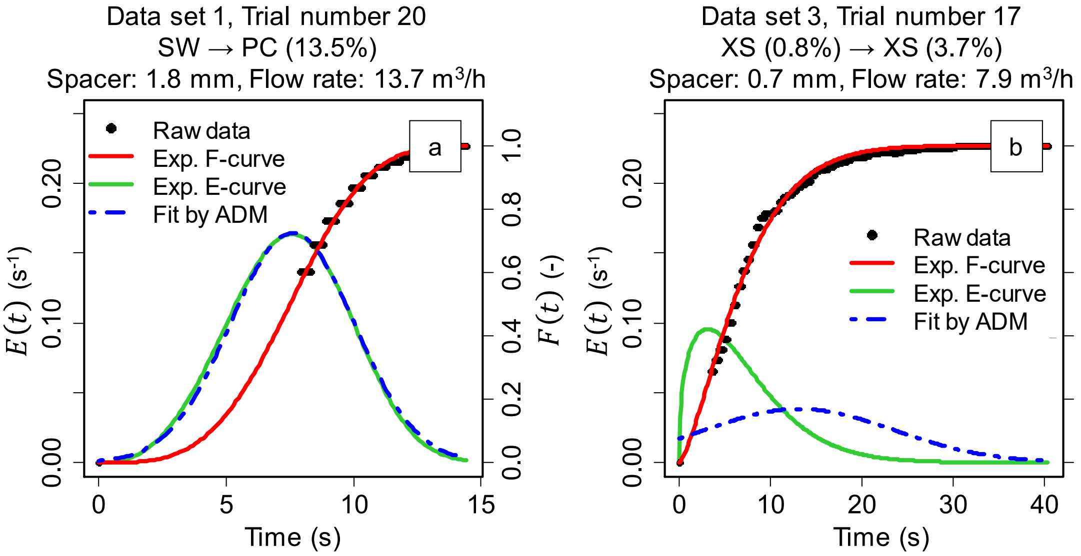

Fig. 53: Comparison of the experimental (Exp. E-curve) and the fitted (Fit by ADM, advection-dispersion model) residence time distribution for a a) nearly symmetric and a b) right skewed curve.

In case of Fig. 53a, the assumption of small deviation from plug flow is reasonable as the density curve is bell-shaped and nearly symmetric. The fitted curve obtained using the advection-dispersion model approximates the experimental curve very well. However, a couple of density curves are right-skewed as shown in Fig. 53b, which indicates large deviation from plug flow. Here, the fitted curve is not at all in accordance with the experimental curve as Eq. 29 cannot approximate the skewed shape. Consequently, curve-fitting based on the density functions is not suitable for all of the experimentally observed residence time curves. The alternative approach to curve-fitting is the method of moments, which is based on the variances (2nd central moment). The variance σ_m^2 for large deviation from plug flow is given in Eq. 30 and the variance σ_e^2 of the experimental curves (Weibull distribution) is generally defined by Eq. 61.

$$\sigma_e^2 = \lambda^2 \cdot \left(\Gamma\left(1 + \frac{2}{\varphi}\right) - \left(\Gamma\left(1 + \frac{1}{\varphi}\right)\right)^2 \right) \qquad (61)$$

In this equation, $\Gamma(\,)$ is the gamma function, while λ and φ are the scale and shape parameter of the Weibull distribution (Eq. 54). In order to quantify the Péclet numbers, the variance σ_m^2 and the variance σ_e^2 of the experimental curves are equated. The Péclet numbers satisfying this equation to a certain accuracy are found using R and are depicted in Fig. 54. The experimental Péclet numbers are in the range between 0.2 and 59. Since the observed Péclet numbers are greater than one with the exception of one observation, the advection-dispersion model appears to be generally applicable. Ebach and White (1958, p. 168) observed Péclet numbers in the range from 0.1 to 1 for the flow of fluids through porous media such as bulks of Raschig rings or spheres.

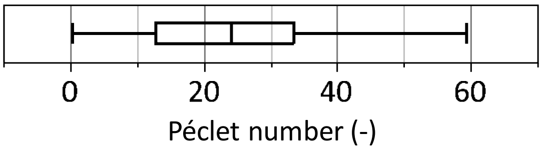

Fig. 54: Outlier box plot of the Péclet numbers quantified based on the advection-dispersion model.

For the flow through different types of circular pipes, Levenspiel (1958, p. 345) presents Péclet numbers ranging from 0.1 to 10. Gauwbergen and Baeyens (1997, p. 297), who investigate the flow of water through spiral-wound membranes, report Péclet numbers in the range from 20 to approximately 40. This is in good accordance with the values reported for the spiral-wound membranes but clearly exceeds those for the flow through pipes and porous media. Based on the length of the entire experimental setup and the average velocity in the spiral-wound membrane, the average axial dispersion coefficients are calculated.

Fig. 55 shows the distribution of the axial dispersion coefficients, which take values between $4.3 \cdot 10^{-3}$ and 2.5 m^2/s. These values are great compared to an exemplary molecular diffusion coefficient D_m of $2.1 \cdot 10^{-12}$ m^2/s determined for the diffusion of a casein micelle in an aqueous solution. This estimate is based on the Stokes-Einstein equation in Eq. 8. The required particle radius (100 nm, casein micelle), the viscosity (1 mPas, water), and the temperature (283 K) take practically relevant values. These estimates validate the basic assumption that the molecular diffusion plays a secondary role as it is 10^9 times lower than the dispersive currents.

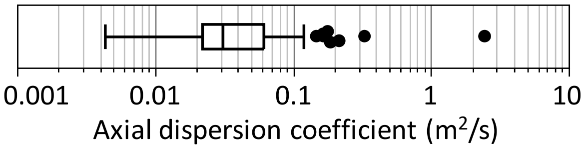

Fig. 55: Outlier box plot of the axial dispersion coefficients representing the entire experimental setup.

The leading question of the following section is whether the displacement curves can be described in an accurate way by assuming that the displacement behavior is determined by the spiral-wound membrane in the first place and that the dispersion coefficient is constant. It is expected that the advection-dispersion model leads to a better approximation of the observed displacement curves than the compartment model applied in section 7.1.2 as the dispersion inducing the sigmoid shape is considered. Furthermore, the axial dispersion coefficient allows the consideration of variables such as the product viscosity and the thickness of the spacer. However, it must be assumed that the axial dispersion coefficient is constant along the whole test rig. This is presumably not the case because the dispersion is likely to vary in the different sections of the test rig.

Furthermore, the viscosity of the protein concentrate changes because it is shear-thinning and because it is successively mixed with the displacement fluid. This doubtlessly affects the extent of dispersion as well.

7.2.2 Application of the advection-dispersion model and discussion of the results

Using the Péclet numbers quantified based on the method of moments, the density curves are calculated numerically based on Eq. 26. Therefore, the actual (time-varying) flow velocities ranging from 0.06 to 0.55 m/s are used (Fig. 46). The advection-dispersion model allows the representation of the displacement curves as a function of the time t and the position x. In order to assess the development of the curves, different positions depicted in Fig. 56 are considered explicitly.

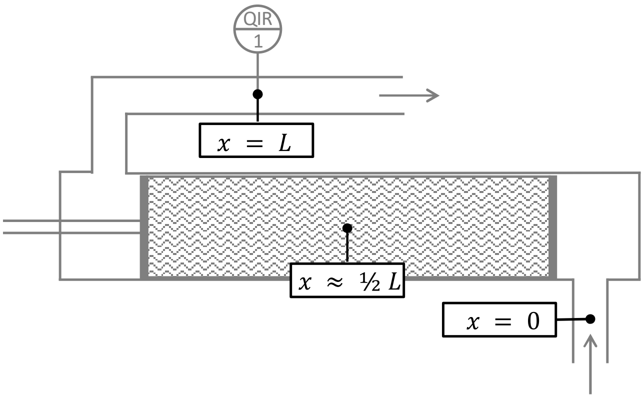

Fig. 56: Local resolution of displacement curves determined based on the advection-dispersion model for an overall axial dispersion coefficient. (inlet $x = 0$, center $x \approx ½\,L$, and outlet $x = L$).

Fig. 57 and Fig. 58 contain exemplary results allowing the assessment of the impact of the flow rate and the product viscosity on the suitability of the advection-dispersion model. In both figures, the straight lines represent the experimental displacement curves and the dashed lines are the calculated cumulative frequency curves at the inlet ($x = 0$), the center ($x \approx ½\,L$), and the outlet ($x = L$) of the experimental setup. Herein, the shape of the curves depends on the position and change from asymptotic at the inlet to sigmoid at the exit.

Fig. 57a shows the displacement of marked water by soft water with an average flow rate of 14.1 m^3/h. The advection-dispersion model allows a good description of the curve measured at the outlet of the plant. However, the reduction of the average flow rate to 4.4 m^3/h (Fig. 57b) leads to severe deviations between the calculated and actually observed curve. Thus, comparably with the compartment model, the flow rate clearly affects the accuracy of the advection-dispersion model.

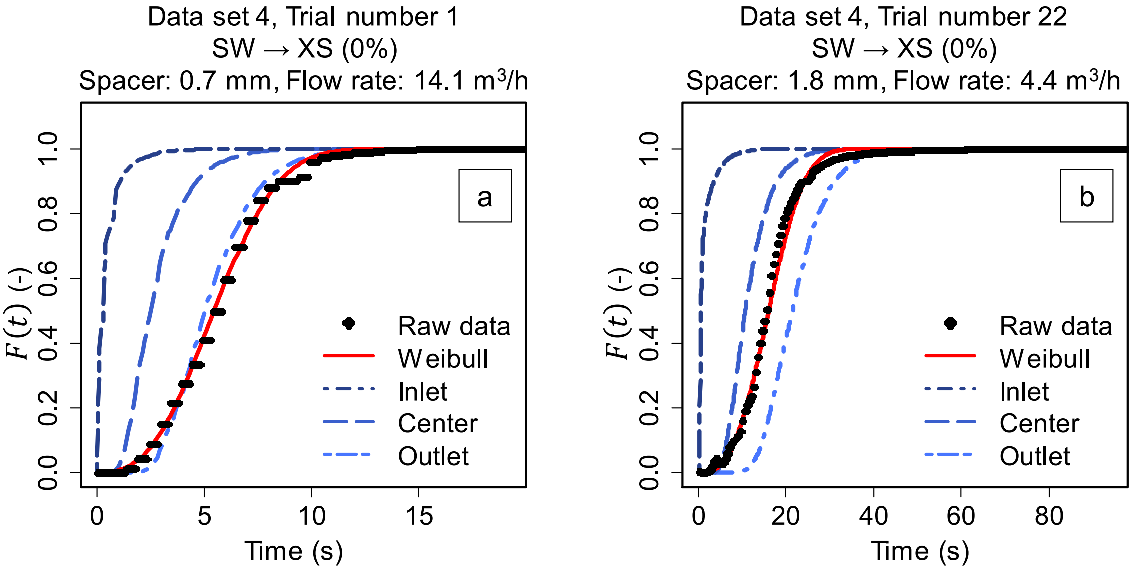

Fig. 57: Calculated displacement curves with local resolution for a a) high flow rate ($RMSE_{4,1}$: 4.1%) and a b) low flow rate ($RMSE_{4,22}$: 13.6%). Circles and straight lines represent the experimental observation and dashed lines result from the calculations.

This holds also true with regard to the displacement of high viscosity products (Fig. 58). While the accordance between the experimental and the calculated curve is good at high flow rates (Fig. 58a), the deviations are much larger for low flow rates as shown in Fig. 58b. Finally, the examples show clearly that the advection-dispersion model approximates some of the experimental curves very well. However, as some of the calculated curves deviate to a considerable extent.

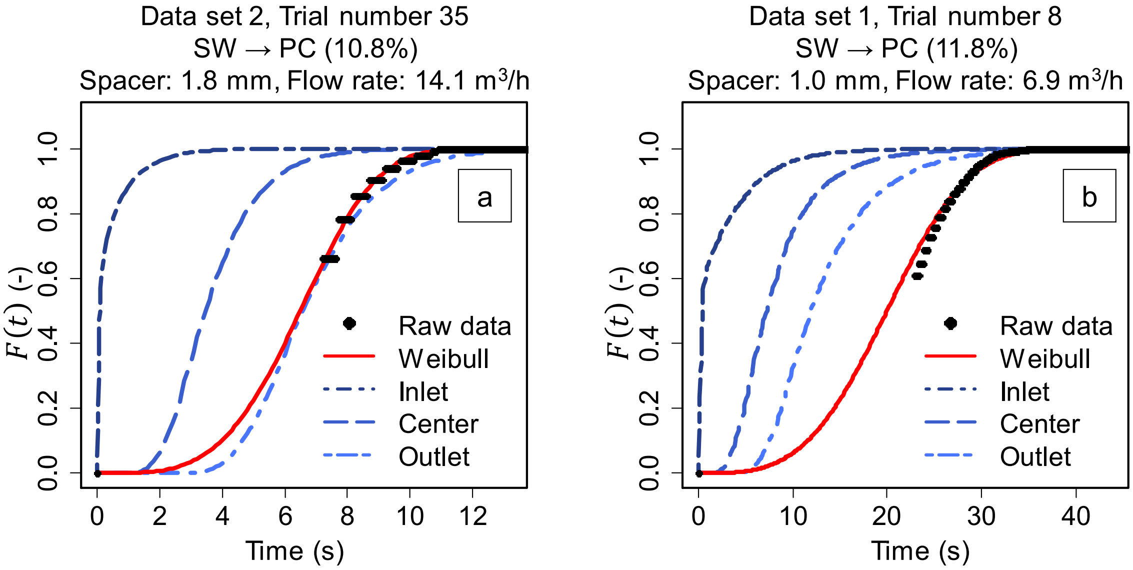

Fig. 58: Calculated displacement curves with local resolution for a a) high flow rate ($RMSE_{2,35}$: 4.0%) and a b) low flow rate ($RMSE_{1,8}$: 13.0%). Circles and straight lines represent the experimental observation and dashed lines result from the calculations.

For quantifying the deviations between the experimental and the calculated curves, the root mean square errors are indicated in the legends of Fig. 57 and Fig. 58. Besides, these are listed in the appendix J. The lower the root mean square error is, the better is the accordance between the curves. Considering a root mean square errors of 5% as low enough to ensure an acceptable approximation, the model is applicable to only 18% of all experimental curves, which gives rise to question the general applicability of the advection-dispersion model.

7.2.3 Reviewing the general applicability of the advection-dispersion model

Reviewing the boundary conditions underlying the advection-dispersion model, the unsatisfactory results can be explained. The central assumption is that the axial dispersion coefficient within the experimental setup is constant and thus independent of the position and time. This supposition demands that the spiral-wound membrane determines the residence time behavior in the first place, while the impact of the pipes and empty housing sections on the curve shapes is negligible. Obviously, the true circumstances deviate from these assumptions in such a way that the model is unable to approximate the experimental curves sufficiently. Firstly, the independence of the location is violated in two respects. On the one hand, it is reasonable to assume that the dispersion coefficient varies in the sections of the experimental setup due to the different hydrodynamic conditions. The consequence is that the application of the overall dispersion coefficient for the calculation of the displacement curves works only with a certain accuracy as long as the dispersion is small, which is the case at high flow rates. On the other hand, the membrane modules do not fill out the housing perfectly, which results in the existence of a gap as shown in Fig. 59.

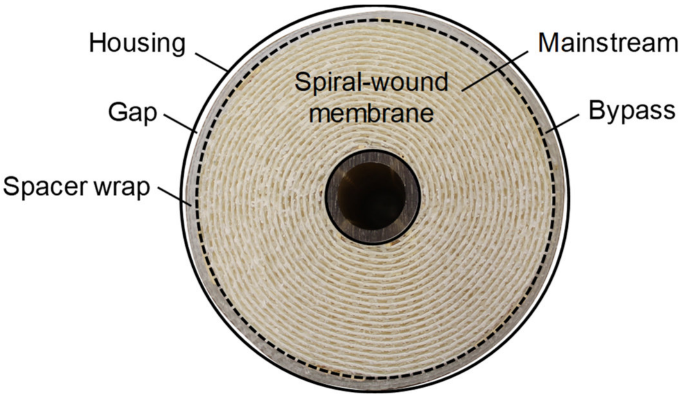

Fig. 59: Photograph of the front side of a spiral-wound membrane.

It is conceivable that a bypass flow around the module influences the observed residence time behavior. While high flow rates lead to a low radial velocity distribution, it can be expected that the liquid distribution at the front side of the membrane module is very uneven at low flow rates. Finally, the displacement describes the exchange of one fluid by another, which is by implication that the dispersion coefficient changes as a function of volume shares of the fluids. Thus, the dispersion coefficient is not independent of the time. Assessing the efforts on describing the residence time distribution presented in the preceding sections, it becomes evident that both the compartment model and the advection-dispersion model show severe inadequacies concerning their ability to approximate the experimental displacement curves but clearly have their strengths as well. The advantage of the compartment model is its general idea of considering each section of the experimental setup as an individual compartment exhibiting a particular hydrodynamic behavior. Concerning the advection-dispersion model, it is reasonable to assume that it reflects the underlying mechanisms taking place in the spiral-wound membrane during the displacement process. However, the impact of the other sections on the residence time distribution curves is too high to apply the advection-dispersion model for the entire setup. Thus, the combination of the two models in order to improve the ability to approximate the experimental displacement curves is expedient.

7.3 Hybrid models

In order to describe the displacement curves and to examine the hydrodynamic processes in spiral-wound membranes based on a more suitable mechanistic model, the compartment model and the advection-dispersion model are used in combination in the following. By this, the strengths of the two models are combined resulting in a more detailed representation of the reality.

7.3.1 Development of the hybrid models

The schematic representation of the experimental setup in Fig. 49 shows that the fluid passes through an inlet pipe ($C1$), enters the empty sections of the housing ($C2$), flows through the flow channels of the spiral-wound membrane ($C3$), enters the housing ($C4$) again, and leaves the setup through an outlet pipe ($C5$), where the monitoring device is located. Considering these sections as compartments showing ideal plug and mixed flow behavior is not expedient with regard to the description of the residence time distribution because the actually prevailing hydrodynamic processes are not reflected by the model (section 7.1.2). Consequently, the particularities of the different compartments must be considered in a more precise way. Prior to moving on to adapted variants of a hybrid model, the basics of the hybrid model are presented in order to clarify the procedure for developing the more detailed models.

Basic structure of the hybrid models

In order to enable the calculation of the displacement curves, the compartment model is combined with the advection-dispersion model as visualized in Fig. 60. Herein, the hydrodynamics of the pipes ($C1$ and $C5$) and in particular of the spiral-wound membrane ($C3$) are considered as plug flow with axial dispersion, which is indicated by the arrows in the plug-flow compartments.

In this model each compartment i imprints a particular shape on the input function resulting in the residence time distribution function $E_i(t)$, which can be observed by means of a suitable monitoring device. The way the hydrodynamics in compartment i influence the shape of the incoming function $x(t)$ is expressed by the transfer function $h_i(t)$.

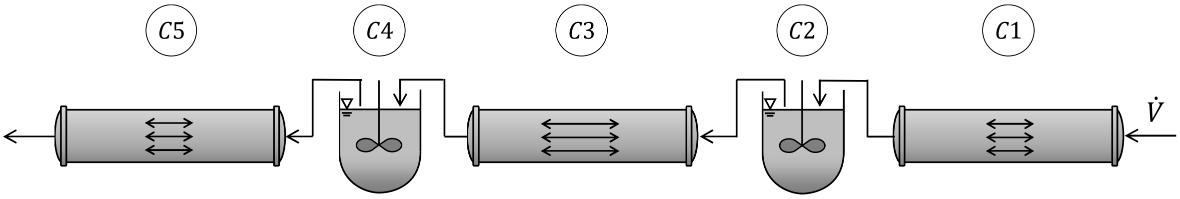

Fig. 60: Basic hybrid model (without bypass flows).

To couple the incoming function and the compartment-specific transfer function a mathematical operation in Eq. 62 needs to be applied, which is called convolution and indicated by an asterisk ($*$). In practice, the convolution is performed by means of the Fourier transforms ($X(\omega)$, $H_i(\omega)$, and $Y_i(\omega)$) of the time-dependent functions ($x(t)$, $h_i(t)$, and $y_i(t)$) as can be retraced in section 4.5 (Levenspiel, 1999, p. 271). In order to differentiate the observed residence time distribution curves $E(t)$ observed at the outlet of the experimental setup from the calculated distribution curves, $y_i(t)$ is used to denote the calculated output function of compartment i.

$$y_i(t) = x(t) * h_i(t) \tag{62}$$

In contrast to the output function $y_i(t)$, which can be taken from literature or determined based on experiments, the transfer function $h_i(t)$ of the compartment i is unknown. Thus, the first step towards calculating the residence time distribution function $y(t)$ at the outlet of the experimental setup is the determination of the transfer function $h_i(t)$ of each compartment i. As indicated in Eq. 63, this is done by deconvolution using the Fourier transforms of the time-dependent functions. The second step is the convolution of the Fourier transform of the step input function $X(\omega)$ with the Fourier transforms of the transfer functions $H_i(\omega)$ (Eq. 64). Finally, the inverse Fourier transform of $Y(\omega)$ equals the output function $y(t)$, which can be compared to the experimentally accessible displacement curves $E(t)$. These steps are performed using the fft-function (fast Fourier transform) in R as can be retraced in the appendix N.

$$H_i(\omega) = \frac{Y_i(\omega)}{X(\omega)} \tag{63}$$

$$Y(\omega) = X(\omega) \cdot H_1(\omega) \cdot H_2(\omega) \cdot H_3(\omega) \cdot H_4(\omega) \cdot H_5(\omega) \tag{64}$$

The output functions $y_i(t)$ of the compartments i used for the calculation of the residence time distribution function $y(t)$ at the outlet of the experimental setup can be found in Eq. 65 and 66. The sections before and after the membrane ($C2$ and $C4$) are treated as continuous stirred tanks (Eq. 65), while $C1$, $C3$, and $C5$ are considered as plug flow reactors with axial dispersion (Eq. 66). Here, it is assumed that the extent of dispersion in the pipes ($C1$ and $C5$) and in the spiral-wound membrane ($C3$) differs as indicated by the length of the arrows in the plug flow reactors in Fig. 60. Thus, two different axial dispersion coefficients $D_{a,i}$, are employed in Eq. 66 with the index i referring to the respective compartment. In these equations, $\dot{V}$ is the flow rate, V_i is the volume of compartment i, u_i is the average flow velocity in compartment i, and L_i is the length of compartment i.

$$y_i(t) = \frac{\dot{V}}{V_i} \cdot exp\left(-\frac{t \cdot \dot{V}}{V_i}\right) \tag{65}$$

$$y_i(t) = \frac{\dot{V}}{V_i} \cdot \frac{1}{\sqrt{\left(4 \cdot \pi \cdot \left(\frac{D_{a,i}}{u_i \cdot L_i}\right)\right)}} \cdot exp\left(-\left(\frac{\left(1 - \frac{t \cdot \dot{V}}{V_i}\right)^2}{4 \cdot \left(\frac{D_{a,i}}{u_i \cdot L_i}\right)}\right)\right) \tag{66}$$

As visualized in Fig. 59, the housing and the spiral-wound membrane form a gap, which suggests the existence of a bypass flow around the module during the displacement process. Furthermore short-circuit flows before and after the module in the empty housing sections ($C2$ and $C4$, Fig. 49) are conceivable. Consequently, the presented basic model is adapted accordingly in the following.

Variants of the hybrid model

The existence of a bypass flow around the spiral-wound membrane can be expected because of two reasons. Firstly, the modules are non-circular to a certain extent as visualized in Fig. 59. This leads to a gap between the housing and the module. Secondly, the membranes are wrapped in a particular spacer net (Fig. 31, wrap). Because the porosity of this wrapping is lower compared to that of the feed spacers, the backpressure is lower within the wrap. The lower backpressure in the gap and in the spacer wrap fosters the flow around the spacer-filled channels of the spiral-wound membranes. Besides this bypass flow, short-circuit flows before and after the module are further flow disturbances arising due to the constructive design of the inlet and the outlet in the empty section of the housings (Fig. 49).

Thus, the assumption of transfer functions derived from idealized reactor models will introduce prediction inaccuracies. To mitigate these inadequacies, the model is augmented accordingly. As indicated in Fig. 61, short-circuit flows ($C2$ and $C4$) and a bypass flow ($C3$) around the spiral-wound membrane are introduced. In order to typify the flow patterns, the bypass flow is modelled as a continuous stirred tank (hybrid model I) on the one hand and as a plug flow with axial dispersion (hybrid model II) on the other hand. The share of the total volume flow entering the compartment i is denoted as main stream $\dot{V}_{i,a}$ and equals $\alpha_i \cdot \dot{V}$, while the side stream $\dot{V}_{i,b}$ is determined by $(1 - \alpha_i) \cdot \dot{V}$. Thus, α_i define volume shares. The mathematical expressions for the output functions $y_i(t)$ of each compartment i are listed in Eqs. 67 – 70. Variables referring to the considered compartment i are V_i, u_i, L_i, and $D_{a,i}$, which characterize the volume, the average flow velocity, the length, and the axial dispersion coefficient, respectively.

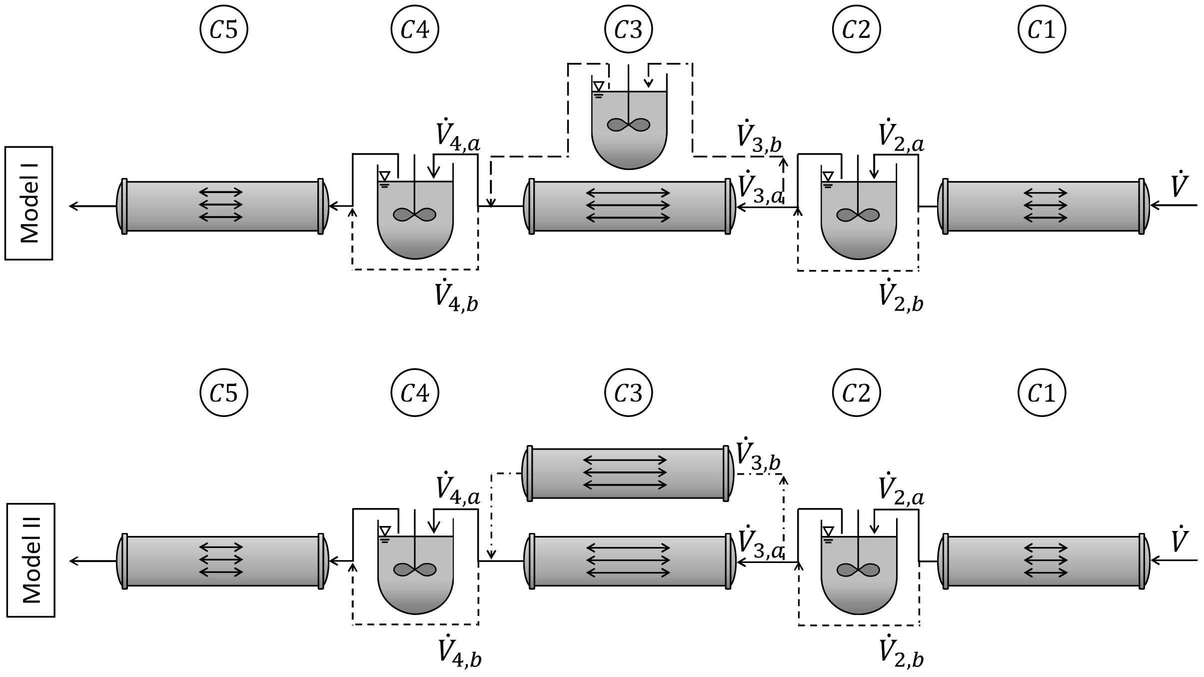

Fig. 61: Variants of the hybrid model with short-circuit flows before and behind the membrane module (dashed lines) and a bypass around the spiral-wound membrane (dotted lines). In hybrid model I, the bypass around the spiral-wound membrane is modelled as continuous stirred tank and in hybrid model II, the bypass is modelled as plug flow reactor with axial dispersion.

Eq. 67 characterizes the flow through the compartments $C2$ and $C4$ each considered as continuous stirred tank with a short-circuit flow. The pipe sections ($C1$ and $C5$) as well as the spiral-wound membrane ($C3$) are modelled as plug flow reactors with axial dispersion as represented by the advection-dispersion model in Eq. 68 with each having their own axial dispersion coefficients $D_{a,i}$. Besides, the spiral-wound membrane has an additional bypass flow considered as continuous stirred tank (Eq. 69, hybrid model I) or plug flow reactor with axial dispersion (Eq. 70, hybrid model II). For hybrid model II, the axial dispersion coefficient in the wrap is assumed to equal the axial dispersion coefficient in the module itself.

$$y_i(t) = \frac{\left(\alpha_i \cdot \dot{V}\right)^2}{V_i \cdot \dot{V}} \cdot exp\left(-\frac{t \cdot \alpha_i \cdot \dot{V}}{V_i}\right) \tag{67}$$

$$y_{i,a}(t) = \frac{\alpha_i \cdot \dot{V}}{V_{i,a}} \cdot \frac{1}{\sqrt{\left(4 \cdot \pi \cdot \left(\frac{D_{a,i}}{u_{i,a} \cdot L_i}\right)\right)}} \cdot exp\left(-\left(\frac{\left(1 - \frac{t \cdot \alpha_i \cdot \dot{V}}{V_{i,a}}\right)^2}{4 \cdot \left(\frac{D_{a,i}}{u_{i,a} \cdot L_i}\right)}\right)\right) \tag{68}$$

Model I

$$y_{i,b}(t) = \frac{(1-\alpha_i) \cdot \dot{V}}{V_{i,b}} \cdot exp\left(-\frac{t \cdot (1-\alpha_i) \cdot \dot{V}}{V_{i,b}}\right) \tag{69}$$

Model II

$$y_{i,b}(t) = \frac{(1-\alpha_i) \cdot \dot{V}}{V_{i,b}} \cdot \frac{1}{\sqrt{\left(4 \cdot \pi \cdot \left(\frac{D_{a,i}}{u_{i,b} \cdot L_i}\right)\right)}} \cdot exp\left(-\left(\frac{\left(1 - \frac{t \cdot (1-\alpha_i) \cdot \dot{V}}{V_{i,b}}\right)^2}{4 \cdot \left(\frac{D_{a,i}}{u_{i,b} \cdot L_i}\right)}\right)\right) \tag{70}$$

The flow velocities, however, differ and depend on the extent of the bypass flow. In order to obtain the sum of the two phases, the output functions for the main stream $y_{3,a}(t)$ and the bypass flow $y_{3,b}(t)$ are summed up (Eq. 71) since these flows are parallel. Having redefined the individual output functions $y_i(t)$, the deconvolution (Eq. 63) and the convolution (Eq. 64) as described in the previous paragraph has to be repeated in order to obtain the overall output function $y(t)$.

$$y_3(t) = y_{3,a}(t) + y_{3,b}(t) \tag{71}$$

For the calculation of the displacement curves, it is assumed that the volume shares and the axial dispersion coefficients in the two pipe sections are equal ($\alpha_2 = \alpha_4$ and $D_{a,1} = D_{a,5}$). This means that the extent of short-circuit flow in the empty sections of the housings and that the axial dispersion coefficients in the pipes do not differ, respectively. The shares of the total volume flow α_2 or α_4 (empty housing sections) take values between 0 and 1, while α_3 (spiral-wound membrane) ranges from 0.5 to 1. The axial dispersion coefficients $D_{a,3}$ (spiral-wound membrane) and $D_{a,1}$ or $D_{a,5}$ (pipe sections) are varied in the range from 10^{-4} to 10^{-1} m^2/s. The limit values for the axial dispersion coefficients $D_{a,i}$ and the volume shares α_i are derived from literature (Gauwbergen and Baeyens, 1997, p. 294; Taylor, 1954, p. 446) and preceding calculations with larger increments (not shown), respectively. The calculation of the displacement curves is performed using R (appendix N), where the selection of the best fit is based on the sum of squared errors (Eq. 42).

It is expected that the hybrid models provide better results compared to the advection-dispersion model (section 7.2) as the boundary conditions can be assumed to be satisfied with the exception of the time-independency. Before moving on to the results, the effects of the model parameters on the shape of the resulting residence time curves are studied.

7.3.2 Effects of the model parameters on the curve shape

The aim of the modelling is to learn more about the hydrodynamic processes determining the displacement behavior. Thus, the fitting parameters are varied to study their effects on the displacement curves subsequently.

These fitting parameters are the axial dispersion coefficients in the spiral-wound membrane $D_{a,3}$ and in the pipes $D_{a,1} = D_{a,5}$, the bypass volume flow around the spiral-wound membrane $(1 - \alpha_3)$, and the short-circuit flow in the empty housing sections $(1 - \alpha_2) = (1 - \alpha_4)$. In the next paragraph, the effects of the different variables on the shape of the resulting displacement curves are discussed.

Effects of the axial dispersion coefficient

Using the basic model (Fig. 60), the effects of the axial dispersion coefficient $D_{a,3}$ in the spiral-wound membrane on the shape of the displacement curve are visualized in Fig. 62, where the remaining variables are constant.

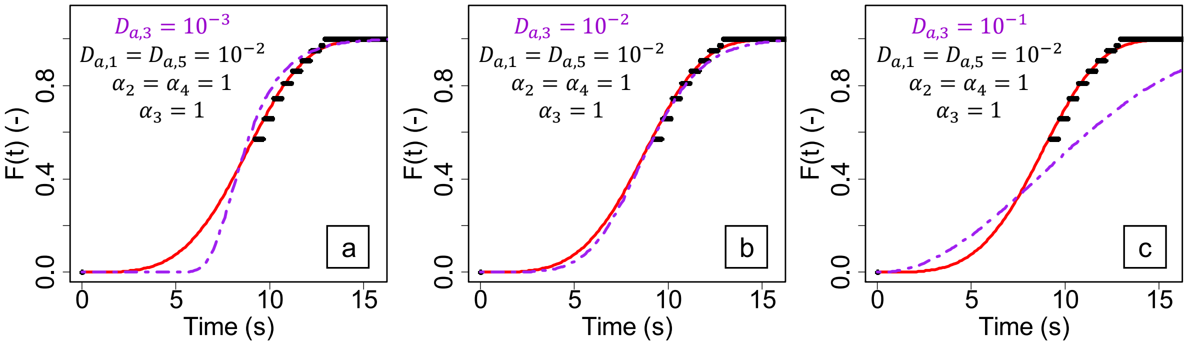

Fig. 62: Variation of the axial dispersion coefficient in the spiral-wound membrane $D_{a,3}$. Circles and straight lines represent the experimental observation and dashed lines result from the calculations.

For an axial dispersion coefficient $D_{a,3}$ of 10^{-3} m^2/s (Fig. 62a), there is a dead time before the steep ascent of the curve inducing a rather asymptotic shape. Here, the mixing compartments determine the shape of the curve, which is why the curve resembles the model curves in Fig. 51. Reducing $D_{a,3}$ from 10^{-3} to 10^{-4} m^2/s, induces a very slight prolongation of the dead time at the beginning, while a further reduction of $D_{a,3}$ below 10^{-4} does not induce any alteration of the curve shape (not shown). In case the axial dispersion coefficient $D_{a,3}$ in the spiral-wound membrane takes values between 10^{-3} and 10^{-2} m^2/s (Fig. 62b), the curves show a sigmoid shape on realistic time scales. This is that the curves reach 1 more or less simultaneously with the actually observed residence time curves. Increasing the axial dispersion coefficient $D_{a,3}$ to 10^{-1} m^2/s (Fig. 62c) leads to a still sigmoid but increasingly flat curve shape. The time until the curve approximates 1 is far beyond the observed residence time. Concerning the axial dispersion coefficients in the pipes ($D_{a,1}$ or $D_{a,5}$), an increase from 10^{-4} to 10^{-2} m^2/s induces a very slight shift to the right. However, the alteration of the curve shape is very small, which is why this coefficient only serves for fine tuning.

Altogether, the similarity of the shape of the calculated and the observed residence time curves suggests that the hybrid model represents the actual hydrodynamic processes during the displacement to a certain extent. An adaption of the axial dispersion coefficient in the spiral-wound membrane has a strong effect on the curve shape, which supports the assumption that the membrane compartment affects the shape of the overall displacement curve considerably. In order to improve the approximation of the model to the observed displacement curves, a bypass around the module and a short-circuit flow before and after the spiral-wound membrane are considered. Since it is unclear how to model the bypass, a stirred-tank bypass (hybrid model I) and a plug-flow bypass with axial dispersion (hybrid model II) are assumed.

Interplay of the stirred-tank bypass and the short-circuit flow

Fig. 63 gives an idea of how the existence of a bypass showing the characteristics of a mixer around the module and the short-circuit flow affect the cumulative distribution curves separately.

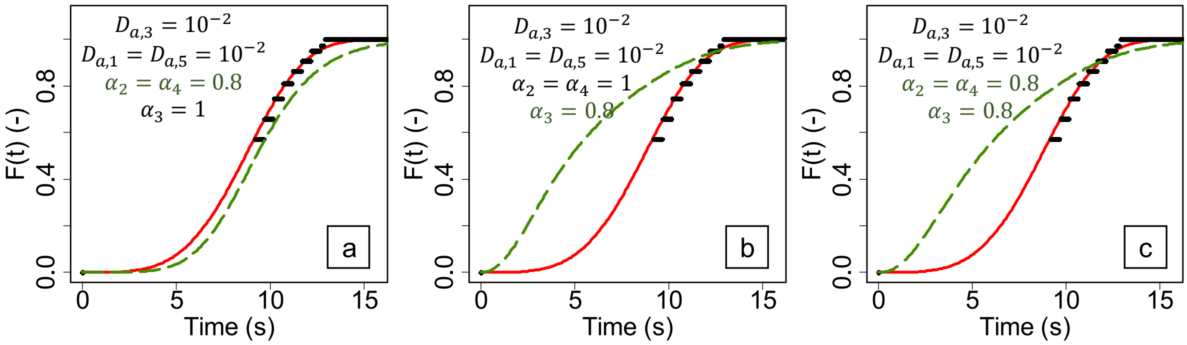

Fig. 63: Effect of stirred-tank-bypass around the module and short-circuit flow in the empty housing defined by the volume shares α_3 and α_2. Circles and straight lines represent the experimental observation and dashed lines result from the calculations.

In order to study the effect of the bypass flow in the compartment $C3$ and the short-circuit flow in the compartments $C2$ and $C4$, the volume shares α_2 $(= \alpha_4)$ and α_3 of the main streams are reduced to 80% successively. If there is a short-circuit flow circumventing the mixing zone immediately before and after the module, α_2 and α_4 are below 1 (Fig. 63a). In comparison to Fig. 62b in the previous paragraph, a shift of the curve to the right can be observed. The reason is that it takes longer until the model product is completely displaced from the compartment $C2$

and $C4$. Thus, the residence time distribution is wider. If a certain share of the total volume flow bypasses the spiral-wound membrane, α_3 is below 1 (Fig. 63b). In this case, the asymptotic shape of an ideal stirred tank reactor imprints on the sigmoid shape induced by the plug flow with dispersion in the spiral-wound membrane. Considering both the bypass around the module and the short-circuit flow, the shape of the curve is determined by the bypass and its position is shifted to the right due to the short-circuit flow as shown in Fig. 63c. Another possibility to describe the bypass flow around the spiral-wound membrane mathematically is considering it as a plug flow reactor with axial dispersion.

Interplay of the plug-flow bypass and the short-circuit flow

Compared to the model above, in which the bypass around the spiral-wound membrane is considered as continuous stirred tank, the plug-flow bypass influences the resulting shape of the displacement curves in another manner.

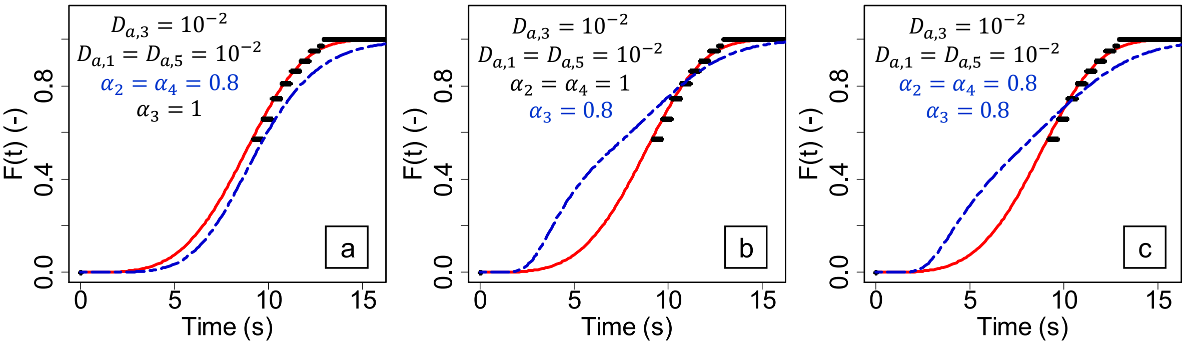

Fig. 64: Effect of stirred-tank-bypass around the module and short-circuit flow in the empty housing defined by the volume shares α_3 and α_2. Circles and straight lines represent the experimental observation and dashed lines result from the calculations.

As α_3 equals 1 in Fig. 64a, this curve does not deviate from Fig. 63a. However, Fig. 64b shows that the bypass modelled based on the advection-dispersion model imprints another sigmoid shape causing a bending of the curve. The resulting curve is double-sigmoid with two inflection points. Combining the bypass and the short-circuit flow, the resulting curve in Fig. 64c shows again characteristics of both disturbances. In the following, the applicability of the hybrid model and its two variants is tested by examining the accordance with the experimental curves.

7.3.3 Reviewing the general applicability of the hybrid models

In order to describe the residence time distributions observed during the displacement experiments, the parameters of the hybrid models are adapted. The values determined for the axial dispersion coefficients in the pipe sections ($D_{a,1}$ and $D_{a,5}$) and in the spiral-wound membrane ($D_{a,3}$) as well as the volume shares indicating the magnitude of the main streams in the empty sections of the housing (α_2) and in the membrane module (α_3) can be found in the appendix J.

Fig. 65 allows the comparison of experimental and calculated residence time distributions, which are chosen from the appendices A – D as examples of good accordance between observation and prediction. In order to compare the suitability of the models for one experimental curve, the root mean square error is used, which is listed in the appendix J as well. Both model variants are capable of describing the experimental displacement curves in Fig. 65 with root mean square errors of less than 0.02, which means that the mean deviation accounts for less than 2%. This is remarkable because the shapes of the curves take the two extremes, a sigmoid (Fig. 65a) and an asymptotic (Fig. 65b) shape.

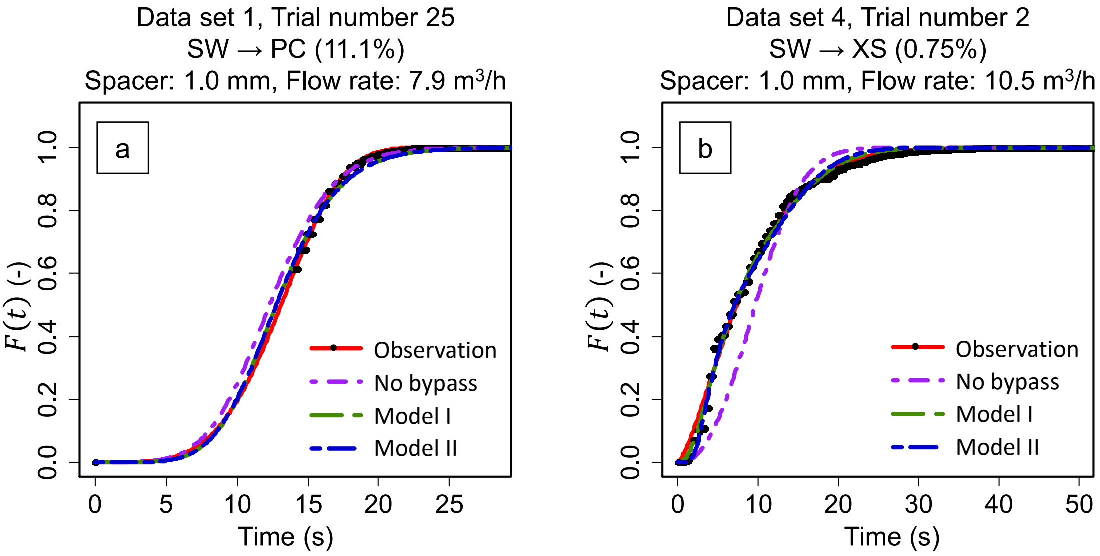

Fig. 65: Good representation of the experimental results by the hybrid models (hybrid model I: stirred-tank bypass, hybrid model II: plug-flow bypass with axial dispersion). Circles and straight lines represent the experimental observation and dashed lines result from the calculations.

Assuming that a curve showing a root mean square error of 5% is still a good approximation, the hybrid model considering the bypass around the spiral-wound membrane as continuous stirred tank (hybrid model I) allows the description of 58% of all experimental curves (appendix J). Considering the model with a plug-flow-bypass (hybrid model II), 75% of all experimental curves can be approximated. Altogether, 83% of the curves can be described with a good accuracy based on at least one of the two variants of the hybrid model. This value is due to the fact that a couple of curves can be approximated by both models, while in other cases only one or none of the two models is applicable with the required accuracy.

Fig. 66 shows two examples visualizing that the models can lead to different results for a given situation. While a plug-flow bypass allows the approximation in Fig. 66a, this model does not provide a good result in Fig. 66b. Again, the two examples represent the two extremes. While the experimental curve in Fig. 66a is nicely sigmoid, the curve in Fig. 66b shows a rather asymptotic shape.

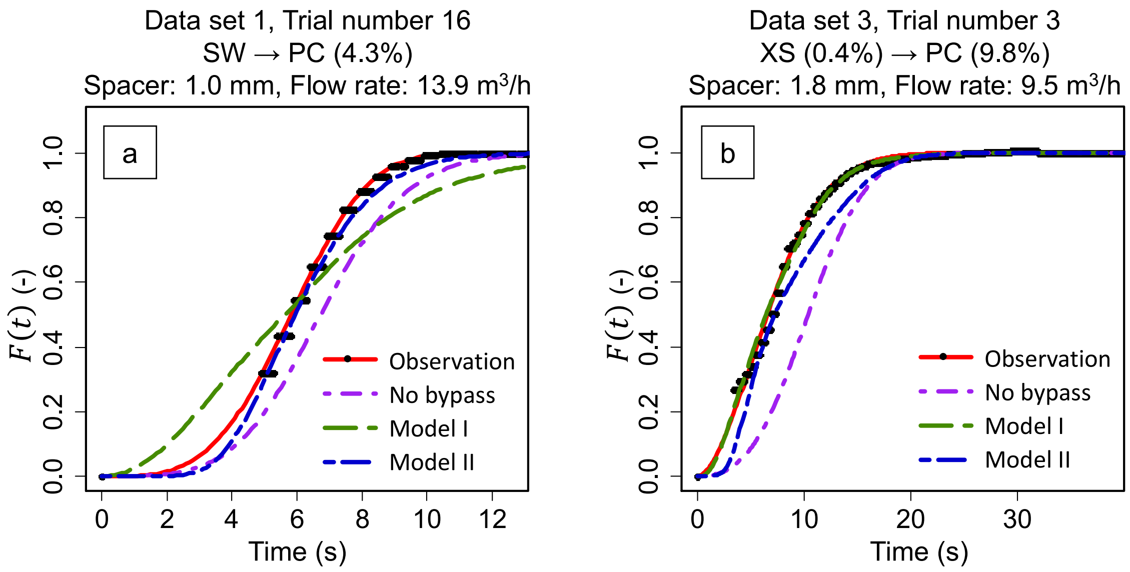

Fig. 66: Good and bad representation of the experimental results by the hybrid models (hybrid model I: stirred-tank bypass, hybrid model II: plug-flow bypass with axial dispersion). Circles and straight lines represent the experimental observation and dashed lines result from the calculations.

urthermore, the necessity of considering deviations from the ideal hydrodynamic behavior by the two variants of the hybrid model becomes clear because the basic model without bypass does not provide an accurate description of the observed curves. However, there are still experimental curves for which the deviations are very large as shown in Fig. 67. Here, the experimental curves cannot be approximated sufficiently by neither of the model variants, which is remarkable as the curve shapes are not exceptional.

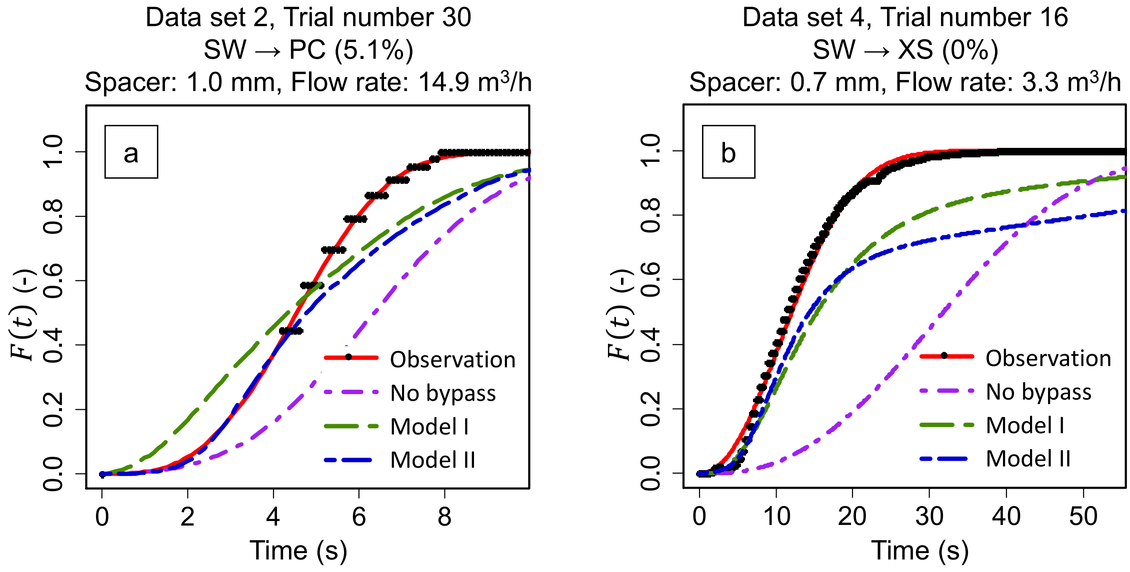

Fig. 67: Bad representation of the experimental results by the hybrid models (hybrid model I: stirred-tank bypass, hybrid model II: plug-flow bypass with axial dispersion). Circles and straight lines represent the experimental observation and dashed lines result from the calculations.

In Fig. 67a, the root mean square errors for the two model variants are 10.3% (hybrid model I) and 9.4% (hybrid model II). The examples in Fig. 67b even show root mean square errors of 15.7% (hybrid model I) and 20.6% (hybrid model II). The reasons entailing such lacks of fit could not be identified so far.

For practical reasons, it is expedient to know which model works better in which case. It turns out that the suitability of the models depends largely on the shape of the curves. This can be quantified by the shape parameter of the Weibull distribution (Fig. 54). The shape parameter indicates sigmoid shapes by high and asymptotic shapes by low values. In Fig. 68, the difference of the root mean square errors ($RMSE_I - RMSE_{II}$) for the two variants of the hybrid model considering the bypass as continuous stirred tank (hybrid model I) or as plug flow with axial dispersion (hybrid model II) are plotted against the shape parameter of the Weibull distribution. It is visible that hybrid model I describes asymptotic shapes better than hybrid model II as the differences are negative. In contrast, considering the bypass as a plug flow reactor with axial dispersion improves the approximation of the calculated curve to rather sigmoid experimental curves. Thus, as soon as the shape parameter is greater than roughly 2.5, the applicability of hybrid model II is superior compared to that of hybrid model I.

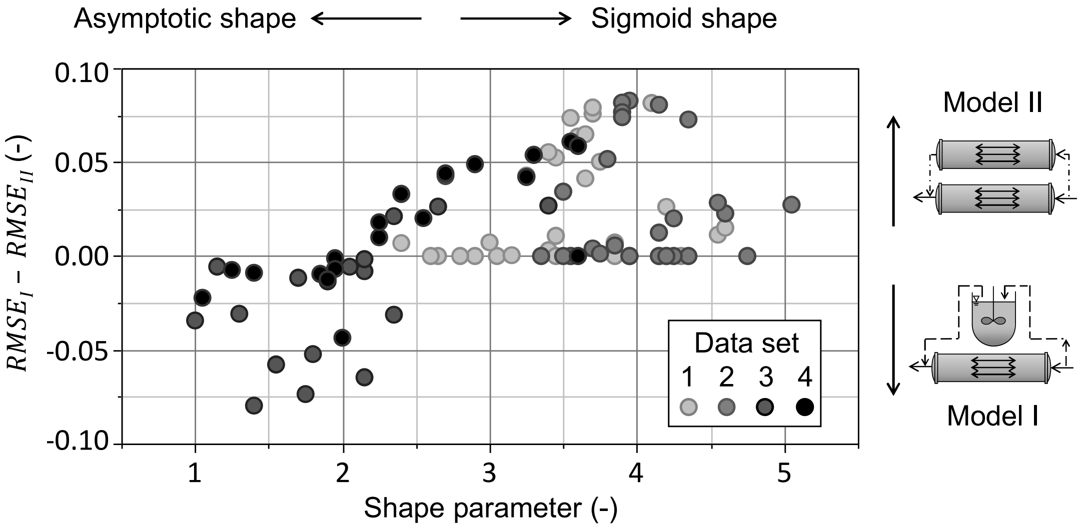

Fig. 68: Relationship between the difference in root mean square errors ($RMSE$) for the hybrid models (hybrid model I: stirred-tank bypass, hybrid model II: plug-flow bypass with axial dispersion) and the shape parameter of the Weibull distribution.

Considering the source of the data points indicated by the color code in Fig. 68, it becomes obvious that all observed displacement curves from data set 1 and 2 show a sigmoid shape and that hybrid model II leads to the best approximation in these cases. In contrast, hybrid model I works better as soon as xanthan solution serve either as model product or as displacing fluid (data set 3 and 4).

Summarizing the results, 83% of the observed displacement curves can be described with a mean deviation of less than 5%, which is why the applicability of the models can be considered as good. As this thesis focuses on the displacement of fluids from spiral-wound membranes, the factors influencing the axial dispersion coefficients in the spiral-wound membrane and the bypass volume flow around the module are subject of the next chapter. In contrast, the axial dispersion coefficients in the pipes as well as the magnitude of the short-circuit flows before and after the membrane modules will not be considered in the following but can be found in the appendix J.

8 Practical relevance of the mechanistic models

The mechanistic models ought to improve the understanding of the hydrodynamics and to allow the quantification of the dispersion during the displacement process. Therefore, different models are applied to describe the experimental displacement curves in the preceding sections. It is assumed that the most accurate model represents the hydrodynamic processes prevailing in the spiral-wound membrane section during the displacement in the best way. The direct comparison of the models with regard to their ability to approximate the experimental displacement curves allows the choice of the best model for characterizing the hydrodynamics.

For the following calculations, all experimental observations were used. The results can be accessed in the appendix M.

8.1 Comparison of the models

The comparison of the models with regard to their ability to approximate the experimental displacement curves in Fig. 69 is based on the root mean square error. The horizontal corners of the confidence diamonds indicate the position of the mean values and the vertical corners give the 95% confidence interval of the means.

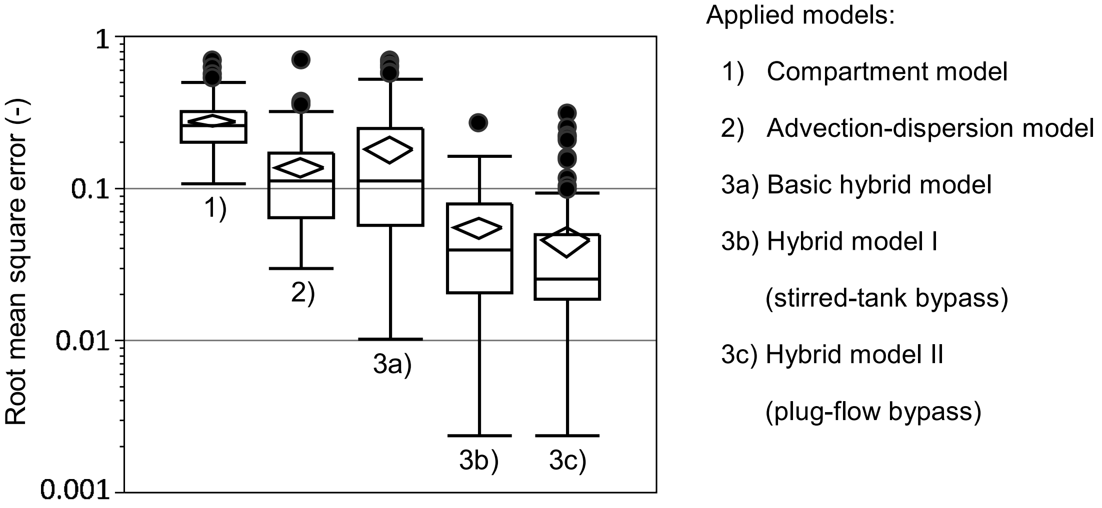

Fig. 69: Model comparison based on the outlier box plots of the root mean square errors. Confidence diamonds indicate the mean (horizontal edges) and the 95% confidence interval (vertical edges).

As expected, the compartment model (1) leads to the worst representation of the measured curves as it shows the highest root mean square errors. The reason is that the model does not consider important process parameters such as the fluid viscosity and lacks furthermore variability. The application of the advection-dispersion model (2) results in both good and bad approximations. While the displacement of low viscosity fluids at high flow rates can be described with a high accuracy, the model fails reliably for the inverse case. The same applies for the basic hybrid model (3a) as well. Nevertheless, the consideration of axial dispersion in the spiral-wound membrane and the pipes clearly improves the applicability of this model compared to the basic compartment model (1). However, the hydrodynamic processes in the experimental setup seem not to be represented accurately enough by the model. The best approximation of the observed displacement curves is possible based on the two variants of the hybrid model (3b and c). Referring to the mean values of the root mean square errors, there is no significant difference between the two model variants (model 3b and c) because the confidence diamonds overlap. However, Fig. 68 shows that hybrid model I leads to better results for asymptotic curves and that hybrid model II is advantageous in case of sigmoid displacement curves.

The focus of the preceding sections is on the description of the residence time distributions observed during displacement experiments. Therefore, the axial dispersion coefficients and the volume shares determining the magnitude of the main streams are adapted as fitting parameters. In order to learn more about the hydrodynamics in and around the spiral-wound membranes, the two variants of the hybrid model (model 3b and c) are used to quantify the axial dispersion coefficient in the spiral-wound membrane and the bypass flow around the module as a function of the process conditions in the following.

8.2 Characterization of the hydrodynamics in spiral-wound membranes

The Péclet numbers or the axial dispersion coefficients derived from the advection-dispersion model in section 7.2 can be interpreted as a measure for the dispersion along the entire length of the experimental setup. In contrast, using the mechanistic models in section 7.3, the assessed axial dispersion coefficients describe exclusively the axial dispersion in the spiral-wound membrane. Considering future applications and the examination of the processes during the displacement of non-Newtonian fluids from spiral-wound membranes, a prediction model for the axial dispersion coefficient is a useful tool.

8.2.1 Presentation of the approach

A basic prerequisite for obtaining an accurate statistical prediction model is an orthogonal and balanced data set because these properties are decisive for the success of the modelling. A data set is orthogonal with regard to the main effects and balanced if the respective regression coefficients can be estimated independently of each other and if the data set comprises an equal number of realizations for each factor level. Considering the list of experiments (appendix J) for which an accurate model could be found ($RMSE$ < 5%), it becomes clear that the prerequisite of a balanced data set is not met.

In order to clarify the relationships between the process conditions and the axial dispersion coefficient in the spiral-wound membrane nevertheless, a new custom design of experiments is created, which can be found in the appendix K.

The data set contains the flow rate (3.4 …14.4 m^3/h), the aspect ratio (0.53 … 0.59), the consistency index of the model product (–3.0 … 0.5 Pa·s^n) and the consistency index of the displacing fluid (–3.0 … 0.5 Pa·s^n) as possible influencing factors. The experimental values are drawn from the existing data sets listed in the appendices F – I. Although, an impact of the consistency index of the displacing fluid on the residence time is considered unlikely in section 6.2, it should be checked whether this holds also true for the axial dispersion coefficient.

8.2.2 Description and interpretation of the results

Tab. 7 gives the parameter estimates and the corresponding p-values for the statistical model allowing the prediction of the logarithm of the axial dispersion coefficient in the spiral-wound membranes. Fig. 70 is provided for the visual assessment of the accordance of the model and the observations.

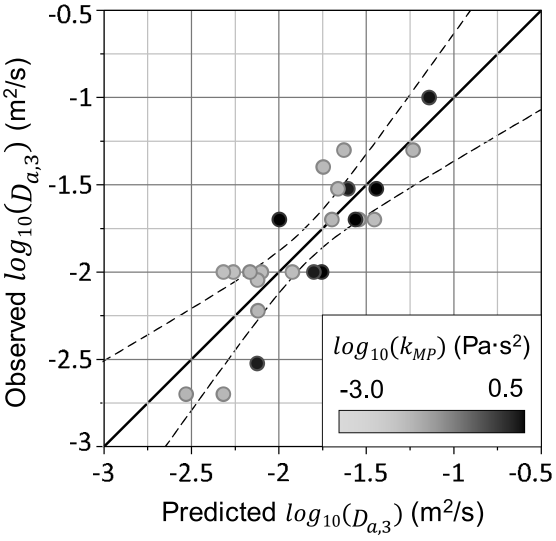

R^2 = 0.73, $RMSE$ = 0.24 s /

Shapiro-Wilk test: W = 0.957, p-value = 0.385

Fig. 70: Parity plot for the axial dispersion coefficient $D_{a,3}$ with 95% confidence interval.

Tab. 7: Parameter estimates and corresponding p-values for the prediction of the logarithm of the axial dispersion coefficient $D_{a,3}$. The arrow (↓) marks model effects considered due to the heredity restriction.

Model

Model effect	Estimate	P-value
$Intercept$	-2.038	$5.068 \cdot 10^{-17}$
$log_{10}(k_{MP})$	$4.113 \cdot 10^{-1}$	$2.096 \cdot 10^{-5}$
$\dot{V}_F$	$1.231 \cdot 10^{-1}$	$6.059 \cdot 10^{-2}$ ↓
${\dot{V}_F}^2$	$2.957 \cdot 10^{-1}$	$2.460 \cdot 10^{-4}$

According to the results of the statistical modelling, the axial dispersion coefficient does only depend on the consistency index of the model product $log_{10}(k_{MP})$ and the flow rate $\dot{V}_F$, while the aspect ratio and the consistency index of the displacing fluid are negligible. Judging based on the Shapiro-Wilk test, the residuals are normally distributed as the p-value indicated in below Fig. 70 is higher than 0.05.

Fig. 71 shows a parity plot containing the data used for modelling (grey, appendix K) and the validation data (black, appendix L). The fact that the validation data is entirely comprised in the 95% prediction interval of the model specified in Tab. 7 indicates that the model possesses general validity to a certain extent.

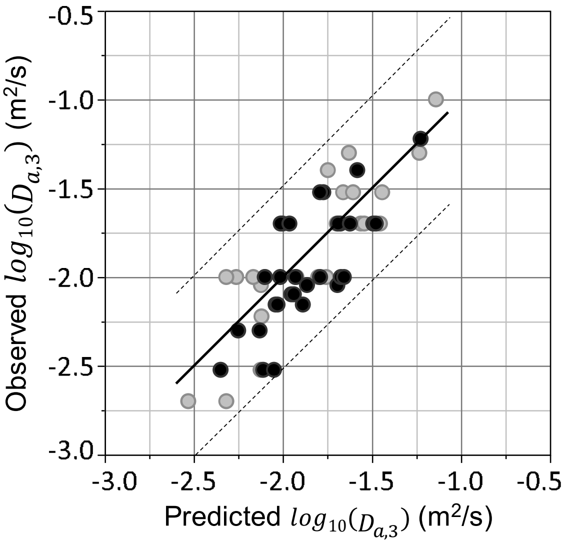

Fig. 71: Validation of the model in Tab. 7. Modelling data points (appendix K) are grey and validation data points (appendix L) are black. Dashed lines indicate the 95% prediction interval for the model.

According to Danckwerts (1953, p. 3861), the dispersion coefficient represents the interaction of the material parameters, such as the fluid viscosity, as well as the flow velocity, and the geometry of the flow channel. However, the model specified in Tab. 7 does not include the aspect ratio characterizing the channel geometry nor the consistency index of the displacing fluid representing its viscosity. This issue is discussed in the following.

8.2.3 Discussion of the results

Unexpectedly, the aspect ratio and the consistency index of the displacing fluid are not comprised in the statistical model specified in Tab. 7, which suggests that these factors do not affect the axial dispersion coefficient in the spacer-filled channels of the spiral-wound membrane. Presumably, the geometric difference between the differently thick spacers and the impact of the displacing fluid's viscosity are not large enough to induce an effect being significantly more pronounced than the signal-to-noise-ratio. Here, it is recalled that the axial dispersion coefficients are no accurate measurement values monitored with a particular sensor. The determination of the axial dispersion coefficients based on the mechanistic models is inherently afflicted with inaccuracies since the calculated residence time curves do not coincide with the experimental observations to 100%. Besides, the viscosity of the xanthan solutions decreases sharply with increasing shear rates as discussed in section 6.2. Thus, the difference between water and xanthan solutions as displacing fluid may be too small to be detected as significant influencing factor. The fact that the aspect ratio and the consistency index of the displacing fluid are not considered in the model is detrimental to the predictive power of the model, however, not unfounded. At least, the impact of the flow rate and the consistency index of the model product on the axial dispersion coefficient can be confirmed doubtlessly by the statistical model (Tab. 7).

In order to analyze the implications of the identified relationships (Tab. 7), Fig. 72a shows the axial dispersion coefficient in the spiral-wound membranes as a function of the consistency index of the model product and the flow rate. Besides, Fig. 72b relates the residence time defined by model 2 in Tab. 5 to these process conditions as well. Hence, Fig. 72 allows to explore possible relationships between the axial dispersion coefficient $D_{a,3}$ in the spiral-wound membrane and the observed residence time.

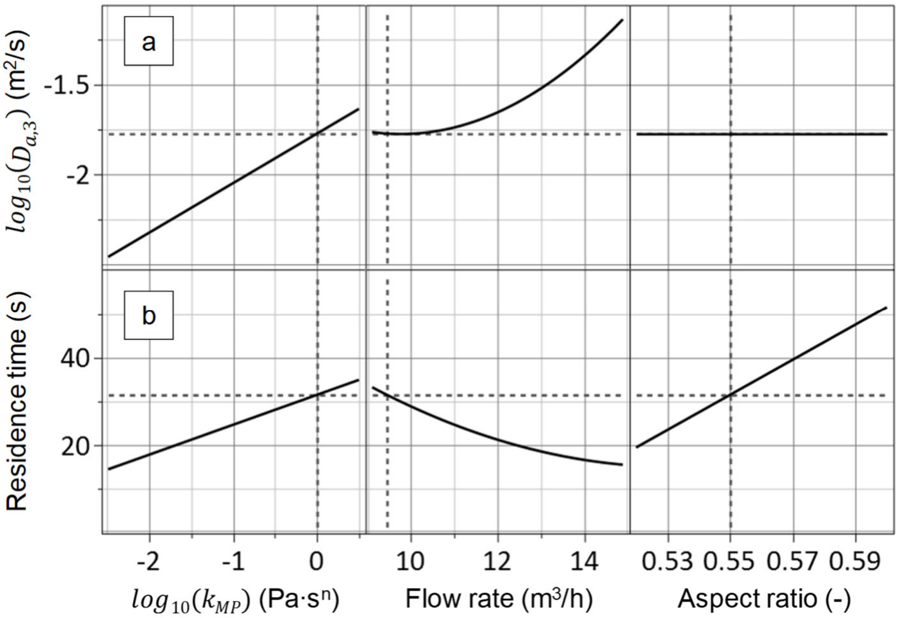

Fig. 72: Visualization of the functional relationships of the a) axial dispersion coefficient $D_{a,3}$ in the spiral-wound membrane and the b) residence time defined by 2 model in Tab. 5 with the consistency index of the model product ($log_{10}(k_{MP})$), the flow rate, and the aspect ratio.

Both responses increase with increasing product viscosities. With regard to the flow rate, however, the trends are inverse. While the axial dispersion coefficient increases with increasing flow rates, the residence time decreases. This latter observation is explained by the increase of the mass transfer at high flow rates, which improves the displacement efficiency. In contrast, the fact that the axial dispersion coefficient increases with increasing flow rates is rather contradictory because this suggest that the mixing in the longitudinal direction increases as well. Intense mixing in the longitudinal direction, however, is expected to have a converse effect on the residence time because it leads to a wide dispersion zone.

Nevertheless, Fig. 73 shows a comparable relationship between the flow rates and the axial dispersion coefficients in spiral-wound membranes derived from the Péclet numbers provided by Gauwbergen and Baeyens (1997, p. 297). For the calculation of the axial dispersion coefficients, it is assumed that the characteristic length comprised in the Péclet number (Eq. 13) equals the module length of 0.32 m. These data are particularly interesting because the authors measure the conductivity signal in the housing immediately behind the spiral-wound membrane, which leads to the axial dispersion coefficients in the spiral-wound membrane by design. Consequently, the relationship shown in Fig. 73 confirms the plausibility of the calculations presented above. Finally, it can only be stated that high flow rates apparently go hand in hand with high axial dispersion coefficients and short residence times.

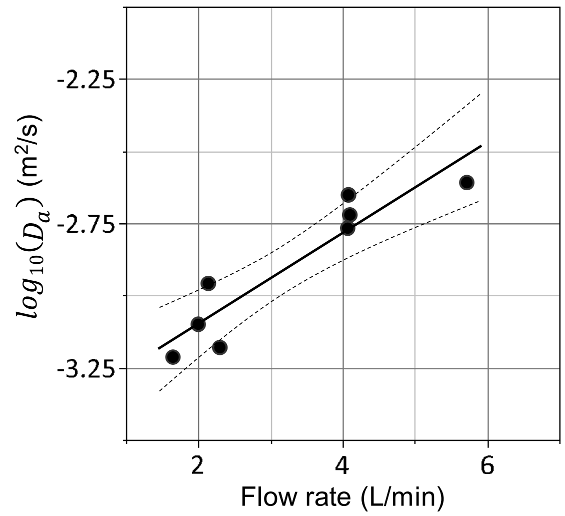

Fig. 73: Relationship between the axial dispersion coefficient D_a (Fig. 11) derived from the results of Gauwbergen and Baeyens (1997, p. 297) and the flow rate. Dashed lines indicate the 95% confidence interval for the fit.

Besides, the amount of the fluid bypassing the spiral-wound membrane depends on the flow rate as well. Concerning the aspect ratio or the flow properties of the fluids, however, no correlations can be observed. Fig. 74 provides the mean values of the bypass flow with the 95% confidence intervals of the means related to the total flow rate. The extent of the bypass flow decreases with decreasing flow rates from approximately 30 to 10% of the total volume flow. This observation can presumably be explained based on the existence of a radial velocity distribution. While the flow directed to the front side of the spiral-wound membrane is relatively even at high flow rates of more 10 m^3/h, there is a radial velocity distribution at low flow rates of about 5 m^3/h.

Considering the velocity distribution shown in Fig. 23, the velocity is lower at the bottom of the housing compared to the top. As the flow velocities are very low compared to the values provided in Fig. 46, this image clearly represents the case of low flow rates.

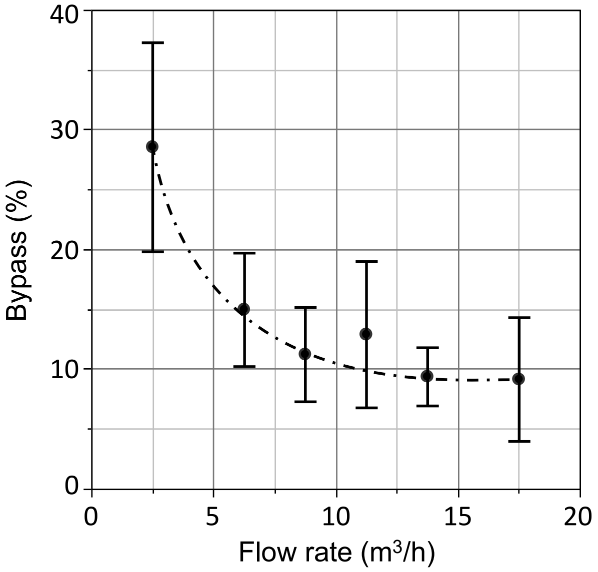

Fig. 74: Mean values of the bypass flow around the spiral-wound membrane on a percentage basis (referred to the total flow rate) as function of flow rate. Error bars indicate the 95% confidence intervals of the mean values. The line is a guide for the eyes.

Thus, the fluid is likely to flow preferentially through the spacer wrap and the gap because the backpressure is lower compared to the center of the module. The results presented so far describe the residence time behavior of a viscous model product during the displacement from only one industrial-scale spiral-wound membrane integrated in a test rig on a pilot scale. For a deviating plant design, however, it is expected that the results are not applicable because the signal monitored at the outlet is affected considerably by the remaining plant components. In order to describe arbitrary membrane plants comprising a multitude of spiral-wound membranes, the mechanistic models can be adapted correspondingly.

8.3 Displacement of protein concentrates from industrial-scale plants

The results presented in the preceding sections are valid for the displacement of a viscous product from one spiral-wound membrane integrated in a housing on a pilot scale as shown in Fig. 49. In industrial applications, however, it is common practice that housings are longer and equipped with a number of membranes in series. In order to extend the practical relevance of the findings, the residence time behavior of a viscous product in housings equipped with four spiral-wound membranes is estimated based on hybrid model II (section 7.3.1).

8.3.1 Presentation of the approach and the expectations

The basis of the following calculations is the hybrid model with a plug-flow bypass (Fig. 61, hybrid model II) adapted to represent a variable number of housings equipped with 4 spiral-wound membranes as depicted in Fig. 75. These housings are composed of eight compartments: The inlet pipe ($C1$), the empty housing section at the inlet ($C2$), four spiral-wound membranes ($C3 - C6$), the empty housing at the outlet ($C7$), and the outlet pipe ($C8$).

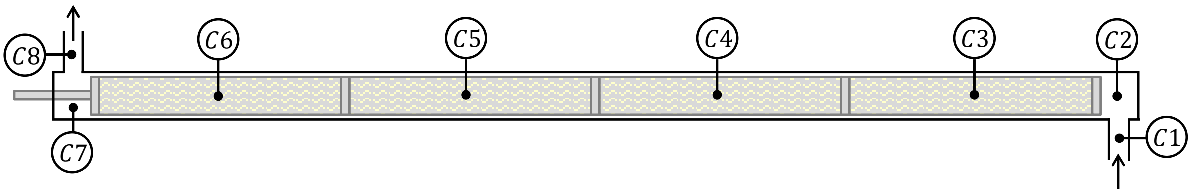

Fig. 75: Schematic representation of an industrial-scale housing.

The length of the pipes ($C1$ and $C8$) is set to 0.5 m each, while the remaining dimensions are considered close enough to reality. The total void volume of one housing is 89.5 L. Equipped with 4 spiral-wound membranes, the void volumes account for 43.4, 49.0, and 54.1 L for the three spacer thicknesses 0.7, 1.0, and 1.8, respectively. For comparison purposes, the required model parameters α_2, α_3, $D_{a,1}$, and $D_{a,3}$ are equal to those found to lead to the best approximation of the model to the experimental data (section 7.3.3, appendix J). $(1 - \alpha_2)$ and $(1 - \alpha_3)$ are the shares of the total volume flow constituting the short-circuit flow ($C2$ and $C7$) and the bypass flow around the membrane modules ($C3 - C6$), respectively. The axial dispersion coefficients in the pipes and in the spiral-wound membranes are denoted as $D_{a,1}$ and $D_{a,3}$.

Considering typical membrane plant designs in the industry, the maximum number of housings connected in series is 3 (Schwinge et al., 2004b, p. 131). Consequently, the displacement of a viscous product from 1, 2, and 3 industrial-scale housings equipped with 4 spiral-wound membranes each is calculated in the following. The calculation is performed in R and can be retraced in the appendix O, while the results can be found in the appendix M.

The aim of this chapter is to assess whether the residence times observed for the pilot-scale experiments are transferable to industrial-scale plant configurations. Therefore, the relative residence time is used, which gives the ratio of the residence times determined for pilot-scale and industrial-scale housings. It is expected that the transferability of the experimental results is limited because the impact of the flow disturbances caused by the design of the inlet and outlet is more pronounced for small housings.

8.3.2 Description and discussion of the results

Fig. 76 shows two exemplary residence time curves for 3 housings equipped with 4 spiral-wound membranes each (dashed lines, 3 x 4 SWM) and the corresponding experimental observations for the pilot-scale plant equipped with 1 module (straight lines, 1 x 1 SWM). The two examples represent a best- (Fig. 76a) and a worst- (Fig. 76b) case scenario. Fig. 76a shows the displacement of a low viscous concentrate by soft water with a high flow rate, while Fig. 76b illustrates the inverse case with a high viscous concentrate and a rather low flow rate.

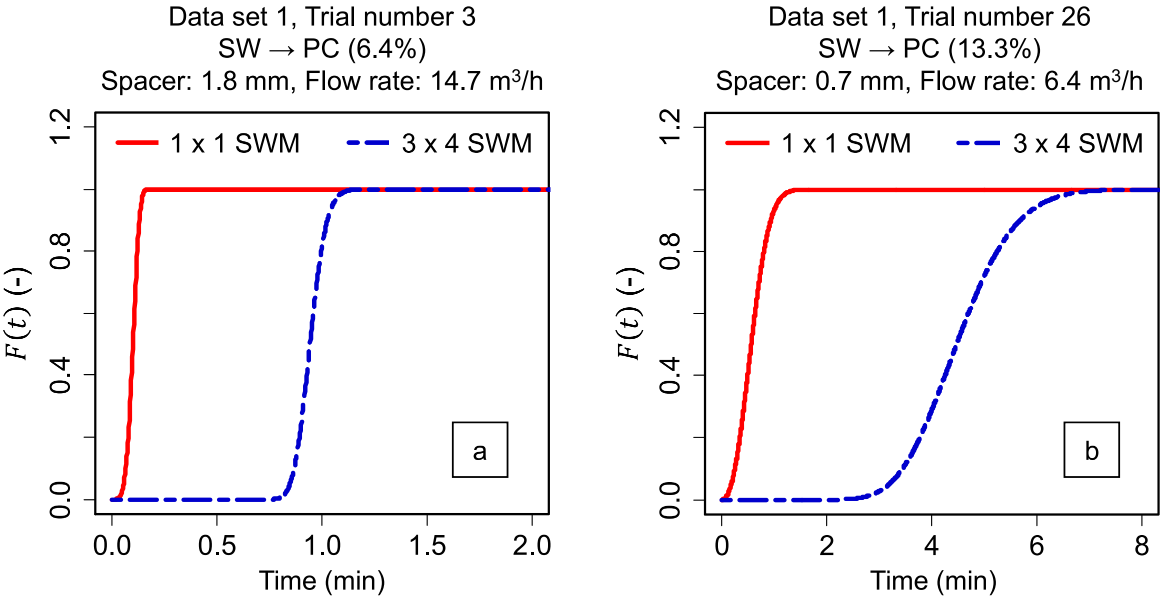

$D_{a,3}$: 0.0001 m²/s, $D_{a,1}$: 0.1 m²/s, short circuit: 15%, bypass: 10%

$D_{a,3}$: 0.04 m²/s, $D_{a,1}$: 0.1 m²/s, short circuit: 80%, bypass: 5%

Fig. 76: Residence time curves for the displacement of milk protein concentrate by soft water at a) a high flow rate and b) a low flow rate. Straight lines represent the experimental observation (1 x 1 SWM), while dashed lines result from the calculations (3 x 4 SWM).

For the best-case scenario, 3 housings are displaced within 66 s, which is very fast as this value is only 1.7 times the hydraulic residence time. For the worst-case scenario, the displacement takes already 5.6 times the hydraulic residence time. For comparison purposes, Fig. 77a gives an overview of the residence times determined for different membrane plant designs including the configurations considered in Fig. 76. While the 25 and 75% quartiles of the residence times (top and bottom of the boxes) are 13 and 27 s for the pilot-scale plant (1 x 1), the corresponding values are 79 and 154 s for 3 housings on an industrial scale (3 x 4). Thus, the examples shown in Fig. 76 do in fact represent best- and worst-case scenarios.

In order to assess whether the residence time of a viscous product in a plant on an industrial scale can be estimated based on an experiment on a pilot scale, the mean values of the relative residences time are considered in Fig. 77b.

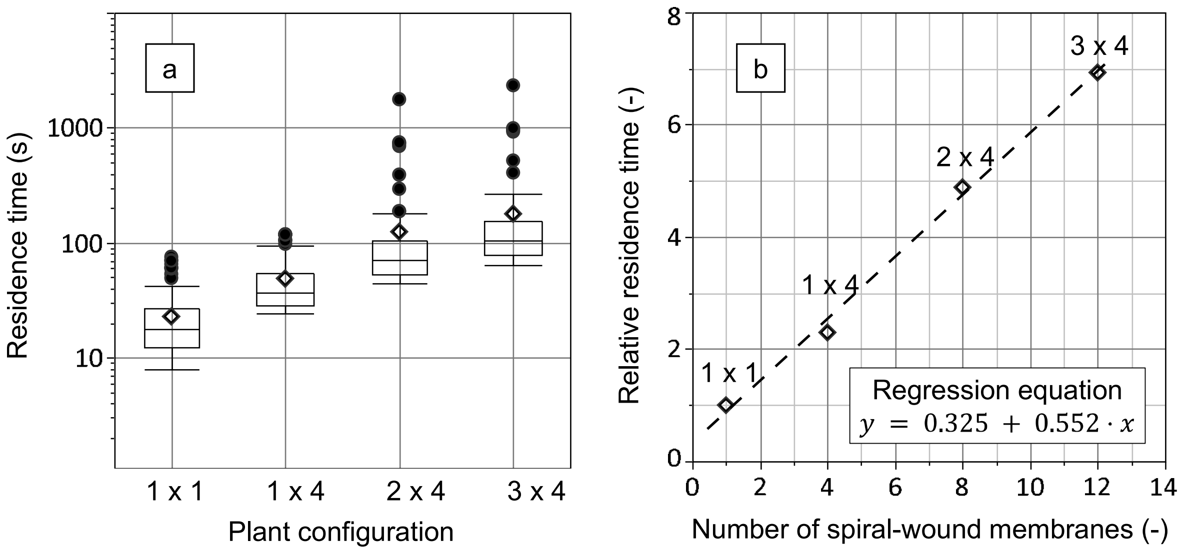

Fig. 77: a) Outlier box plots of the residence times for the displacement of different plant configurations, where the first number denotes the number of housings connected in series and the second number indicates the number of spiral-wound membranes per housing. Filled circles represent outliers and empty diamonds are mean values. b) Mean values of the relative residence times as a function of the number of spiral-wound membranes.

The relative residence time relates the time required for the displacement of 1 or more housings on an industrial-scale to the residence time observed for the test rig on a pilot-scale equipped with only 1 membrane module. Fig. 77b suggests that the displacement of a housing equipped with 4 spiral-wound membranes (1 x 4) does not take 4 times the time required for the displacement of 1 membrane module (1 x 1) as the relative residence time is only 2.3. However, the relative residence time increases linearly with an increasing number of spiral-wound membranes.

8.3.3 Discussion of the results

Comparing the results of the calculations in Fig. 76 with the statistical model in Fig. 42, the same trend can be observed: low product viscosities, high flow rates, and low aspect ratios lead to the shortest residence times. While an unfavorable factor level combination leads to a prolongation of the residence time of a few seconds for the displacement of a single spiral-wound membrane, the same factor level combination can cause a time difference on the order of minutes for the displacement of industrial-scale housings. Consequently, the adaption of the flow rate and the spacer dimensions to the prevailing protein concentration seems to offer the possibility of reducing the residence time to an economically relevant extent.

The consideration of the relative residence time in Fig. 77b shows that summing up the number of membranes and multiplying this value by the residence time observed for pilot-scale experiments with a single spiral-wound membrane is not expedient. The reason is that the relative residence times are smaller than one might expect based on this straightforward computation. However, the liner relationship indicated in Fig. 77b allows an estimation of the residence times to be anticipated for industrial plant configurations based on pilot-scale experiments anyway. Besides this estimation basis, the linear relationship provides information of the hydrodynamics and supports the initial expectation of a limited transferability of the pilot-scale results. The linear relationship between the residence time and the number of spiral-wound membranes implies that the residence time in larger-scale plants depends on the membrane modules in the first place and that the remaining segments barely affect the residence time behavior. This is not improbable because the share of the total plant volume taken up by the membranes is much higher for an industrial-scale plant compared to a pilot-scale plant.

For a final evaluation of the practical applicability of the results it is required to take into account that the permeate valve of an industrial plant needs to exists and to be closed during the displacement. This is necessary because this was the case during the experiments on a pilot scale (section 4.1.1). If the permeate valve is open during the displacement, the flow perpendicular to the membrane is likely to affect the residence time of the product in the plant, which would falsify the results. Furthermore, the calculations do not consider a concentration gradient in the connected housings, which would be the case in industrial multi-stage plants. However, considering a concentration gradient would require more axial dispersion coefficients representing the progressive dilution of the product by water.

Summarizing the above paragraphs, the calculations underline again that it is important to maximize the flow rate during the displacement, particularly in case of high viscous products. Besides, the initial assumption is confirmed that the transferability of results obtained based on pilot-scale experiments to larger-scale setups is limited. However, based on the linear relationship between the relative residence time and the number of spiral-wound membranes, an estimation of the residence time of a product in an industrial-scale plant is possible to a certain extent. Finally, the validation of these results remains to be done by monitoring the residence time behavior of viscous products in an industrial-scale filtration plant equipped with spiral-wound membranes.

9 Summary

The aim of the displacement process is to replace one fluid by another as completely and quickly as possible. Hence, the uncontrolled mixing of the product with the displacing fluid prior to the production (start-up) or the end of working hours (shut-down) is undesired as it is counterproductive. In order to improve the displacement efficiency, understanding the underlying processes is consequently of great importance to plant operators. However, compared to the flow through pipeline systems, the flow through the spacer-filled channels of spiral-wound membranes is very complex. The consequence is that computational fluid dynamics simulations can only cover the hydrodynamics in spacer-filled flat channels, which exhibit evidently severe geometric differences to spiral-wound membranes on an industrial scale. Besides this, food liquids showing non-Newtonian flow properties are not in the focus of the studies since these introduce further complexity.

In order to fill the knowledge gap, this thesis provides results on the displacement of non-Newtonian fluids from spiral-wound membranes on an experimental basis. Therefore, different model products with Newtonian (water) and non-Newtonian (protein concentrates, xanthan solutions) flow properties were displaced from industrial-scale spiral-wound membranes. Depending on the properties of the model product, the displacement progressions were monitored by means of a turbidity or a conductivity sensor. The experiments were carried out according to statistical designs of experiments, where the flow rate, the geometric dimensions of the feed spacer, the viscosity of the product, and the displacing fluid’s temperature and viscosity were varied. In order to draw conclusions from the observations, two different analytical approaches were chosen. On the one hand, statistical models were used to describe the functional relationships between the residence time and the considered factors. On the other hand, mechanistic models were developed and applied, which characterize the hydrodynamic processes leading to the observed residence time distribution curves. Besides a simple compartment model, the advection-dispersion model, and a combination of both models were used. The idea underlying the compartment model is that each section of the experimental setup can be described based on a basic reactor model of little complexity, which represents the hydrodynamic processes to the highest extent possible. For the advection-dispersion model, it is assumed that the displacement can be described by a plug flow superimposed by axial dispersion.

The analysis of the results based on the statistical models indicates that the flow rate, the geometric dimensions of the feed spacer, and the viscosity of the product do affect the residence time, which equals the time required for the displacement process. The temperature and the viscosity of the displacing fluid, however, do not influence the displacement process significantly for the considered process conditions. In order to reduce the residence time, it is recommended to maximize the flow rate and to choose a spacer with a rather low aspect ratio, which is that the spacer filaments are thin compared to the channel height. Concerning the role of the displacing fluid's properties, the signal-to-noise-ratio is considered too low. This means that the deviation of the flow properties from water induced by a higher temperature or the addition of xanthan gum is not large enough to entail a distinctly deviating residence time. Deploying a less shear-thinning displacing fluid of a high viscosity could lead to a stable interface between the involved fluids being clearly reflected by the residence time behavior.

Using the mechanistic models for the interpretation of the observations gives some insights into the hydrodynamic processes during the displacement if they represent the observed residence time distribution curves sufficiently. This is the case for the hybrid model, which is the combination of the compartment and advections-dispersion model. The simple compartment model and the advection-dispersion model, in contrast, do not approximate the measured residence time distribution curves satisfyingly. The hybrid model reveals that all plant components affect the residence time behavior substantially, which means that they need to be considered for the modelling of the residence time distribution. The core area of the spiral-wound membrane can be modelled as a plug flow reactor with axial dispersion combined with a bypass flow around the module.

Due to the good representation of the experimental data, this model is used to describe the residence time behavior of protein concentrates in a membrane plant on an industrial scale. The basis of the calculations is the assumption that each housing is equipped with four membranes. The obtained results suggest strongly that the linear extrapolation of the residence times obtained based on pilot-scale experiments is not possible when considering the displacement of industrial-scale plants. Furthermore, the calculations reinforce the result of the statistical modelling that the flow rate should take maximal values in order to reduce the residence time of a high viscous protein concentrate in the membrane plant.

10 Conclusions and outlook

The observed residence time behavior is a consequence of the interplay of the properties of the involved fluids, the flow rate, and the geometric dimensions of the feed spacer. In order to review the scope of this working assumption, two approaches are taken. Firstly, the response surface methodology is applied to identify the factors actually determining the residence time and the relevant factor interactions. Secondly, mechanistic models are developed to characterize the hydrodynamic processes prevailing during the displacement of non-Newtonian fluids from spiral-wound membranes.

Based on the functional description of the residence times by statistical models, it can be shown that the viscosity of the displaced fluid, the flow rate, and the geometric dimensions of the feed spacers doubtlessly affect the residence time, which denotes the time required to complete the displacement process. Particularly for high viscous products, the maximization of the flow rate allows a minimization of the residence time. Also a low ratio of the filament thickness and the channel height contribute to short residence times rather than the absolute spacer thickness. In contrast, no clear evidence for the influence of the displacing fluid's viscosity or temperature on the residence time could be found. Thus, the displacement of products by high viscous fluids such as xanthan solutions does not reduce the residence time significantly. Conversely, the preparation and the removal of the xanthan solutions from the plant requires additional efforts. Besides, the mixing of the product with xanthan solutions is undesired.

Using a hybrid model, the description of the observed residence time distribution curves is possible with a high accuracy. The model confirms the assumption that the flow pattern in spiral-wound membranes during the displacement process can be described based on the advection-dispersion model. This is that the flow during the displacement of non-Newtonian fluids resembles plug flow with a certain extent of axial dispersion. Furthermore, the model suggests that there exists a considerable bypass flow around the modules affecting the residence time behavior as well. Finally, it is possible to estimate the residence time behavior for an industrial-scale plant equipped with a number of housings containing several spiral-wound membranes based on this mechanistic model.

Altogether, the thesis provides a data basis for the targeted enhancement of the displacement of non-Newtonian fluids from spiral-wound membranes as it presents an idea of the hydrodynamic processes prevailing locally. This knowledge gained based on statistical and mechanistic models can be a starting point for the optimization of the displacement processes and the plant design with regard to reducing the required amount of displacing fluid and to minimizing the losses of valuable product as part of the discarded mixed phase. For instance, improving the fit of the membrane modules in the housings could reduce the amount of fluid bypassing the core area of the spiral-wound membranes. Besides, adapting the flow control at the inlet and outlet of the housings could contribute to a more even velocity distribution in the radial direction. These practical measures are likely to reduce the volume of the mixed phase and thus the water requirements and product losses.

To expand the benefit of the presented considerations, the hybrid model can be used for further applications since it gives the possibility to assess the residence time distribution of arbitrary plants composed of comparable plant sections. By adapting the model accordingly, the comparison of residence time distributions in a multi-stage plant at different process conditions would be possible. In contrast to the cases considered in this thesis, the viscosity of the product increases from the inlet to the outlet of a multi-stage plant. Going even further, the presented results can be linked to prediction models for the filtration process and the pressure drop. The pressure drop is to be considered during the displacement as well because it can provoke the telescoping of the membranes when exceeding certain values. The telescoping is undesired as the membrane leaves are shifted up against each other irreversibly, which is a damage shortening the service life of the spiral-wound membranes. Coupling the models for the residence time distribution with the models for the filtration process and the pressure drop would allow the a priori determination of the most suitable displacement conditions with regard to overall process efficiency and the total service life of the spiral-wound membranes.

11 References

Akaike, H. (1974). A new look at the statistical model identification. IEEE Transactions on Automatic Control, 19(6), 716–723. doi: 10.1109/TAC.1974.1100705

Alexopoulos, A. H., Maggioris, D., Kiparissides, C. (2002). CFD analysis of turbulence non-homogeneity in mixing vessels: A two-compartment model. Chemical Engineering Science, 57(10), 1735–1752

Amiri, A., Larachi, F., Taghavi, S. M. (2016). Buoyant miscible displacement flows in vertical pipe. Physics of Fluids, 28(10), 102–105. doi: 10.1063/1.4965250

Antrim, B., Lesan, R., Liu, B., Gottberg, A. v. (2005). Worlds largest spiral element - history and development. Desalination, 178(1-3), 313–324. doi: 10.1016/j.desal.2004.11.042

Arora, P., Hoadley, A. F. A., Mahajani, S. M., Ganesh, A. (2017). Compartment model for a dual fluidized bed biomass gasifier. Chemical Engineering Research and Design, 117, 274–286. doi: 10.1016/j.cherd.2016.10.025

Bachmann, P., Tsotsas, E. (2015). Analysis of residence time distribution data in horizontal fluidized beds. Procedia Engineering, 102, 790–798. doi: 10.1016/j.proeng.2015.01.190

Beckman, S. L., Barbano, D. M. (2013). Effect of microfiltration concentration factor on serum protein removal from skim milk using spiral-wound polymeric membranes. Journal of Dairy Science, 96(10), 6199–6212. doi: 10.3168/jds.2013-6655

Bouchoux, A., Debbou, B., Gésan-Guiziou, G., Famelart, M.-H., Doublier, J.-L., Cabane, B. (2009). Rheology and phase behavior of dense casein micelle dispersions. The Journal of Chemical Physics, 131(16), 165106(1–11). doi: 10.1063/1.3245956

Brauer, H. (1979). Turbulenz in mehrphasigen Strömungen. Chemie Ingenieur Technik, 51(10), 934–948. doi: 10.1002/cite.330511006

Bucs, S., Radu, A. I., Lavric, V., Vrouwenvelder, J. S., Picioreanu, C. (2014). Effect of different commercial feed spacers on biofouling of reverse osmosis membrane systems: A numerical study. Desalination, 343, 26–37. doi: 10.1016/j.desal.2013.11.007

Bucs, S. S., Linares, R. V., Marston, J. O., Radu, A. I., Vrouwenvelder, J. S., Picioreanu, C. (2015). Experimental and numerical characterization of the water flow in spacer-filled channels of spiral-wound membranes. Water Research, 87, 299–310. doi: 10.1016/j.watres.2015.09.036

Cao, Z., Wiley, D. E., Fane, A. G. (2001). CFD simulations of net-type turbulence promoters in a narrow channel. Journal of Membrane Science, 185(2), 157–176

Carslaw, H. S. (1921). Introduction to the mathematical theory of the conduction of heat in solids, 2nd edition. Macmillan and Co., Limited, London, available online: https://archive.org/details/in.ernet.dli.2015.162384/page/n37, access date: 20.05.2019

Carslaw, H. S., Jaeger, J. C. (1959). Conduction of heat in solids, 2nd edition. Oxford University Press, Oxford. ISBN: 978-0198533030

Carvalho, I. C. de (1986). Über das Fliessverhalten von Ultrafiltrationskonzentraten aus Milch und dessen Abhängigkeit von der Wärmebehandlung und der Tiefkühllagerung, Dissertation, Technische Universität München

Chen, J.-D. (1987). Radial viscous fingering patterns in Hele-Shaw cells. Experiments in Fluids, 5(6), 363–371

Choppe, E., Puaud, F., Nicolai, T., Benyahia, L. (2010). Rheology of xanthan solutions as a function of temperature, concentration and ionic strength. Carbohydrate Polymers, 82(4), 1228–1235. doi: 10.1016/j.carbpol.2010.06.056

Cooley, J. W., Lewis, P., Welch, P. (1967). Application of the fast Fourier transform to computation of Fourier integrals, Fourier series, and convolution integrals. IEEE Transactions on Audio and Electroacoustics, 15(2), 79–84

Curtis, W. D., Logan, J. D., Parker, W. A. (1982). Dimensional analysis and the pi theorem. Linear Algebra and its Applications, 47, 117–126

Da Costa, A. R., Fane, A. G., Fell, C. J., Franken, A. C. (1991). Optimal channel spacer design for ultrafiltration. Journal of Membrane Science, 62(3), 275–291

Dahbi, L., Alexander, M., Trappe, V., Dhont, J. K. G., Schurtenberger, P. (2010). Rheology and structural arrest of casein suspensions. Journal of Colloid and Interface Science, 342(2), 564–570. doi: 10.1016/j.jcis.2009.10.042

Danckwerts, P. V. (1953). Continuous flow systems. Distribution of residence times. Chemical Engineering Science, 50(24), 3857–3866

Dehkordi, A., Memari, M. (2009). Compartment model for steam reforming of methane in a membrane-assisted bubbling fluidized-bed reactor. International Journal of Hydrogen Energy, 34(3), 1275–1291. doi: 10.1016/j.ijhydene.2008.11.076

Delgado, J. M. P. Q. (2006). A critical review of dispersion in packed beds. Heat Mass Transfer, 42(4), 279–310. doi: 10.1007/s00231-005-0019-0

Disley, T., Gharabaghi, B., Mahboubi, A. A., McBean, E. A. (2015). Predictive equation for longitudinal dispersion coefficient. Hydrological Processes, 29(2), 161–172. doi: 10.1002/hyp.10139

Ebach, E. A., White, R. R. (1958). Mixing of fluids flowing through beds of packed solids. American Institute of Chemical Engineers Journal, 4(2), 161–169

Epstein, M., Burelbach, J. P., Fauske, H. K., Kubo, S., Koyama, K. (2001). Liquid–liquid interface stability in accelerating and constant-velocity tube flows. Nuclear Engineering and Design, 210(1-3), 37–51. doi: 10.1016/S0029-5493(01)00437-X

Fischer, H. B. (1973). Longitudinal dispersion and turbulent mixing in open-channel flow. Annual Review of Fluid Mechanics, 5(1), 59–78

Galván, Z. R. N., Soares, L. d. S., Medeiros, E. A. A., Soares, N. d. F. F., Ramos, A. M., Coimbra, J. S. d. R., Oliveira, E. B. d. (2018). Rheological properties of aqueous dispersions ofxanthan gum containing different chloride salts are impacted by both sizes and net electric charges of the cations. Food Biophysics, 13(2), 186–197. doi: 10.1007/s11483-018-9524-9

Gauwbergen, D. van, Baeyens, J. (1997). Macroscopic fluid flow conditions in spiral-wound membrane elements. Desalination, 110(3), 287–299

Gauwbergen, D. van, Baeyens, J. (2000). Macroscopic fluid flow conditions in spiral wound membrane elements: packed bed approach. Water Science and Technology, 41(10-11), 85–91

Geraldes, V., Semião, V., Pinho, M. N. d. (2002). Flow management in nanofiltration spiral wound modules with ladder-type spacers. Journal of Membrane Science, 203(1-2), 87–102. doi: 10.1016/S0376-7388(01)00753-0

Ghosh, A., Balakrishnana, M., Duaa, M., Bhagat, J. J. (2000). Ultrafiltration of sugarcane juice with spiral wound modules: On-site pilot trials. Journal of Membrane Science, 174(2), 205–216. doi: 10.1016/S0376-7388(00)00393-8

Gimmelshtein, M., Semiat, R. (2005). Investigation of flow next to membrane walls. Journal of Membrane Science, 264(1-2), 137–150. doi: 10.1016/j.memsci.2005.04.033

Haaksman, V. A., Siddiqui, A., Schellenberg, C., Kidwell, J., Vrouwenvelder, J. S., Picioreanu, C. (2017). Characterization of feed channel spacer performance using geometries obtained by X-ray computed tomography. Journal of Membrane Science, 522, 124–139. doi: 10.1016/j.memsci.2016.09.005

Hasson, D., Drak, A., Yang, Q. Semiat, R. (2006). Effect of axial dispersion on the concentration polarization level in spiral wound modules. Desalination, 199(1-3), 451–453. doi: 10.1016/j.desal.2006.03.103

Haynes, W. M. ((2016). CRC handbook of chemistry and physics: A ready-reference book of chemical and physical data, 97th edition. CRC Press, Boca Raton, London, New York. ISBN: 9781498754293

Hennico, A., Jacques, G., Vermeulen, T. (1963). Longitudinal dispersion in packed extraction columns. Lawrence Berkeley National Laboratory. LBNL report number: UCRL-10696. available online: https://escholarship.org/uc/item/73w813gv, access date: 16.07.2019

Henningsson, M., Regner, M., Östergren, K., Trägårdh, C., Dejmek, P. (2007). CFD simulation and ERT visualization of the displacement of yoghurt by water on industrial scale. Journal of Food Engineering, 80(1), 166–175. doi: 10.1016/j.jfoodeng.2006.04.058

Hofmann, A. (2018). Physical chemistry essentials, 6th edition. Springer International Publishing. ISBN: 978-3-319-74166-6

Hosseini, S., Danilov, V. A., Vijay, P., Tadé, M. O. (2011). Improved tank in series model for the planar solid oxide fuel cell. Industrial & Engineering Chemistry Research, 50(2), 1056–1069. doi: 10.1021/ie101129k

Hunt, A. G., Skinner, T. E., Ewing, R. P., Ghanbarian-Alavijeh, B. (2011). Dispersion of solutes in porous media. The European Physical Journal B, 80(4), 411–432. doi: 10.1140/epjb/e2011-10805-y

Hutter, C., Zenklusen, A., Lang, R., Rudolf von Rohr, P. (2011). Axial dispersion in metal foams and streamwise-periodic porous media. Chemical Engineering Science, 66(6), 1132–1141. doi: 10.1016/j.ces.2010.12.016

Jakubith, M. (1998). Grundoperationen und chemische Reaktionstechnik: Eine Einführung in die Technische Chemie. Wiley-VCH, Weinheim. ISBN: 3-527-28870-8

Jha, B., Cueto-Felgueroso, L., Juanes, R. (2011). Fluid mixing from viscous fingering. Physical Review Letters, 106(19), 194502(1-4). doi: 10.1103/PhysRevLett.106.194502

Karniadakis, G. E., Mikic, B. B., Patera, A. T. (1988). Minimum-dissipation transport enhancement by flow destabilization: Reynolds' analogy revisited. Journal of Fluid Mechanics, 192, 365–391. doi: 10.1017/S0022112088001909

Katopodes, N. D. (2019). Viscous fluid flow, 324–426. doi: 10.1016/B978-0-12-815489-2.00005-8. In Katopodes (Author) Free-surface flow, Butterworth-Heinemann, ISBN: 978-0-12-815489-2

Kavianipour, O., Ingram, G. D., Vuthaluru, H. B. (2017). Investigation into the effectiveness of feed spacer configurations for reverse osmosis membrane modules using computational fluid dynamics. Journal of Membrane Science, 526, 156–171. doi:10.1016/j.memsci.2016.12.034

Ké, D. D. E., Turcotte, G. (1980). Viscosity of biomaterials. Chemical Engineering Communications, 6(4-5), 273–282

Khayet, M., Abu Seman, M. N., Hilal, N. (2010). Response surface modeling and optimization of composite nanofiltration modified membranes. Journal of Membrane Science, 349(1-2), 113–122. doi: 10.1016/j.memsci.2009.11.031

Kieferle, I., Meintrup, D., Kulozik, U. (2019a). Interrelations between consecutive process steps: Using the example of the displacement of dispersions subsequently to the filtration. Journal of Food Engineering, 155–164. doi: 10.1016/j.jfoodeng.2019.06.002

Kieferle, I., Hiller, K., Kulozik, U., Germann, N. (2019b). Rheological properties of fresh and reconstituted milk concentrates under standard and processing conditions. Journal of Colloid and Interface Science, 458–464. doi: 10.1016/j.jcis.2018.11.048

Kistler, A. L., Vrebalovich, T. (1966). Grid turbulence at large Reynolds numbers. Journal of Fluid Mechanics, 26(1), 37–47. doi: 10.1017/S0022112066001071

Koutsou, C. P., Yiantsios, S. G., Karabelas, A. J. (2009). A numerical and experimental study of mass transfer in spacer-filled channels: Effects of spacer geometrical characteristics and Schmidt number. Journal of Membrane Science, 326(1), 234–251. doi: 10.1016/j.memsci.2008.10.007

Kulozik, U., Kessler, H.-G. (1988). Permeation rate during reverse osmosis of milk influenced by osmotic pressure and deposit formation. Journal of Food Science, 53(5), 1377–1383

Laan, E. T. van der (1958). Letters to the Editors: Notes on the diffusion-type model for longitudinal mixing in flow (Levenspiel and Smith, 1957). Chemical Engineering Science, 7, 187–191

Lau, K. K., Abu Bakar, M. Z., Ahmad, A. L., Murugesan, T. (2009). Feed spacer mesh angle: 3D modeling, simulation and optimization based on unsteady hydrodynamic in spiral wound membrane channel. Journal of Membrane Science, 343(1-2), 16–33. doi: 10.1016/j.memsci.2009.07.001

Levenspiel, O. (1958). Longitudinal mixing of fluids flowing in circular pipes. Industrial & Engineering Chemistry, 50(3), 343–346

Levenspiel, O. (1999). Chemical reaction engineering, 3rd edition. John Wiley & Sons, Inc., New York. ISBN: 9780471254249

Levenspiel, O., Smith, W. K. (1957). Notes on the diffusion-type model for the longitudinal mixing of fluids in flow. Chemical Engineering Science, 6(4-5), 227–235

Lewis, D. J. (1950). The instability of liquid surfaces when accelerated in a direction perpendicular to their planes. II. Proceedings of the Royal Society of London. Series A. Mathematical and Physical Sciences, 202(1068), 81–96

Li, Y., Tung, K. (2008). The effect of curvature of a spacer-filled channel on fluid flow in spiral-wound membrane modules. Journal of Membrane Science, 319(1-2), 286–297. doi: 10.1016/j.memsci.2008.03.069

Li, H., Chen, V. (2010). Chapter 10 - Membrane fouling and cleaning in food and bio-processing: in: Z. F. Cui, H. S. Muralidhara, Membrane Technology, Elsevier, 213–254. doi: 10.1016/B978-1-85617-632-3.00010-0

Mao, Z.-S., Xiong, T., Chen, J. (1998). Residence time distribution of liquid flow in a trickle bed evaluated using FFT deconvolution. Chemical Engineering Communications, 169(1), 223–244. doi: 10.1080/00986449808912730

Mishra, M., Martin, M., Wit, A. d. (2008). Differences in miscible viscous fingering of finite width slices with positive or negative log-mobility ratio. Physical Review E, 78(6), 066306(1-11). doi: 10.1103/PhysRevE.78.066306

Mojab, S. M., Pollard, A., Pharoah, J. G., Beale, S. B., Hanff, E. S. (2014). Unsteady laminar to turbulent flow in a spacer-filled channel. Flow, Turbulence and Combustion, 92(1-2), 563–577. doi: 10.1007/s10494-013-9514-4

Myers, R. H., Montgomery, D. C., Anderson-Cook, C. M. (2009). Response surface methodology: Process and product optimization using designed experiments, 3rd edition. Wiley series in probability and statistics. Wiley, Hoboken, NJ. ISBN: 978-0-470-17446-3

Ogata, A., Banks, R. B. (1961). A solution of the differential equation of longitudinal dispersion in porous media: Fluid movement in earth materials. US Government Printing Office

Pawlowski, J. (1971). Die Ähnlichkeitstheorie in der physikalisch-technischen Forschung: Grundlagen und Anwendung. Springer, Berlin, Heidelberg. ISBN: 3-540-05227-5

Phillips, F. M., Castro, M. C. (2003). Groundwater dating and residence-time measurements, 451–497. doi: 10.1016/B0-08-043751-6/05136-7. In J. I. Drever (Ed.), Treatise on Geochemistry (Vol. 5), Elsevier, ISBN: 0-08-043751-6

Picioreanu, C., Vrouwenvelder, J. S., Loosdrecht, M. C. M. van (2009). Three-dimensional modeling of biofouling and fluid dynamics in feed spacer channels of membrane devices. Journal of Membrane Science, 345(1-2), 340–354. doi: 10.1016/j.memsci.2009.09.024

Prausnitz, J. M., Wilhelm, R. H. (1956). Turbulent concentration fluctuations through electrical conductivity measurements. Review of Scientific Instruments, 27(11), 941–943

Ptaszek, A. (2010). Rheological equation of state for shear-thickening food systems. Journal of Food Engineering, 100(2), 322–328

Ranade, V. V., Kumar, A. (2006). Fluid dynamics of spacer filled rectangular and curvilinear channels. Journal of Membrane Science, 271(1-2), 1–15. doi: 10.1016/j.memsci.2005.07.013

Ransohoff, T. C., Radke, C. J. (1987). Laminar flow of a wetting liquid along the corners of a predominantly gas-occupied noncircular pore. Journal of Colloid and Interface Science, 121(2), 392–401. doi: 10.1016/0021-9797(88)90442-0

Ribadeau-Dumas, B., Grappin, R. (1989). Milk protein analysis. Le Lait, 69(5), 357–416. doi: 10.1051/lait:1989527

Roblet, C., Amiot, J., Lavigne, C., Marette, A., Lessard, M., Jean, J., Ramassamy, C., Moresoli, C., Bazinet, L. (2012). Screening of in vitro bioactivities of a soy protein hydrolysate separated by hollow fiber and spiral-wound ultrafiltration membranes. Food Research International, 46(1), 237–249. doi: 10.1016/j.foodres.2011.11.014

Rott, N. (1990). Note on the history of the Reynolds number. Annual Review of Fluid Mechanics, 22(1), 1–12

Sachs, L. (1992). Angewandte Statistik, 7., völlig neu bearbeitete Auflage. Springer Berlin Heidelberg. ISBN: 9783662057476

Saffman, P. G., Taylor, G. I. (1958). The penetration of a fluid into a porous medium or Hele-Shaw cell containing a more viscous liquid. Proceedings of the Royal Society of London. Series A. Mathematical and Physical Sciences, 245(1242), 312–329

Santos, J., Geraldes, V., Velizarov, S., Crespo, J. G. (2007). Investigation of flow patterns and mass transfer in membrane module channels filled with flow-aligned spacers using computational fluid dynamics (CFD). Journal of Membrane Science, 305(1-2), 103–117. doi: 10.1016/j.memsci.2007.07.036

Schock, G., Miquel, A. (1987). Mass transfer and pressure loss in spiral wound modules. Desalination, 64, 339–352. doi: 10.1016/0011-9164(87)90107-X

Schulenburg, D. A. Graf von der, Vrouwenvelder, J. S., Creber, S., Loosdrecht, M. v., Jing, Y., Johns, M. L. (2008). Nuclear magnetic resonance microscopy studies of membrane biofouling. Journal of Membrane Science, 323(1), 37–44. doi: 10.1016/j.memsci.2008.06.012

Schwinge, J., Wiley, D. E., Fletcher, D. F. (2002a). A CFD study of unsteady flow in narrow spacer-filled channels for spiral-wound membrane modules. Desalination, 146(1), 195–201. doi: 10.1016/S0011-9164(02)00470-8

Schwinge, J., Wiley, D. E., Fletcher, D. F. (2002b). Simulation of the flow around spacer filaments between channel walls. 2. Mass-transfer enhancement. Industrial & Engineering Chemistry Research, 41(19), 4879–4888. doi: 10.1021/ie011015o

Schwinge, J., Wiley, D. E., Fletcher, D. F. (2002c). Simulation of the flow around spacer filaments between narrow channel walls. 1. Hydrodynamics. Industrial & Engineering Chemistry Research, 41(12), 2977–2987. doi: 10.1021/ie010588y

Schwinge, J., Wiley, D. E., Fane, A. G. (2004a). Novel spacer design improves observed flux. Journal of Membrane Science, 229(1-2), 53–61. doi: 10.1016/j.memsci.2003.09.015

Schwinge, J., Neal, P. R., Wiley, D. E., Fletcher, D. F., Fane, A. G. (2004b). Spiral wound modules and spacers - Review and analysis. Journal of Membrane Science, 242(1-2), 129–153. doi: 10.1016/j.memsci.2003.09.031

Schwister, K. (2018). Taschenbuch der Verfahrenstechnik, 5. Auflage. Fachbuchverlag Leipzig im Carl Hanser Verlag, München. ISBN: 978-3-446-44778-3

Schwister, K., Leven, V. (2013). Verfahrenstechnik für Ingenieure: Lehr- und Übungsbuch: Tabellen. Hanser, München. ISBN: 978-3-446-43070-9

Scovazzi, G., Wheeler, M. F., Mikelić, A., Lee, S. (2017). Analytical and variational numerical methods for unstable miscible displacement flows in porous media. Journal of Computational Physics, 335, 444–496. doi: 10.1016/j.jcp.2017.01.021

Shakaib, M., Hasani, S., Mahmood, M. (2009). CFD modeling for flow and mass transfer in spacer-obstructed membrane feed channels. Journal of Membrane Science, 326(2), 270–284. doi: 10.1016/j.memsci.2008.09.052

Shi, B., Marchetti, P., Peshev, D., Zhang, S., Livingston, A. G. (2015). Performance of spiral-wound membrane modules in organic solvent nanofiltration – Fluid dynamics and mass transfer characteristics. Journal of Membrane Science, 494, 8–24. doi: 10.1016/j.memsci.2015.07.044

Siddiqui, A., Lehmann, S., Haaksman, V., Ogier, J., Schellenberg, C., Loosdrecht, M. C. M. van, Kruithof, J. C., Vrouwenvelder, J. S. (2017). Porosity of spacer-filled channels in spiral-wound membrane systems: Quantification methods and impact on hydraulic characterization. Water Research, 119, 304–311. doi: 10.1016/j.watres.2017.04.034

Song, L., Ma, S. (2005). Numerical studies of the impact of spacer geometry on concentration polarization in spiral wound membrane modules. Industrial & Engineering Chemistry Research, 44(20), 7638–7645. doi: 10.1021/ie048795w

Sousa, P., Soares, A., Monteiro, E., Rouboa, A. (2014). A CFD study of the hydrodynamics in a desalination membrane filled with spacers. Desalination, 349, 22–30. doi: 10.1016/j.desal.2014.06.019

Sreedhar, N., Thomas, N., Al-Ketan, O., Rowshan, R., Hernandez, H. H., Abu Al-Rub, R. K., Arafat, H. A. (2018). Mass transfer analysis of ultrafiltration using spacers based on triply periodic minimal surfaces: Effects of spacer design, directionality and voidage. Journal of Membrane Science, 561, 89–98

Steinhauer, T., Lonfat, J., Hager, I., Gebhardt, R., Kulozik, U. (2015). Effect of pH, trans-membrane pressure and whey proteins on the properties of casein micelle deposit layers. Journal of Membrane Science, 493, 452–459. doi: 10.1016/j.memsci.2015.06.007

Sternling, C. V., Scriven, L. E. (1959). Interfacial turbulence: Hydrodynamic instability and the Marangoni effect. American Institute of Chemical Engineers Journal, 5(4), 514–523. doi: 10.1002/aic.690050421

Stevens, K., Fuller, M. (2015). 9 – Thermoregulation and clothing comfort, 117–138. doi: 10.1016/B978-0-85709-538-1.00009-2. In J. McCann, D. Bryson (Eds.), Textile-led Design for the Active Ageing Population, Woodhead Publishing, ISBN: 9780857095381.

Tang, C. Y., Chong, T. H., Fane, A. G. (2011). Colloidal interactions and fouling of NF and RO membranes: A review. Advances in Colloid and Interface science, 164(1-2), 126–143. doi: 10.1016/j.cis.2010.10.007

Taylor, G. I. (1950). The instability of liquid surfaces when accelerated in a direction perpendicular to their planes. I. Proceedings of the Royal Society of London. Series A. Mathematical and Physical Sciences, 201(1065), 192–196. doi: 10.1098/rspa.1950.0052

Taylor, G. I. (1954). The dispersion of matter in turbulent flow through a pipe. Proceedings of the Royal Society of London. Series A. Mathematical and Physical Sciences, 223(1155), 446–468. doi: 10.1098/rspa.1954.0130

Thiess, H., Leuthold, M., Grummert, U., Strube, J. (2017). Module design for ultrafiltration in biotechnology: Hydraulic analysis and statistical modeling. Journal of Membrane Science, 540, 440–453. doi: 10.1016/j.memsci.2017.06.038

Trachsel, F., Günther, A., Khan, S., Jensen, K. F. (2005). Measurement of residence time distribution in microfluidic systems. Chemical Engineering Science, 60(21), 5729–5737. doi: 10.1016/j.ces.2005.04.039

Trinidad, P., Ponce de León, C., Walsh, F. C. (2006). The application of flow dispersion models to the FM01-LC laboratory filter-press reactor. Electrochimica Acta, 52(2), 604–613. doi: 10.1016/j.electacta.2006.05.040

Vélez-Ruiz, J. F., Barbosa-Cánovas, G. V. (1998). Rheological properties of concentrated milk as a function of concentration, temperature and storage time. Journal of Food Engineering, 35(2), 177–190. doi: 10.1016/S0260-8774(98)00019-3

Vitagliano, V., Lyons, P. A. (1956). Diffusion coefficients for aqueous solutions of sodium chloride and barium chloride. Journal of the American Chemical Society, 78, 1549–1552. doi: 10.1021/ja01589a011

Vrouwenvelder, J. S., Bakker, S. M., Cauchard, M., Le Grand, R., Apacandié, M., Idrissi, M., Lagrave, S., Wessels, L. P., van Paassen, J. A. M., Kruithof, J. C., van Loosdrecht, M. C. M. (2007). The membrane fouling simulator: A suitable tool for prediction and characterisation of membrane fouling. Water Science and Technology, 55(8-9), 197–205. doi: 10.2166/wst.2007.259

Wade, L. G. (2006). Organic chemistry, 6th edition. Pearson Prentice Hall, Upper Saddle River, NJ. ISBN: 9780131478718

Wagner, J. (2001). Membrane filtration handbook: Practical tips and hints, 2nd edition. Osmonics, Inc., available online: http://www.soulwaterfilter.com/images/pro6/pdf3/MORE%20INFO.pdf, access date: 03.07.2019

Walenta, W., Kessler, H. G. (1990a). Contribution to the mixing behaviour of non-Newtonian fluids of high viscosity in pipe systems. ZFL - Internationale Zeitschrift für Lebensmittel-technologie, 41(4), 20–25

Walenta, W., Kessler, H. G. (1990b). On the exhausting behaviour of two fluids with different viscosity flowing in series in a pipe. ZFL - Internationale Zeitschrift für Lebensmittel-technologie, 41(11), 62–66

Wang, T., Zhang, Z., Ren, X., Qin, L., Zheng, D., Li, J. (2014). Direct observation of single- and two-phase flows in spacer filled membrane modules. Separation and Purification Technology, 125, 275–283. doi: 10.1016/j.seppur.2014.01.040

Weibull, W. (1951). A statistical distribution function of wide applicability. Journal of Applied Mechanics, 18(3), 293–297

Weinekötter, R., Gericke, H. (1995). Mischen von Feststoffen: Prinzipien, Verfahren, Mischer. Springer Berlin, Heidelberg. ISBN: 978-3-540-58567-1

White, F. M. (2011). Fluid mechanics, 7th edition. McGraw-Hill, New York. ISBN: 978-0-07-352934-9

Wiklund, J., Stading, M., Trägårdh, C. (2010). Monitoring liquid displacement of model and industrial fluids in pipes by in-line ultrasonic rheometry. Journal of Food Engineering, 99(3), 330–337. doi: 10.1016/j.jfoodeng.2010.03.011

Wilde, K. (1978). Wärme- und Stoffübergang in Strömungen: Ein Grundkurs für Studierende und Ingenieure Band 1 Erzwungene und Freie Strömung, 2. Auflage. Steinkopff, Heidelberg. ISBN: 3642723349

Wyatt, N. B., Liberatore, M. W. (2009). Rheology and viscosity scaling of the poly-electrolyte xanthan gum. Journal of Applied Polymer Science, 114(6), 4076–4084. doi: 10.1002/app. 31093

Yianatos, J., Vinnett, L., Panire, I., Alvarez-Silva, M., Díaz, F. (2017). Residence time distribution measurements and modelling in industrial flotation columns. Minerals Engineering, 110, 139–144. doi: 10.1016/j.mineng.2017.04.018

Zeng, Y., Mu, S. J., Lou, S. J., Tartakovsky, B., Guiot, S. R., Wu, P. (2005). Hydraulic modeling and axial dispersion analysis of UASB reactor. Biochemical Engineering Journal, 25(2), 113–123. doi: 10.1016/j.bej.2005.04.024

Zimmerer, C. C., Kottke, V. (1996). Effects of spacer geometry on pressure drop, mass transfer, mixing behavior, and residence time distribution. Desalination, 104(1-2), 129–134. doi: 10.1016/0011-9164(96)00035-5

12 Appendix

A. Displacement curves for data set 1 (SW → PC)

The diagrams contain the raw signals (raw data) monitored during the displacement experiments, the approximation by the cumulative Weibull distribution function (Weibull fit), and the results of the hybrid models visualized in Fig. 60 and Fig. 61 (section 7.3).

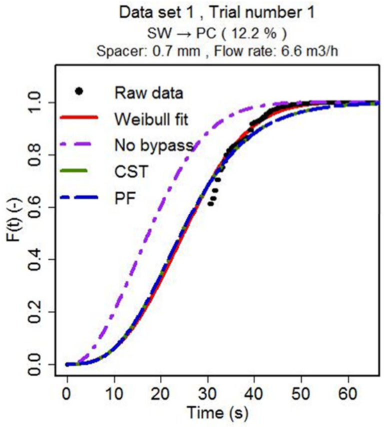

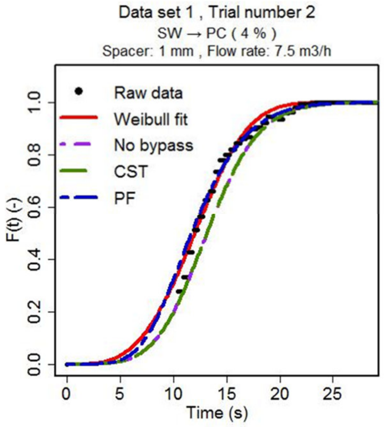

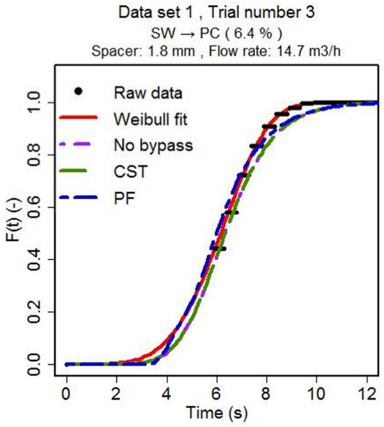

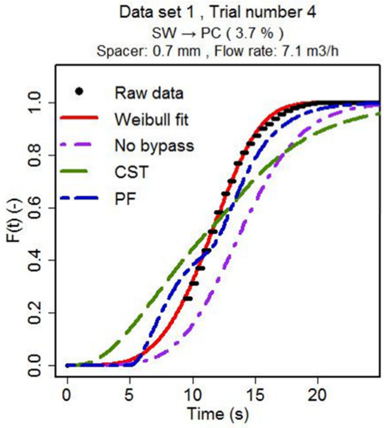

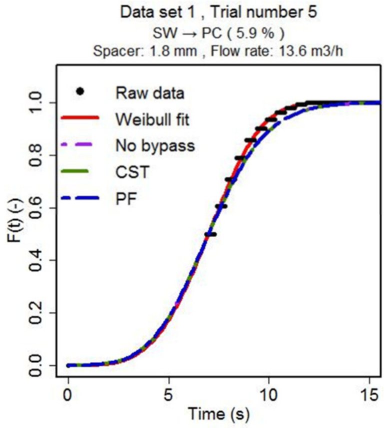

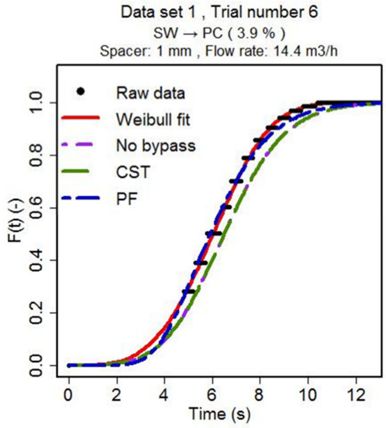

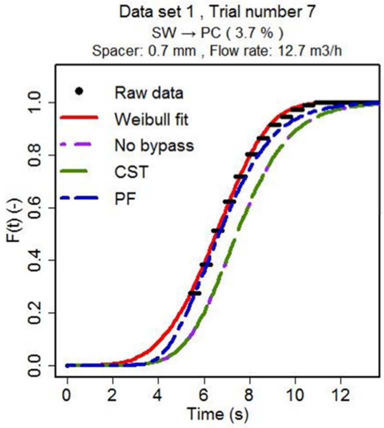

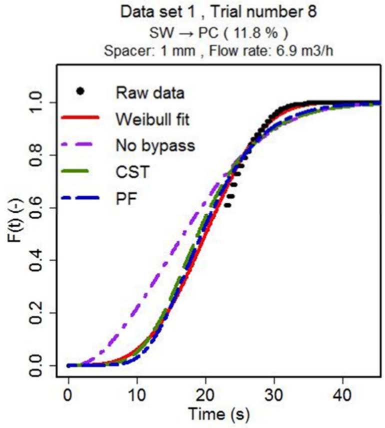

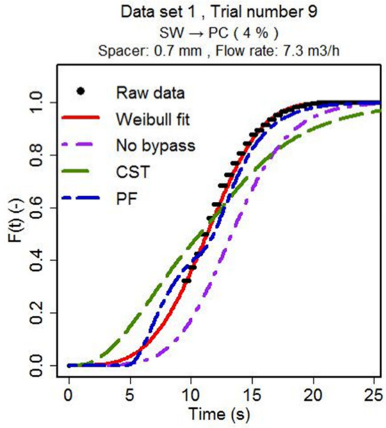

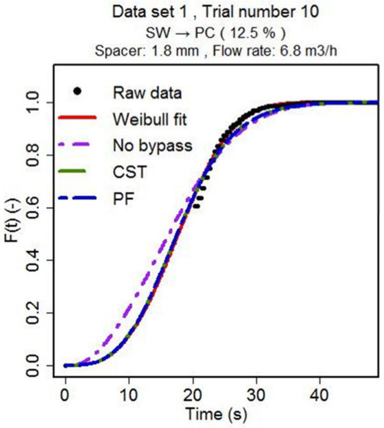
Data set 1 , Trial number 10
SW → PC (12.5 %)
Spacer: 1.8 mm , Flow rate: 6.8 m3/h
Raw data
Weibull fit
No bypass
CST
PF
F(t) (-)
0.0
0.2
0.4
0.6
0.8
1.0
0
10
20
30
40
Time (s)

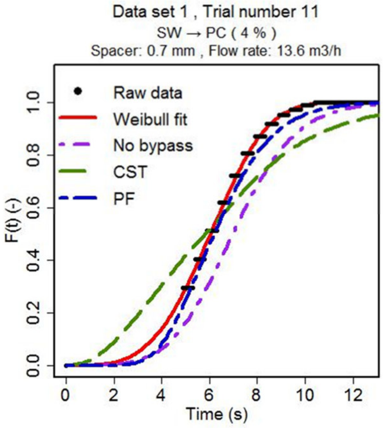
Data set 1 , Trial number 11
SW → PC (4 %)
Spacer: 0.7 mm , Flow rate: 13.6 m3/h
Raw data
Weibull fit
No bypass
CST
PF
F(t) (-)
0.0
0.2
0.4
0.6
0.8
1.0
0
2
4
6
8
10
12
Time (s)

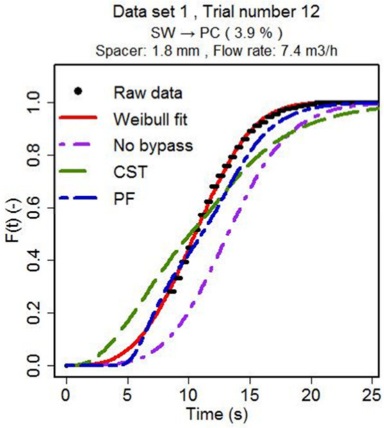
Data set 1 , Trial number 12
SW → PC (3.9 %)
Spacer: 1.8 mm , Flow rate: 7.4 m3/h
Raw data
Weibull fit
No bypass
CST
PF
F(t) (-)
0.0
0.2
0.4
0.6
0.8
1.0
0
5
10
15
20
25
Time (s)

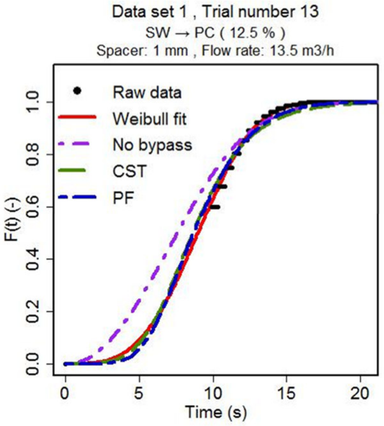
Data set 1 , Trial number 13
SW → PC (12.5 %)
Spacer: 1 mm , Flow rate: 13.5 m3/h
Raw data
Weibull fit
No bypass
CST
PF
F(t) (-)
0.0
0.2
0.4
0.6
0.8
1.0
0
5
10
15
20
Time (s)

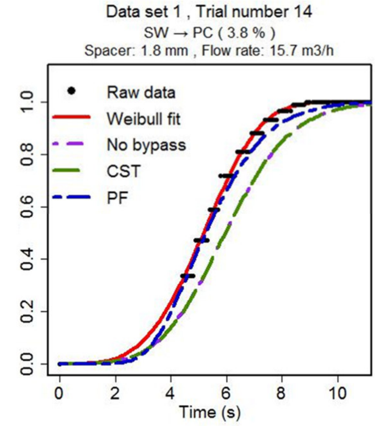
Data set 1 , Trial number 14
SW → PC (3.8 %)
Spacer: 1.8 mm , Flow rate: 15.7 m3/h
Raw data
Weibull fit
No bypass
CST
PF
F(t) (-)
0.0
0.2
0.4
0.6
0.8
1.0
0
2
4
6
8
10
Time (s)

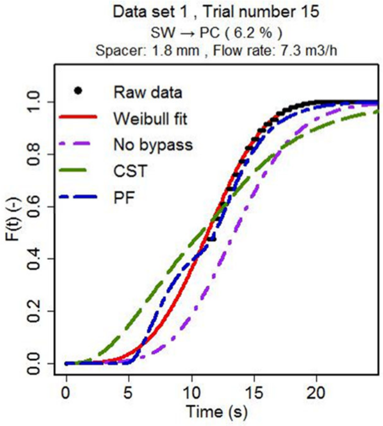
Data set 1 , Trial number 15
SW → PC (6.2 %)
Spacer: 1.8 mm , Flow rate: 7.3 m3/h
Raw data
Weibull fit
No bypass
CST
PF
F(t) (-)
0.0
0.2
0.4
0.6
0.8
1.0
0
5
10
15
20
Time (s)

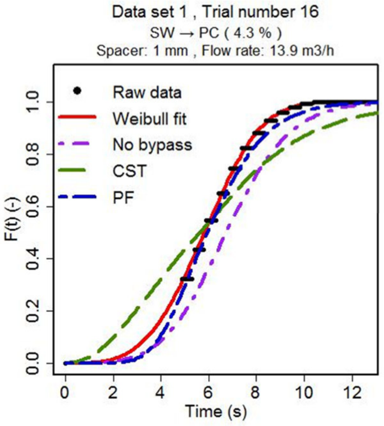
Data set 1 , Trial number 16
SW → PC (4.3 %)
Spacer: 1 mm , Flow rate: 13.9 m3/h
Raw data
Weibull fit
No bypass
CST
PF
F(t) (-)
0.0
0.2
0.4
0.6
0.8
1.0
0
2
4
6
8
10
12
Time (s)

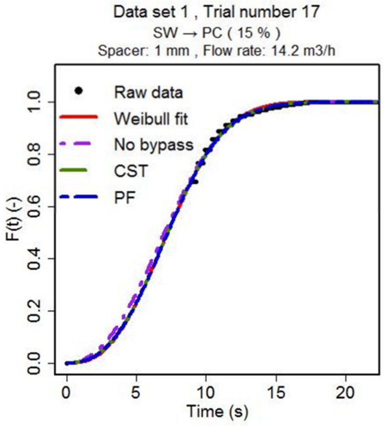
Data set 1 , Trial number 17
SW → PC (15 %)
Spacer: 1 mm , Flow rate: 14.2 m3/h
Raw data
Weibull fit
No bypass
CST
PF
F(t) (-)
0.0
0.2
0.4
0.6
0.8
1.0
0
5
10
15
20
Time (s)

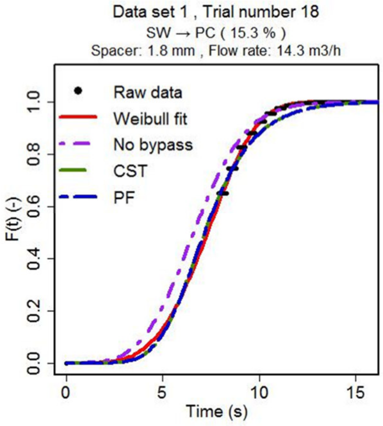
Data set 1 , Trial number 18
SW → PC (15.3 %)
Spacer: 1.8 mm , Flow rate: 14.3 m3/h
Raw data
Weibull fit
No bypass
CST
PF
F(t) (-)
0.0
0.2
0.4
0.6
0.8
1.0
0
5
10
15
Time (s)

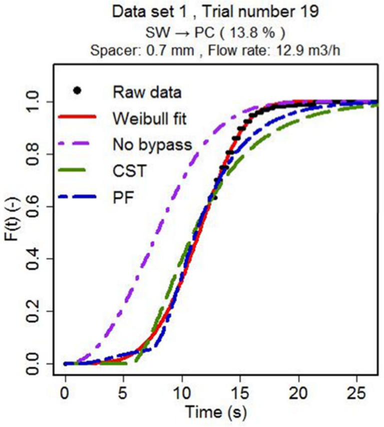
Data set 1 , Trial number 19
SW → PC (13.8 %)
Spacer: 0.7 mm , Flow rate: 12.9 m3/h
Raw data
Weibull fit
No bypass
CST
PF
F(t) (-)
0.0
0.2
0.4
0.6
0.8
1.0
0
5
10
15
20
25
Time (s)

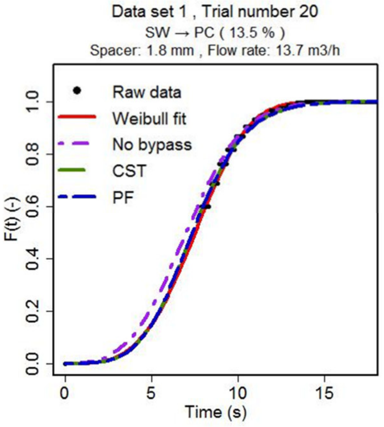
Data set 1 , Trial number 20
SW → PC (13.5 %)
Spacer: 1.8 mm , Flow rate: 13.7 m3/h
Raw data
Weibull fit
No bypass
CST
PF
F(t) (-)
0.0
0.2
0.4
0.6
0.8
1.0
0
5
10
15
Time (s)

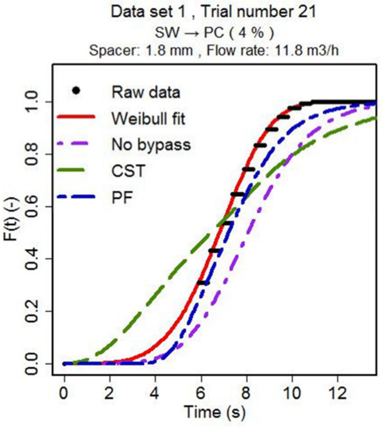
Data set 1 , Trial number 21
SW → PC (4 %)
Spacer: 1.8 mm , Flow rate: 11.8 m3/h
Raw data
Weibull fit
No bypass
CST
PF
F(t) (-)
0.0
0.2
0.4
0.6
0.8
1.0
0
2
4
6
8
10
12
Time (s)

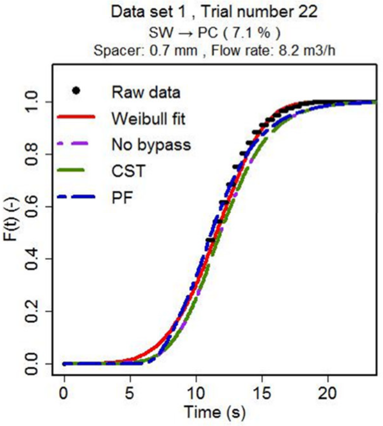
Data set 1 , Trial number 22
SW → PC (7.1 %)
Spacer: 0.7 mm , Flow rate: 8.2 m3/h
Raw data
Weibull fit
No bypass
CST
PF
F(t) (-)
0.0
0.2
0.4
0.6
0.8
1.0
0
5
10
15
20
Time (s)

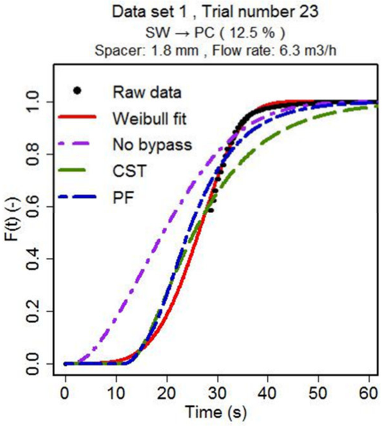
Data set 1 , Trial number 23
SW → PC (12.5 %)
Spacer: 1.8 mm , Flow rate: 6.3 m3/h
Raw data
Weibull fit
No bypass
CST
PF
F(t) (-)
0.0
0.2
0.4
0.6
0.8
1.0
0
10
20
30
40
50
60
Time (s)

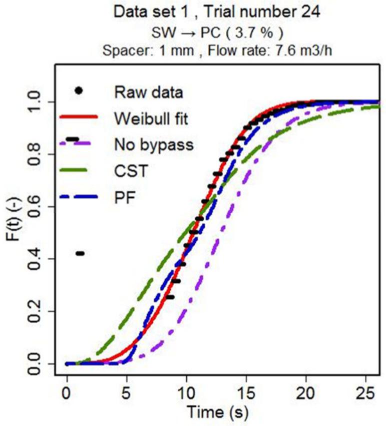
Data set 1 , Trial number 24
SW → PC (3.7 %)
Spacer: 1 mm , Flow rate: 7.6 m3/h
Raw data
Weibull fit
No bypass
CST
PF
F(t) (-)
0.0
0.2
0.4
0.6
0.8
1.0
0
5
10
15
20
25
Time (s)

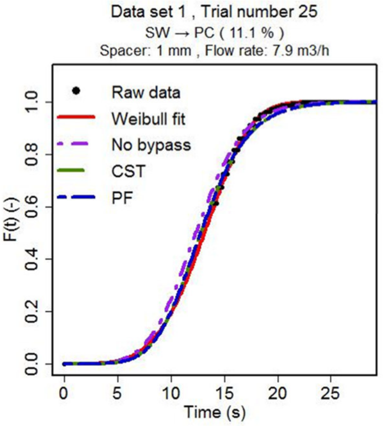
Data set 1 , Trial number 25
SW → PC (11.1 %)
Spacer: 1 mm , Flow rate: 7.9 m3/h
Raw data
Weibull fit
No bypass
CST
PF
F(t) (-)
0.0
0.2
0.4
0.6
0.8
1.0
0
5
10
15
20
25
Time (s)

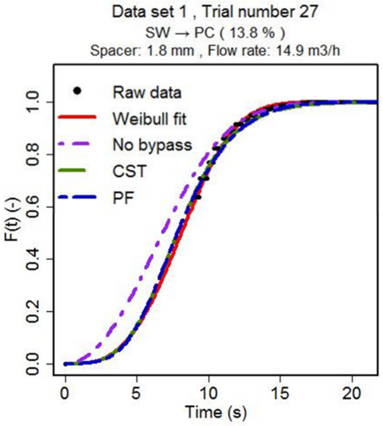
Data set 1 , Trial number 27
SW → PC (13.8 %)
Spacer: 1.8 mm , Flow rate: 14.9 m3/h
Raw data
Weibull fit
No bypass
CST
PF
F(t) (-)
0.0
0.2
0.4
0.6
0.8
1.0
0
5
10
15
20
Time (s)

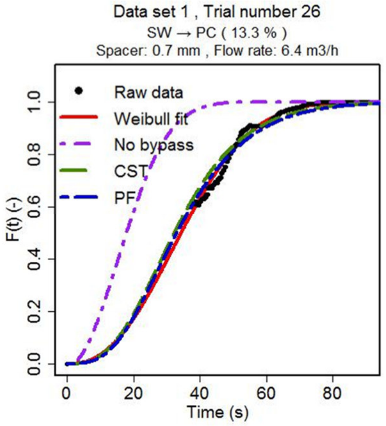
Data set 1 , Trial number 26
SW → PC (13.3 %)
Spacer: 0.7 mm , Flow rate: 6.4 m3/h
Raw data
Weibull fit
No bypass
CST
PF
F(t) (-)
0.0
0.2
0.4
0.6
0.8
1.0
0
20
40
60
80
Time (s)

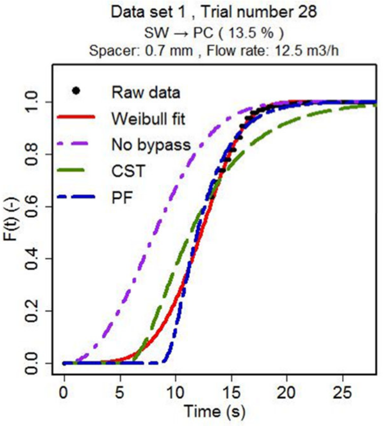
Data set 1 , Trial number 28
SW → PC (13.5 %)
Spacer: 0.7 mm , Flow rate: 12.5 m3/h
Raw data
Weibull fit
No bypass
CST
PF
F(t) (-)
0.0
0.2
0.4
0.6
0.8
1.0
0
5
10
15
20
25
Time (s)

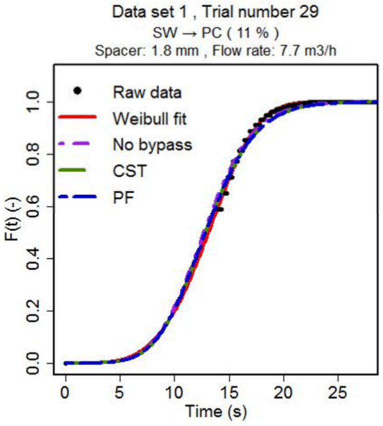
Data set 1 , Trial number 29
SW → PC (11 %)
Spacer: 1.8 mm , Flow rate: 7.7 m3/h
Raw data
Weibull fit
No bypass
CST
PF
F(t) (-)
0.0
0.2
0.4
0.6
0.8
1.0
0
5
10
15
20
25
Time (s)

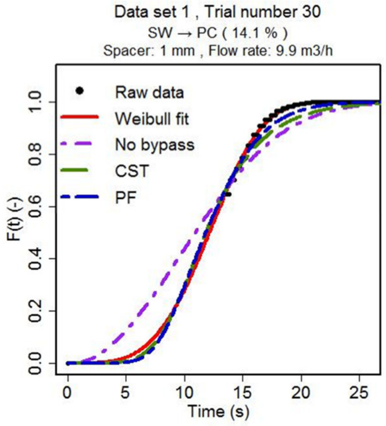
Data set 1 , Trial number 30
SW → PC (14.1 %)
Spacer: 1 mm , Flow rate: 9.9 m3/h
Raw data
Weibull fit
No bypass
CST
PF
F(t) (-)
0.0
0.2
0.4
0.6
0.8
1.0
0
5
10
15
20
25
Time (s)

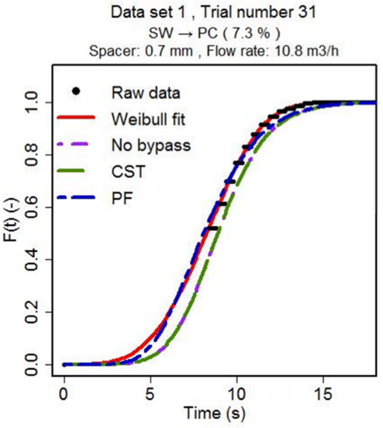
Data set 1 , Trial number 31
SW → PC (7.3 %)
Spacer: 0.7 mm , Flow rate: 10.8 m3/h
Raw data
Weibull fit
No bypass
CST
PF
F(t) (-)
0.0
0.2
0.4
0.6
0.8
1.0
0
5
10
15
Time (s)

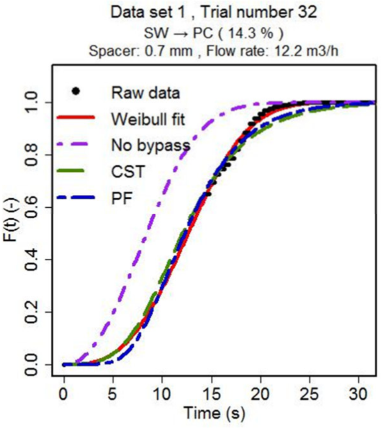
Data set 1 , Trial number 32
SW → PC (14.3 %)
Spacer: 0.7 mm , Flow rate: 12.2 m3/h
Raw data
Weibull fit
No bypass
CST
PF
F(t) (-)
0.0
0.2
0.4
0.6
0.8
1.0
0
5
10
15
20
25
30
Time (s)

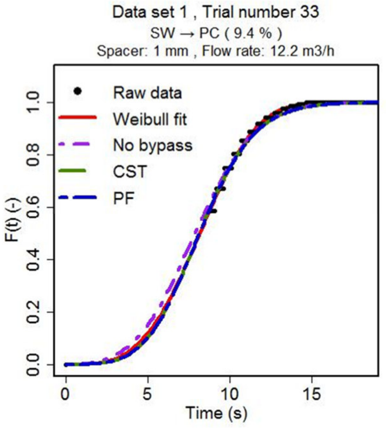
Data set 1 , Trial number 33
SW → PC (9.4 %)
Spacer: 1 mm , Flow rate: 12.2 m3/h
Raw data
Weibull fit
No bypass
CST
PF
F(t) (-)
0.0
0.2
0.4
0.6
0.8
1.0
0
5
10
15
Time (s)

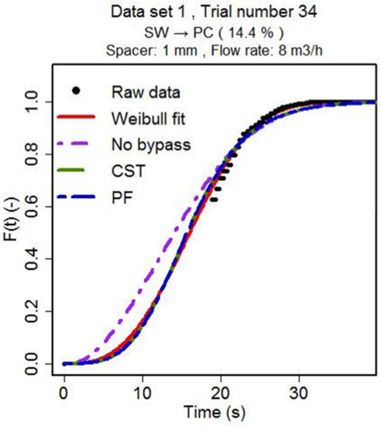

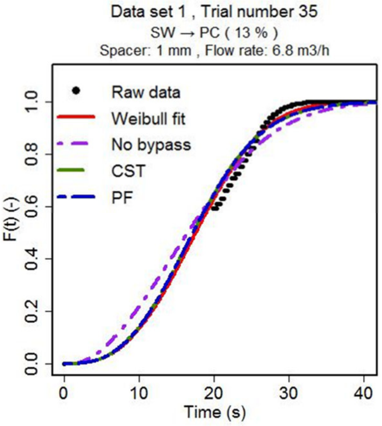

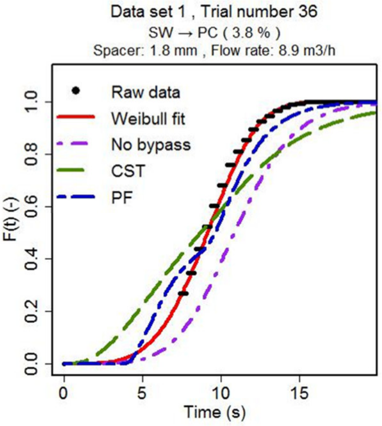

B. Displacement curves for data set 2 (SW → PC)

The diagrams contain the raw signals (raw data) monitored during the displacement experiments, the approximation by the cumulative Weibull distribution function (Weibull fit), and the results of the hybrid models visualized in Fig. 60 and Fig. 61 (section 7.3).

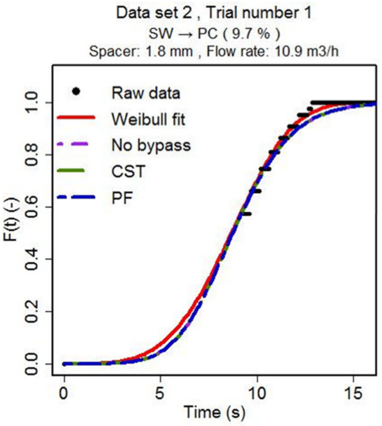

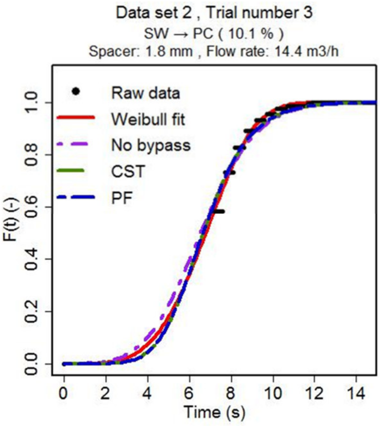

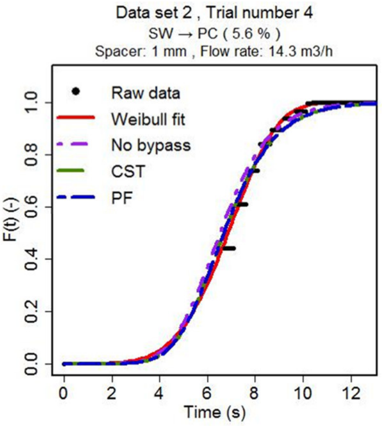

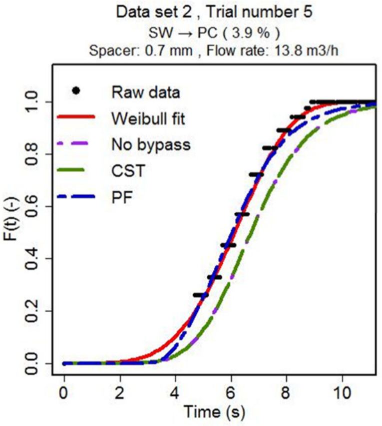

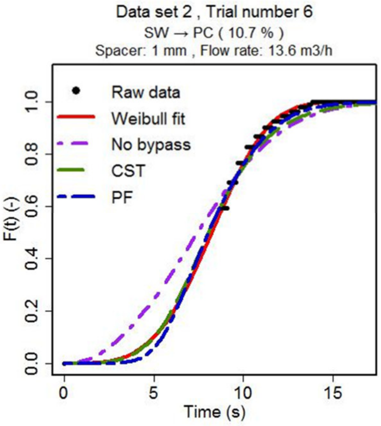

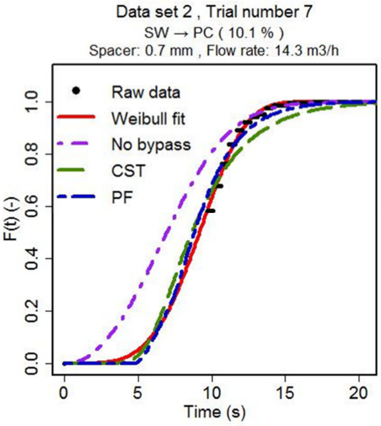

Data set 2 , Trial number 8
SW → PC (5.6 %)
Spacer: 1.8 mm , Flow rate: 14 m3/h

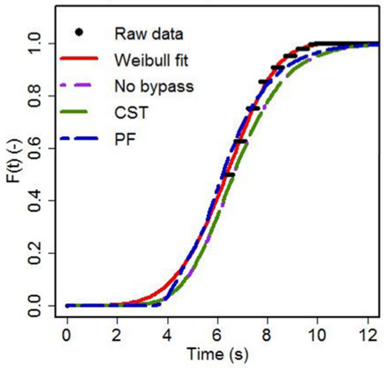

Data set 2 , Trial number 9
SW → PC (10.5 %)
Spacer: 0.7 mm , Flow rate: 13.4 m3/h

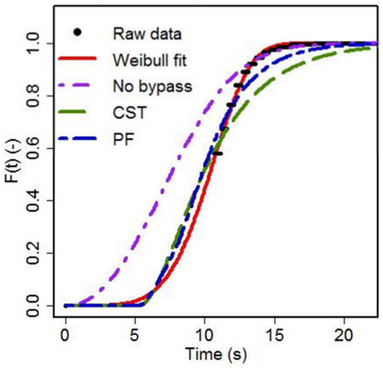

Data set 2 , Trial number 10
SW → PC (4.1 %)
Spacer: 1.8 mm , Flow rate: 14.7 m3/h

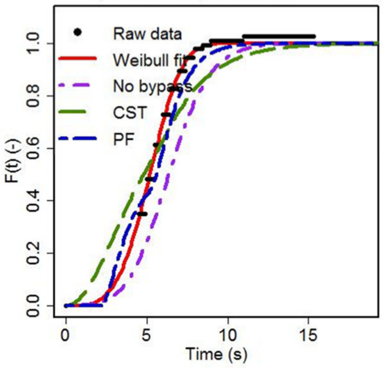

Data set 2 , Trial number 11
SW → PC (9.1 %)
Spacer: 0.7 mm , Flow rate: 13 m3/h

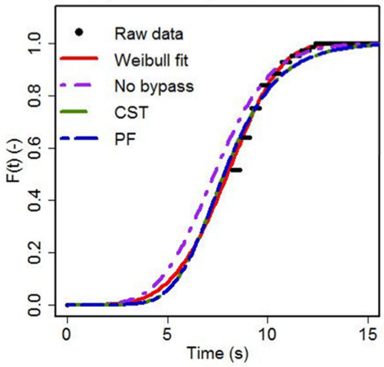

Data set 2 , Trial number 12
SW → PC (3.9 %)
Spacer: 1 mm , Flow rate: 13.9 m3/h

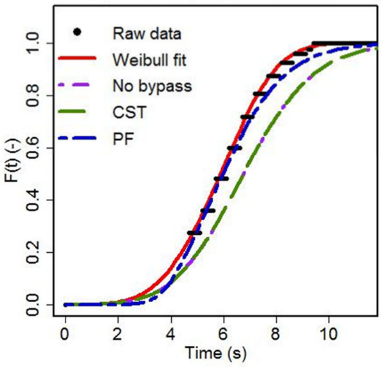

Data set 2 , Trial number 13
SW → PC (4 %)
Spacer: 1.8 mm , Flow rate: 13.9 m3/h

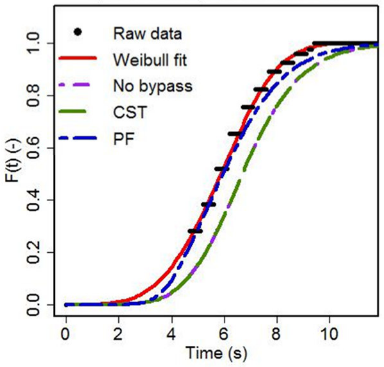

Data set 2 , Trial number 14
SW → PC (10.7 %)
Spacer: 1.8 mm , Flow rate: 13.8 m3/h

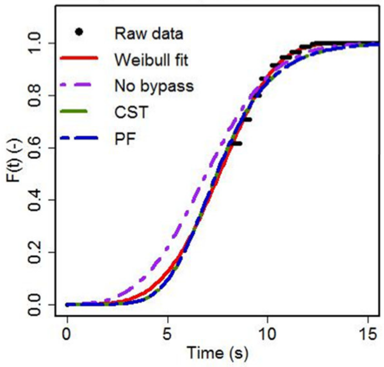

Data set 2 , Trial number 15
SW → PC (9.3 %)
Spacer: 0.7 mm , Flow rate: 13.7 m3/h

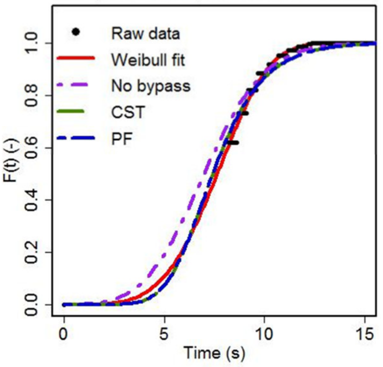

Data set 2 , Trial number 16
SW → PC (9.3 %)
Spacer: 1 mm , Flow rate: 14.2 m3/h

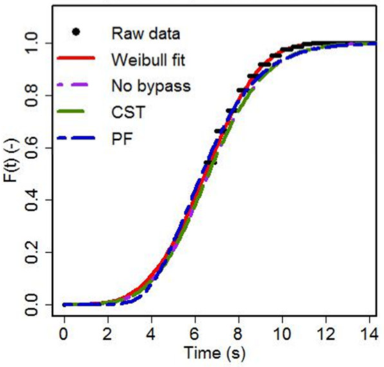

Data set 2 , Trial number 17
SW → PC (6.1 %)
Spacer: 0.7 mm , Flow rate: 13.9 m3/h

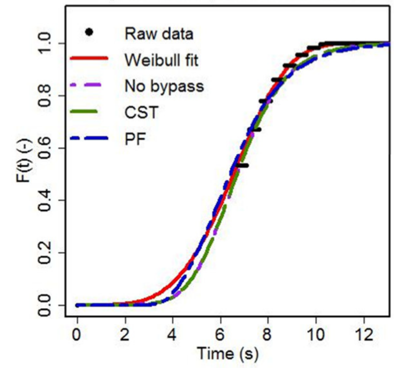

Data set 2 , Trial number 18
SW → PC (3.9 %)
Spacer: 1 mm , Flow rate: 13.5 m3/h

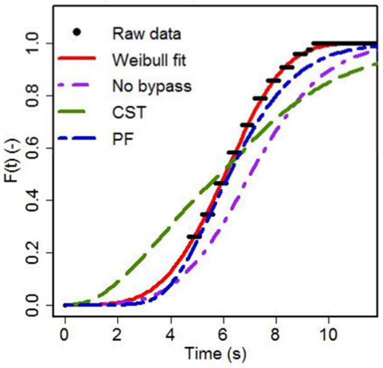

Data set 2 , Trial number 19
SW → PC (10.4 %)
Spacer: 1.8 mm , Flow rate: 7.5 m3/h

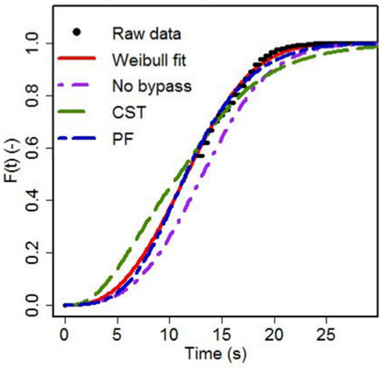

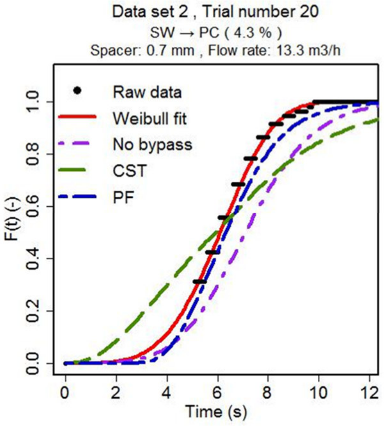
Data set 2 , Trial number 20
SW → PC (4.3 %)
Spacer: 0.7 mm , Flow rate: 13.3 m3/h

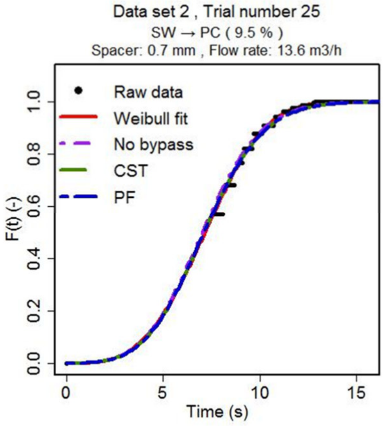
Data set 2 , Trial number 25
SW → PC (9.5 %)
Spacer: 0.7 mm , Flow rate: 13.6 m3/h

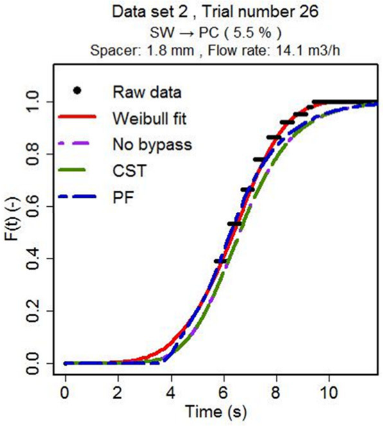
Data set 2 , Trial number 26
SW → PC (5.5 %)
Spacer: 1.8 mm , Flow rate: 14.1 m3/h

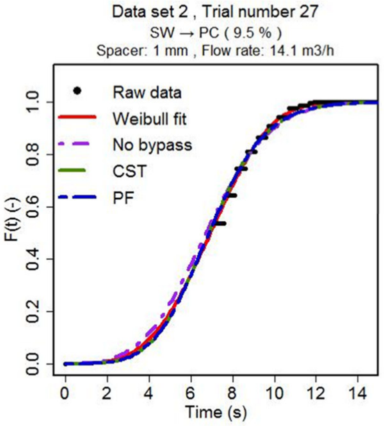
Data set 2 , Trial number 27
SW → PC (9.5 %)
Spacer: 1 mm , Flow rate: 14.1 m3/h

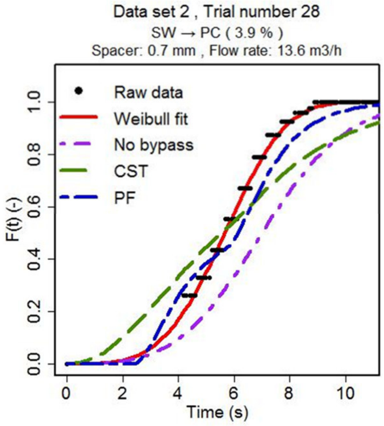
Data set 2 , Trial number 28
SW → PC (3.9 %)
Spacer: 0.7 mm , Flow rate: 13.6 m3/h

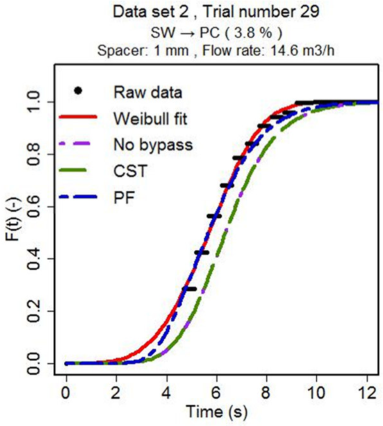
Data set 2 , Trial number 29
SW → PC (3.8 %)
Spacer: 1 mm , Flow rate: 14.6 m3/h

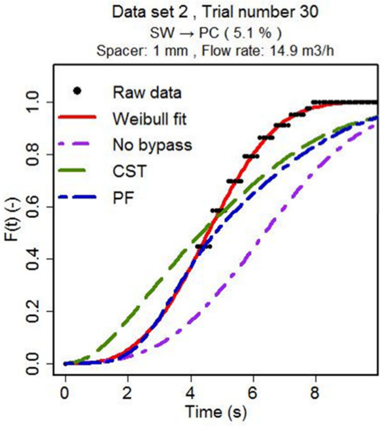
Data set 2 , Trial number 30
SW → PC (5.1 %)
Spacer: 1 mm , Flow rate: 14.9 m3/h

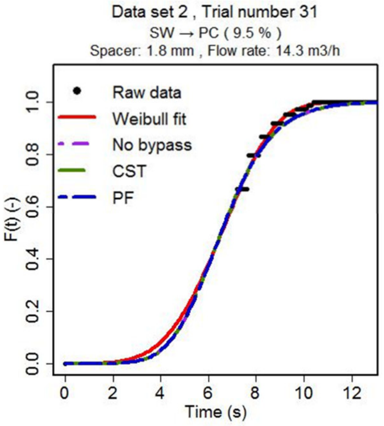
Data set 2 , Trial number 31
SW → PC (9.5 %)
Spacer: 1.8 mm , Flow rate: 14.3 m3/h

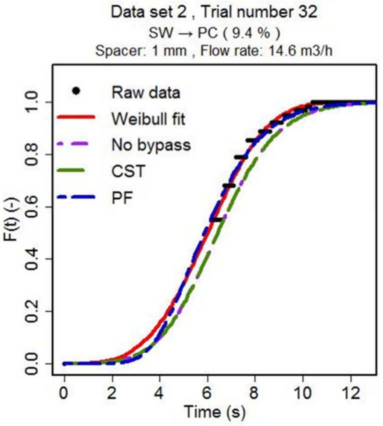
Data set 2 , Trial number 32
SW → PC (9.4 %)
Spacer: 1 mm , Flow rate: 14.6 m3/h

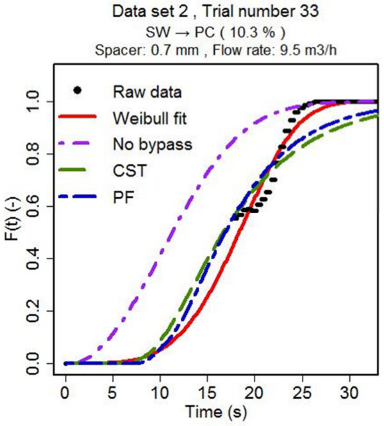
Data set 2 , Trial number 33
SW → PC (10.3 %)
Spacer: 0.7 mm , Flow rate: 9.5 m3/h

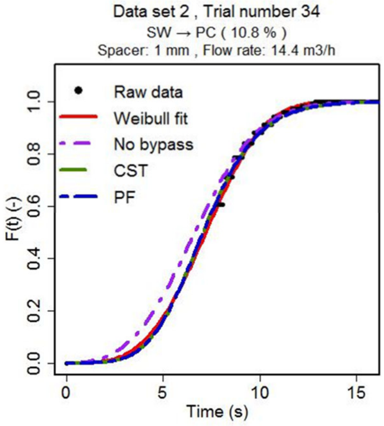
Data set 2 , Trial number 34
SW → PC (10.8 %)
Spacer: 1 mm , Flow rate: 14.4 m3/h

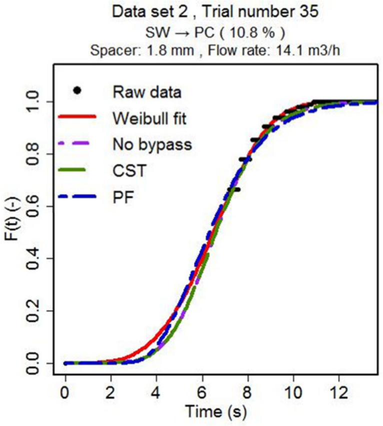
Data set 2 , Trial number 35
SW → PC (10.8 %)
Spacer: 1.8 mm , Flow rate: 14.1 m3/h

C. Displacement curves for data set 3 (XS → PC)

The diagrams contain the raw signals (raw data) monitored during the displacement experiments, the approximation by the cumulative Weibull distribution function (Weibull fit), and the results of the hybrid models visualized in Fig. 60 and Fig. 61 (section 7.3).

Data set 3 , Trial number 1
SW → PC (3.6 %)
Spacer: 0.7 mm , Flow rate: 5 m3/h

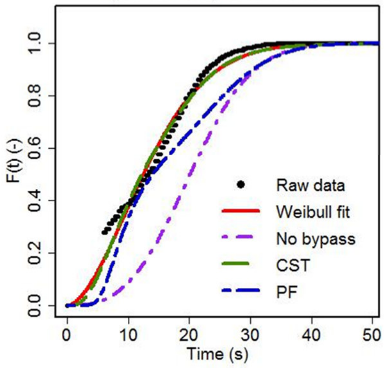

Data set 3 , Trial number 2
XS (0.8 %) → PC (9.5 %)
Spacer: 1 mm , Flow rate: 4.8 m3/h

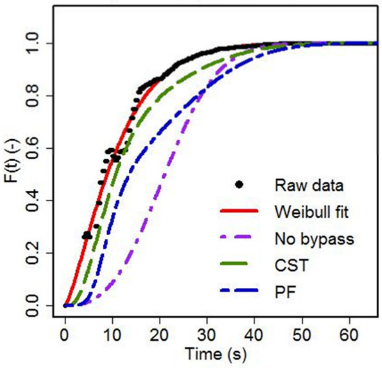

Data set 3 , Trial number 3
XS (0.4 %) → PC (9.8 %)
Spacer: 1.8 mm , Flow rate: 9.5 m3/h

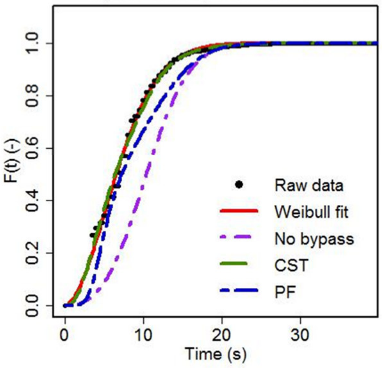

Data set 3 , Trial number 4
XS (0.8 %) → PC (13.7 %)
Spacer: 1.8 mm , Flow rate: 3.5 m3/h

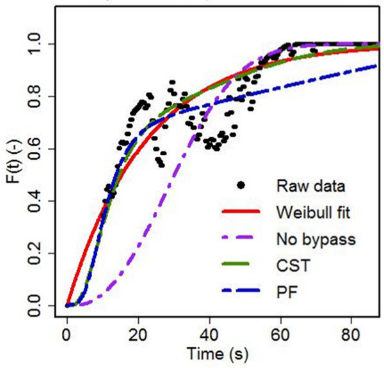

Data set 3 , Trial number 5
SW → PC (3.6 %)
Spacer: 0.7 mm , Flow rate: 14 m3/h

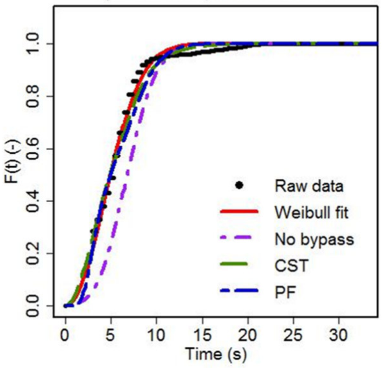

Data set 3 , Trial number 6
XS (0.8 %) → PC (3.6 %)
Spacer: 1.8 mm , Flow rate: 5.6 m3/h

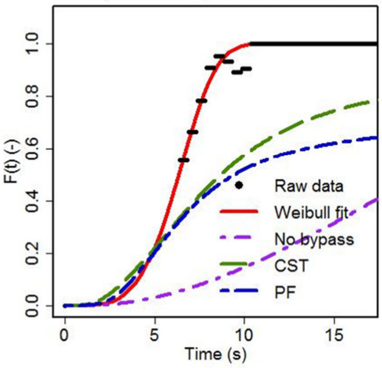

Data set 3 , Trial number 7
XS (0.4 %) → PC (9.8 %)
Spacer: 1 mm , Flow rate: 6.6 m3/h

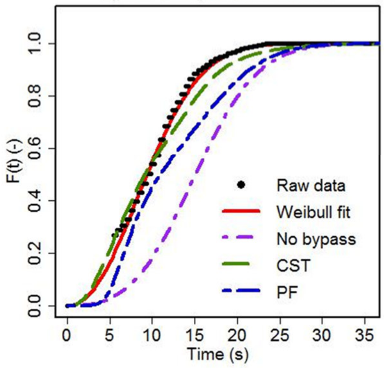

Data set 3 , Trial number 8
SW → PC (13 %)
Spacer: 0.7 mm , Flow rate: 7.4 m3/h

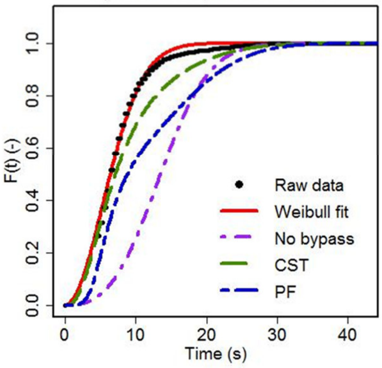

Data set 3 , Trial number 9
XS (0.8 %) → PC (12.9 %)
Spacer: 0.7 mm , Flow rate: 5.5 m3/h

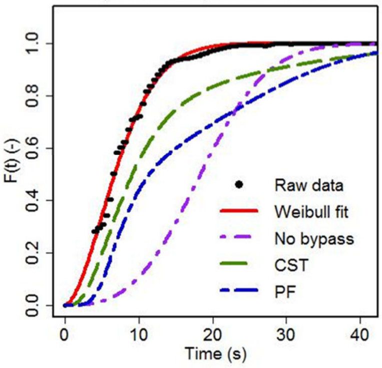

Data set 3 , Trial number 7
XS (0.4 %) → PC (9.8 %)
Spacer: 1 mm , Flow rate: 6.6 m3/h

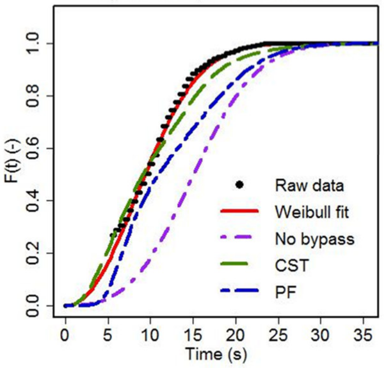

Data set 3 , Trial number 8
SW → PC (13 %)
Spacer: 0.7 mm , Flow rate: 7.4 m3/h

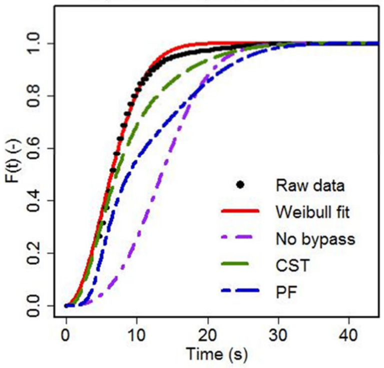

Data set 3 , Trial number 9
XS (0.8 %) → PC (12.9 %)
Spacer: 0.7 mm , Flow rate: 5.5 m3/h

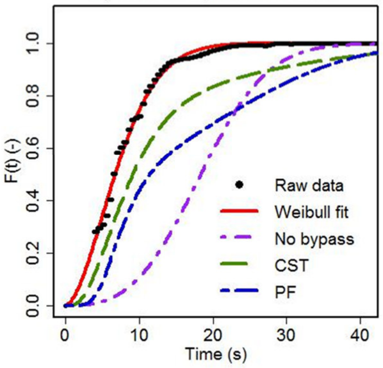

Data set 3 , Trial number 10
XS (0.4 %) → PC (12.2 %)
Spacer: 1 mm , Flow rate: 7.4 m3/h

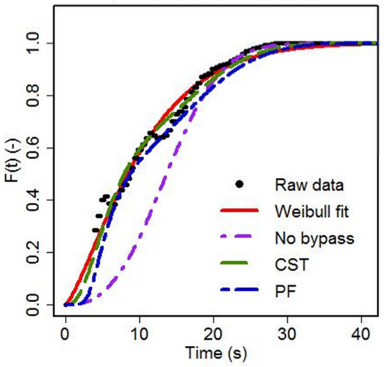

Data set 3 , Trial number 11
XS (0.8 %) → PC (9.9 %)
Spacer: 0.7 mm , Flow rate: 12 m3/h

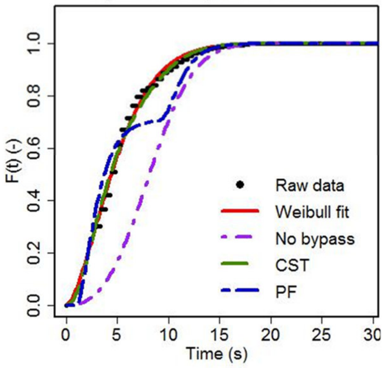

Data set 3 , Trial number 12
XS (0.8 %) → PC (3.8 %)
Spacer: 1.8 mm , Flow rate: 13.6 m3/h

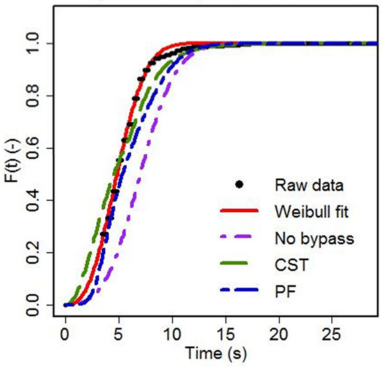

Data set 3 , Trial number 13
XS (0.8 %) → PC (13.1 %)
Spacer: 1.8 mm , Flow rate: 11.9 m3/h

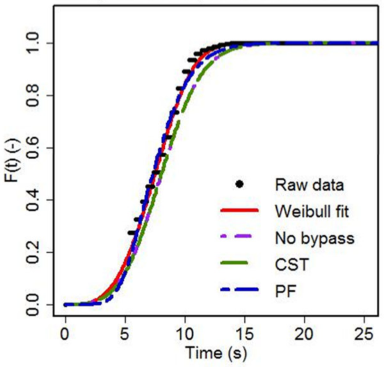

Data set 3 , Trial number 14
SW → PC (13.1 %)
Spacer: 1.8 mm , Flow rate: 12.9 m3/h

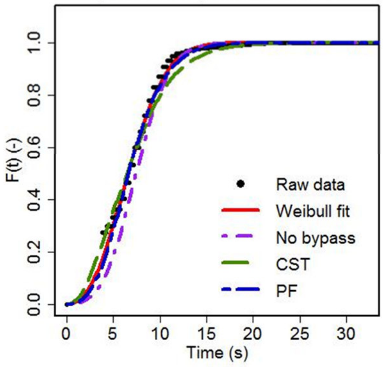

Data set 3 , Trial number 15
SW → PC (3.8 %)
Spacer: 1.8 mm , Flow rate: 5.3 m3/h

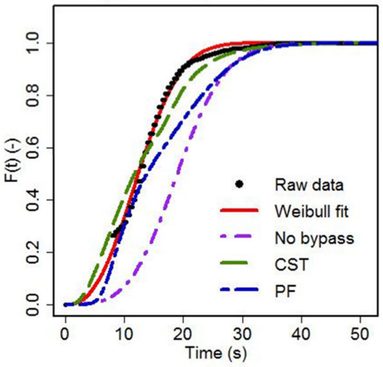

Data set 3 , Trial number 16
SW → PC (13.6 %)
Spacer: 0.7 mm , Flow rate: 1.8 m3/h

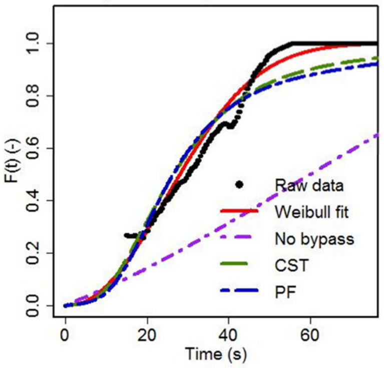

Data set 3 , Trial number 17
XS (0.8 %) → PC (3.7 %)
Spacer: 0.7 mm , Flow rate: 7.9 m3/h

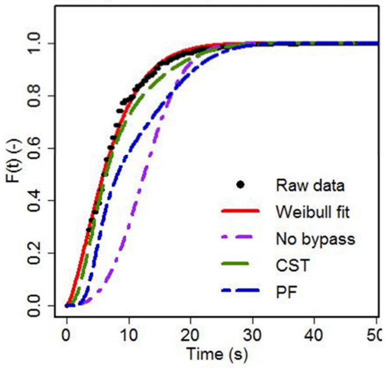

Data set 3 , Trial number 18
XS (0.4 %) → PC (13 %)
Spacer: 1 mm , Flow rate: 13.1 m3/h

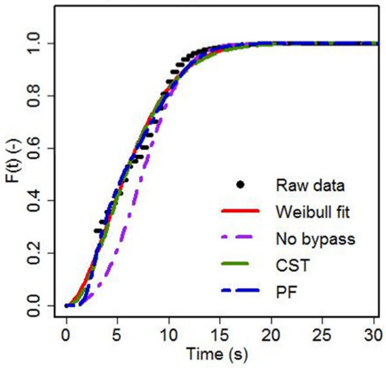

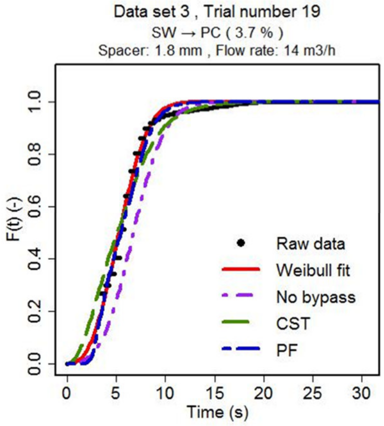

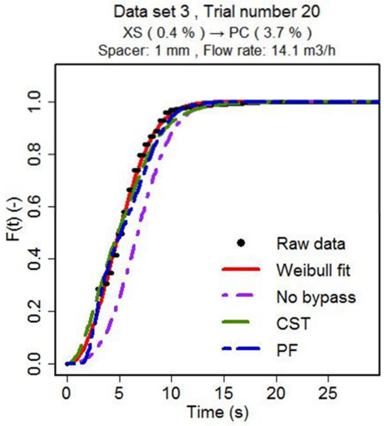

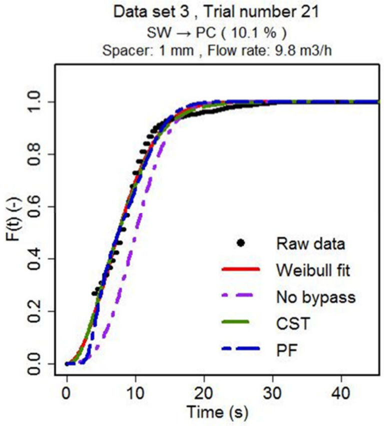

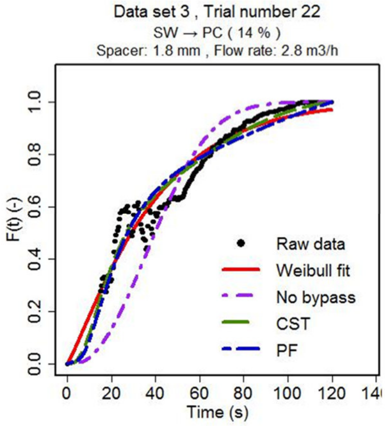

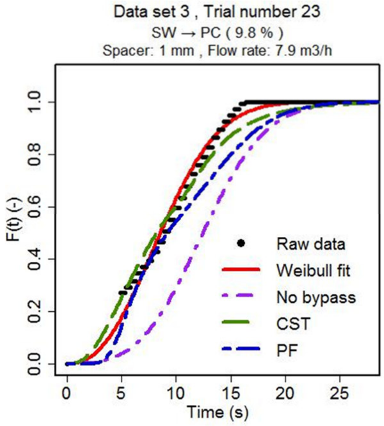

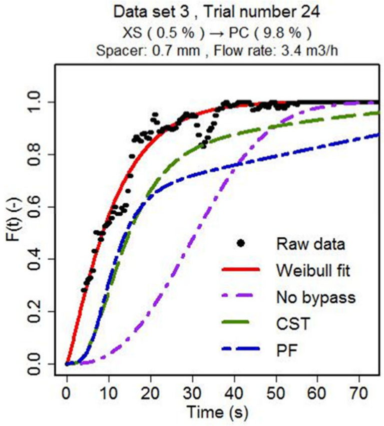

D. Displacement curves for data set 4 (SW → XS)

The diagrams contain the raw signals (raw data) monitored during the displacement experiments, the approximation by the cumulative Weibull distribution function (Weibull fit), and the results of the hybrid models visualized in Fig. 60 and Fig. 61 (section 7.3).

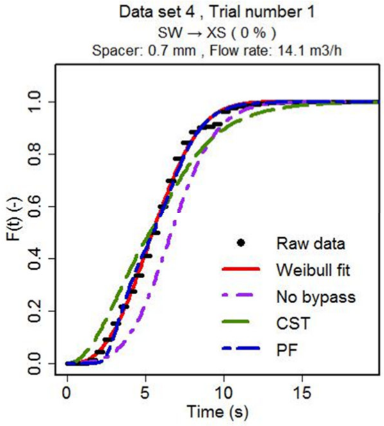

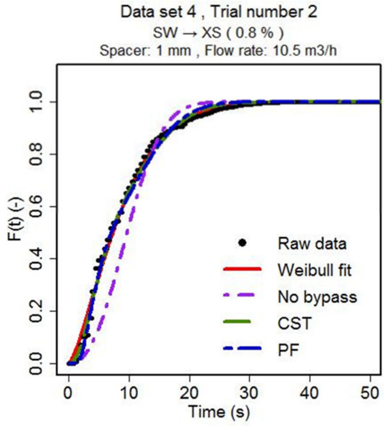

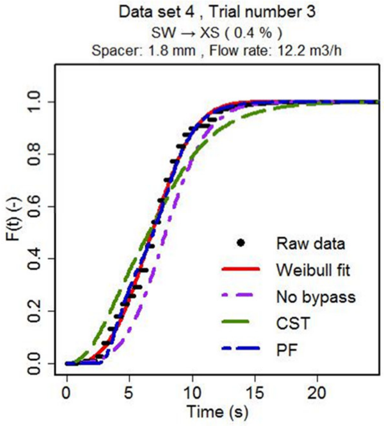

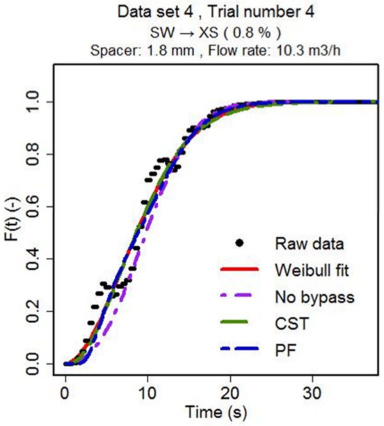
Data set 4 , Trial number 4
SW → XS (0.8 %)
Spacer: 1.8 mm , Flow rate: 10.3 m3/h

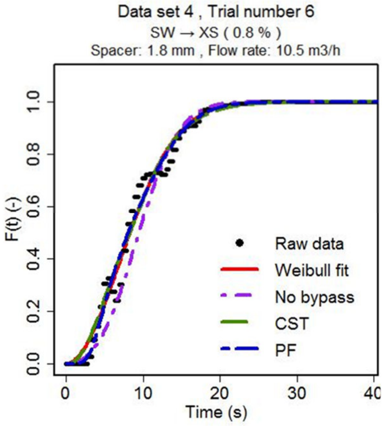
Data set 4 , Trial number 6
SW → XS (0.8 %)
Spacer: 1.8 mm , Flow rate: 10.5 m3/h

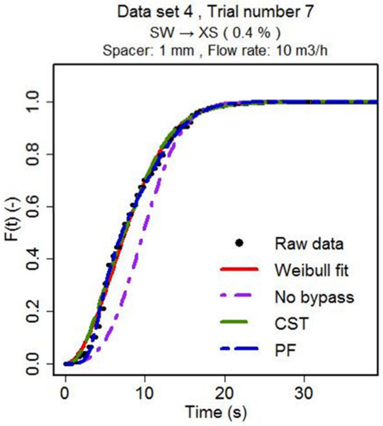
Data set 4 , Trial number 7
SW → XS (0.4 %)
Spacer: 1 mm , Flow rate: 10 m3/h

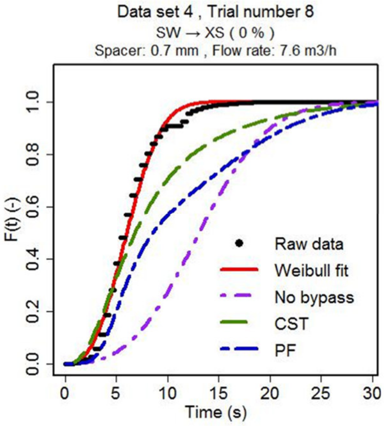
Data set 4 , Trial number 8
SW → XS (0 %)
Spacer: 0.7 mm , Flow rate: 7.6 m3/h

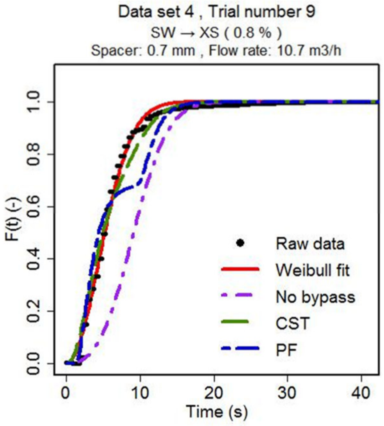
Data set 4 , Trial number 9
SW → XS (0.8 %)
Spacer: 0.7 mm , Flow rate: 10.7 m3/h

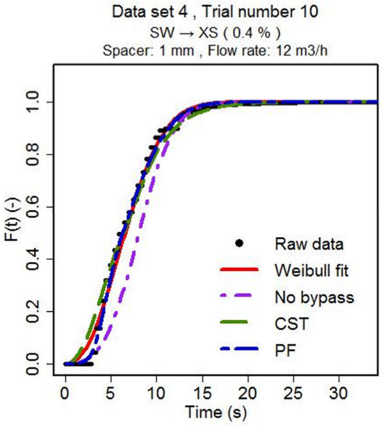
Data set 4 , Trial number 10
SW → XS (0.4 %)
Spacer: 1 mm , Flow rate: 12 m3/h

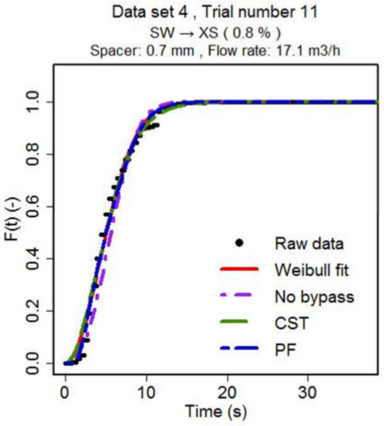
Data set 4 , Trial number 11
SW → XS (0.8 %)
Spacer: 0.7 mm , Flow rate: 17.1 m3/h

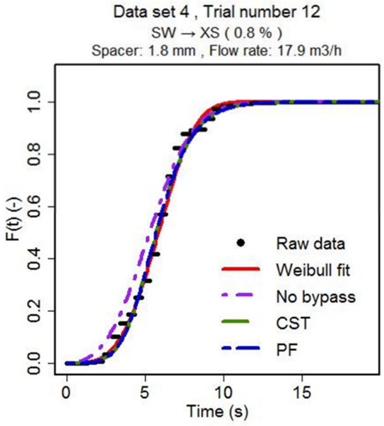
Data set 4 , Trial number 12
SW → XS (0.8 %)
Spacer: 1.8 mm , Flow rate: 17.9 m3/h

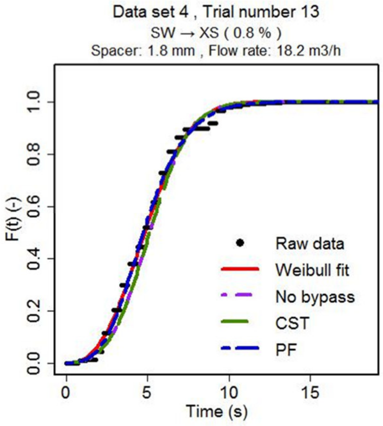
Data set 4 , Trial number 13
SW → XS (0.8 %)
Spacer: 1.8 mm , Flow rate: 18.2 m3/h

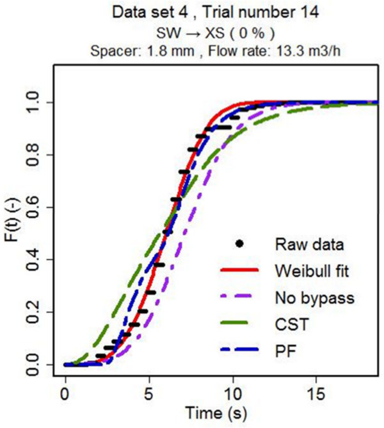
Data set 4 , Trial number 14
SW → XS (0 %)
Spacer: 1.8 mm , Flow rate: 13.3 m3/h

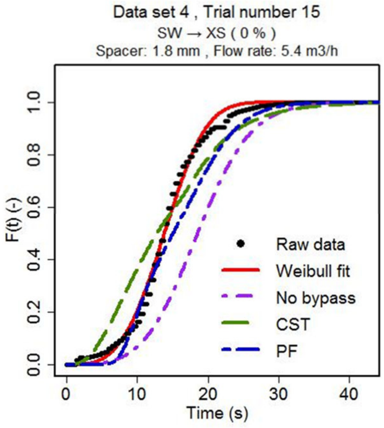
Data set 4 , Trial number 15
SW → XS (0 %)
Spacer: 1.8 mm , Flow rate: 5.4 m3/h

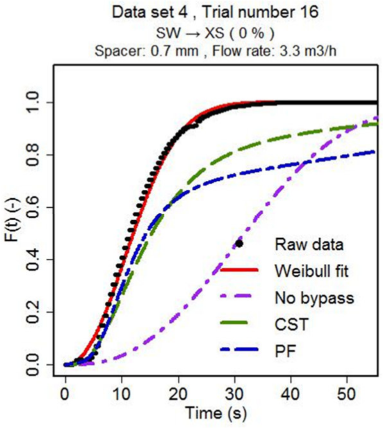
Data set 4 , Trial number 16
SW → XS (0 %)
Spacer: 0.7 mm , Flow rate: 3.3 m3/h

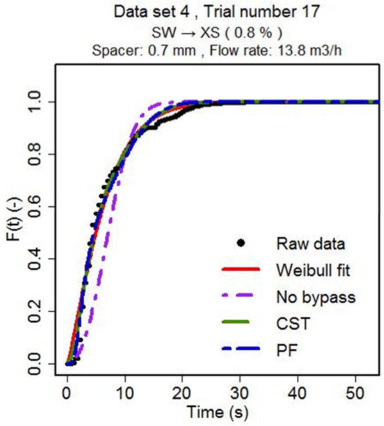
Data set 4 , Trial number 17
SW → XS (0.8 %)
Spacer: 0.7 mm , Flow rate: 13.8 m3/h

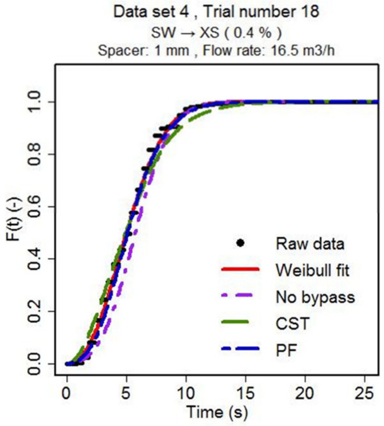
Data set 4 , Trial number 18
SW → XS (0.4 %)
Spacer: 1 mm , Flow rate: 16.5 m3/h

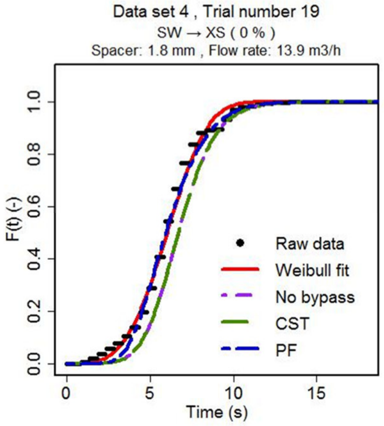
Data set 4 , Trial number 19
SW → XS (0 %)
Spacer: 1.8 mm , Flow rate: 13.9 m3/h

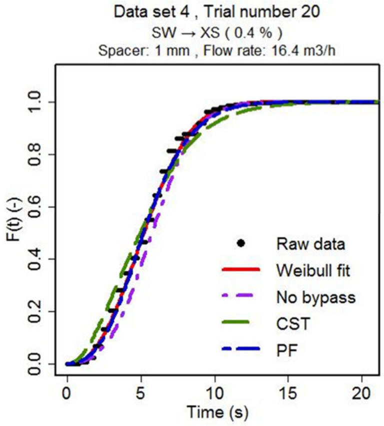
Data set 4 , Trial number 20
SW → XS (0.4 %)
Spacer: 1 mm , Flow rate: 16.4 m3/h

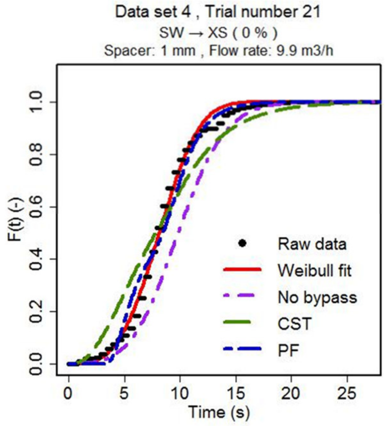
Data set 4 , Trial number 21
SW → XS (0 %)
Spacer: 1 mm , Flow rate: 9.9 m3/h

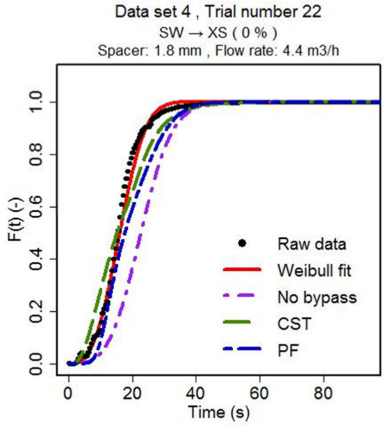
Data set 4 , Trial number 22
SW → XS (0 %)
Spacer: 1.8 mm , Flow rate: 4.4 m3/h

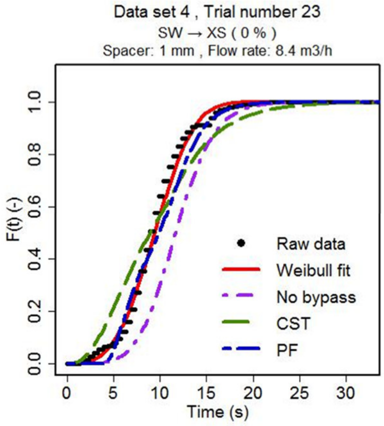
Data set 4 , Trial number 23
SW → XS (0 %)
Spacer: 1 mm , Flow rate: 8.4 m3/h

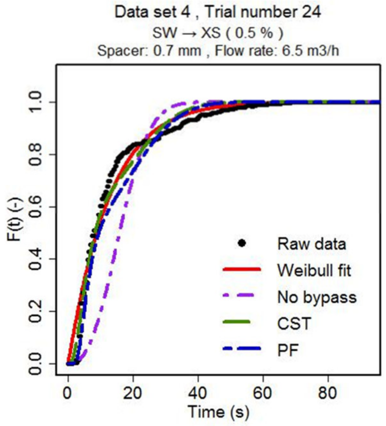
Data set 4 , Trial number 24
SW → XS (0.5 %)
Spacer: 0.7 mm , Flow rate: 6.5 m3/h

E. Calculation of the hydraulic diameter

Tab. E1: Spacer and housing dimensions. Calculation of the porosity and the hydraulic diameter of the spacers according to Schock and Miquel (1987, Eqs. 17, 20, 21, 22).

				Spacer type			
Variable			Data origin/formula	feed, 0.7 mm	feed, 1.0 mm	feed, 1.8 mm	wrap
Specific spacer volume	m^3/m^2	V_s	$\rightarrow volume\ displacement\ method$	$1.2332\cdot10^{-4}$ ± $6.8\cdot10^{-6}$	$2.0071\cdot10^{-4}$ ± $2.95\cdot10^{-5}$	$4.9303\cdot10^{-4}$ ± $2.087\cdot10^{-5}$	$6.6984\cdot10^{-4}$ ± $1.853\cdot10^{-5}$
Channel height	mm	h	$\rightarrow caliper$	0.70 ± 0.00	1.03 ± 0.03	1.83 ± 0.03	1.43 ± 0.09
Filament diameter	mm	d_f	$\rightarrow caliper$	0.41 ± 0.08	0.55 ± 0.06	1.01 ± 0.05	–
Pipe Radius	m	R	$\rightarrow caliper$	0.160			
Mesh length	mm	l_m	$\rightarrow image\ analysis$	2.77 ± 0.37	3.70 ± 0.43	3.89 ± 0.37	3.78 ± 0.70
Specific spacer filament length	m/m^2	l_s	$\rightarrow image\ analysis$	676.5 ± 5.4	519.3 ± 12.9	516.4 ± 8.6	472.0 ± 9.8
Feed spacer length	m	L	$\rightarrow manufacturer\ information$	0.965			
Feed spacer width	m	W	$\rightarrow manufacturer\ information$	0.934	0.914	0.900	0.900
Number of pockets	–	N	$\rightarrow manufacturer\ information$	13	11	8	1
Spacer area	m^2	A_s	$L \cdot W \cdot N$	11.719	9.704	6.949	0.869
Channel volume	m^3	V_c	$A_s \cdot h$	$7.969\cdot10^{-3}$	$10.87\cdot10^{-3}$	$15.01\cdot10^{-3}$	$1.390\cdot10^{-3}$
Equivalent filament radius	mm	r_e	$\sqrt{\frac{V_s}{\pi \cdot l_s}}$	0.241	0.351	0.551	0.672
Specific spacer surface	m^2/m^2	S_s	$r_e^2 \cdot \left(2 \cdot \pi \cdot \frac{1}{A_s} - \frac{l_s}{l_m}\right)$	1.009	1.124	1.735	1.943

Tab. E1: Spacer and housing dimensions. Calculation of the porosity and the hydraulic diameter of the spacers according to Schock and Miquel (1987, Eqs. 17, 20, 21, 22).

				Spacer type			
Variable			Data origin / formula	feed, 0.7 mm	feed, 1.0 mm	feed, 1.8 mm	wrap
Porosity	–	ε_s	$1-\frac{0.5\cdot\pi\cdot d_f^2}{l_m\cdot h}$	0.85	0.85	0.70	0.53
Hydraulic diameter	mm	$d_{h,s}$	$\frac{4\cdot\varepsilon_s}{\frac{2\cdot(W+h)}{W\cdot h}+(1-\epsilon_s)\cdot\left(\frac{4}{d_f}\right)}$	0.796	1.140	1.233	0.767

Tab. E2: Calculation of the porosity and the hydraulic diameter of the membranes. The second index indicates to which spacer type the dimension refers (feed spacer: f, spacer wrap: w).

				Spiral-wound membrane type		
Variable			Formula	0.7 mm	1.0 mm	1.8 mm
Channel surface	m^2	S_c	$A_S\cdot 2$	23.438	19.408	13.898
Pipe surface	m	S_P	$2\cdot\pi\cdot R\cdot L$	0.485		
Total pipe volume	m^3	V_p	$\pi\cdot R^2\cdot L$	$19.41\cdot10^{-3}$		
Fit gap volume	m^3	V_g	$\pi\cdot(R^2-(R-0.001)^2)\cdot L$	$9.674\cdot10^{-4}$		
Porosity	–	ε_{SWM}	$\frac{(V_{c,f}-V_{s,f})+(V_{c,w}-V_{s,w})+V_g}{V_p}$	0.43	0.50	0.56
Hydraulic diameter	mm	$d_{h,SWM}$	$\frac{4\cdot V_P\cdot\varepsilon_{SWM}}{S_c+S_{s,f}+S_{s,w}+S_p}$	0.916	1.226	1.602

F. Experimental results for data set 1 (SW → PC)

Trial Number	Random Block	Flow rate (m^3/h)		Displacement Temperature (°C)		Protein Concentration (%)	
		Target	Actual	Target	Actual	Target	Actual
1	1	7.50	6.59	30.00	30.25	11.90	12.23
2	1	7.50	7.46	28.00	28.08	3.54	3.97
3	2	17.50	14.65	30.00	29.33	6.07	6.38
4	2	7.50	7.14	30.00	29.97	3.54	3.71
5	3	15.00	13.55	10.00	10.60	5.63	5.93
6	3	15.50	14.42	10.00	10.62	3.54	3.89
7	4	15.00	12.69	30.00	30.16	3.54	3.74
8	4	7.50	6.92	23.00	23.50	11.90	11.81
9	5	7.50	7.34	10.00	10.52	3.54	4.05
10	5	7.50	6.76	10.00	10.91	11.90	12.53
11	6	15.00	13.56	10.00	10.28	3.54	3.99
12	6	7.50	7.44	11.00	11.46	3.54	3.92
13	7	15.50	13.53	28.00	27.49	11.90	12.52
14	7	17.50	15.66	10.00	10.59	3.54	3.80
15	8	7.50	7.32	30.00	29.54	5.84	6.24
16	8	15.50	13.94	30.00	29.72	3.50	4.27
17	9	15.50	14.16	10.00	11.04	13.83	15.04
18	9	17.50	14.31	30.00	33.31	13.83	15.31
19	10	15.00	12.90	30.00	30.54	13.94	13.82
20	10	16.00	13.72	20.00	20.21	12.89	13.52
21	11	13.50	11.78	28.00	28.09	3.50	3.97
22	11	9.00	8.19	14.00	14.25	6.78	7.13
23	12	7.50	6.28	30.00	29.87	13.94	12.51
24	12	7.50	7.60	10.00	10.49	3.50	3.73
25	13	8.50	7.94	30.00	30.65	10.63	11.05
26	13	7.50	6.43	10.00	10.73	13.94	13.29
27	14	17.50	14.94	10.00	11.05	13.94	13.78
28	14	15.00	12.53	10.00	10.72	12.89	13.54
29	15	8.50	7.72	27.00	26.36	10.63	10.96
30	15	11.50	9.92	30.00	30.08	13.24	14.13
31	16	12.00	10.78	26.00	25.78	6.78	7.26
32	16	15.00	12.19	13.00	13.84	13.94	14.29
33	17	13.00	12.22	18.00	18.25	10.23	9.42
34	17	9.00	8.01	10.00	11.06	13.94	14.40
35	18	7.50	6.82	13.00	13.47	12.53	13.04
36	18	9.50	8.94	20.00	20.09	3.50	3.83

Trial Number	log10(k_{MP}) (Pa·s^n)	Fluid Index (-)	Spacer Thickness (mm)	Aspect Ratio (-)	Concentrate Temperature (°C)		Rinsing Time (s)	Mixed Phase Volume (L)
					Target	Actual		
1	-0.72	0.74	0.7	0.59	10.00	10.29	53.5	98
2	-2.57	0.98	1.0	0.53	10.00	9.96	23.5	49
3	-2.16	0.96	1.8	0.55	10.00	9.96	10.0	41
4	-2.61	0.99	0.7	0.59	10.00	9.94	20.0	40
5	-2.24	0.96	1.8	0.55	10.00	9.99	12.5	47
6	-2.58	0.98	1.0	0.53	10.00	9.96	10.5	42
7	-2.60	0.98	0.7	0.59	10.00	9.94	11.0	39
8	-0.85	0.77	1.0	0.53	10.00	10.98	36.5	70
9	-2.56	0.98	0.7	0.59	10.00	9.94	20.5	42
10	-0.63	0.73	1.8	0.55	10.00	10.06	39.5	74
11	-2.57	0.98	0.7	0.59	10.00	9.94	10.5	40
12	-2.58	0.98	1.8	0.55	10.00	9.95	20.5	42
13	-0.63	0.73	1.0	0.53	10.00	12.72	17.0	64
14	-2.60	0.98	1.8	0.55	10.00	9.96	9.0	39
15	-2.18	0.96	1.8	0.55	10.00	9.96	20.0	41
16	-2.52	0.98	1.0	0.53	10.00	9.96	10.5	41
17	0.19	0.59	1.0	0.53	10.00	10.05	18.0	71
18	0.28	0.58	1.8	0.55	10.00	10.06	13.0	52
19	-0.23	0.65	0.7	0.59	10.00	9.91	21.5	73
20	-0.32	0.67	1.8	0.55	10.00	9.93	14.5	55
21	-2.57	0.98	1.8	0.55	10.00	9.95	11.0	36
22	-2.01	0.94	0.7	0.59	10.00	9.96	19.0	43
23	-0.64	0.73	1.8	0.55	10.00	9.99	49.5	84
24	-2.61	0.98	1.0	0.53	10.00	9.99	21.0	44
25	-1.06	0.81	1.0	0.53	10.00	9.99	23.5	52
26	-0.40	0.68	0.7	0.59	10.00	10.64	75.5	133
27	-0.24	0.66	1.8	0.55	10.00	11.02	17.5	73
28	-0.32	0.67	0.7	0.59	10.00	9.93	22.5	78
29	-1.09	0.81	1.8	0.55	10.00	9.94	23.0	49
30	-0.13	0.64	1.0	0.53	10.00	11.58	21.5	59
31	-1.98	0.94	0.7	0.59	10.00	9.93	14.5	43
32	-0.07	0.63	0.7	0.59	10.00	12.51	25.5	86
33	-1.49	0.88	1.0	0.53	10.00	9.96	15.3	52
34	-0.03	0.62	1.0	0.53	10.00	13.83	32.0	71
35	-0.48	0.70	1.0	0.53	10.00	9.94	33.5	63
36	-2.59	0.98	1.8	0.55	10.00	9.95	16.0	40

G. Experimental results for data set 2 (SW → PC)

Trial Number	Random Block	Flow rate (m³/h)		Displacement Temperature (°C)		Protein Concentration (%)	
		Target	Actual	Target	Actual	Target	Actual
1	1	14.00	10.95	20.00	18.86	8.87	9.66
3	1	14.00	14.43	20.00	20.75	9.29	10.14
4	1	14.00	14.35	20.00	20.62	5.38	5.64
5	2	14.00	13.84	20.00	19.83	3.51	3.93
6	9	14.00	13.61	20.00	18.90	10.50	10.72
7	2	14.00	14.35	20.00	19.95	10.50	10.10
8	2	14.00	13.99	20.00	20.02	5.38	5.63
9	3	14.00	13.39	20.00	18.68	10.50	10.51
10	3	14.00	14.72	20.00	19.75	3.51	4.14
11	3	14.00	12.97	20.00	20.69	8.87	9.14
12	3	14.00	13.89	20.00	20.45	3.51	3.87
13	4	14.00	13.93	20.00	20.63	3.51	3.95
14	4	14.00	13.75	20.00	20.53	10.50	10.73
15	4	14.00	13.66	20.00	19.57	9.20	9.34
16	4	14.00	14.15	20.00	21.25	9.11	9.34
17	5	14.00	13.90	20.00	24.45	5.74	6.14
18	5	14.00	13.46	20.00	19.76	3.51	3.90
19	9	14.00	7.54	20.00	21.57	10.50	10.39
20	5	14.00	13.32	20.00	20.56	3.89	4.30
25	7	14.00	13.59	20.00	21.41	9.53	9.53
26	7	14.00	14.08	20.00	20.46	5.38	5.46
27	7	14.00	14.12	20.00	20.80	10.18	9.47
28	7	14.00	13.55	20.00	20.61	3.51	3.93
29	8	14.00	14.62	20.00	23.09	2.89	3.78
30	8	14.00	14.86	20.00	21.57	5.01	5.09
31	8	14.00	14.27	20.00	23.91	8.87	9.49
32	8	14.00	14.56	20.00	18.90	9.20	9.37
33	10	14.00	9.54	20.00	20.22	3.89	10.32
34	10	14.00	14.38	20.00	14.64	10.50	10.77
35	10	14.00	14.12	20.00	20.75	10.50	10.82

Trial Number	$\log_{10}(k_{MP})$ (Pa·s^n)	n_{MP} (-)	Spacer Thickness (mm)	Aspect Ratio (-)	Concentrate Temperature (°C)		Rinsing Time (s)	Mixed Phase Volume (L)
					Target	Actual		
1	-1.43	0.87	1.8	0.55	10.00	9.94	13.0	40
3	-1.30	0.85	1.8	0.55	10.00	10.01	12.0	48
4	-2.29	0.97	1.0	0.53	10.00	9.98	10.5	42
5	-2.58	0.98	0.7	0.59	10.00	9.98	9.0	35
6	-1.15	0.82	1.0	0.53	10.00	10.68	14.0	53
7	-1.32	0.85	0.7	0.59	10.00	9.95	17.0	68
8	-2.30	0.97	1.8	0.55	10.00	9.93	10.0	39

Trial Number	$\log_{10}(k_{MP})$ (Pa·s^n)	n_{MP} (-)	Spacer Thickness (mm)	Aspect Ratio (-)	Concentrate Temperature (°C)		Rinsing Time (s)	Mixed Phase Volume (L)
					Target	Actual		
9	-1.21	0.83	0.7	0.59	10.00	9.37	18.0	67
10	-2.54	0.98	1.8	0.55	10.00	9.97	15.5	63
11	-1.56	0.89	0.7	0.59	10.00	9.98	12.5	45
12	-2.59	0.98	1.0	0.53	10.00	9.93	9.5	37
13	-2.57	0.98	1.8	0.55	10.00	9.94	9.5	37
14	-1.15	0.82	1.8	0.55	10.00	10.23	12.5	48
15	-1.51	0.88	0.7	0.59	10.00	10.84	12.5	47
16	-1.51	0.88	1.0	0.53	10.00	9.93	11.5	45
17	-2.20	0.96	0.7	0.59	10.00	9.99	10.5	41
18	-2.58	0.98	1.0	0.53	10.00	9.96	9.5	36
19	-1.24	0.84	1.8	0.55	10.00	9.91	24.0	50
20	-2.52	0.98	0.7	0.59	10.00	9.93	9.9	37
25	-1.46	0.87	0.7	0.59	10.00	10.01	13.0	49
26	-2.33	0.97	1.8	0.55	10.00	9.96	9.5	37
27	-1.47	0.88	1.0	0.53	10.00	9.96	12.0	47
28	-2.58	0.98	0.7	0.59	10.00	9.96	9.0	34
29	-2.60	0.98	1.0	0.53	10.00	9.96	10.0	41
30	-2.39	0.97	1.0	0.53	10.00	9.97	8.0	33
31	-1.47	0.88	1.8	0.55	10.00	10.00	10.5	42
32	-1.50	0.88	1.0	0.53	10.00	10.02	10.5	42
33	-1.26	0.84	0.7	0.59	10.00	9.95	26.5	70
34	-1.14	0.82	1.0	0.53	10.00	9.98	13.0	52
35	-1.12	0.82	1.8	0.55	10.00	9.98	11.0	43

H. Experimental results for data set 3 (XS → PC)

Trial Number	Random Block	Flow rate (m³/h)		Displacement Temperature (°C)	Xanthan Concentration (%)	Protein Concentration (%)	
		Target	Actual	Actual	Actual	Target	Actual
1	1	14.00	10.95	9.75	0.00	3.60	3.63
2	1	14.00	14.43	9.27	0.75	9.88	9.47
3	1	14.00	14.35	9.53	0.38	9.88	9.78
4	2	14.00	13.84	8.17	0.75	16.15	13.69
5	2	14.00	13.61	6.93	0.00	3.60	3.65
6	2	14.00	14.35	9.13	0.75	3.60	3.57
7	3	14.00	13.99	8.01	0.38	9.88	9.84
8	3	14.00	13.39	10.06	0.00	16.15	12.96
9	3	14.00	14.72	8.27	0.75	16.15	12.86
10	4	14.00	12.97	9.18	0.38	16.15	12.25
11	4	14.00	13.89	10.79	0.75	9.88	9.86
12	4	14.00	13.93	9.23	0.75	3.60	3.77
13	5	14.00	13.75	9.09	0.75	16.15	13.08
14	5	14.00	13.66	9.24	0.00	16.15	13.11

Trial Number	Random Block	Flow rate (m³/h)		Displacement Temperature (°C)	Xanthan Concentration (%)	Protein Concentration (%)	
		Target	Actual	Actual	Actual	Target	Actual
15	5	14.00	14.15	8.42	0.00	3.60	3.80
16	6	14.00	13.90	10.95	0.00	16.15	13.55
17	6	14.00	13.46	7.69	0.75	3.60	3.66
18	6	14.00	7.54	8.54	0.38	16.15	13.00
19	7	14.00	13.32	7.12	0.00	3.60	3.69
20	7	14.00	13.59	7.02	0.38	3.60	3.74
21	7	14.00	14.08	6.06	0.00	9.88	10.05
22	8	14.00	14.12	8.29	0.00	16.15	14.04
23	8	14.00	13.55	11.51	0.00	9.88	9.78
24	8	14.00	14.62	8.22	0.45	9.88	9.77

Trial Number	Spacer Thickness (mm)	$\log_{10}(k_{MP})$ (Pa·sn)	n_{MP} (-)	$\log_{10}(k_{DF})$ (Pa·sn)	n_{DF} (-)	Product Temperature (°C)	Rinsing Time (s)	Mixed Phase Volume (L)
1	0.7	-2.49	0.99	-2.92	0.97	10.00	38.5	54
2	1	-1.35	0.88	0.52	0.28	9.92	42.0	57
3	1.8	-1.27	0.87	0.00	0.37	10.00	29.5	78
4	1.8	-0.14	0.66	0.52	0.28	9.94	70.5	69
5	0.7	-2.49	0.99	-2.92	0.97	10.01	25.5	99
6	1.8	-2.50	0.99	0.52	0.28	10.03	14.0	22
7	1	-1.26	0.86	0.00	0.37	9.99	24.5	45
8	0.7	-0.37	0.70	-2.92	0.97	9.92	28.5	59
9	0.7	-0.40	0.71	0.52	0.28	9.86	29.0	44
10	1	-0.59	0.74	0.00	0.37	9.91	31.9	65
11	0.7	-1.25	0.86	0.52	0.28	9.97	19.0	63
12	1.8	-2.47	0.98	0.52	0.28	9.93	18.0	68
13	1.8	-0.34	0.70	0.52	0.28	9.93	17.5	58
14	1.8	-0.33	0.69	-2.92	0.97	9.90	24.9	89
15	1.8	-2.47	0.98	-2.92	0.97	10.08	40.0	59
16	0.7	-0.19	0.67	-2.92	0.97	9.90	61.0	30
17	0.7	-2.49	0.99	0.52	0.28	9.98	40.0	88
18	1	-0.36	0.70	0.00	0.37	9.87	20.0	73
19	1.8	-2.49	0.99	-2.92	0.97	10.00	17.5	68
20	1	-2.48	0.98	0.00	0.37	10.10	11.5	45
21	1	-1.20	0.85	-2.92	0.97	9.91	26.5	72
22	1.8	-0.03	0.64	-2.92	0.97	10.18	65.5	50
23	1	-1.27	0.86	-2.92	0.97	9.98	22.5	49
24	0.7	-1.27	0.87	0.16	0.34	9.94	60.0	56

I. Experimental results for data set 4 (SW → XS)

Trial Number	Random Block	Flow rate (m^3/h)		$\log_{10}(k_{MP})$ (Pa·s^n)	n_{MP} (-)	$\log_{10}(k_{DF})$ (Pa·s^n)	n_{DF} (-)
		Target	Actual				
1	1	15.00	14.08	-2.92	0.97	-2.88	1.00
2	1	10.00	10.38	0.52	0.28	-2.88	1.00
3	1	10.00	12.04	0.00	0.37	-2.89	1.00
4	2	10.00	10.15	0.52	0.28	-2.88	1.00
6	2	5.00	10.20	0.52	0.28	-2.87	1.00
7	3	10.00	9.87	0.00	0.37	-2.88	1.00
8	3	5.00	7.55	-2.92	0.97	-2.90	1.00
9	3	10.00	10.74	0.52	0.28	-2.90	1.00
10	4	10.00	11.97	0.00	0.37	-2.91	1.00
11	4	15.00	16.95	0.52	0.28	-2.89	1.00
12	4	15.00	17.59	0.52	0.28	-2.89	1.00
13	5	15.00	18.04	0.52	0.28	-2.90	1.00
14	5	15.00	13.25	-2.92	0.97	-2.90	1.00
15	5	5.00	5.35	-2.92	0.97	-2.89	1.00
16	6	5.00	3.27	-2.92	0.97	-2.88	1.00
17	6	10.00	13.53	0.52	0.28	-2.88	1.00
18	6	15.00	16.17	0.00	0.37	-2.88	1.00
19	7	15.00	13.86	-2.92	0.97	-2.88	1.00
20	7	15.00	16.28	0.00	0.37	-2.89	1.00
21	7	10.00	9.86	-2.92	0.97	-2.88	1.00
22	8	5.00	4.44	-2.92	0.97	-2.88	1.00
23	8	10.00	8.31	-2.92	0.97	-2.87	1.00
24	8	5.00	6.44	0.16	0.34	-2.88	1.00

Trial Number	Spacer Thickness (mm)	Displacement Temperature (°C)	Product Temperature (°C)	Xanthan Concentration (%)	Protein Concentration (%)	Rinsing Time (s)	Mixed Phase Volume (L)
1	0.7	9.37	10.00	0.00	0.00	14.5	57
2	1	10.11	9.92	0.75	0.00	37.0	107
3	1.8	10.23	10.00	0.38	0.00	18.0	60
4	1.8	9.89	9.94	0.75	0.00	27.0	76
6	1.8	8.61	10.03	0.00	0.00	27.0	76
7	1	9.47	9.99	0.75	0.00	26.5	73
8	0.7	10.97	9.92	0.38	0.00	19.5	41
9	0.7	10.89	9.86	0.00	0.00	34.0	101
10	1	11.75	9.91	0.75	0.00	27.5	91
11	0.7	10.76	9.97	0.38	0.00	19.0	89
12	1.8	10.87	9.93	0.75	0.00	14.0	68
13	1.8	11.52	9.93	0.75	0.00	13.9	70
14	1.8	11.42	9.90	0.75	0.00	14.0	52
15	1.8	10.88	10.08	0.00	0.00	33.5	50
16	0.7	9.37	9.90	0.00	0.00	39.0	35

Trial Number	Spacer Thickness (mm)	Displacement Temperature (°C)	Product Temperature (°C)	Xanthan Concentration (%)	Protein Concentration (%)	Rinsing Time (s)	Mixed Phase Volume (L)
17	0.7	9.96	9.98	0.00	0.00	33.5	126
18	1	9.60	9.87	0.75	0.00	16.5	74
19	1.8	9.79	10.00	0.38	0.00	14.0	54
20	1	10.26	10.10	0.00	0.00	15.0	68
21	1	9.76	9.91	0.38	0.00	20.5	56
22	1.8	9.36	10.18	0.00	0.00	61.0	75
23	1	8.63	9.98	0.00	0.00	23.5	54
24	0.7	9.38	9.94	0.00	0.00	70.0	125

J. Parameters of mechanistic models

Applied models:

1) Compartment model
2) Advection-dispersion model
3a) Basic hybrid model
3b) Hybrid model I (stirred-tank bypass)
3c) Hybrid model II (plug-flow bypass)

Model parameters:

- Axial dispersion coefficient for the whole experimental setup: D_a
- Axial dispersion coefficient in the spiral-wound membrane $D_{a,3}$
- Volume share bypassing the spiral-wound membrane: $(1-\alpha_3)$
- Axial dispersion coefficient in the pipe sections: $D_{a,1}=D_{a,5}$
- Volume share using the short-circuit in the empty sections of the housing: $(1-\alpha_2)$

Data Set, Trial Number		Model 1	Model 2		Model 3b				
		$RMSE$	D_a	$RMSE$	$D_{a,3}$	$D_{a,1}$	α_2	α_3	$RMSE$
1	1	0.2663	0.1499	0.2622	0.0600	0.1000	0.30	1.00	0.0180
1	2		0.0194	0.0405	0.0100	0.0050	1.00	1.00	0.0702
1	3		0.0196	0.0475	0.0080	0.0001	1.00	1.00	0.0427
1	4	0.3515	0.0122	0.0925	0.0001	0.1000	0.60	0.85	0.1269
1	5		0.0283	0.0384	0.0200	0.0250	1.00	1.00	0.0210
1	6	0.2593	0.0316	0.0497	0.0200	0.0003	1.00	1.00	0.0627
1	7	0.2737	0.0233	0.1457	0.0100	0.0250	1.00	1.00	0.1202
1	8	0.2218	0.0458	0.2549	0.0100	0.1000	0.40	1.00	0.0331
1	9	0.3217	0.0169	0.0951	0.0001	0.0001	0.60	0.85	0.1057
1	10	0.1598	0.0377	0.1283	0.0200	0.0001	0.55	1.00	0.0139
1	11	0.3184	0.0296	0.1063	0.0001	0.0001	0.55	0.85	0.1143
1	12	0.3571	0.0146	0.1485	0.0001	0.0001	0.65	0.85	0.0914
1	13		0.0694	0.2094	0.0200	0.0001	0.50	1.00	0.0236
1	14	0.2942	0.0256	0.0869	0.0200	0.0003	1.00	1.00	0.1147
1	15	0.3268	0.0131	0.1151	0.0001	0.0001	0.60	0.85	0.1041
1	16	0.2885	0.0279	0.0341	0.0001	0.1000	0.55	0.85	0.1097

Data Set, Trial Number		Model 1	Model 2		Model 3b				
		$RMSE$	D_a	$RMSE$	$D_{a,3}$	$D_{a,1}$	α_2	α_3	$RMSE$
1	17	0.1618	0.0891	0.0899	0.0600	0.0050	0.80	1.00	0.0024
1	18	0.1228	0.0319	0.1297	0.0100	0.0250	0.70	1.00	0.0235
1	19	0.2140	0.0760	0.3221	0.0001	0.0100	0.30	1.00	0.0630
1	20	0.1262	0.0402	0.0845	0.0200	0.0001	0.80	1.00	0.0136
1	21		0.0138	0.0911	0.0001	0.1000	0.60	0.85	0.1372
1	22		0.0161	0.2075	0.0070	0.0001	1.00	1.00	0.0393
1	23	0.2999	0.0322	0.2878	0.0001	0.0001	0.25	1.00	0.0780
1	24	0.3265	0.0162	0.0475	0.0001	0.0001	0.65	0.85	0.0955
1	25		0.0184	0.1613	0.0080	0.1000	0.85	1.00	0.0197
1	26	0.3200	2.5869	0.2648	0.1000	0.1000	0.20	1.00	0.0253
1	27	0.1591	0.0791	0.1345	0.0300	0.1000	0.50	1.00	0.0193
1	28	0.2656	0.0702	0.3687	0.0001	0.1000	0.30	1.00	0.0710
1	29	0.1321	0.0156	0.0809	0.0080	0.1000	0.95	1.00	0.0160
1	30		0.0386	0.2290	0.0090	0.0001	0.50	1.00	0.0294
1	31	0.2439	0.0271	0.1476	0.0100	0.0100	1.00	1.00	0.0703
1	32		0.1664	0.2815	0.0400	0.1000	0.30	1.00	0.0301
1	33	0.1565	0.0400	0.1175	0.0200	0.0100	0.85	1.00	0.0108
1	34		0.0657	0.1944	0.0200	0.1000	0.45	1.00	0.0149
1	35	0.1781	0.0515	0.1737	0.0300	0.1000	0.60	1.00	0.0104
1	36	0.3152	0.0122	0.1013	0.0001	0.0001	0.60	0.85	0.1246
2	1	0.2584	0.0219	0.0461	0.0100	0.0075	1.00	1.00	0.0208
2	3	0.1309	0.0279	0.0827	0.0100	0.1000	0.90	1.00	0.0187
2	4	0.1452	0.0244	0.1443	0.0090	0.1000	0.90	1.00	0.0231
2	5	0.2910	0.0237	0.1620	0.0100	0.0001	1.00	1.00	0.0946
2	6	0.1351	0.0482	0.1982	0.0200	0.0001	0.60	1.00	0.0231
2	7	0.2118	0.0643	0.3526	0.0060	0.1000	0.40	1.00	0.0490
2	8	0.2597	0.0186	0.0454	0.0080	0.0001	1.00	1.00	0.0543
2	9	0.1994	0.0475	0.3617	0.0001	0.0001	0.35	1.00	0.0729
2	10	0.3227	0.0202	0.1517	0.0001	0.1000	0.65	0.85	0.1005
2	11		0.0336	0.2764	0.0100	0.1000	0.75	1.00	0.0233
2	12	0.3194	0.0229	0.0341	0.0200	0.0001	1.00	1.00	0.1195
2	13	0.3280	0.0210	0.1046	0.0100	0.0001	1.00	1.00	0.1170
2	14	0.1409	0.0335	0.0792	0.0100	0.0001	0.70	1.00	0.0215
2	15	0.1420	0.0376	0.2399	0.0100	0.0001	0.75	1.00	0.0247
2	16	0.2255	0.0336	0.0658	0.0200	0.0003	1.00	1.00	0.0267
2	17	0.2638	0.0301	0.1565	0.0100	0.0001	1.00	1.00	0.0379
2	18		0.0228	0.0432	0.0001	0.0001	0.55	0.85	0.1196
2	19	0.2573	0.0276	0.0742	0.0001	0.0001	0.55	0.85	0.0571
2	20		0.0229	0.1251	0.0001	0.0003	0.55	0.85	0.1305
2	25	0.1887	0.0518	0.1715	0.0300	0.0001	0.95	1.00	0.0073
2	26	0.2759	0.0186	0.0509	0.0080	0.0003	1.00	1.00	0.0487
2	27	0.1825	0.0419	0.1026	0.0200	0.1000	0.90	1.00	0.0112
2	28	0.3897	0.0247	0.0742	0.0001	0.0001	0.60	0.85	0.1203
2	29	0.3307	0.0257	0.0347	0.0100	0.0001	1.00	1.00	0.0995
2	30	0.5026	0.0268	0.1926	0.0060	0.1000	0.75	0.85	0.1034
2	31	0.2300	0.0245	0.0310	0.0100	0.0003	1.00	1.00	0.0190

Data Set, Trial Number		Model 1	Model 2		Model 3b				
		$RMSE$	D_a	$RMSE$	$D_{a,3}$	$D_{a,1}$	α_2	α_3	$RMSE$
2	32	0.2909	0.0350	0.0307	0.0200	0.0003	1.00	1.00	0.0561
2	33	0.2319	0.0799	0.3604	0.0050	0.0001	0.25	1.00	0.0745
2	34	0.1550	0.0494	0.1232	0.0200	0.1000	0.75	1.00	0.0144
2	35	0.2382	0.0276	0.0402	0.0100	0.0003	1.00	1.00	0.0302
3	1	0.3606	0.0318	0.0817	0.0030	0.0750	1.00	0.85	0.0090
3	2	0.4318	0.0269	0.2239	0.0200	0.0001	1.00	0.75	0.0658
3	3	0.3036	0.0421	0.1659	0.0030	0.0001	0.95	0.85	0.0094
3	4	0.3133	0.1010	0.1957	0.0200	0.0250	1.00	0.65	0.0431
3	5	0.2450	0.0736	0.0377	0.0001	0.0750	0.70	0.85	0.0202
3	6	0.6886	0.0033	0.6938	0.1000	0.0001	1.00	0.70	0.2678
3	7		0.0214	0.1627	0.0010	0.0001	1.00	0.85	0.0382
3	8	0.4023	0.0198	0.1680	0.0400	0.0050	1.00	0.80	0.0708
3	9	0.5611	0.0121	0.2556	0.0900	0.0001	1.00	0.75	0.1437
3	10	0.3150	0.0961	0.1349	0.0100	0.0050	0.85	0.65	0.0219
3	11	0.3444	0.0717	0.0975	0.0200	0.0005	1.00	0.80	0.0097
3	12	0.3223	0.0293	0.1709	0.0001	0.0001	0.85	0.85	0.0509
3	13	0.1893	0.0282	0.0485	0.0200	0.0001	1.00	1.00	0.0445
3	14	0.1793	0.0598	0.0583	0.0001	0.0001	0.50	0.85	0.0307
3	15	0.3617	0.0121	0.2022	0.0001	0.0001	1.00	0.85	0.0510
3	16	0.3419	0.0044	0.2364	0.1000	0.1000	0.95	0.70	0.0392
3	17	0.3716	0.0488	0.1125	0.0300	0.0001	1.00	0.75	0.0362
3	18	0.2279	0.1180	0.0672	0.0300	0.0250	0.55	0.85	0.0076
3	19	0.2446	0.0373	0.1136	0.0001	0.1000	0.65	0.85	0.0467
3	20	0.2547	0.0587	0.0690	0.0001	0.1000	0.70	0.85	0.0265
3	21	0.2339	0.0617	0.0662	0.0020	0.0500	0.65	0.85	0.0070
3	22	0.2950	0.1872	0.1617	0.0090	0.0250	0.65	0.55	0.0264
3	23	0.3493	0.0253	0.1235	0.0001	0.1000	0.85	0.85	0.0462
3	24	0.5571	0.0137	0.2942	0.1000	0.0001	1.00	0.75	0.1645
4	1	0.2823	0.0513	0.0408	0.0001	0.1000	0.60	0.85	0.0604
4	2	0.2131	0.1878	0.0638	0.0200	0.1000	0.55	0.65	0.0112
4	3	0.2274	0.0334	0.0750	0.0001	0.0750	0.55	0.85	0.0645
4	4	0.2043	0.0972	0.0630	0.0060	0.1000	0.45	0.85	0.0057
4	6	0.1979	0.0814	0.0719	0.0001	0.0003	0.45	0.80	0.0080
4	7	0.2429	0.0661	0.0724	0.0010	0.0075	0.65	0.85	0.0082
4	8	0.5291	0.0098	0.2426	0.0600	0.0025	1.00	0.80	0.1227
4	9	0.3295	0.0221	0.1145	0.0090	0.0001	1.00	0.80	0.0306
4	10	0.2212	0.0305	0.0509	0.0001	0.1000	0.60	0.85	0.0268
4	11	0.2026	0.1655	0.1331	0.0001	0.0100	0.45	0.85	0.0090
4	12	0.1073	0.0522	0.0775	0.0200	0.0001	0.70	1.00	0.0141
4	13	0.1797	0.0754	0.0452	0.0400	0.1000	1.00	1.00	0.0297
4	14		0.0231	0.0888	0.0001	0.0001	0.60	0.85	0.0973
4	15	0.3395	0.0086	0.1595	0.0001	0.1000	0.80	0.85	0.0893
4	16	0.6212	0.0049	0.3134	0.1000	0.0001	1.00	0.75	0.1574
4	17	0.2115	0.3340	0.0529	0.0500	0.0001	0.60	0.65	0.0109
4	18	0.1953	0.0884	0.0318	0.0001	0.0750	0.50	0.85	0.0291
4	19	0.2523	0.0257	0.0751	0.0100	0.0001	1.00	1.00	0.0778

Data Set, Trial Number		Model 1	Model 2		Model 3b				
		$RMSE$	D_a	$RMSE$	$D_{a,3}$	$D_{a,1}$	α_2	α_3	$RMSE$
4	20	0.1979	0.0828	0.0300	0.0001	0.1000	0.50	0.85	0.0404
4	21	0.2768	0.0225	0.0410	0.0001	0.0050	0.60	0.85	0.0813
4	22	0.2720	0.0090	0.1362	0.0001	0.0001	0.85	0.85	0.0515
4	23	0.2876	0.0187	0.0560	0.0001	0.0100	0.65	0.85	0.0780
4	24	0.2632	0.2184	0.0952	0.0200	0.0500	1.00	0.60	0.0234

Data Set, Trial Number		Model 3a			Model 3c				
		$D_{a,3}$	$D_{a,1}$	$RMSE$	$D_{a,3}$	$D_{a,1}$	α_2	α_3	$RMSE$
1	1	0.0100	0.0075	0.0102	0.0600	0.1000	0.30	1.00	0.0180
1	2	0.0200	0.0250	0.0875	0.0100	0.1000	1.00	0.90	0.0177
1	3	0.0400	0.1000	0.0591	0.0001	0.1000	0.85	0.90	0.0276
1	4	0.0200	0.0010	0.2984	0.0001	0.0025	1.00	0.85	0.0643
1	5	0.0300	0.0050	0.2837	0.0200	0.0250	1.00	1.00	0.0210
1	6	0.0500	0.0003	0.3062	0.0100	0.0003	0.90	0.90	0.0214
1	7	0.0300	0.0250	0.2250	0.0050	0.0250	1.00	0.90	0.0386
1	8	0.0200	0.0001	0.0337	0.0050	0.1000	0.50	0.95	0.0223
1	9	0.0300	0.0250	0.0570	0.0001	0.1000	1.00	0.85	0.0408
1	10	0.0200	0.0008	0.0798	0.0200	0.0001	0.55	1.00	0.0139
1	11	0.0200	0.0005	0.0647	0.0100	0.0250	1.00	0.90	0.0384
1	12	0.0200	0.0001	0.0814	0.0020	0.0050	1.00	0.85	0.0486
1	13	0.0100	0.0001	0.0875	0.0100	0.0001	0.70	0.95	0.0206
1	14	0.0300	0.1000	0.0745	0.0100	0.0003	1.00	0.90	0.0356
1	15	0.0300	0.0001	0.0501	0.0001	0.0750	1.00	0.85	0.0404
1	16	0.0200	0.0003	0.0279	0.0100	0.0001	1.00	0.90	0.0361
1	17	0.0100	0.0001	0.0290	0.0600	0.0050	0.80	1.00	0.0024
1	18	0.0200	0.0250	0.1080	0.0100	0.0250	0.70	1.00	0.0235
1	19	0.0200	0.0050	0.0786	0.0001	0.0250	0.40	0.70	0.0368
1	20	0.0300	0.0001	0.0108	0.0200	0.0001	0.80	1.00	0.0136
1	21	0.0080	0.0003	0.0452	0.0030	0.0005	1.00	0.90	0.0681
1	22	0.0300	0.1000	0.0175	0.0010	0.1000	0.85	0.90	0.0279
1	23	0.0300	0.0250	0.0723	0.0001	0.0010	0.35	0.95	0.0536
1	24	0.0100	0.0001	0.0687	0.0010	0.0050	1.00	0.85	0.0402
1	25	0.0200	0.1000	0.0207	0.0080	0.1000	0.85	1.00	0.0197
1	26	0.0400	0.0003	0.0746	0.0400	0.1000	0.20	0.95	0.0184
1	27	0.0100	0.0003	0.0147	0.0200	0.1000	0.70	0.95	0.0188
1	28	0.0200	0.0003	0.0384	0.0001	0.0250	0.55	0.60	0.0502
1	29	0.1000	0.0001	0.3136	0.0080	0.1000	0.95	1.00	0.0160
1	30	0.0100	0.0003	0.0216	0.0050	0.1000	0.75	0.95	0.0222
1	31	0.0100	0.1000	0.0289	0.0100	0.0025	0.95	0.90	0.0200
1	32	0.0100	0.0001	0.0562	0.0100	0.1000	0.35	0.95	0.0228
1	33	0.0900	0.0001	0.0832	0.0200	0.0100	0.85	1.00	0.0108
1	34	0.1000	0.1000	0.1192	0.0200	0.1000	0.45	1.00	0.0149
1	35	0.0080	0.0001	0.0297	0.0300	0.1000	0.60	1.00	0.0104
1	36	0.1000	0.0003	0.2076	0.0001	0.0750	1.00	0.85	0.0594
2	1	0.0100	0.0010	0.3861	0.0100	0.0075	1.00	1.00	0.0208
2	3	0.0200	0.0001	0.6735	0.0100	0.1000	0.90	1.00	0.0187

Data Set, Trial Number		Model 3a			Model 3c				
		$D_{a,3}$	$D_{a,1}$	$RMSE$	$D_{a,3}$	$D_{a,1}$	α_2	α_3	$RMSE$
2	4	0.0090	0.0001	0.3435	0.0090	0.1000	0.90	1.00	0.0231
2	5	0.0200	0.0001	1.0289	0.0030	0.0001	1.00	0.90	0.0219
2	6	0.0900	0.0001	0.1455	0.0070	0.0250	0.90	0.95	0.0219
2	7	0.0500	0.0005	0.0584	0.0001	0.1000	0.55	0.95	0.0290
2	8	0.0100	0.0001	0.0953	0.0001	0.1000	0.90	0.90	0.0259
2	9	0.0600	0.0750	0.1260	0.0001	0.0001	0.50	0.95	0.0455
2	10	0.1000	0.0001	0.6891	0.0001	0.0005	1.00	0.85	0.0489
2	11	0.0300	0.0001	0.4031	0.0100	0.1000	0.75	1.00	0.0233
2	12	0.0500	0.0250	0.1438	0.0070	0.0001	1.00	0.90	0.0367
2	13	0.0300	0.0003	0.1608	0.0070	0.0001	1.00	0.90	0.0352
2	14	0.0200	0.0001	0.5656	0.0100	0.0001	0.70	1.00	0.0215
2	15	0.0400	0.0003	0.1569	0.0100	0.0001	0.75	1.00	0.0247
2	16	0.0300	0.0750	0.1821	0.0090	0.1000	0.80	0.90	0.0227
2	17	0.0200	0.0100	0.3915	0.0030	0.0025	0.80	0.90	0.0254
2	18	0.0200	0.0001	0.3120	0.0090	0.0250	1.00	0.90	0.0429
2	19	0.0200	0.0001	0.6379	0.0200	0.0050	1.00	0.90	0.0144
2	20	0.0300	0.0500	0.2972	0.0050	0.0250	1.00	0.90	0.0498
2	25	0.0200	0.0100	0.4868	0.0300	0.0001	0.95	1.00	0.0073
2	26	0.0400	0.0001	0.1841	0.0001	0.1000	0.85	0.90	0.0260
2	27	0.0500	0.0001	0.6209	0.0200	0.1000	0.90	1.00	0.0112
2	28	0.0200	0.0001	0.4169	0.0001	0.0250	1.00	0.85	0.0653
2	29	0.0300	0.0050	0.5252	0.0070	0.0005	1.00	0.90	0.0255
2	30	0.0300	0.0001	0.1479	0.0300	0.0008	1.00	0.85	0.0940
2	31	0.0300	0.0003	0.1343	0.0100	0.0003	1.00	1.00	0.0190
2	32	0.0900	0.1000	0.0577	0.0100	0.0250	0.90	0.90	0.0218
2	33	0.0500	0.0003	0.0416	0.0001	0.0001	0.30	0.95	0.0575
2	34	0.0400	0.1000	0.0323	0.0200	0.1000	0.75	1.00	0.0144
2	35	0.0200	0.0250	0.1312	0.0060	0.1000	0.80	0.90	0.0245
3	1	0.0500	0.0005	0.0280	0.0100	0.0010	1.00	0.75	0.0825
3	2	0.0400	0.0100	0.1492	0.0200	0.0001	1.00	0.75	0.1535
3	3	0.0300	0.0600	0.1653	0.0200	0.0500	1.00	0.80	0.0616
3	4	0.0200	0.0100	0.2090	0.1000	0.0250	0.95	0.50	0.0774
3	5	0.0400	0.0002	0.1082	0.0200	0.0001	1.00	0.80	0.0259
3	6	0.0500	0.0000	0.5749	0.1000	0.0001	1.00	0.50	0.3094
3	7	0.0200	0.0000	0.2301	0.0100	0.0001	1.00	0.80	0.1029
3	8	0.0300	0.0060	0.2787	0.0300	0.0050	1.00	0.75	0.1583
3	9	0.0200	0.0000	0.4001	0.0300	0.0001	1.00	0.70	0.2502
3	10	0.0200	0.0001	0.0924	0.0200	0.0050	1.00	0.70	0.0526
3	11	0.0090	0.0100	0.2676	0.0001	0.0008	0.95	0.60	0.0675
3	12	0.0100	0.0003	0.1398	0.0200	0.0250	1.00	0.85	0.0650
3	13	0.0400	0.0025	0.2563	0.0100	0.1000	0.90	0.90	0.0176
3	14	0.0200	0.0010	0.0701	0.0500	0.0250	1.00	0.90	0.0094
3	15	0.0500	0.0750	0.0423	0.0080	0.0010	1.00	0.80	0.0979
3	16				0.1000	0.1000	0.85	0.50	0.0472
3	17	0.0400	0.0750	0.0453	0.0300	0.0001	1.00	0.75	0.1159
3	18	0.0300	0.0001	0.1147	0.0200	0.1000	0.85	0.75	0.0192
3	19	0.0300	0.0025	0.3615	0.0060	0.0001	1.00	0.85	0.0204

Data Set, Trial Number		Model 3a			Model 3c				
		$D_{a,3}$	$D_{a,1}$	$RMSE$	$D_{a,3}$	$D_{a,1}$	α_2	α_3	$RMSE$
3	20	0.0400	0.0002	0.1132	0.0100	0.0001	1.00	0.80	0.0281
3	21	0.0300	0.0600	0.1022	0.0100	0.1000	1.00	0.80	0.0205
3	22	0.0200	0.0000	0.1189	0.0300	0.0250	0.50	0.50	0.0320
3	23	0.0200	0.0000	0.2005	0.0100	0.0001	1.00	0.80	0.0775
3	24	0.0200	0.0000	0.4034	0.1000	0.0001	1.00	0.50	0.2151
4	1	0.0300	0.0002	0.1046	0.0060	0.0003	1.00	0.85	0.0164
4	2	0.0600	0.0800	0.0830	0.0300	0.1000	0.75	0.70	0.0201
4	3	0.0200	0.0008	0.0813	0.0020	0.1000	0.90	0.85	0.0155
4	4	0.0500	0.0800	0.0500	0.0100	0.1000	0.60	0.75	0.0153
4	6	0.0400	0.0800	0.0506	0.0200	0.1000	0.65	0.80	0.0149
4	7	0.0300	0.0001	0.1011	0.0200	0.1000	0.95	0.80	0.0205
4	8	0.0300	0.0040	0.3689	0.0300	0.0025	1.00	0.75	0.2210
4	9	0.0400	0.0100	0.1863	0.0001	0.1000	1.00	0.65	0.0741
4	10	0.0300	0.0008	0.0830	0.0200	0.0001	0.95	0.85	0.0168
4	11	0.0900	0.1000	0.0336	0.0300	0.1000	0.60	0.80	0.0102
4	12	0.0500	0.0001	0.0535	0.0200	0.0001	0.70	1.00	0.0141
4	13	0.0400	0.1000	0.0297	0.0500	0.0001	0.85	0.90	0.0095
4	14	0.0200	0.0200	0.1125	0.0010	0.1000	1.00	0.85	0.0363
4	15	0.0090	0.0000	0.1868	0.0030	0.0001	1.00	0.85	0.0783
4	16	0.0200	0.0000	0.4623	0.1000	0.0001	1.00	0.50	0.2057
4	17	0.0900	0.0001	0.0825	0.0700	0.0001	0.85	0.70	0.0183
4	18	0.0500	0.0006	0.0525	0.0700	0.0025	1.00	0.90	0.0111
4	19	0.0100	0.0001	0.0778	0.0100	0.0001	1.00	0.90	0.0191
4	20	0.0500	0.0006	0.0435	0.0700	0.0001	0.95	0.90	0.0073
4	21	0.0200	0.0001	0.1134	0.0010	0.0001	1.00	0.85	0.0275
4	22	0.0090	0.0100	0.1495	0.0060	0.0075	1.00	0.85	0.0650
4	23	0.0100	0.0002	0.1305	0.0020	0.0003	1.00	0.85	0.0358
4	24	0.0400	0.0020	0.1338	0.0300	0.0025	1.00	0.65	0.0456

K. Design of experiments – Axial dispersion coefficient in spiral-wound membranes (sampled from data sets 1 – 4)

Data Set, Trial Number		Aspect Ratio (-)	$\log_{10}(k_{MP})$ Pa·s^n)		$\log_{10}(k_{DF})$ (Pa·s^n)		Flow rate (m^3/h)		$D_{a,3}$ (m^2/s)	Bypass (%)
			Target	Actual	Target	Actual	Target	Actual		
2	18	0.53	-2.50	-2.45	-3.00	-2.99	10.50	13.46	0.009	10
3	2	0.53	-2.50	-1.35	0.50	0.52	14.00	4.85	0.02	15
1	10	0.55	0.50	-0.51	-1.25	-2.89	7.00	6.76	0.02	0
1	20	0.55	0.20	-0.20	-3.00	-3.00	13.23	13.72	0.02	0
3	10	0.53	0.50	-0.59	-1.25	0.00	14.00	7.38	0.01	35
4	23	0.53	-2.50	-2.92	-1.25	-2.87	7.00	8.36	0.002	15
3	3	0.55	0.50	-1.27	0.50	0.00	14.00	9.53	0.003	15
4	19	0.55	-2.50	-2.92	-1.25	-2.88	14.00	13.91	0.01	10
4	1	0.59	-2.50	-2.92	-3.00	-2.88	14.00	14.13	0.006	10
3	9	0.59	0.50	-0.40	0.50	0.52	7.00	5.48	0.03	25
3	8	0.59	-1.00	-0.37	-3.00	-2.92	7.00	7.42	0.04	10

Data Set, Trial Number		Aspect Ratio (-)	log$_{10}$(k$_{MP}$) Pa·s^{n})		log$_{10}$(k$_{DF}$) (Pa·s^{n})		Flow rate (m^3/h)		$D_{a,3}$ (m^2/s)	Bypass (%)
			Target	Actual	Target	Actual	Target	Actual		
4	17	0.59	0.50	0.52	-3.00	-2.88	14.00	13.85	0.05	35
2	11	0.59	-1.00	-1.43	-1.25	-3.00	10.50	12.97	0.01	0
1	35	0.53	0.50	-0.35	-3.00	-2.93	7.00	6.82	0.03	0
3	24	0.59	-2.50	-1.27	0.50	0.16	7.00	3.38	0.1	25
2	1	0.55	-1.00	-1.30	-1.25	-2.99	10.50	10.95	0.01	0
3	13	0.55	-1.00	-0.34	0.50	0.52	7.00	11.94	0.01	10
3	14	0.55	-2.50	-0.33	0.50	-2.92	10.50	12.91	0.05	10
1	31	0.59	-1.00	-1.85	-1.25	-3.04	10.50	10.78	0.01	10
3	18	0.53	0.50	-0.36	0.50	0.00	10.50	13.12	0.03	15
2	34	0.53	-1.00	-1.01	-3.00	-2.94	14.00	14.38	0.02	0
1	12	0.55	-2.50	-2.45	-3.00	-2.90	7.00	7.44	0.002	15
1	2	0.53	-1.00	-2.44	0.50	-3.05	7.00	7.46	0.01	10
3	11	0.59	-1.00	-1.25	0.50	0.52	14.00	12.02	0.02	20

L. Validation data (sampled from data sets 1 – 4)

Data Set, Trial Number		Aspect Ratio (-)	log$_{10}$(k$_{MP}$) Pa·s^{n})		log$_{10}$(k$_{DF}$) (Pa·s^{n})		Flow rate (m^3/h)		$D_{a,3}$ (m^2/s)	Bypass (%)
			Target	Actual	Target	Actual	Target	Actual		
1	16	0.53	–	-2.40	–	-3.06	–	13.94	0.01	10
1	17	0.53	–	0.31	–	-2.90	–	14.16	0.06	0
1	25	0.53	–	-0.93	–	-3.06	–	7.94	0.008	0
1	33	0.53	–	-1.36	–	-2.98	–	12.22	0.02	0
1	34	0.53	–	0.09	–	-2.90	–	8.01	0.02	0
1	6	0.53	–	-2.46	–	-2.89	–	14.42	0.01	10
2	12	0.53	–	-2.46	–	-3.00	–	13.89	0.007	10
2	16	0.53	–	-1.38	–	-3.01	–	14.15	0.009	10
2	27	0.53	–	-1.35	–	-3.00	–	14.12	0.02	0
2	29	0.53	–	-2.47	–	-3.02	–	14.62	0.007	10
2	30	0.53	–	-2.27	–	-3.01	–	14.86	0.03	15
2	4	0.53	–	-2.17	–	-3.00	–	14.35	0.009	0
4	10	0.53	–	0.00	–	-2.91	–	6.33	0.02	15
4	2	0.53	–	0.52	–	-2.88	–	10.49	0.02	35
1	21	0.55	–	-2.44	–	-3.05	–	11.78	0.003	10
1	29	0.55	–	-0.96	–	-3.04	–	7.72	0.008	0
1	5	0.55	–	-2.12	–	-2.89	–	13.55	0.02	0
2	13	0.55	–	-2.45	–	-3.00	–	13.93	0.007	10
2	14	0.55	–	-1.02	–	-3.00	–	13.75	0.01	0
2	19	0.55	–	-1.11	–	-3.01	–	7.54	0.02	10
2	31	0.55	–	-1.34	–	-3.03	–	14.27	0.01	0
4	15	0.55	–	-2.92	–	-2.89	–	5.37	0.003	15
1	11	0.59	–	-2.44	–	-2.89	–	13.56	0.01	10
1	26	0.59	–	-0.27	–	-2.89	–	6.43	0.04	5
1	7	0.59	–	-2.48	–	-3.06	–	12.69	0.005	10
2	15	0.59	–	-1.38	–	-2.99	–	13.66	0.01	0

Data Set, Trial Number		Aspect Ratio (-)	log10(kMP) Pa·s^n)		log10(kDF) (Pa·s^n)		Flow rate (m^3/h)		$D_{a,3}$ (m^2/s)	Bypass (%)
			Target	Actual	Target	Actual	Target	Actual		
2	20	0.59	–	-2.39	–	-3.00	–	13.32	0.005	10
2	25	0.59	–	-1.33	–	-3.01	–	13.59	0.03	0
2	5	0.59	–	-2.45	–	-2.99	–	13.84	0.003	10
4	24	0.59	–	0.16	–	-2.88	–	6.51	0.02	40

M. Residence times – Displacement of industrial-scale plants

Data Set, Trial Number		Displacement Scenario	Residence time (s)			
			1 x 1 SWM	1 x 4 SWM	2 x 4 SWM	3 x 4 SWM
1	1	SW → PC	53.5	105.5	188.7	265
1	2	SW → PC	39.5	81.4	141.1	200.5
1	3	SW → PC	10.5	27.7	51.8	74.5
1	4	SW → PC	20.5	51.5	91.9	131.2
1	5	SW → PC	17	37.5	77.8	110.4
1	6	SW → PC	9	24.2		
1	7	SW → PC	20	50.3	91.2	130.8
1	8	SW → PC	10.5	27.3	50.5	
1	9	SW → PC	18	36.4	65.8	93.4
1	10	SW → PC	13	30.2	56	80.7
1	11	SW → PC	21.5	45.1	75.2	106.6
1	12	SW → PC	23.5	54.5	100.1	143.1
1	13	SW → PC	14.5	34.1	60.3	86.4
1	14	SW → PC	11	31	57.5	83.1
1	15	SW → PC	19	46.5	84.4	122
1	16	SW → PC	49.5	98.1	175.5	250.6
1	17	SW → PC	21	48.9	88.7	126.9
1	18	SW → PC	23.5	54.8	100.4	145
1	19	SW → PC	75.5	118.8	295.2	408.4
1	20	SW → PC	17.5	33.9	74.3	104.9
1	21	SW → PC	22.5	48.9	88.6	128.8
1	22	SW → PC	23	56.3	103	148.6
1	23	SW → PC	10	24.8	45.9	66.4
1	24	SW → PC	21.5	53.8	102.3	146
1	25	SW → PC	14.5	36.2	66.8	95.9
1	26	SW → PC	25.5	53.5	98.5	139
1	27	SW → PC	15.3	37.6	67.2	96.5
1	28	SW → PC	32	69.2	120	170.5
1	29	SW → PC	33.5	79.7	144	204.1
1	30	SW → PC	16	40.7	74.4	106.6
1	31	SW → PC	20	51.3	93.4	134
1	32	SW → PC	12.5	30.4	59.5	85.5
1	33	SW → PC	10.5	26.7	49.4	70.9
1	34	SW → PC	11	29	53.8	77.7
1	35	SW → PC	36.5	84.9	159.8	227
1	36	SW → PC	20.5	50.2	91	130.4
2	1	SW → PC	13	36.3	70.9	102.4

Data Set, Trial Number		Displacement Scenario	Residence time (s)			
			1 x 1 SWM	1 x 4 SWM	2 x 4 SWM	3 x 4 SWM
2	3	SW → PC	15.5	24.5	44.6	63.9
2	4	SW → PC	12.5	32.6	60.6	87.5
2	5	SW → PC	9.5	26.7	49.7	
2	6	SW → PC	9.5	26.7	49.7	
2	7	SW → PC	12.5	31.5	58.5	84.3
2	8	SW → PC	12.5	31.3	57.4	83
2	9	SW → PC	11.5	27.7	50.9	73
2	10	SW → PC	10.5	27.2	50.1	72.3
2	11	SW → PC	9.5	27.7	52.1	74.9
2	12	SW → PC	24	53.6	107.8	152.7
2	13	SW → PC	9.9	27.5	51.1	73.8
2	14	SW → PC	13	32.8	60.5	86.7
2	15	SW → PC	9.5	25.9	47.8	69.2
2	16	SW → PC	12	31.8	56.8	81.6
2	17	SW → PC	9	26.8	48.5	69.5
2	18	SW → PC	10	25.3	47.1	67.9
2	19	SW → PC	12	28.9	53.2	76.9
2	20	SW → PC	8	28.3	50.5	70.8
2	25	SW → PC	10.5	28.7	53.2	77.1
2	26	SW → PC	10.5	26.6	48.8	70
2	27	SW → PC	26.5	68.6	120.9	171.8
2	28	SW → PC	13	32.1	57	81.9
2	29	SW → PC	11	27.6	50.3	72.3
2	30	SW → PC	10.5	28.6	52.8	76.6
2	31	SW → PC	9	26.3	48.4	70.1
2	32	SW → PC	14	33.4	73.1	104.3
2	33	SW → PC	17	36.6	67	96.7
2	34	SW → PC	10	25.8	47.6	69
2	35	SW → PC	18	40.4	73.6	106
3	1	XS → PC	38.5	95.2	162.5	225.5
3	2	XS → PC	31.9	76.7	123.2	169.1
3	3	XS → PC	19	38.4	63	86.6
3	4	XS → PC	18	29	54	75.9
3	5	XS → PC	17.5	33.4	60.7	87
3	6	XS → PC	24.9	36.3	66.4	93.6
3	7	XS → PC	40	86.1	147.2	205.4
3	8	XS → PC	61	117.9	1774.9	2348
3	9	XS → PC	40	64.2	110.8	152.5
3	10	XS → PC	20	37.2	61.4	85.3
3	11	XS → PC	17.5	27.4	48.7	
3	12	XS → PC	42	106.1	188.5	258.7
3	13	XS → PC	11.5	29.2	51.2	
3	14	XS → PC	26.5	43.4	75.4	105.7
3	15	XS → PC	65.5	118.5	695.6	930.6
3	16	XS → PC	22.5	55	95.2	133.3
3	17	XS → PC	60	118.3	720.6	958
3	18	XS → PC	29.5	50.6	83.3	115.7

Data Set, Trial Number		Displacement Scenario	Residence time (s)			
			1 x 1 SWM	1 x 4 SWM	2 x 4 SWM	3 x 4 SWM
3	19	XS → PC	70.5	118.2	742.1	983.5
3	20	XS → PC	25.5	29	53.1	
3	21	XS → PC	14	118.3	391.7	520.1
3	22	XS → PC	24.5	67.1	116	162.1
3	23	XS → PC	28.5	69.3	119.6	164.4
3	24	XS → PC	29	104.3	182.6	249.1
4	1	SW → XS	14.5	26.9	48	68.4
4	2	SW → XS	27.5	36.5	62	87.2
4	3	SW → XS	19	29.4	46.7	65.1
4	4	SW → XS	14	25.7		
4	5	SW → XS	13.9	24.4		
4	6	SW → XS	14	27.2	49.6	71
4	7	SW → XS	33.5	72.8	131	186.2
4	8	SW → XS	39	118.3	748.2	994.5
4	9	SW → XS	33.5	42.8	71	95
4	10	SW → XS	16.5	25.9	52.1	73.3
4	11	SW → XS	14	27.5	50.8	
4	12	SW → XS	37	55.8	88.8	121.9
4	13	SW → XS	15	28.5		
4	14	SW → XS	20.5	37.2	67.5	96.5
4	15	SW → XS	61	94.8	167.7	236.3
4	16	SW → XS	23.5	45.4	81.3	116.2
4	17	SW → XS	70	93.7	160.2	218.1
4	18	SW → XS	18	31.1	55.9	79.8
4	19	SW → XS	27	46.6	80.1	111.7
4	20	SW → XS				
4	21	SW → XS	27	50.6	78	108.6
4	22	SW → XS	26.5	42.4	78.1	108.8
4	23	SW → XS	19.5	67.1	115.7	159.1
4	24	SW → XS	34	42.5	70.4	97.5

N. R scripts – Mechanistic models

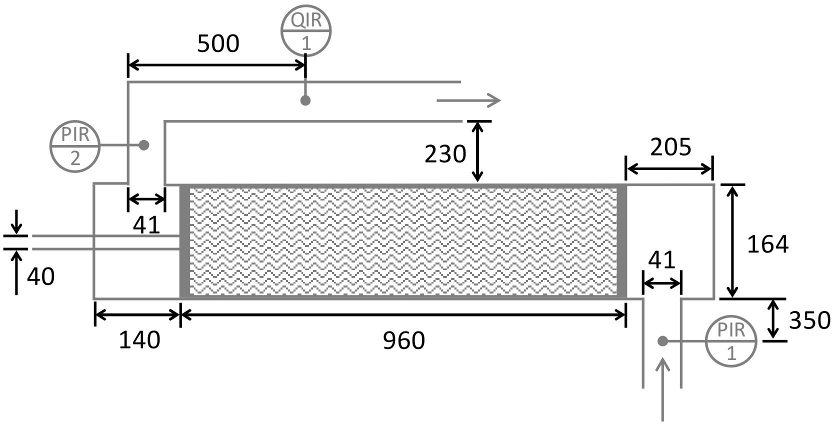

Fig. M1: Dimensions (mm) of the experimental setup.

```
# Load general information
setwd("Z:\\Eigene Dokumente\\...")
AnalysisData <- read.table("AnalysisData.csv")
# [1] Test Series, [2] Experiment Number [3] Protein Concentration (%), [4] Spacer
  Thickness (mil), [5] Hydraulic Diameter [m], [8] Flow Rate (m3/h), [9] Porosity
(-),
  [11] Displacement Time (s), [12] Xanthan Concentration (%)

# Normalized cumulative distribution curves of all experiments in a list
SumCurves <- read.table("SumCurves.csv")
# Flow rates of all experiments in a list
VolumeFlows <- read.table("VolumeFlows.csv")
# Shape and scale parameters of all experiments in a matrix
WeibullParams <- read.table("WeibullParams.csv")
# Denotation of all experiments in a matrix
ExpRuns <- names(SumCurves)
ExpRuns <- ExpRuns[2:length(ExpRuns)]

# Volume pipe
V1 <- pi*((0.0408/2)^2)*(0.35)
# Volume mixing zone
V2 <- pi*((0.164/2)^2)*0.205
# Total volume spiral-wound membrane
V3 <- pi*((0.164/2)^2)*0.96
# Volume mixing zone
V4 <- pi*(((0.164/2)^2)-((0.04/2)^2))*0.14
# Volume pipe
V5 <- pi*((0.0408/2)^2)*(0.23+0.5)
```

```
#############################
############### Compartment model
#############################
tR.diff <- rep(NA, length(ExpRuns))
SSE <- rep(NA, length(ExpRuns))

for (i in 1:length(ExpRuns)){

  tR <- AnalysisData[i, 11]                              # residence time [s]
  time <- seq(0, tR-0.2, 0.1)
  V.Flow <- VolumeFlows[[1+i]]                           # feed volume flow [m3/h]
  V.F <- rep(NA, length(time))
  V.F <- V.Flow[1:length(time)]/3600
  F.t <- (exp(-(2*V.F*(time-
((V1+V3+V5)/V.F)))/((V2+V4)/2)))*(1+(2*time*V.F)/((V2+V4)/2))
  F.t <- 1-F.t

  SC <- SumCurves[[1+i]]
  scaleP <- WeibullParams[i,2]
  shapeP <- WeibullParams[i,3]
  WeibullPlot <- (1-exp(-(scaleP*time)^shapeP))

  tR.W <- time[which.max(WeibullPlot>0.99)]               # SM = single module
  tR.BC <- time[which.max(F.t>0.99)]                      # MSP = multi stage
  tR.diff[i] <- tR.W-tR.BC

  # sum of squared errors (SSE)
  SSE[i] <- sum((WeibullPlot[1:(tR*10-0.1)]-F.t[1:(tR*10-0.1)])^2)
}


#############################
################ Advection-dispersion model
#############################
L.R <- 2.39                   # module length + mixing zones + pipes
time <- seq(0, 120, 0.1)      # max. observed residence time = 113.5 s
position <- seq(0, L, 0.01)
SSE <- rep(NA, length(ExpRuns))

for (i in 1:length(ExpRuns)){

  tR <- AnalysisData[i, 11]     # residence time [s]
  d.h <- AnalysisData[i, 5]     # hydraulic diameter (m)
  c.0 <- AnalysisData[i, 3]     # initial protein concentration (%)
  c.X <- AnalysisData[i, 12]    # xanthan concentration (%)
```

```
  FVol <- VolumeFlows[[1+i]]    # feed volume flow [m3/h]
  V.F <- c(FVol[1:(tR*10-0.1)], rep(mean(FVol[((tR*10)-20):(tR*10-0.1)]),
        (length(  time)-(tR*10))))
  SC <- SumCurves[[1+i]]
  scaleP <- Weibull_Params[i,2]
  shapeP <- Weibull_Params[i,3]
  WeibullPlot <- 1-exp(-(scaleP*time)^shapeP)

  F.t.matrix <- matrix(nrow=length(time), ncol=length(position), NA)
  C.t.matrix <- matrix(nrow=length(time), ncol=length(position), NA)
  F.t.matrix[1, ] <- 0
  C.t.matrix[1, ] <- c.0

  for (j in 2:(length(time))){
    for (k in 2:(length(position)-1)){
      u.ax <- (V.F[j]/3600)/A.eff
      D.ax <- (u.ax*L)/AnalysisData[i, 13]  # Péclet number ()
      z <- (position[k]-u.ax*time[j])/(2*sqrt(D.ax*time[j]))
      # erf(z) = 2*pnorm(sqrt(2)*z) - 1
      F.t.matrix[j,k] <- 1/2*(1-(2*pnorm(sqrt(2)*z)-1))
      c.out <- (1-F.t.matrix[j,k])*c.0
      C.t.matrix [j,k] <- c.out
    }
  }
  # sum of squared errors (SSE)
  SSE[i] <- sum((WeibullPlot[1:(tR*10)]-F.t.matrix[(1:(tR*10)),
           (length(position)-(  L-L.R)*100-1)])^2)
}



#############################
############### Hybrid models
#############################

# Mathematical approach
# 1. Deconvolution of output functions after step input function in order to
     obtain transfer functions of the compartments
# 2. Convolution of transfer functions of single compartments
# 3. Comparison of convolutes with measurements signals
# input function + system / transfer function = output function
# x = input vector, h = system / transfer function of compartment,
  y = output function ~ convolution of x and h


a <- seq(1,9,1)
b <- c(2.5,5,7.5,10)
```

```
# axial dispersion coefficient in compartment 3
D.ax.SWM <- c(10^-4, a*10^-3, a*10^-2, 10^-1)

# axial dispersion coefficient in compartment 1 and 5
D.ax.P <- c(10^-4, b*10^-4, b*10^-3, b*10^-2)
# share of total volume flow entering compartment 2 and 4
FV.main.mix <- rev(seq(0, 1, 0.05))
# share of total volume flow entering compartment 3
FV.main.SWM <- rev(seq(0.5, 1, 0.05))
# Creation of full factorial design
Parameters <- expand.grid(Factor1 = D.ax.SWM, Factor2 = D.ax.P,
              Factor3 = FV.main.mix, Factor4 = FV.main.SWM)
Parameters <- cbind(Parameters, rep(NA, nrow(Parameters)))
Best.Params <- matrix(NA, nrow=length(ExpRuns), ncol=5)


for (i in 1: length(ExpRuns))
  # porosity porous medium [-]
  epsilon <- if(d.h==0.000766674) {0.43179589} else if (d.h==0.001066011) {0.49987558} else {0.56347376}
  # aspect ratio [-]
  a.R <- if(d.h==0.000766674) {0.587301587} else if (d.h==0.001066011) {0.532258065} else {0.553030303}
  # effective area [m2]
  A.eff <- (((6.3/2)*0.0254)^2)*pi*epsilon

  ExpSumCurve <- as.matrix(SumCurves[i+1])
  scaleP <- Weibull_Params_Table[i,2]
  tR <- AnalysisData[i, 11]                  # residence time [s]
  time <- seq(0, 119.9, 0.1)
  FV <- AnalysisData[i,8]/3600               # average flow rate [m3/s]
  time <- seq(0, (length(time)/10-0.1), 0.1)
  shapeP <- Weibull_Params_Table[i,3]
  WeibullPlot <- (1-exp(-(scaleP*time)^shapeP))

  for (u in 1:(nrow(Parameters))) {
    D.SWM <- Parameters[u, 1]
    D.P <- Parameters[u, 2]
    FV.m <- FV*Parameters[u, 3]
    FV.by.SWM <- FV*(1-Parameters[u, 4])
    FV.SWM <- if (Parameters[u, 4]==1) {FV} else {FV*Parameters[u, 4]}
    V.by.SWM <- (pi*(((0.164^2)-(0.158^2))/4)*0.96)
    V.SWM <- if (Parameters[u, 4]==1) {V3} else {V3-V.by.SWM}
    u.SWM <- (FV.SWM)/A.eff.SWM
    # 0.52993 = porosity of spacer wrap
    u.by.SWM <- (FV.by.SWM)/((pi*(((0.164^2)-(0.158^2))/4)*0.52993)/epsilon)
```

No bypass

```
    # output function compartment 1: Impulse + Pipe / Plug flow
    E.yc1 <- {(1/(V1/FV))*(1/(sqrt(4*pi*(D.P/(u.P*L.P1)))))
             *exp(-(((1-time/(V1/FV))^2)/(4*(D.P/(u.P*L.P1)))))}
    # output function compartment 2: Impulse + Mixing zone / Stirred tank reactor
    E.yc2 <- {((FV.m^2)/(V2*FV))*exp(-(FV.m/V2)*time)}
    # output function compartment 3: Impulse + SWM / Plug flow + Dispersion
    E.yc3 <- ((1/(V.SWM/FV.SWM))*(1/(sqrt(4*pi*(D.SWM/(u.SWM*L.SWM)))))
              *exp(-(((1-time/(V.SWM/FV.SWM))^2)/(4*(D.SWM/(u.SWM*L.SWM))))))
    # output function compartment 4: Impulse + Mixing zone / Stirred tank reactor
    E.yc4 <- {((FV.m^2)/(V4*FV))*exp(-(FV.m/V4)*time)}
    # output function compartment 5: Impulse + Pipe5 / Plug flow
    E.yc5 <- {(1/(V5/FV))*(1/(sqrt(4*pi*(D.P/(u.P*L.P5)))))
              *exp(-(((1-time/(V5/FV))^2)/(4*(D.P/(u.P*L.P5)))))}
```

Model I (stirred-tank bypass)

```
    E.yc1 <- {(1/(V1/FV))*(1/(sqrt(4*pi*(D.P/(u.P*L.P1)))))
             *exp(-(((1-time/(V1/FV))^2)/(4*(D.P/(u.P*L.P1)))))}
    # output function compartment 2: Stirred tank reactor + Bypass
    E.yc2 <- {((FV.m^2)/(V2*FV))*exp(-(FV.m/V2)*time)}

    # output function compartment 3: Plug flow + Dispersion + Bypass
    E.yc3.main <- ((1/(V.SWM/FV.SWM))*(1/(sqrt(4*pi*(D.SWM/(u.SWM*L.SWM)))))
                   *exp(-(((1-time/(V.SWM/FV.SWM))^2)/(4*(D.SWM/(u.SWM*L.SWM))))))
    E.yc3.by <- (FV.SWM/V.by.SWM)*exp(-((FV.by.SWM/V.by.SWM)*time))
    E.yc3   <- if (Parameters[u, 4]==1) {E.yc3.main} else {E.yc3.main + E.yc3.by}
    # output function compartment 4: Stirred tank reactor + Bypass
    E.yc4 <- {((FV.m^2)/(V4*FV))*exp(-(FV.m/V4)*time)}
    # output function compartment 5: Plug flow
    E.yc5 <- {(1/(V5/FV))*(1/(sqrt(4*pi*(D.P/(u.P*L.P5)))))
             *exp(-(((1-time/(V5/FV))^2)/(4*(D.P/(u.P*L.P5)))))}
```

Model II (plug-flow bypass)

```
        # output function compartment 1: Impulse + Pipe / Plug flow
    E.yc1 <- {(1/(V1/FV))*(1/(sqrt(4*pi*(D.P/(u.P*L.P1)))))
             *exp(-(((1-time/(V1/FV))^2)/(4*(D.P/(u.P*L.P1)))))}
    # output function compartment 2: Stirred tank reactor + Bypass
    E.yc2 <- {((FV.m^2)/(V2*FV))*exp(-(FV.m/V2)*time)}
    # output function compartment 3: Plug flow + Dispersion + Bypass
    E.yc3.main <- ((1/(V.SWM/FV.SWM))*(1/(sqrt(4*pi*(D.SWM/(u.SWM*L.SWM)))))
                   *exp(-(((1-time/(V.SWM/FV.SWM))^2)/(4*(D.SWM/(u.SWM*L.SWM))))))

    E.yc3.by <-((1/(V.by.SWM/FV.by.SWM))*(1/(sqrt(4*pi*(D.SWM/(u.by.SWM*L.SWM)))))
                 *exp(-(((1-time/(V.by.SWM/FV.by.SWM))^2)
                 /(4*(D.SWM/(u.by.SWM*L.SWM))))))
    E.yc3   <- if (Parameters[u, 4]==1) {E.yc3.main} else {E.yc3.main+E.yc3.by}
```

```
    # output function compartment 4: Stirred tank reactor + Bypass
    E.yc4 <- {((FV.m^2)/(V4*FV))*exp(-(FV.m/V4)*time)}
    # output function compartment 5: Impulse + Pipe5 / Plug flow
    E.yc5 <- {(1/(V5/FV))*(1/(sqrt(4*pi*(D.P/(u.P*L.P5)))))
             *exp(-(((1-time/(V5/FV))^2)/(4*(D.P/(u.P*L.P5)))))}

    # Input signal: Impulse function
    scaleP.in <- 1/0.1
    shapeP.in <- 100
    E.xin.0 <- (scaleP.in*shapeP.in)*(scaleP.in*time)^(shapeP.in-1)
               *exp(-(scaleP.in*time)^shapeP.in)

    ######### Deconvolution of discrete cumulative distributions


    # Fast Fourier Transform fft() for convolution
    E.Xin.0 <- fft(E.xin.0)
    E.Yc1 <- fft(E.yc1)
    E.Yc2 <- fft(E.yc2)
    E.Yc3 <- fft(E.yc3)
    E.Yc4 <- fft(E.yc4)
    E.Yc5 <- fft(E.yc5)

    # H = Y/X
    E.Hc1 <- E.Yc1/E.Xin.0
    E.Hc2 <- E.Yc2/E.Xin.0
    E.Hc3 <- E.Yc3/E.Xin.0
    E.Hc4 <- E.Yc4/E.Xin.0
    E.Hc5 <- E.Yc5/E.Xin.0
    # Convolution of discrete cumulative distributions: ouput = input * transfer
    out.E.Yc1 <- E.Xin.0*E.Hc1
    out.E.Yc2 <- out.E.Yc1*E.Hc2
    out.E.Yc3 <- out.E.Yc2*E.Hc3
    out.E.Yc4 <- out.E.Yc3*E.Hc4
    out.E.Yc5 <- out.E.Yc4*E.Hc5
    # abbreviation: out.E.Yc5 <- E.Xin.0*E.Hc1*E.Hc2*E.Hc3*E.Hc4*E.Hc5
    conv.E.yc1 <- Re(fft(out.E.Yc1, inverse=TRUE)/length(out.E.Yc1))
    conv.E.yc2 <- Re(fft(out.E.Yc2, inverse=TRUE)/length(out.E.Yc2))
    conv.E.yc3 <- Re(fft(out.E.Yc3, inverse=TRUE)/length(out.E.Yc3))
    conv.E.yc4 <- Re(fft(out.E.Yc4, inverse=TRUE)/length(out.E.Yc4))
    conv.E.yc5 <- Re(fft(out.E.Yc5, inverse=TRUE)/length(out.E.Yc5))

    ######## Calculation of discrete cumulative distribution (cumulative
distribution curve)
    conv.F.yc5 <- rep(NA, length(time))
    for (p in 1:length(time)) {
      conv.F.yc5[p] <- sum(conv.E.yc5[1:p]*0.1)
    }
    conv.F.yc5 <- conv.F.yc5/sum(conv.E.yc5*0.1)
```

```
    # Sum of squared errors
    Parameters[u,5] <- sum((WeibullPlot[1:(tR*10)]-conv.F.yc5[1:(tR*10)])^2)
  }
  RMSE.min <- which.min(Parameters[ ,5])
}
```

O. R script – Displacement of industrial-scale plants

```
#############################
############### Hybrid model II (plug-flow bypass)
#############################

# Load general information
setwd("Z:\\Eigene Dokumente\\...")
AnalysisData <- read.table("AnalysisData.csv")
# [1] Test Series, [2] Experiment Number [3] Protein Concentration (%), [4] Spacer
  Thickness (mil), [5] Hydraulic Diameter [m], [8] Flow Rate (m3/h), [9] Porosity
(-),
  [11] Displacement Time (s), [12] Xanthan Concentration (%)

# Normalized cumulative distribution curves of all experiments in a list
SumCurves <- read.table("SumCurves.csv")
# Flow rates of all experiments in a list
VolumeFlows <- read.table("VolumeFlows.csv")
# Shape and scale parameters of all experiments in a matrix
WeibullParams <- read.table("WeibullParams.csv")
# Denotation of all experiments in a matrix
ExpRuns <- names(SumCurves)
ExpRuns <- ExpRuns[2:length(ExpRuns)]

Parameters <- read.table("Parameters.csv")
# Model parameters of all experiments in a matrix
# [1] axial dispersion coefficient in compartment 3-6, [2] axial dispersion
  coefficient in compartment 1 and 8, [3] share of total volume flow entering
  compartment 2 and 7, [4] share of total volume flow entering compartment 3,
  [5] sum of squared errors

# Volume pipe = PFR
V1 <- pi*((0.0408/2)^2)*(0.35)
# Volume mixing zone = CSTR
V2 <- pi*((0.164/2)^2)*0.205
# Total volume of spiral-wound membrane
V3 <- pi*((0.164/2)^2)*0.96
# Volume mixing zone
V4 <- pi*(((0.164/2)^2)-((0.04/2)^2))*0.14
```

```
# Volume pipe
V5 <- pi*((0.0408/2)^2)*(0.23+0.5)

MultiStage <- matrix(NA, nrow=(length(ExpRuns)), ncol=2)

for (i in 1:length(ExpRuns)) {
  ExpSumCurve <- as.matrix(SumCurves[i+1])
  scaleP <- Weibull_Params_Table[i,2]
  tR <- AnalysisData[i, 11]         # residence time [s]
  time <- seq(0, 2999.9, 0.1)
  FV <- AnalysisData[i,8]/3600      # mean of flow rate during displacement [m3/s]

  time <- seq(0, (length(time)/10-0.1), 0.1)
  shapeP <- Weibull_Params_Table[i,3]
  WeibullPlot <- (1-exp(-(scaleP*time)^shapeP))


  #########
  d.h <- AnalysisData[i, 5]         # hydraulic diameter (Schock & Miquel, Eq. 14)
  c.0 <- AnalysisData[i, 3]         # initial protein concentration (%)
  c.X <- AnalysisData[i, 12]        # xanthan concentration
  # porosity porous medium [-]
  epsilon <- if(d.h==0.000766674) {0.43179589} else if
            (d.h==0.001066011) {0.49987558} else {0.56347376}
  # aspect ratio [-]
  a.R <- if(d.h==0.000766674) {0.587301587} else if
     (d.h==0.001066011) {0.532258065} else {0.553030303}
  # effective area [m2]
  A.eff.SWM <- (((6.3/2)*0.0254)^2)*pi*epsilon
  u.P <- FV/(pi*(0.0408/2)^2)
  L.P1 <- 0.35
  L.SWM <- 0.96
  L.P5 <- (0.23+0.50)
    ########## Output functions of compartments
  D.SWM <- Parameters[i, 1]
  D.P <- Parameters[i, 2]
  FV.m <- FV*Parameters[i, 3]
  FV.by.SWM <- FV*(1-Parameters[i, 4])
  FV.SWM <- if (Parameters[i, 4]==1) {FV} else {FV*Parameters[i, 4]}
  V.by.SWM <- (pi*(((0.164^2)-(0.158^2))/4)*0.96)
  V.SWM <- if (Parameters[i, 4]==1) {V3} else {V3-V.by.SWM}
  u.SWM <- (FV.SWM)/A.eff.SWM
  # 0.52993 = porosity of spacer wrap
  u.by.SWM <- (FV.by.SWM)/((pi*(((0.164^2)-(0.158^2))/4)*0.52993)/epsilon)
```

```
# output function compartment 1: Plug flow
  E.yc1 <- {(1/(V1/FV))*(1/(sqrt(4*pi*(D.P/(u.P*L.P1)))))
           *exp(-(((1-time/(V1/FV))^2)/(4*(D.P/(u.P*L.P1)))))}
  # output function compartment 2: Stirred tank reactor + Bypass
  E.yc2 <- {((FV.m^2)/(V2*FV))*exp(-(FV.m/V2)*time)}
  # output function compartment 3: Plug flow + Dispersion + Bypass
  E.yc3.main <- ((1/(V.SWM/FV.SWM))*(1/(sqrt(4*pi*(D.SWM/(u.SWM*L.SWM)))))
                 *exp(-(((1-time/(V.SWM/FV.SWM))^2)/(4*(D.SWM/(u.SWM*L.SWM))))))
  E.yc3.by <- ((1/(V.by.SWM/FV.by.SWM))*(1/(sqrt(4*pi*(D.SWM/(u.by.SWM*L.SWM)))))
               *exp(-(((1-
time/(V.by.SWM/FV.by.SWM))^2)/(4*(D.SWM/(u.by.SWM*L.SWM))))))
  E.yc3.1   <- if (Parameters[i, 4]==1) {E.yc3.main} else {E.yc3.main+E.yc3.by}
  E.yc3.2   <- E.yc3.1
  E.yc3.3   <- E.yc3.1
  E.yc3.4   <- E.yc3.1
  # output function compartment 4:Stirred tank reactor + Bypass
  E.yc4 <- {((FV.m^2)/(V4*FV))*exp(-(FV.m/V4)*time)}
  # output function compartment 5: Impulse + Pipe5 / Plug flow
  E.yc5 <- {(1/(V5/FV))*(1/(sqrt(4*pi*(D.P/(u.P*L.P5)))))
           *exp(-(((1-time/(V5/FV))^2)/(4*(D.P/(u.P*L.P5)))))}

  # Input signal: Impulse function
  # The shapeP must be reduced from 100 (1 SWM) to 5 (40SWM) because the time
    scale changes from 120 s to 50 min. Otherwise, the Fourier transformation
    introduces NaNs.
  scaleP.in <- 1/0.1
  shapeP.in <- 5
  E.xin.0 <- (scaleP.in*shapeP.in)*(scaleP.in*time)^(shapeP.in-1)
             *exp(-(scaleP.in*time)^shapeP.in)


  ################ Deconvolution of discrete cumulative distributions


  # Fast Fourier Transform fft() for convolution
  E.Xin.0 <- fft(E.xin.0)
  E.Yc1 <- fft(E.yc1)
  E.Yc2 <- fft(E.yc2)
  E.Yc3.1 <- fft(E.yc3.1)
  E.Yc3.2 <- fft(E.yc3.2)
  E.Yc3.3 <- fft(E.yc3.3)
  E.Yc3.4 <- fft(E.yc3.4)
  E.Yc4 <- fft(E.yc4)
  E.Yc5 <- fft(E.yc5)



  # H = Y/X
  E.Hc1 <- E.Yc1/E.Xin.0
```

```
  E.Hc2 <- E.Yc2/E.Xin.0
  E.Hc3.1 <- E.Yc3.1/E.Xin.0
  E.Hc3.2 <- E.Yc3.2/E.Xin.0
  E.Hc3.3 <- E.Yc3.3/E.Xin.0
  E.Hc3.4 <- E.Yc3.4/E.Xin.0
  E.Hc4 <- E.Yc4/E.Xin.0
  E.Hc5 <- E.Yc5/E.Xin.0

  # Convolution of discrete cumulative distributions: output = input * transfer
  out.E.Yc5 <- E.Xin.0*E.Hc1*E.Hc2*E.Hc3.1*E.Hc3.2*E.Hc3.3*E.Hc3.4*E.Hc4*E.Hc5
# *E.Hc1*E.Hc2*E.Hc3.1*E.Hc3.2*E.Hc3.3*E.Hc3.4*E.Hc4*E.Hc5 ...
                    # append desired number of additional housings

  conv.E.yc5 <- Re(fft(out.E.Yc5, inverse=TRUE)/length(out.E.Yc5))


  ############# Calculation of discrete cumulative distribution

  conv.F.yc5 <- rep(NA, length(time))
  for (p in 1:length(time)) {
    conv.F.yc5[p] <- sum(conv.E.yc5[1:p]*0.1)
  }
  conv.F.yc5 <- conv.F.yc5/sum(conv.E.yc5*0.1)

  tR.SM <- time[which.max(WeibullPlot>0.99)]                # SM = single module
  tR.MS <- time[which.max(conv.F.yc5>0.99)]                 # MSP = multi stage
  if(length(tR.MS)==0){next}
  MultiStage[i,1] <- tR.SM
  MultiStage[i,2] <- tR.MS
}
```